UNIVERSITY OF SOUTHAMPTON

FACULTY OF ENGINEERING AND THE ENVIRONMENT

INSTITUTE OF SOUND AND VIBRATION RESEARCH

Aerodynamic Broadband Noise from Contra-Rotating Open Rotors

by

Vincent Blandeau

Thesis for the degree of Doctor of Philosophy

March 2011

To my parents and Charlotte

UNIVERSITY OF SOUTHAMPTON

ABSTRACT

FACULTY OF ENGINEERING AND THE ENVIRONMENT
INSTITUTE OF SOUND AND VIBRATION RESEARCH

Doctor of Philosophy

Aerodynamic Broadband Noise from Contra-Rotating Open Rotors

by Vincent Blandeau

In recent years, there has been growing interest in contra-rotating open rotors (CRORs) for use as the power plants on aircraft, since they are estimated to burn 20% to 30% less fuel than equivalent turbofan engines for short-haul flights. However, one of the main challenges for their introduction is their very high levels of noise emissions. There is therefore a need for schemes by which the noise from CRORs can be predicted and hence reduced. Nearly all of the research effort on the prediction and reduction of CROR noise has been so far focused on the tonal component, whereas broadband noise emissions remain poorly understood. Nevertheless, it is shown that broadband noise emissions from CRORs can be significant, hence the necessity of the present research.

In this thesis, broadband noise emissions from uninstalled CRORs are investigated for the first time. It is assumed that the two most significant sources of broadband noise in uninstalled CRORs are the broadband rotor-wake/rotor interaction noise (BRWI) and the broadband rotor trailing edge noise (BRTE). Fast semi-analytical prediction schemes are developed for these sources of broadband noise, which exhibit good agreement with noise measurements from a scaled model CROR. The relative importance of the BRWI and BRTE noise sources is investigated for a realistic CROR configuration at assumed take-off, cruise and approach-type conditions. It is predicted that both broadband noise sources are significant at assumed take-off, whereas only the BRTE noise contributes to the total broadband noise emissions at assumed cruise and approach. A parameter study is conducted to investigate the effects on CROR broadband noise emissions of variations in rotor-rotor separation distance, rotor speed and blade number at constant engine power, torque split and solidity.

The validity of two widely used approximations for fan broadband noise predictions is also studied: Amiet's approximate BRTE model and the use of isolated airfoil theory for turbulence-cascade interaction noise. Criteria for the validity of Amiet's approximate model are established by comparing it to the general BRTE noise model developed in this work. The two models are shown to differ in the low and high frequency limits, but excellent agreement is observed for realistic rotor configurations over most of the audible frequency range. In addition, sound power predictions from isolated airfoils and blade cascades in a turbulent flow are compared. Excellent agreement is observed between an isolated airfoil model and a cascade model for frequencies higher than a critical frequency. Below this critical frequency, agreement is poor for high solidity cascades but is reasonable for low solidity cascades, typical of CRORs, thus validating the use of isolated airfoil theory in the BRWI model.

Contents

List of Tables

List of Figures

Declaration of authorship

I, VINCENT BLANDEAU, declare that the thesis entitled 'Aerodynamic Broadband Noise from Contra-Rotating Open Rotors' and the work presented in the thesis are both my own, and have been generated by me as the result of my own original research. I confirm that:

- this work was done wholly or mainly while in candidature for a research degree at this University;
- where any part of this thesis has previously been submitted for a degree or any other qualification at this University or any other institution, this has been clearly stated;
- where I have consulted the published work of others, this is always clearly attributed;
- where I have quoted the work of others, the source is always given. With the exception of such quotations, this thesis is entirely my own work;
- I have acknowledged all main sources of help;
- where the thesis is based on work done by myself jointly with others, I have made clear what was done by others and what I have contributed myself;
- parts of this work have been published, as listed in Section 1.4.

Signed:.....

Date:.....

Acknowledgements

First and foremost, I would like to express my deep gratitude to my supervisor Phil Joseph for his invaluable support and his constant availability, which were critical for the completion of this work. His enthusiasm, his encouragement and his cheerful nature were greatly appreciated. It was a real pleasure to work with him at the Institute of Sound and Vibration Research (ISVR).

I received a generous financial help for my doctoral studies from the FP7 European project DREAM (valiDation of Radical Engine Architecture systeMs) and from Rolls-Royce plc., for which I am very grateful.

During the realisation of this research, I had the chance to have a number of fruitful collaborative interactions with many individuals, to whom I am greatly indebted. In particular, I wish to thank: Tony Parry, Stéphane Baralon and Alexios Zachariadis, from Rolls-Royce, as well as Mike Kingan, Brian Tester, Gwénaël Gabard, Gareth Jenkins and Chris Powles, from the ISVR. Special thanks go to Tony Parry, who regularly provided essential feedback and guidance on my work. I would also like to thank Sue Brindle and Maureen Mew, from the ISVR, for the quality of their management of administrative affairs, and my examiners Alan McAlpine and Nigel Peake, for the time spent to appraise this work.

I spent three very nice years in Southampton and met many people who became good friends and who are all warmly thanked. In particular, I wish to thank the students and post-docs from the ISVR for all the nice times and for contributing to a unique atmosphere, in the office and/or in the pub, namely: Mat, Albert, Prathiban, Delphine, George, Olivier, Saverio, Jack, Adriana, Martina, Samuel, Mike, Gareth, Katie, Niamh, Chris P., Chris L. and Chris H., Mahdi, Phil McL., Carlos, Luis, Zbigniew, Vincent J., Greg, Oliviero, Eugene, Emmet, Odenir, Feargus, Hessam, Prateek, Iansteel, and many others...

Finally, I would like to thank my parents and family, whose help and advice have been precious during all my studies. And, last but not least, a big thank you to Charlotte, whose presence, love and support during these three years, and despite the distance, gave me the energy to carry this work through and has been indispensable.

Nomenclature

Abbreviations

BRTE	Broadband noise due to Rotor Trailing Edge interaction
BRWI	Broadband noise due to Rotor-Wake/rotor Interaction
CAA	Computational Aeroacoustics
CFD	Computational Fluid Dynamics
CROR	Contra-Rotating Open Rotors
FW-H	Ffowcs Williams and Hawkings equation.
OAPWL	OverAll sound PoWer Level [dB]
PSD	Power Spectral Density
PWL	sound PoWer Level [dB]
SPL	Sound Pressure Level [dB]
SROR	Single Rotating Open Rotors

Greek Letters

α	blade stagger angle
$\bar{\omega}$	$\bar{\omega} = \omega\delta^*/U_X$
β_C	Clauser's pressure gradient parameter
β_X	$\beta_X = \sqrt{1 - M_X^2}$
Δl_r	spanwise correlation length of the unsteady blade loading [m]
Δr	strip width [m]
ΔSPL_{high}	high frequency error of Amiet's BRTE model [dB]
ΔSPL_{low}	low frequency error of Amiet's BRTE model [dB]
δ	boundary layer thickness [m]
$\delta\,(.)$	Dirac delta function
$\delta\,[.]$	Kronecker delta function
δ^*	displacement thickness [m]
Δp	unsteady blade loading (or 'pressure jump') [kg.m^{-1}.s^{-2}]
η	rotor-rotor axial separation distance (at the hub) [m]
κ_l	aeroacoustic coupling wavenumber in BRTE model [m^{-1}]
κ_{qmn}	aeroacoustic coupling wavenumber in BRWI model [m^{-1}]
μ_a	acoustic reduced frequency, $\mu_a = \frac{k_X M_X b}{\beta_X^2}$

μ_h	hydrodynamic reduced frequency, $\mu_h = \frac{k_X b}{\beta_X^2}$
ν	kinematic viscosity [$m^2.s$]
Ω	rotor angular speed [$rad.s^{-1}$]
ω	angular frequency [$rad.s^{-1}$]
ω_ϕ	Doppler-shifted angular frequency in Amiet's BRTE model [$rad.s^{-1}$]
ω_l	Doppler-shifted angular frequency in the exact BRTE model [$rad.s^{-1}$]
ω_{qmn}	interaction angular frequency in BRWI model [$rad.s^{-1}$]
Φ_{pp}	wavenumber spectrum of the surface pressure [$Pa^2.s$]
Φ_{ww}	wavenumber spectrum of the turbulent upwash velocity [$m^5.s^{-2}$]
Π	Cole's wake law parameter
ψ	azimuthal angle for the chordwise location of the source
ρ_0	density of fluid [$kg.m^{-3}$]
τ	source emission time [s]
τ_w	wall shear stress [Pa]
Θ	momentum thickness [m]

Roman Letters

$\bar{r}$	spanwise location of the midpoint of the j^{th} strip [m]
$\mathcal{L}^{\mathrm{LE}}$	unsteady loading term due to leading edge interaction
$\mathcal{L}^{\mathrm{TE}}$	unsteady loading term due to trailing edge interaction
$\mathcal{P}$	sound power [W.s]
$\overline{w^2}$	mean square turbulent velocity [$m^2.s^{-2}$]
a	empirical wake parameter, $a = 0.637$
$A(\theta, M_X)$	$A(\theta, M_X) = \sqrt{1 - M_X^2 \sin^2\theta}$
AoA	angle of attack of the rotor blades [deg]
B	rotor blade number
b	$b = c/2$ [m]
b_W	half-wake width [m]
c	blade chord length [m]
c_0	speed of sound [$m.s^{-1}$]
C_d	drag coefficient
C_f	skin friction coefficient, $C_f = \tau_w / \left(0.5\rho_0 U_X^2\right)$
c_l	azimuthal phase speed of the mode l [$m.s^{-1}$]
C_p	pressure coefficient
d	azimuthal gap between blades [m]
D_ϕ	directivity term of Amiet's BRTE model
D_l	modal directivity term of the BRTE model
D_{ml}	modal directivity term of BRWI noise model [m^{-1}]
E^*	complex conjugate of the Fresnel integral
F	function for the effects of flow on sound power radiation (Eq. B.5)
f_c	critical frequency at which the first cascade mode cuts on [Hz]
f_m	Fourier components of wake profile

f_W	wake profile function
f_{high}	high frequnecy limit of validity of Amiet's BRTE model [Hz]
f_{low}	low frequency limit of validity of Amiet's BRTE model [Hz]
f_{shaft}	shaft frequency, $f_{shaft} = \Omega/2\pi$ [Hz]
g^{LE}	flat plate response function due to leading edge interaction
g^{TE}	flat plate response function due to trailing edge interaction
k_e	$k_e = \frac{\sqrt{\pi}}{L}\frac{\Gamma(5/6)}{\Gamma(1/3)}$
k_0	acoustic wavenumber, $k_0 = \omega/c_0$ [m^{-1}]
$K_{X,l}$	discrete values taken by k_X in the BRTE model [m^{-1}]
$K_{X,qmn}, K_{Y,qmn}$	discrete values taken by k_X and k_Y in the BRWI model [m^{-1}]
L	turbulence integral lengthscale [m]
l	azimuthal acoustic mode order
l_r	spanwise correlation length of surface pressure [m]
l_{max}	limit above which the azimuthal modes l are cut-off
m, n	scattering indices for front and rear rotors respectively
M_X	$M_X = U_X/c_0$
M_x	flight Mach number
M_ϕ	$M_\phi = U_\phi/c_0$
m_{max}	limit for summation over m
N_j	number of strips
q	turbulence azimuthal mode order
R_0	distance between observer and point source on a rotor blade [m]
r_0	distance between the observer and the centre of the rotor disk [m]
R_T	ratio of outer-to-inner timescales of boundary layer, $R_T = (u_\tau\delta/\nu)\sqrt{C_f/2}$
Re_c	chord-based Reynolds number
S	Sears function
s	airfoil sweep distance [m]
S_2	total surface area of rear rotor blades [m^2]
S_{pp}	PSD of the far-field radiated pressure [Pa^2.s.rad^{-1}]
S_{qq}	wavenumber cross-spectrum of the surface pressure [$\mathrm{kg}^2.\mathrm{m}^{-1}.\mathrm{s}^{-3}$]
T	averaging time [s]
t	observer time [s]
u_0	mean wake centerline velocity deficit [m.s$^-$1]
U_c	eddy convection velocity in the boundary layer [m.s^{-1}]
U_ϕ	rotor tangential speed [m.s^{-1}]
u_τ	friction velocity [m.s^{-1}]
U_X	free stream velocity relative to the chord of the rotor blades [m.s^{-1}]
w	upwash velocity of isotropic homogeneous turbulence [m.s^{-1}]
w_W	upwash velocity from turbulent wakes [m.s^{-1}]
$\mathcal{W}$	upwash velocity of turbulence in wavenumber domain [$\mathrm{m}^4.\mathrm{s}^{-1}$]
X_η	helical convection distance of the front rotor wakes [m]

X_Θ	normalised helical convection distance of the front rotor wakes

Symbols

$\breve{(.)}$	quantity expressed following Chapman's similarity rule
$\hat{(.)}$	quantity expressed in the frequency domain
$(.)_i$	$i = 1, 2$ denotes a quantity associated to the front or rear rotor respectively
$(.)_{1/3}$	noise level integrated over third-octaves
$[.]_t$	quantity expressed at observer time
$\langle . \rangle$	expected value
$\tilde{(.)}$	quantity in a rotating reference frame fixed to a blade

Vectors and Matrices

(r_0, θ, ψ_0)	spherical coordinate system for far-field observer
(x_2, y_2, z_2)	Cartesian coordinate system with origin at centre of rear rotor disk
$\mathbf{k} = (k_r, k_X, k_Y)$	turbulent wavenumber vector of incoming gust, [m^{-1}]
$\mathbf{x}_i = (r, x_i, \phi_i)$	cylindrical coordinate system bound to an airfoil
$\mathbf{X}_i = (r, X_i, Y_i)$	cylindrical coordinate system bound to an airfoil
$d\mathbf{F}$	elemental force vector exerted on the fluid by an element of the rotor blade [$\mathrm{N.m}^{-2}$]

Chapter 1

Introduction

1.1 Contra-Rotating Open Rotors

Since the introduction of the first jet airliners in the 1950s, there has been a continuous effort to reduce the impact of air transport on the communities around airports, in terms of air quality (reduction of NO_x and particulate matter emissions), climate change (reduction of CO_2 emissions) and aircraft noise. Global air traffic is expected to increase significantly in the next 20 years, by approximately 5% per year for passenger flights and 6% per year for freight (Airbus [4], Boeing [33]). There is, therefore, an urgent need for the aerospace community to design, integrate and validate new concepts of aircraft engines to reduce fuel consumption and noise emissions, in agreement with the environmental ACARE goals for 2020 (ACARE [2]).

The use of Contra-Rotating Open Rotors (CRORs, see Fig. 1.1) as an alternative to turbofan engines for power plants on aircrafts is one of the most promising strategies for meeting the ACARE goals regarding NO_x and CO_2 emissions (DREAM proposal [54]), since they are estimated to burn up to 20% to 30% less fuel than equivalent turbofan engines and 5% less fuel than equivalent Single-Rotating Open Rotors (SRORs), for short-haul flights (see for example Ref. [145, 18]). Contrary to traditional turbofans, the absence of a duct in SRORs and CRORs yields a very high effective bypass ratio, thus resulting in improved propulsive efficiency at low flight speeds, and thus most suitable for short-haul flights. In addition to this, the rear contra-rotating rotor in CROR engines converts the azimuthal velocity component of the flow downstream of the front rotor (or 'swirl') into additional axial thrust and, therefore, yields an increased efficiency compared to SRORs.

One of the main challenges for the introduction of CRORs in civil aviation, which led to the rejection of the concept in the early 1990s, is their very high levels of noise emissions. Since there is now a strong desire from the industry to continue with the investigation of the use of CRORs, there is the need to identify strategies to reduce their noise. As for gas-turbine

(a) (b)

Figure 1.1: Contra-rotating open rotors in (a) puller and (b) pusher configuration. Credits Rolls-Royce.

engines, CRORs are complex aeroacoustic systems in which a large number of different tonal and broadband noise sources are present. The noise emissions of CRORs exhibit a highly dissonant tonal content which is generally much higher in level than the tonal noise of equivalent SRORs. This feature is shown in Fig. 1.2 (reproduced from Hubbard [93]) where measurements of the sound pressure level (SPL) are presented for a CROR and a SROR engines with the same blade number and geometry, operated at the same tip speed and at the same power per rotor. The additional tonal noise sources in CRORs, compared to SRORs, can be due to the interaction of the viscous wakes and the tip-vortex shed from the front rotor with the rear rotor and to the interaction of each rotor with the potential field of the other rotor, if the gap between the two rotors is small (see Hanson [85], for example).

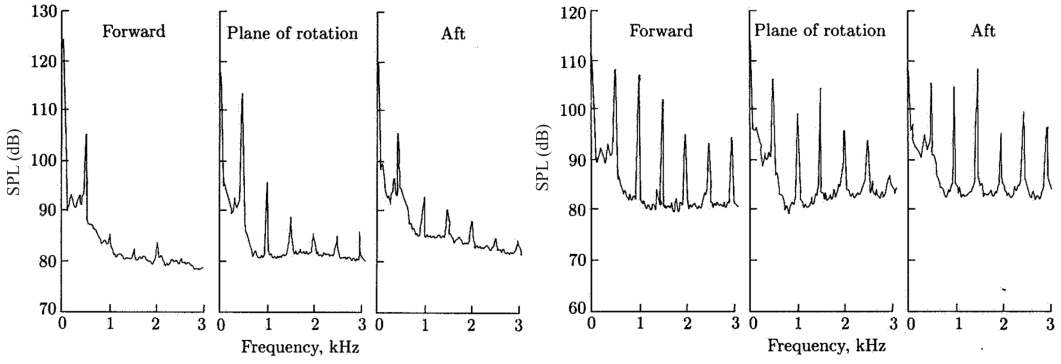

Figure 1.2: Example of measured sound pressure levels from (a) a SROR and (b) a CROR. Reproduced from Hubbard [93].

Because of their high level of tonal noise emissions, nearly all of the research effort on the prediction and reduction of CROR noise has been focused on the tonal component (see Section 1.3.3). However, broadband noise emissions from CRORs remain poorly understood and prediction methods are not in existence (except for the rotor trailing edge noise, which is a source of broadband noise common to all fans; see Section 1.2.2). The main aim of this

thesis is to provide such prediction methods and to improve the understanding of broadband noise emissions from CRORs.

1.2 Broadband noise emissions of CRORs

1.2.1 Significance of broadband noise emissions of CRORs

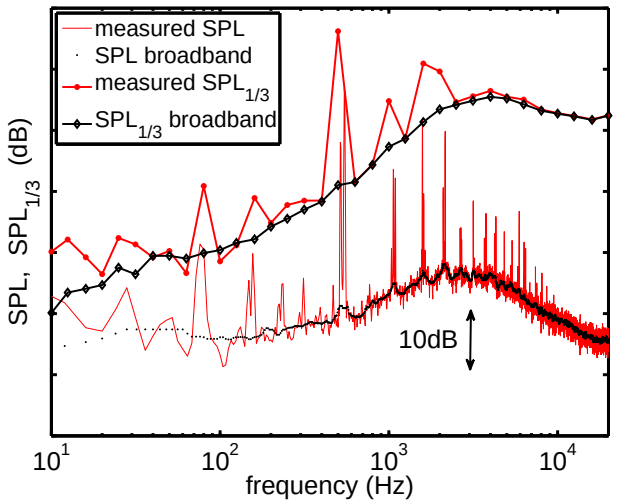

Figure 1.3: Contribution of the broadband component in noise measurements of a 1/5-scale CROR model, from a Rolls-Royce rig, in the plane of the rear rotor disk.

The broadband noise component of CROR noise has often been regarded as insignificant compared to the tonal noise component (Hubbard [93], for example). However, the research effort in the 1980s and early 1990s has produced several concepts by which the tonal noise of CRORs can be significantly reduced, such as reducing the rear rotor diameter to avoid tip-vortex interaction noise, using swept rotor blades and choosing appropriate blade numbers to minimise interaction tones.

Figure 1.3 presents the noise measurements of a $1/5^{\text{th}}$ scale, 7x7 bladed CROR model, performed by Rolls-Royce in the late 1980s (Kirker [102]). Measured narrow band and third octave sound pressure levels (denoted by SPL and $\text{SPL}_{1/3}$, respectively) are presented. The contribution of the broadband noise has been extracted from the measured data using a median filtering technique and is also shown. The experimental data shown here were recorded by a microphone at 90° from the engine axis in the transonic windtunnel of the Aircraft Research Association (ARA) in Bedford, United Kingdom. Although the measured SPL is rich in tones that protrude above the broadband noise up to about 10kHz, the contribution of the tones to $\text{SPL}_{1/3}$ is weak compared to the broadband noise at frequencies above 2000Hz for this configuration. Note that, since these results were obtained from measurements on a $1/5^{\text{th}}$ scale model, the frequency above which the contribution of the

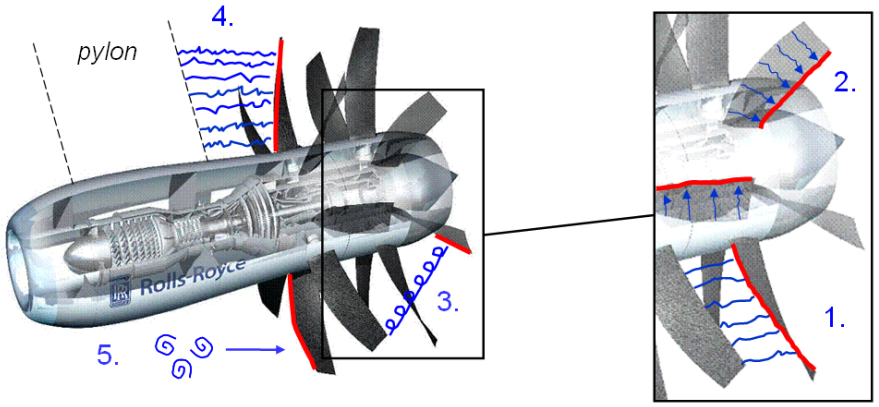

Figure 1.4: Possible main sources of broadband noise in an installed CROR : (1) rotor-wake/rotor interaction noise, (2) rotor trailing edge noise, (3) tip-vortex interaction noise, (2) pylon-wake/rotor interaction noise, (5) turbulence ingestion noise.

broadband noise is dominant would be approximately 400Hz for an equivalent full scale CROR.

However, although Fig. 1.3 shows that broadband noise is significant for a single CROR configuration, a more complete study is required to analyse the relative importance of tonal and broadband noise emissions in CRORs for a range of configurations and operating conditions. Such a parameter study could be performed by using fast prediction methods, such as semi-empirical models, to predict tonal and broadband noise. One of the main aims of the present research (see Section 1.4) is to develop such tools for broadband noise predictions.

Note that the experimental data shown in Fig. 1.3 was extracted and analysed by Brian Tester, associate consultant at the Institue of Sound and Vibration Research, as part of a joint study.

1.2.2 Possible sources of broadband noise in CRORs

Since there has been no investigation of CROR broadband noise prior to the current research, it is difficult to know *a priori* which aerodynamic processes can be a significant source of broadband noise. However, possible sources of broadband noise from CRORs can be listed by analogy with the broadband noise of turbofans and SRORs, for which there is much more work in the literature. Taking this approach, the main possible sources of broadband noise in an installed CROR, in a pusher configuration (see Fig. 1.4), have been identified as:

1. The impingement of the turbulent wakes shed from the front rotor onto the leading edge of the rear rotor blades.

2. The interaction of the boundary layer turbulence of each rotor blades (front and rotor) with their trailing edge (or rotor 'self-noise').

3. The impingement of the turbulent tip-vortex of the front rotor onto the leading edge of the rear rotor blades.

4. The impingement of the turbulent wake shed from an upstream pylon onto the leading edge of the front rotor blades.

5. The ingestion of turbulence by the front rotor (atmospheric turbulence, fuselage boundary layer turbulence, etc.).

Sources 4 and 5 are greatly affected by the location of the engines on the aircraft (wing or tail mounting, proximity of the fuselage boundary layer, etc.) and by the choice of CROR configuration (pusher or puller). At the time of writing, the installation of CRORs is still subject to many uncertainties and it is not clear yet whether the puller or the pusher configuration will be retained as the best option for CRORs. It has therefore been decided that the current research would be focused on the broadband noise from *uninstalled* CRORs and that sources 4 and 5 will not be considered here.

Moreover, in modern CROR designs, the diameter of the rear rotor is often less than that of the front rotor, in order to avoid the impingement of the front rotor tip-vortex onto the rear rotor. This design has been shown to reduce significantly the tonal noise induced by tip-vortex interaction and is expected to have a similar impact on broadband noise emissions, i.e. source 3 in the list above. The two main sources of broadband noise in modern uninstalled CRORs are, therefore, expected to be the broadband noise due to rotor-wake/rotor interaction (source 1, denoted by BRWI) and the broadband noise due to rotor trailing edge interaction (source 2, denoted by BRTE). The main aim of the current research is to develop models for the prediction of these two sources of broadband noise, to understand their relative importance, and to suggest strategies for their reduction.

1.3 Literature review

In this section, existing methods used to model the BRTE noise are first reviewed. No model for BRWI noise was in existence prior to this study, but many models for the noise due to turbulence/leading edge interaction, which quantifies the source of BRWI noise, are available and reviewed in this section. Since the vast majority of the literature on CROR noise focuses on tonal noise, the existing methods for the prediction of CROR tonal noise are also presented. Finally, a review of the main experimental results of CROR noise is provided.

1.3.1 Prediction of rotor trailing edge broadband noise

Methods to predict BRTE noise (source 2 in Section 1.2.2) are already in existence in the literature, since this mechanism is the dominant source of broadband noise in all fans operating in a non-turbulent flow. The modelling of the source of BRTE noise, which is the interaction of the boundary layer turbulence with the blade trailing edge, is reviewed first in this section. A review of existing methods for the application of such source models to the BRTE noise radiated by rotating blades is then provided.

1.3.1.1 Turbulence/trailing edge interaction noise

Many models have been developed since the 1970s to predict the noise radiation due to trailing edge interaction, with particular application to the trailing edge noise of stationary blades in a uniform flow. These methods can be classified into two main groups: semi-analytical models, which often assume that the blades are thin unloaded flat plates, and numerical models, which have the capability to treat real airfoil geometries. An overview of these methods is presented below.

Analytical models

Early semi-analytical models for predicting the radiated noise due to trailing edge interaction (Ffowcs Williams and Hall [62] (1970), Crighton and Leppington [48] (1970) and others; see the review by Howe [89] (1978)) were derived by considering trailing edge interaction as the scattering of a distribution of quadrupole sources by a half-plane and using the acoustic analogy of Lighthill [104] (1952) to predict the radiated noise. This approach is rarely used, however, due to the difficulty in identifying the turbulence input. A widely used alternative approach (from the work of Chase [42, 43] (1972, 1975), Chandiramani [40] (1974) and Amiet [8, 11] (1976, 1978)), which is consistent with the previous method, is to consider that the source of trailing edge noise is quantified by the convected surface pressure beneath the turbulent boundary layer, close to the trailing edge, which is expressed in terms of its wavenumber spectrum. This approach is consistent with the previous one but has been more widely used, since the surface pressure spectrum is a quantity easier to identify than the distribution of quadrupole sources.

More recently, Glegg [71] (1998) derived a model that takes into account the effects of the acoustic scattering by adjacent blades (or 'cascade effects') on the trailing edge noise radiated by a fan blade. These effects are not expected to be significant for low-solidity fans, like CRORs, however and are not included in the present work. Moreover, all the aforementioned models neglect the effects of the back-scattering of the trailing edge noise by the leading edge of the blade. These effects were first modelled by Howe [91] (2001), for low Mach number flows, and then by Roger and Moreau [130] (2005) for arbitrary

Mach numbers. Roger and Moreau also showed that the effects of back-scattering are only significant at reduced frequencies less than 1 and for low Mach number flows; these effects are therefore likely to be negligible in high speed propellers such as CRORs and are not included in the present work.

CAA methods

The recent growth in computer power has allowed a number of computational aeroacoustics (CAA) methods to be used to predict the trailing edge noise of stationary blades. These methods are often based on acoustic analogies and, therefore, take the approach of splitting the computational domain between the source region, which is treated using computational fluid dynamic (CFD) techniques, and the acoustic domain, which is treated using a propagation model. Many propagation models can be used for the problem of trailing edge noise but the accurate description of the source of broadband noise is difficult and has been the focus of many authors in recent years. The most accurate numerical methods to predict trailing edge noise are Direct Numerical Simulations (DNS; see Sandberg et al. [137] (2007), Sandberg and Sandham [136] (2008), Jones et al. [96] (2008), for example), in which the Navier-Stokes equation is solved by including all the scales of the turbulent flow and, therefore, avoiding any modelling approximation. However, DNS methods require a very high computational effort and are so far limited to low Reynolds number flows, which prohibits their use for aeroengine applications. For example, the chord-based Reynolds number of the flow in Sandberg and Jones [135] (2010) is $Re_c = 5 \times 10^4$, whereas the Reynolds numbers of interest in CRORs are generally about $Re_c \approx 5 \times 10^6$. Other numerical methods (Large Eddy Simulations, Detached Eddy Simulations, stochastic methods, etc.) to predict trailing edge noise can be applied to much higher Reynolds numbers than DNS methods, at the cost of modelling approximations of the turbulent flow field. However, their high computational cost makes them unsuitable for use in parameter studies from which strategies for broadband noise reduction can be deduced, and which are of interest in the present work. The use of semi-analytical models to quantify the source of the BRTE noise radiation in CRORs is therefore preferred to CAA techniques in the present work.

1.3.1.2 Trailing edge noise radiation from rotating blades

Two approaches are generally used to predict the broadband trailing edge noise radiated from rotating blades: the methods based on the exact Ffowcs Williams and Hawkings equation (noted here FW-H, see Ref. [63] (1969)) and the methods based on Amiet's approximate model, as described below.

The first general framework for broadband noise predictions from rotating blades is generally attributed to Ffowcs-Williams and Hawkings [64] (1969), who applied the exact FW-H equation to point dipole sources in circular motion, but without specifying the nature of the

source of sound. Kim and George [100] (1982) were the first to use the exact FW-H equation to develop a model of trailing edge noise for rotating blades, but they approximated the unsteady blade loading along the chord as a point force. The model of Kim and George has been subsequently extended by Glegg and Jochault [76] (1998) for ducted fans and using a cascade response function [71] (1998), and by Zhou and Joseph [159] (2006) for open propellers using Amiet's isolated airfoil response function [8, 11] (1976, 1978), extended to take into account the contribution of skewed gusts.

The FW-H approach for predicting the noise due to rotating blades was considered as computationally expensive when it was first introduced in the 1970s. In response, therefore, a simplified alternative approach was proposed by Amiet [10] (1977). This approach, which has been widely used since, consists of approximating the circular motion of the blades by a series of translations of the blades over an infinitesimally short distance. Amiet's approach was claimed to be valid at high frequencies and low rotor speed, where the effects of rotation on the noise are small. Amiet's method has been first applied to the leading edge rotor noise by Paterson and Amiet [125] (1979) and to trailing edge rotor noise by Schlinker and Amiet [138] (1981). This formulation has since been extensively used in recent years and applied to the prediction of leading edge and trailing edge broadband noise of low-speed fans (see for instance Rozenberg et al. [134] (2010), Roger et al. [132] (2006), Fedala et al. [61] (2010)), helicopter rotor (Amiet [13] (1989), Amiet et al. [14] (1990)), wind turbines (Glegg et al. [73] (1987)) and open propeller broadband noise (Pagano et al. [119] (2010)). However, the validity of the approximations made in Amiet's approach has not been studied previously. This is discussed in the present thesis in Chapter 5.

Casper and Farassat [39] (2004) developed a time-domain model for the trailing edge noise of a stationary airfoil in a flow. They used the flat plate response function of Amiet to validate their method but claimed that it can be applied to the prediction of the trailing edge noise from rotating blades with realistic geometry. Casper and Farassat's method has been recently applied to the prediction of trailing edge noise from rotating blades by Barbarino et al. [17]. However, such time-domain methods present a significant computational overhead compared to frequency-domain methods, due to the difficult estimation of retarded times. In the present thesis, a frequency-domain rotor trailing edge noise model is derived in Chapter 3 by extending the model due to Kim and George [100] to take into account the effects of non-compact sources.

1.3.2 Prediction of rotor-wake/rotor interaction broadband noise

Unlike BRTE noise, reviewed in Section 1.3.1, the problem of broadband noise due to rotor-wake/rotor interaction (BRWI) (source 1 in Section 1.2.2) is encountered only in CRORs and has not been addressed before. However, many models are in existence for the source of BRWI broadband noise, which is characterised by the unsteady loading of the rear rotor blades due to the impingement of turbulence on their leading edge. A review of the general

problem of the broadband noise due to the impingement of turbulence on the leading of a blade is provided in this section.

1.3.2.1 Turbulence/leading edge interaction noise

Flat plate response functions

The prediction of the unsteady loading of airfoils due to the interaction with flow inhomogeneities has been of interest for aerodynamicists and aeroacousticians since the 1930s. The foundations of this research topic were laid through the pioneering work of Sears [140] (1941), who first derived an analytical model for the unsteady lift and moment of a flat plate encountering a 2D incompressible sinusoidal gust. A vast amount of research has since been done to extend this approach to more realistic geometries and flow conditions. In the 1970s, analytical solutions were derived to extend the Sears approach to 2D compressible flows (Osborne [118] (1973) and Amiet [5] (1974), for example, both valid at low reduced frequency only) and 3D incompressible flows (Filotas [65] (1969), Graham [79] (1970) and others). A closed-form solution for the general 3D compressible problem cannot be obtained analytically, but Graham [80] (1970) found that the general problem can be deduced from the 2D compressible and the 3D incompressible problems, for which analytic solutions can be derived, depending on whether the spanwise phase speed of the gust at the airfoil leading edge is subsonic or supersonic. An alternative approximate approach to derive the unsteady loading of a flat plate encountering a compressible gust is to consider that the contribution of the initial leading edge interaction and the contribution of the trailing edge back-scattering can be separated. Taking this approach, which is valid at high reduced frequency, Adamczyk [3] (1974) and later Amiet [7] (1976) derived closed-form flat plate response functions in the form of a sum of two terms, representing the leading edge interaction and the trailing edge back-scattering.

Single airfoil models

Amiet [6] (1976) used the aforementioned aerodynamic flat plate theories to predict broadband noise emissions due to a stationary airfoil in a turbulent flow. For this purpose, he proposed a quasi closed-formed approach by using either his low frequency flat plate response function (Ref. [5] (1974)) or the high frequency response function of Adamczyk [3] depending on whether the reduced wavelength of the gust was, respectively, larger or smaller than a quarter of the airfoil chord. Paterson and Amiet [124] (1977) validated experimentally Amiet's leading edge broadband noise model and investigated the approximation of unloaded, thin flat plate. They showed that the effects of angle of attack on the radiated noise were small but that the noise from thick airfoils was underpredicted at high frequency due to the use of flat plate models. This observation was subsequently confirmed by several

studies, for example by the analytical studies of Gershfeld [70] (2004) and Glegg and Devenport [74] (2009) and the experiments of Devenport et al. [50] (2010). Recently, Glegg and Devenport [75] (2010) developed a panel method to model the unsteady blade loading and the radiated noise due to airfoils of arbitrary shape in a turbulent flow, which was shown to be accurate up to a reduced frequency of 40. Noise predictions using this panel method exhibited good agreement (within 2dB or better) with the noise measurements of Devenport et al. [50] for three different airfoils under investigation, of varying thickness, chord and camber. However, the thickness of CROR blades is generally small and, therefore, the flat plate approximation made in Amiet's model is assumed to be reasonable in the present work.

Blade cascades

For high solidity blade cascades, acoustic interference between adjacent blades must be taken into account in the modelling of the unsteady blade loading, and hence sound radiation. The unsteady loading of a blade in a cascade due to the impingement of a vortical gust is generally expressed in terms of an integral equation, that can be solved either numerically using the co-location technique (see Smith [143] (1972) and Whitehead [149] (1987)) or analytically using the Wiener-Hopf technique (see Peake [126] (1993), Glegg [72] (1999) and Posson [128, 129] (2010), for example). The computational effort required to compute broadband noise radiation using these cascade methods is, however, much larger than using the single airfoil methods presented above. Due to the low solidity of CRORs, cascade effects are expected to be of moderate importance for CROR noise radiation, but it is unclear whether these effects can be ignored. This will be discussed in Chapter 6 of the present thesis.

CAA methods

As for the trailing edge noise, reviewed in Section 1.3.1.1, CAA techniques have also been applied by several authors to predict the broadband noise due turbulence/leading edge interaction (see for example Casalino et al. [37] (2003), Ewert et al. [59] (2010), Dieste and Gabard [51] (2010), Atassi and co-workers [139, 15] (1995, 2004) and others). However, as discussed in Section 1.3.1.1 for rotor trailing edge noise prediction, the use of CAA techniques to predict CROR leading edge noise (due to rotor-wake/rotor interaction) faces a computational overhead that prohibits their use for extensive parameter studies by which CROR broadband noise can be reduced. The use of semi-analytical models is therefore preferred in the present work.

1.3.3 Prediction of tonal noise emissions of CRORs

The earliest publication on the noise from CRORs is due to Hubbard [92] (1948), who carried out noise measurements on static model-scale CRORs and investigated the effects on the radiated tonal noise of varying blade numbers and the rotor-rotor separation distance. He was the first to recognize that there could be constructive and destructive acoustic interferences between the tonal noise generated by each rotors, and developed a simple model that describes this phenomenon based on Gutin's theory [82, 83] (1936, 1948) of the noise due to rotating steady blade forces. Hubbard's pioneering work was considerably extended by Hanson [85] (1985), who developed an analytical frequency domain model to predict the tonal noise due to any aerodynamic interaction between the two rotors of CRORs (such as viscous wakes interaction, potential field interaction and tip vortex interaction), provided that the chordwise distributions of unsteady lift and drag over the blades are known. This interaction tonal noise model, combined with Hanson's formulation [84] (1980) for the tonal noise of SRORs, provided the first comprehensive model for the prediction of CROR tonal noise. The contribution of potential field interaction noise in CRORs was first modelled by Parry [121, 122] (1988, 1989), who derived flat plate response functions for upstream (rear rotor potential field interaction with front rotor blades) and downstream (front rotor potential field interaction with rear rotor blades) potential field interactions. The tonal noise due to tip-vortices of the front rotor impinging onto the rear rotor was first modelled by Majjigi et al. [108] (1989), who used a 2D representation of the tip-vortices. This work was recently extended by Kingan and Self [101] (2009), who modelled the tip vortices more realistically as helical vortex tubes. The most comprehensive code available in the literature for CROR tonal noise prediction is the CRPFAN code developed by Whitfield et al. [150, 151] (1990) which takes into account the noise sources described above (but not the noise due to potential field interaction) using frequency domain semi-analytical models, and includes some effects of installation on the radiated tonal noise (engine angle of attack, presence of a fuselage, presence of a wing lifting line, and presence of an upstream pylon).

Very little research focused on the noise from CRORs has been conducted between the early 1990s and early 2000s, since the industry decided to suspend research into CRORs. However, because the investigation of CRORs is now once again of interest for engine manufacturers, a number of studies of CROR tonal noise have been published in recent years. Several of these studies (for example Stuermer and Yin [146, 147] (2009, 2010), Zachariadis [157] (2010) and Spalart et al. [144] (2010)) investigated CROR tonal noise using high-fidelity CFD methods, which were not available (due to computational cost) in the 1980s when the noise of CRORs was first investigated. These CFD models are often coupled to time-domain methods for noise radiation, often based on the work of Farassat and co-workers (see Ref. [60] (2010), for example), and are intended to be able to model the blades geometry in greater detail than the frequency domain methods based on Hanson's approach, described above, which are significantly faster.

1.3.4 Measurements of CROR noise

This section presents some of the main published measurements of CROR noise. Note that most of these noise measurements were performed to investigate the tonal noise only and, therefore, the mechanisms and characteristics of broadband noise radiation were hardly ever mentioned in these references. For this reason, extra care should be taken when using these data for the investigation of broadband noise from CRORs. One potential difficulty in the analysis of measured broadband noise data from CRORs is the presence of haystacking for open-jet wind tunnel measurements. Because of the proximity (in frequency) of the adjacent interaction tones in the measured noise signals, haystacking may obscure the true broadband noise levels in ways that are difficult to quantify.

Apart from the early measurements made by Hubbard [92] in 1948, most of the experimental work investigating noise emissions from CRORs has been conducted during the 1980s. Large part of published data from such experiments comes from the extensive noise measurement campaigns conducted at NASA Langley and NASA Lewis. Block and co-workers. [31, 30, 29, 32] (1985-1986) studied experimentally in the open-jet wind tunnel at NASA Langley the variation of the overall sound pressure level (OASPL) of both SRORs and CRORs with and without pylon and engine angle of attack. The effects of engine angle of attack on the radiated tonal noise were investigated experimentally, at about the same time, by Dittmar [52] (1986) in the closed-jet supersonic wind tunnel at NASA Lewis. The studies of both Block and Dittmar showed that the effects of engine angle of attack on the tonal noise of CRORs could be significant and should be included in prediction codes. Dittmar and Stang [53] (1987) investigated the effects of a 'cropped' rear rotor for the reduction of the tip-vortex interaction noise, with very good noise reductions in SPL of up to 10dB for certain tones. A comprehensive experimental study was also performed by Magliozzi et al.[107] in which the emitted noise of several open rotor configurations was compared, including tractor and pusher CROR configurations, SROR configurations, pusher CROR with an upstream pylon, different rotor-rotor spacing and different engine angles of attack. Magliozzi et al. also compared their noise measurements with the tonal noise prediction model of Hanson [85]. They obtained good agreement for the near-field measurements and reasonable agreement for the far-field measurements. Parameter studies of the noise performance of CRORs were presented by Fuji et al. [66] (1986) and Metzger and Brown [110] (1987), where the effects on the radiated tonal noise of the variation of front and rear tip speeds and rotor-rotor spacing were investigated. Another extensive parameter study, investigating the effects on the noise of blade number and blade sweep, was performed on a 1/5 scale CROR in the transonic closed-jet wind tunnel of ARA, and partially presented by Kirker [102] (1990).

A flight test was conducted by Woodward et al. [154] in 1989, in which a CROR was installed on a Boeing 727 in place of the right side turbofan engine. Noise measurements were performed on the fuselage of the aircraft, on the ground and from an instrumented Learjet chase plane on the side of the Boeing 727. The flight data of Woodward were compared

to the full aircraft noise predictions obtained from the code of Whitfield et al. [150]. Poor agreement was obtained for the fuselage noise measurements but reasonable agreement was observed for the ground and Learjet sideline noise measurements. In 1993, Woodward et al. [153] also measured the noise of CRORs with a forward-swept front rotor with the hope of reducing the tip-vortex interaction noise. The introduction of forward sweep on the front rotor resulted in poor aeroelastic performance and increase in noise on the configuration tested. Woodward et al. suggested to pursue the study of forward-swept front rotors in CRORs but the decision in the early 1990s of stopping the investigation of CRORs put this investigation to an end.

In recent years, due to the renewed interest in CRORs, several extensive measurement campaigns of CROR noise have been initiated as part of the european project DREAM [54] and the NASA/General Electrics cooperative program, in particular. These measurement campaigns are still ongoing at the time of writing and only a few preliminary experimental results have been released so far (see Ricouard et al. [95], Omaïs et al. [117] or Siller and Funke [141] for the DREAM project, and Envia et al. [57] for the NASA/General Electrics cooperative program).

1.4 Original contributions

The main original contributions of this thesis are listed below:

1. A semi-analytical model predicting the broadband noise due to the impingement of rotor wake turbulence onto the leading edge of a rotor in CRORs has been developed for the first time. This model has been published in the AIAA Journal (Blandeau and Joseph [20]). A fast approximate alternative to this general model has also been developed subsequently and is presented in this thesis.

2. A semi-analytical model for rotor trailing edge broadband noise has been developed. This model follows an approach similar to the model due to Kim and George [100], which is extended to take into account the effects of non-compact noise sources.

3. The effects of variations in rotor-rotor gap, rotor speed and blade number on the broadband noise emissions from uninstalled CRORs have been investigated at constant engine power, solidity and equal torque split and for three operating conditions. This work has been accepted for publication in the Internation Journal of Aeroacoustics (Blandeau et al. [27])

4. The relative importance of BRWI noise and BRTE noise in CRORs has been investigated for a realistic CROR configuration at three different flight conditions.

5. The validity of the approximate BRTE noise model due to Amiet [10] has been studied. This widely used model, in which the effects of rotation are treated approximately,

has been analytically compared to the equivalent BRTE noise model based on the approach of Kim and George [100], in which the effects of rotation are treated exactly. The validity of Amiet's model has then been tested for different fan configurations (an open rotor at take-off and cruise, a cooling fan and a wind turbine). This work has been accepted for publication in the AIAA Journal (Blandeau and Joseph [24]).

6. An analytical expression has been derived for the sound power radiation due to an isolated flat plate airfoil in a 2D turbulent flow and radiated upstream and downstream of a hypothetical fan axis. The isolated airfoil model has been compared to the cascade model due to Cheong et al. [45] in order to investigate the validity of using isolated airfoil models for application to CROR and turbofan broadband noise predictions. This study has been accepted for publication in the Journal of the Acoustical Society of America (Blandeau et al. [26]).

7. Closed-form asymptotic solutions, that are valid in the high and low frequency limits, for arbitrary Mach number and stagger angle, have been derived for the upstream and downstream sound powers predicted by the isolated airfoil model.

8. New results have been presented for the effects of variation in chord length on the sound power radiated by a flat plate airfoil in a turbulent stream.

9. An empirical model is provided for the mean and turbulent wake parameters, used as inputs to the BRWI noise model.

10. Several existing models for the surface pressure spectrum, which quantifies the source of BRTE noise, were reviewed and tested against measurements on a NACA0012 by Garcia Sagrado [68].

Some of the work presented in this thesis has also been presented by the author in international conferences and workshops (see Refs. [28, 19, 22, 25, 21, 23]).

1.5 Thesis structure

Chapter 2 presents the derivation of the BRWI noise model. Insight into the modal behaviour of the model is provided. An empirical model for the mean and turbulent wake parameters is given. The analytical flat plate response functions used in this model are also described in detail. A fast approximate BRWI model is derived assuming zero correlation between the broadband noise generated by adjacent rotor blades.

Chapter 3 presents the derivation of the BRTE noise model, extending the approach of Kim and George [100] to take into account the effects of non-compact sources. A number of existing models for the surface pressure spectrum, which quantifies the source of BRTE noise, are given and validated against data measured on a NACA0012 airfoil. Turbulent

boundary layer parameters input to BRTE model are obtained by use of the panel method code XFOIL [55], whose predictions are also compared to measurements.

Chapter 4 presents CROR broadband noise predictions using the models described in the two previous chapters. First, a comparison between the noise predictions and measurements is presented. The BRTE noise model is first validated against single rotor measurements and both the BRTE and the BRWI models are then validated against CROR noise measurements. The relative importance of the BRWI noise and the BRTE noise is then investigated for a realistic, but hypothetical, CROR configuration at assumed take-off, cruise and approach-type conditions. A parameter study based on this configuration is also conducted to study the effects on broadband noise emissions of variations in rotor-rotor gap, rotor speed and blade number, while the engine power, torque split and solidity are kept constant.

Chapter 5 presents a study of the validity of the widely used, but approximate, BRTE noise model due to Amiet [10]. This model is compared analytically to the model presented in Chapter 3 and criteria for the validity of Amiet's model are established. Predictions by the two models are then compared for different fan applications, including an open rotor at take-off and cruise conditions, a cooling fan and a wind turbine.

Chapter 6 presents a comparison of the sound power radiation from single airfoils and cascades in a turbulent flow. A single airfoil model for the sound power radiated upstream and downstream of the fan axis is presented. Closed-form expressions for the upstream and downstream sound powers are derived and new results are shown for the effects of chord length on sound power radiation. The isolated airfoil model is then compared to an equivalent cascade model for different cascade configurations, in order to study the validity of the isolated airfoil approximation for application to CROR and turbofan broadband noise predictions.

Chapter 2

A model for rotor-wake/rotor interaction broadband noise

A semi-analytical model for the prediction of the Broadband noise due to Rotor-Wake/rotor Interaction (BRWI) in contra-rotating open rotors (CRORs) is presented in this chapter. This frequency domain noise model is based on the approach of Ffowcs Williams and Hawkings [64] for the noise from rotating sources. The unsteady loading of the rear rotor blades is modelled using classical isolated flat-plate airfoil theory of Amiet [5, 7]. Strip theory is used to treat the spanwise variations of aerodynamic quantities and blade geometry. The turbulent rotor wake is assumed to be homogeneous and isotropic turbulence that is modulated by an infinite train of wake profiles. The model is presented in detail and insight into its modal behaviour is provided. A simplified model is deduced from the general model by assuming that the correlation between noise sources on adjacent blades is small. An empirical model to predict the mean and turbulent wake parameters is presented.

2.1 Model description

2.1.1 Rotor-wake/rotor interaction

Turbulent wakes are shed from the trailing edge of the front rotor and convected in a helical motion onto the leading edge of the rear rotor. This impingement of the wake turbulence generates a stochastic unsteady loading on the rear rotor blades that radiates as broadband noise.

Figure 2.1 presents a representation of the rotor-wake/rotor interaction problem and introduces the main geometrical parameters of the model. The blade numbers and the angular velocity of the rotors are denoted by B_i and Ω_i respectively, where the subscript $(.)_i$, with i =1 or 2, denotes quantities associated to the front or rear rotor respectively. At any radial

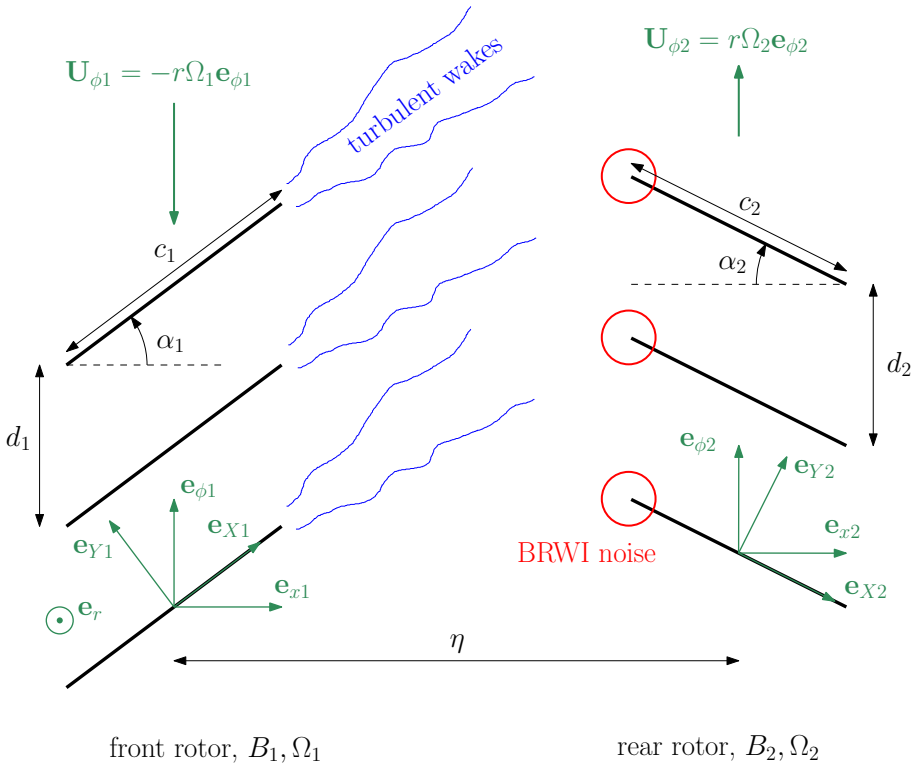

Figure 2.1: Rotor-wake/rotor interaction in a 2D slice of a CROR, unrolled at radius r.

position r, the front and rear rotors are represented by two infinite cascades of flat plates of chords c_i and stagger angles α_i, rotating at speeds $\mathbf{U}_{\phi 1} = -r\Omega_1\mathbf{e}_{\phi 1}$ and $\mathbf{U}_{\phi 2} = r\Omega_2\mathbf{e}_{\phi 2}$, respectively. The blades are separated azimuthally by the distance $d_1 = 2\pi r/B_1$ and $d_2 = 2\pi r/B_2$. The axial separation distance between the mid-chord disks of the two rotors at the hub is denoted by η.

The cylindrical coordinate systems (r, x_i, ϕ_i) and (r, X_i, Y_i) are defined in Fig. 2.1 and are related to each other by a rotation about the $\mathbf{e}_r$ axis equal to the stagger angle α_i, as

$$\begin{bmatrix} \mathbf{e}_{x1} \\ \mathbf{e}_{\phi 1} \end{bmatrix} = \begin{bmatrix} \cos\alpha_2 & -\sin\alpha_2 \\ \sin\alpha_2 & \cos\alpha_2 \end{bmatrix} \begin{bmatrix} \mathbf{e}_{X1} \\ \mathbf{e}_{Y1} \end{bmatrix}, \quad \begin{bmatrix} \mathbf{e}_{x2} \\ \mathbf{e}_{\phi 2} \end{bmatrix} = \begin{bmatrix} \cos\alpha_2 & \sin\alpha_2 \\ -\sin\alpha_2 & \cos\alpha_2 \end{bmatrix} \begin{bmatrix} \mathbf{e}_{X2} \\ \mathbf{e}_{Y2} \end{bmatrix}, \quad (2.1)$$

and

$$\begin{bmatrix} \mathbf{e}_{X1} \\ \mathbf{e}_{Y1} \end{bmatrix} = \begin{bmatrix} \cos\alpha_1 & \sin\alpha_1 \\ -\sin\alpha_1 & \cos\alpha_1 \end{bmatrix} \begin{bmatrix} \mathbf{e}_{x1} \\ \mathbf{e}_{\phi 1} \end{bmatrix}, \quad \begin{bmatrix} \mathbf{e}_{X2} \\ \mathbf{e}_{Y2} \end{bmatrix} = \begin{bmatrix} \cos\alpha_2 & -\sin\alpha_2 \\ \sin\alpha_2 & \cos\alpha_2 \end{bmatrix} \begin{bmatrix} \mathbf{e}_{x2} \\ \mathbf{e}_{\phi 2} \end{bmatrix}, \quad (2.2)$$

where $\mathbf{e}$ denotes the unit vector associated with each coordinate.

These coordinate systems are associated with the rotating reference frames $\tilde{\mathbf{x}}_i = r\mathbf{e}_r + x_i\mathbf{e}_{xi} + r\tilde{\phi}_i\mathbf{e}_{\phi i}$ and $\tilde{\mathbf{X}}_i = r\mathbf{e}_r + \tilde{X}_i\mathbf{e}_{Xi} + \tilde{Y}_i\mathbf{e}_{Yi}$, fixed on the mid chord of a reference blade. The tilde $(\tilde{})$ denotes a quantity expressed in a rotating reference frame fixed to a blade. In order to express the broadband noise radiated to the far-field, two corresponding reference frames

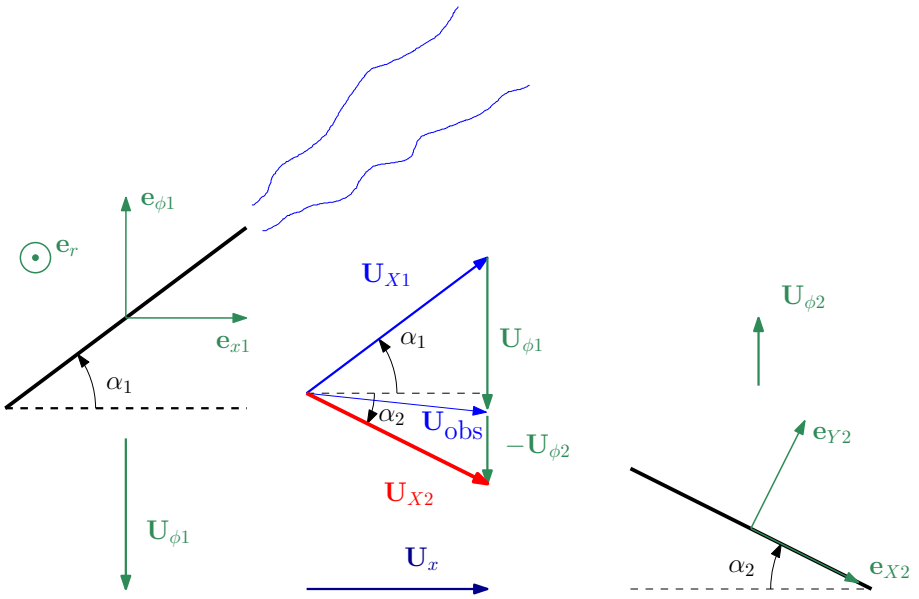

Figure 2.2: Definition of the relative mean gust velocity $\mathbf{U}_{X2}$ in the rotating airfoil-bound reference frame $\tilde{\mathbf{X}}_2$.

bound to the engine are defined as $\mathbf{X}_i = r\mathbf{e}_r + x_i\mathbf{e}_{xi} + r\phi_i\mathbf{e}_{\phi i}$ and $\mathbf{X}_i = r\mathbf{e}_r + X_i\mathbf{e}_{Xi} + Y_i\mathbf{e}_{Yi}$. The engine-bound and rotating airfoil-bound reference frames can be related through $\tilde{\phi}_1 = \phi_1 + \Omega_1\tau$ and $\tilde{\phi}_2 = \phi_2 - \Omega_2\tau$, where τ is the source emission time.

Figure 2.2 defines the mean gust velocity $\mathbf{U}_{X2}$ in the rear airfoil-bound rotating reference frame $\tilde{\mathbf{X}}_2$. An observer in the reference frame $\tilde{\mathbf{X}}_1$, rotating with the front rotor blades, will 'see' a fluid particle just outside the wake leaving the first blade row in the chordwise direction $\mathbf{e}_{X1}$ with a velocity $\mathbf{U}_{X1}$. However, in the engine-bound reference frame, the wake follows a helical path and the same fluid particle will be convected towards the rear blade row with a mean velocity $\mathbf{U}_{\text{obs}}$. In the reference frame $\tilde{\mathbf{X}}_2$, rotating with the rear rotor blades, the resulting turbulent gust has a mean velocity $\mathbf{U}_{X2}$, defined as the resultant of the mean velocity $\mathbf{U}_{X1}$ and the sum of the rotation azimuthal velocities $\mathbf{U}_{\phi 1} - \mathbf{U}_{\phi 2} = -r\left(\Omega_1 + \Omega_2\right)\mathbf{e}_{\phi 2}$, and which may be expressed as

$$\mathbf{U}_{X2} = r\left(\Omega_1 + \Omega_2\right)\frac{\cos\alpha_1}{\sin\left(\alpha_1 + \alpha_2\right)}\mathbf{e}_{X2}. \tag{2.3}$$

Note also that the relative velocities U_{Xi} and stagger angles α_i can be related to the axial flow speed U_x by $U_x = U_{Xi}\cos\alpha_i$.

One of the most questionable simplifying assumptions made in this model is of representing the unsteady response of the rear rotor blades by those from unloaded flat plates. Recent work by, for example, Devenport et al. [50] has demonstrated, by comparison of the measured noise from real airfoils with noise predictions based on flat plate theory, that an angle of attack of less than about 10° has only a small effect on leading edge noise because of the averaging effect of the turbulence. Angle of attack effects can, however, be significant in non-isotropic turbulence and dependent on airfoil shape. It was found that thicker airfoils

generate significantly less noise at high frequencies. Camber effects were found to be small, however. These experimental results confirm the earlier theoretical predictions by Evers and Peake [58], who showed that broadband noise due to turbulence-cascade interaction was weakly affected by the effects of blade geometry.

2.1.2 Coordinates for radiation to the far-field

In order to specify the location of an acoustic source element on a reference rear rotor blade, with respect to a far-field observer, two coordinate systems must be introduced: a spherical coordinate system (r_0, θ, ψ_0) denoting the location of the centre of the rear rotor disk with respect to the observer, and a Cartesian coordinate system (x_2, y_2, z_2) denoting the location of an acoustic point source element on a blade with respect to the centre of the rear rotor disk. These are defined in Fig. 2.3, which shows the front and side views of a schematic CROR, at flight Mach number $M_x = U_x/c_0$, and details the location of a point source element on the rear rotor blades.

An acoustic point source element on a blade is represented in figures 2.3 (a) and (b) by the elemental force vector $d\mathbf{F}$ (of unit N.m^{-2}) exerted *on* the fluid *by* an element of a blade of the rear rotor (of span dr and chord dX_2) pointing in the opposite direction of the lift at that point. At a given instant in time, $d\mathbf{F}$ can be written in the coordinate system (r, x_2, ϕ_2) as a function of the magnitude of the elemental force dF and of the stagger angle α_2 as

$$d\mathbf{F} = \begin{bmatrix} dF_r \\ dF_\phi \\ dF_x \end{bmatrix} = \begin{bmatrix} 0 \\ dF\cos\alpha_2 \\ dF\sin\alpha_2 \end{bmatrix}, \tag{2.4}$$

where it is assumed that there is no lift in the radial direction.

Since the elemental force vector $d\mathbf{F}$ is located on the surface of the flat plate airfoil, it is convenient to express $d\mathbf{F}$ in the non-orthogonal coordinate system (r, X_2, ϕ_2), as shown in Fig. 2.3 (b), where the chordwise coordinate X_2 is used in place of x_2 and varies between $-c_2/2$ and $c_2/2$. Since the half-chord length appears often in the analysis, the notation $b_i = c_i/2$ is introduced. An additional azimuthal angle ψ_2 is introduced to take into account the chordwise position of the source and the airfoil radial sweep s_2 as

$$\psi_2 = -\left(X_2 + s_2\right)\sin\alpha_2/r. \tag{2.5}$$

Since the airfoils are assumed to be thin flat plates, the coordinate systems (x_2, y_2, z_2) and (r, X_2, ϕ_2) *on the surface* of an airfoil of the rear rotor can be related by

$$\begin{bmatrix} x_2 \\ y_2 \\ z_2 \end{bmatrix} = \begin{bmatrix} \left(X_2 + s_2\right)\cos\alpha_2 \\ r\cos\left(\phi_2 - \psi_2\right) \\ r\sin\left(\phi_2 - \psi_2\right) \end{bmatrix}. \tag{2.6}$$

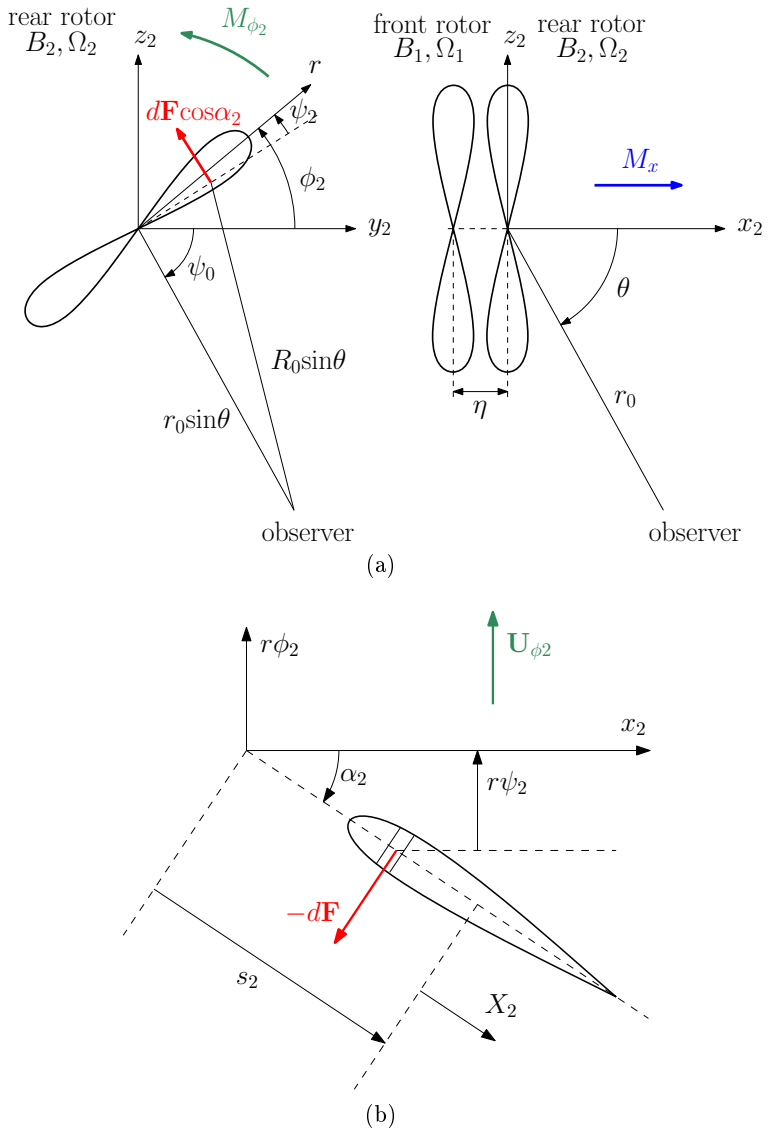

Figure 2.3: Coordinate systems for (a) an observer in the far-field, (b) a point force on a swept blade of the downstream rotor.

Making the far-field approximation allows the source-to-observer distance R_0 to be approximated by r_0 in the amplitude terms. This approximation does not hold in the phase terms, where further accuracy is required. First, in the coordinate system (x_2, y_2, z_2), R_0 can be expressed as a function of the observer position (x_0, y_0, z_0) as

$$R_0 = \sqrt{(x_2 - x_0)^2 + (y_2 - y_0)^2 + (z_2 - z_0)^2}, \tag{2.7}$$

Equation 2.7 can then be approximated by the first order Taylor expansion about the origin[1] which yields

$$R_0 \approx r_0 - \frac{x_2 x_0}{r_0} - \frac{y_2 y_0}{r_0} - \frac{z_2 z_0}{r_0}, \tag{2.8}$$

[1] given by $R_0 \sim r_0 + x_2 \frac{\partial R_0}{\partial x_2}(0) + y_2 \frac{\partial R_0}{\partial y_2}(0) + z_2 \frac{\partial R_0}{\partial z_2}(0)$.

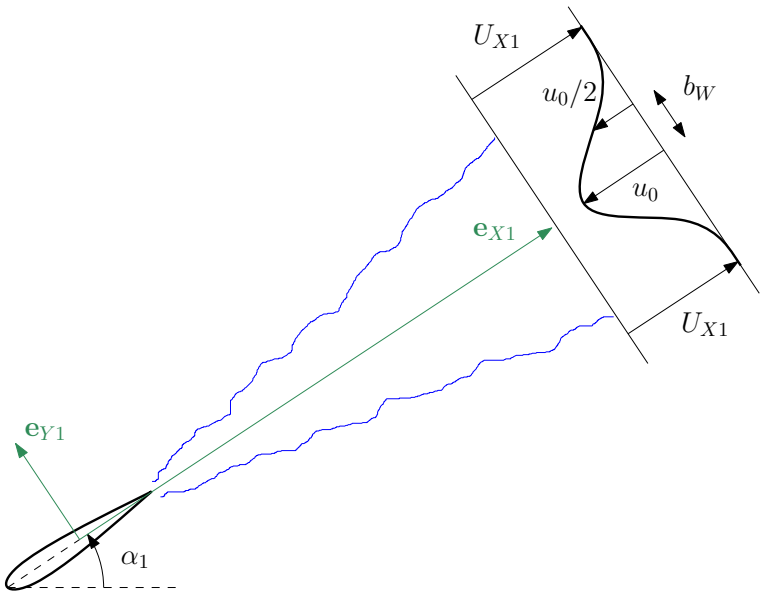

Figure 2.4: Definition of the mean wake parameters.

where from Fig. 2.3 the observer position is given in spherical coordinates by

$$\begin{bmatrix} x_0 \\ y_0 \\ z_0 \end{bmatrix} = \begin{bmatrix} r_0 \cos\theta \\ r_0 \sin\theta \cos\psi_0 \\ -r_0 \sin\theta \sin\psi_0 \end{bmatrix}, \tag{2.9}$$

Substituting Eq. 2.9 and Eq. 2.6 into the Taylor expansion of R_0 (Eq. (2.8)) gives after simplification

$$R_0 \approx r_0 - (X_2 + s_2)\cos\alpha_2 \cos\theta - r\sin\theta\cos\left(\phi_2 - \psi_2 + \psi_0\right). \tag{2.10}$$

Note that the medium of sound radiation is assumed to be at rest in the present analysis. The effects of uniform flow on the sound radiation can, however, be taken into account by means of corrections derived by Chapman [41], as presented in Appendix B.

2.2 Analytical formulation

2.2.1 Turbulent rotor wakes

The model of the turbulent wake velocity follows an approach similar to, for example, Jurdic et al. [98]. The turbulent velocity component of the wakes normal to the blades (or 'upwash velocity') w_W can be expressed in the reference frame $\tilde{\mathbf{X}}_2$ rotating with the rear rotor as a velocity w, that is a random function of space and time, modulated by a deterministic

non-dimensional wake profile function f_W as

$$w_W(\tilde{\mathbf{X}}_2,\tau) = f_W(\tilde{\mathbf{X}}_2,\tau)w(\tilde{\mathbf{X}}_2,\tau). \tag{2.11}$$

The random function $w(\tilde{\mathbf{X}}_2,\tau)$ is assumed to have the same spectral and spatial correlation characteristics as the wake turbulence, which is assumed to be isotropic and homogeneous. The wake profile function $f_W(\tilde{\mathbf{X}}_2,\tau)$ is chosen in this study to be a periodic train of Gaussian profiles characterised by the same centreline velocity deficit u_0 and half-wake width b_W (see Fig. 2.4). This wake turbulence model has been validated recently against measurements by Jurdic et al. [97], who used cyclostationary spectral analysis on measurements of rotor wake turbulence on a rig. Assuming that the profile of a turbulent wake repeats identically in the azimuthal direction $\mathbf{e}_{\phi 1}$ at every blade separation $d_1 = 2\pi r/B_1$, the wake profile function f_W can be expressed as

$$f_W(\tilde{\mathbf{X}}_2,\tau) = \sum_{k=-\infty}^{\infty} \exp\left\{-\frac{a}{b_W^2}\left((\tilde{\mathbf{X}}_2 - \mathbf{U}_{X2}\tau).(\mathbf{e}_{\phi 1} - \mathbf{e}_{x1}\tan\alpha_1) + kd_1\right)^2\right\}, \tag{2.12}$$

where a is an empirical wake parameter set to $a = 0.637$ by Wygnanski et al. [155] from laboratory measurements of 2D turbulent wakes. In the absence of wake turbulence measurements, the mean and turbulent wake parameters can be deduced from the mean streamwise velocity U_{X1} and the drag coefficient of the front airfoils C_d using the empirical models described in Section 2.5.

The wake turbulence model described in Eq. 2.11, which is based on the work of Ventres et al. [148] for the prediction of the broadband noise due to rotor-stator interactions in turbofans (and subsequently used by Nallasamy and Envia [115], Jurdic et al. [98] and Lloyd and Peake [105]), is fundamentally limited to well separated wakes. If the wake width $2b_W$ is not small compared to the blade gap d_1, adjacent wakes will overlap, leading to a correlation between adjacent front blades that cannot occur in practice as adjacent turbulent wakes must be statistically independent. The use of Eq. 2.11 for overlapping wakes will, therefore, yield an unrealistic scaling of the mean square acoustic pressure as B_1^2. The condition $2b_W/d_1 < 1$ is therefore necessary for the current approach to be valid. This condition is, however, generally valid for most realistic configurations of CRORs, due to the low drag coefficient of the front blades (i.e. thin wakes) and the low number of front blades B_1 (i.e. large blade separation).

The turbulent velocity w can be expressed in terms of its wavenumber Fourier transform as

$$\tilde{w}(\tilde{\mathbf{X}}_2 - \mathbf{U}_{X2}\tau) = \frac{1}{(2\pi)^3}\int\int_{-\infty}^{\infty}\int \mathcal{W}(\mathbf{k})\, e^{-i\mathbf{k}.(\tilde{\mathbf{X}}_2 - \mathbf{U}_{X2}\tau)} d\mathbf{k}, \tag{2.13}$$

where $\mathbf{k} = k_r\mathbf{e}_r + k_X\mathbf{e}_{X2} + k_Y\mathbf{e}_{Y2}$ denotes the turbulence wavenumber vector and $\mathcal{W}$ the wavenumber velocity spectrum, both expressed in the reference frame moving with the turbulent gust $\tilde{\mathbf{X}}_2 - \mathbf{U}_{X2}\tau$.

In order to derive an expression for the turbulent upwash velocity, the velocity of the wake turbulence is assumed to be a 'frozen' pattern independent of τ in the reference frame moving with the gust at a velocity $\mathbf{U}_{X2}$ (Taylor's hypothesis). The resulting 'frozen' upwash velocity is defined by $\tilde{w}_W(\tilde{\mathbf{X}}_2 - \mathbf{U}_{X2}\tau) = w_W(\tilde{\mathbf{X}}_2, \tau)$. Applying Poisson's summation formula to Eq. 2.12 (see Appendix A for details) and substituting the result into Eq. 2.11 yields

$$\tilde{w}_W(\tilde{\mathbf{X}}_2 - \mathbf{U}_{X2}\tau) = B_1 \sum_{m=-\infty}^{\infty} f_m(r)\, \tilde{w}(\tilde{\mathbf{X}}_2 - \mathbf{U}_{X2}\tau) e^{-i\frac{mB_1}{r}(\tilde{\mathbf{X}}_2 - \mathbf{U}_{X2}\tau).(\mathbf{e}_{\phi 1} - \mathbf{e}_{x1}\tan\alpha_1)}, \quad (2.14)$$

where the index m denotes the m^{th} harmonic of the blade passing frequency (BPF) $mB_1\Omega_1/2\pi$ (in Hz) of the front rotor and where f_m are the Fourier components of the wake profile given by

$$f_m(r) = \frac{1}{B_1\sigma\sqrt{2\pi}} \exp\left\{-\frac{1}{2}\left(\frac{m}{\sigma}\right)^2\right\}, \quad (2.15)$$

with $\sigma = \frac{r\sqrt{2a}}{B_1 b_W}$. Equation 2.15 suggests that the 'energy' of the upwash velocity is distributed over the indices m following a Gaussian distribution centred at $m = 0$ with 'standard deviation' σ.

Expanding the dot product in Eq. 2.14 gives

$$\begin{aligned}\tilde{w}_W(r, \tilde{X}_2 - U_{X2}\tau, \tilde{Y}_2) = B_1 \sum_{m=-\infty}^{\infty} f_m(r)\, \tilde{w}(r, \tilde{X}_2 - U_{X2}\tau, \tilde{Y}_2) \\ \times e^{-i\frac{mB_1}{r\cos\alpha_1}\left(\tilde{Y}_2\cos(\alpha_1+\alpha_2) - \left(\tilde{X}_2 - U_{X2}\tau\right)\sin(\alpha_1+\alpha_2)\right)}. \quad (2.16)\end{aligned}$$

In order to consider the unsteady loading on the rear rotor, the upwash velocity must be expressed in the coordinate system $\tilde{\mathbf{x}}_2 = (r, \tilde{x}_2, \tilde{\phi}_2)$ so that the dependence on azimuthal coordinate $\tilde{\phi}_2$ is made explicit. Substituting Eq. 2.16 into Eq. 2.14 and using the transformations described in Eq. 2.2 yields

$$\begin{aligned}w_W(r, \tilde{x}_2, \tilde{\phi}_2, \tau) = \frac{B_1}{(2\pi)^3} \sum_{m=-\infty}^{\infty} f_m(r) \int\int_{-\infty}^{\infty}\int \mathcal{W}(k_r, k_X, k_Y)\, e^{-i\left[\left(k_\phi + \frac{mB_1}{r}\right)r\tilde{\phi}_2\right]} \\ \times e^{-i\left[k_r r + \left(k_x - \frac{mB_1}{r}\tan\alpha_1\right)\tilde{x}_2 + mB_1(\Omega_1+\Omega_2)\tau - k_X U_{X2}\tau\right]} dk_r dk_X dk_Y, \quad (2.17)\end{aligned}$$

where k_ϕ and k_x are the turbulent wavenumbers in the azimuthal and axial directions respectively, and are given by

$$\begin{cases} k_\phi = -k_X\sin\alpha_2 + k_Y\cos\alpha_2 \\ k_x = k_X\cos\alpha_2 + k_Y\sin\alpha_2 \end{cases} \quad (2.18)$$

Equation 2.17 is an expression for the upwash turbulence velocity in the reference frame rotating with the rear rotor. In the next section, this expression is used to deduce the unsteady loading on the B_2 blades of the rear rotor.

2.2.2 Unsteady loading of the rear rotor blades due to leading edge interaction

The expression for the unsteady loading on the rear blade row is now presented. According to Amiet [6], the unsteady pressure difference Δp (or 'pressure jump') across an isolated airfoil due to a harmonic vortical gust, with upwash velocity of the form $w(r, X_2, Y_2, \tau) = w_0 e^{-i[k_r r + k_X(X_2 - U_{X2}\tau) + k_Y Y_2]}$, can be written as

$$\Delta p\left(r, X_2, Y_2, \tau\right) = 2\pi\rho_0 U_{X2} w_0 g^{\mathrm{LE}}\left(X_2, k_r, k_X, M_{X2}\right) e^{-i[k_r r + k_Y Y_2 - k_X U_{X2}\tau]}, \tag{2.19}$$

where $M_{Xi} = U_{Xi}/c_0$ is the Mach number of the relative mean flow onto the leading edge of the airfoil and $g^{\mathrm{LE}}(X_2, k_r, k_X, M_{X2})$ is the non-dimensional transfer function between the turbulent upwash velocity and the pressure jump due to leading edge interaction. In this study, the flat plate response functions g^{LE} derived by Amiet [7, 5] are used, as described in Section 2.6. The pressure jump across an arbitrary reference airfoil of the rear rotor, expressed in an airfoil-bound rotating reference frame, is denoted by $\Delta\tilde{p}$. The expression for $\Delta\tilde{p}$ is obtained by substituting the turbulent upwash velocity w_W (Eq. 2.17), estimated at the leading edge of the reference airfoil, into the general formula of Eq. 2.19 and integrating over all turbulence wavenumber components. Noting that on the surface of the flat plate one can make the change of variables $x_2 = (X_2 + s_2)\cos\alpha_2$, $\Delta\tilde{p}$ is expressed in the coordinate system $(r, X_2, \tilde{\phi}_2)$ as

$$\begin{aligned}\Delta\tilde{p}(r, X_2, \tilde{\phi}_2, \tau) = \frac{B_1}{(2\pi)^2}\rho_0 U_{X2} \sum_{m=-\infty}^{\infty} f_m\left(r\right) \int\int_{-\infty}^{\infty} \mathcal{W}\left(k_r, k_X, k_Y\right) \\ \times g^{\mathrm{LE}}\left(X_2, k_r, k_X, M_{X2}\right) e^{-i\left[\left(k_\phi + \frac{mB_1}{r}\right) r\tilde{\phi}_2 + (mB_1(\Omega_1+\Omega_2) - k_X U_{X2})\tau\right]} \\ \times e^{-i\left[k_r r - (s_2 + X_2)\frac{mB_1}{r}\tan\alpha_1\cos\alpha_2\right]} dk_r dk_X dk_Y.\end{aligned} \tag{2.20}$$

The source of broadband noise, specified by the pressure jump across the rear rotor blades, must be expressed in the engine-bound reference frame (r, X_2, ϕ_2) before the far-field noise can be calculated. By considering the rear rotor loading as a series of pulses repeating every B_2 blades, the pressure jump $\Delta p(r, X_2, \phi_2, \tau)$ is deduced from $\Delta\tilde{p}(r, X_2, \tilde{\phi}_2, \tau)$ as

$$\begin{aligned}\Delta p\left(r, X_2, \phi_2, \tau\right) &= \sum_{n=-\infty}^{\infty} \Delta\tilde{p}(r, X_2, \tilde{\phi}_2, \tau)\delta\left(\tilde{\phi}_2 - \frac{2\pi}{B_2}n\right) \\ &= \frac{B_2}{2\pi}\sum_{n=-\infty}^{\infty} \Delta\tilde{p}(r, X_2, \tilde{\phi}_2, \tau) e^{inB_2\tilde{\phi}_2},\end{aligned} \tag{2.21}$$

where δ is the Dirac delta function and where the right hand side expression has been obtained using Poisson's summation formula (see Appendix A).

Following the approach of Hanson and Horan [87], the turbulence velocity is assumed 2π-periodic at a fixed instant in time, and the turbulent velocity field is decomposed in the

azimuthal direction as a sum of Fourier modes of order q. The turbulent azimuthal wavenumber k_ϕ therefore only takes the discrete values

$$k_\phi = k_Y \cos\alpha_2 - k_X \sin\alpha_2 = -\frac{2\pi q}{B_2 d_2} = -\frac{q}{r}. \tag{2.22}$$

Equation 2.22 leads to the following direct relationship between the normal and chordwise turbulent wavenumbers k_Y and k_X:

$$k_Y = k_X \tan\alpha_2 - \frac{q}{r\cos\alpha_2}. \tag{2.23}$$

It will be later shown that k_X is constant at a single frequency. As a consequence, the k_Y integral in Eq. 2.20 can be expressed as a summation using

$$\int_{-\infty}^{\infty} dk_Y \rightarrow \frac{1}{r\cos\alpha_2} \sum_{q=-\infty}^{\infty}. \tag{2.24}$$

Combining Eqs. 2.20 to 2.24 yields an expression for the pressure jump in the engine bound reference frame as

$$\Delta p\left(r, X_2, \phi_2, \tau\right) = \frac{1}{\left(2\pi\right)^3} \frac{\rho_0 U_{X2} B_1 B_2}{r\cos\alpha_2} \sum_{q=-\infty}^{\infty} \sum_{m=-\infty}^{\infty} \sum_{n=-\infty}^{\infty} f_m\left(r\right) \int_{-\infty}^{\infty}\int \mathcal{W}\left(k_r, k_X, k_Y\right)$$
$$\times\, g^{\mathrm{LE}}\left(X_2, k_r, k_X, M_{X2}\right) e^{-i\left[l\phi_2 + k_r r - \frac{mB_1}{r}\tan\alpha_1\cos\alpha_2\left(X_2+s_2\right) + \left(\omega_{qmn} - k_X U_{X2}\right)\tau\right]} dk_r dk_X, \tag{2.25}$$

where the azimuthal acoustic interaction mode l and the interaction frequency ω_{qmn} are given by

$$l = mB_1 - \left(nB_2 + q\right), \tag{2.26}$$

$$\omega_{qmn} = mB_1\Omega_1 + \left(nB_2 + q\right)\Omega_2. \tag{2.27}$$

Note that the only difference between these definitions of l and ω_{qmn} and those obtained by Hanson [85], for the tonal component of the interaction noise of CRORs, is the presence of the azimuthal mode order q of the turbulence, which is equal to 0 in Hanson's formulation.

Equation 2.26 establishes the scattering rule for the acoustic mode order l, resulting from the interaction between the q^{th} azimuthal mode of the turbulence originating from B_1 wakes and the B_2 blades of the downstream rotor. Since the engine is not moving with respect to the observer (i.e. wind-tunnel configuration), the relationship between the emission time τ and the observer time t is

$$\tau = t - R_0/c_0. \tag{2.28}$$

Note that a different relation between τ and t must be used in the case of an engine flying over the observer, as presented in Appendix C.

Substituting Eq. 2.10 and Eq. 2.28 into Eq. 2.25 yields the expression for the pressure jump at the observer time t as

$$\Delta p\left(r, X_2, \phi_2, t\right) = \frac{1}{\left(2\pi\right)^3} \frac{\rho_0 U_{X2} B_1 B_2}{r \cos\alpha_2} \sum_{q=-\infty}^{\infty} \sum_{m=-\infty}^{\infty} \sum_{n=-\infty}^{\infty} f_m\left(r\right)$$
$$\times \int_{-\infty}^{\infty} \int \mathcal{W}\left(k_r, k_X, k_Y\right) g^{\mathrm{LE}}\left(X_2, k_r, k_X, M_{X2}\right) e^{-i\left[l\phi_2 + k_r r - \frac{mB_1}{r}\tan\alpha_1 \cos\alpha_2 (X_2 + s_2)\right]}$$
$$\times e^{i\left(\frac{k_X U_{X2} - \omega_{qmn}}{c_0}\right)\left[c_0 t - r_0 + (X_2 + s_2)\cos\alpha_2 \cos\theta + r\sin\theta\cos(\phi_2 - \psi_2 + \psi_0)\right]} dk_r dk_X, \quad (2.29)$$

Fourier transforming Eq. 2.29 with respect to time t, gives the frequency domain pressure jump, denoted by $\Delta\hat{p}$. For consistency with the wavenumber Fourier transform of Eq. 2.13, the following convention for the frequency domain Fourier transform is used

$$\Delta\hat{p}\left(r, X_2, \phi_2, \omega\right) = \lim_{T\to\infty} \int_{-T}^{T} \Delta p\left(r, X_2, \phi_2, t\right) e^{-i\omega t} dt. \quad (2.30)$$

By use of the identity

$$\lim_{T\to\infty} \int_{-T}^{T} e^{i(k_X U_{X2} - \omega_{qmn} - \omega)t} dt = 2\pi\delta\left(k_X U_{X2} - \omega_{qmn} - \omega\right) \quad (2.31)$$

in Eq. 2.29, the frequency domain pressure jump $\Delta\hat{p}$ is obtained as

$$\Delta\hat{p}\left(r, X_2, \phi_2, \omega\right) = \frac{1}{\left(2\pi\right)^2} \frac{\rho_0 B_1 B_2}{r \cos\alpha_2} \sum_{q=-\infty}^{\infty} \sum_{m=-\infty}^{\infty} \sum_{n=-\infty}^{\infty} f_m\left(r\right)$$
$$\times e^{-il\phi_2} \int_{-\infty}^{\infty} \mathcal{W}\left(k_r, K_{X,qmn}, K_{Y,qmn}\right) g^{\mathrm{LE}}\left(X_2, k_r, K_{X,qmn}, M_{X2}\right) e^{-ik_r r} dk_r$$
$$\times e^{-i\left[k_0 r_0 - \left(\frac{mB_1}{r}\tan\alpha_1 \cos\alpha_2 + k_0 \cos\alpha_2 \cos\theta\right)(X_2 + s_2) - k_0 r \sin\theta\cos(\phi_2 - \psi_2 + \psi_0)\right]}, \quad (2.32)$$

where $k_0 = \omega / c_0$ and the convention $\hat{(.)}$ denotes a quantity in the frequency domain. Note that, following Fourier transformation with respect to t, the k_X integral in Eq. 2.25 vanishes and, at a given frequency, the turbulent wavenumbers k_X and k_Y now take the discrete values

$$K_{X,qmn} = \frac{\omega + \omega_{qmn}}{U_{X2}} \text{ and } K_{Y,qmn} = K_{X,qmn}\tan\alpha_2 - \frac{q}{r\cos\alpha_2}, \quad (2.33)$$

The expression for the pressure jump in Eq. 2.32 quantifies the strength of the equivalent acoustic dipole source distribution on the rear rotor blades from the point of view of an observer in the far-field. It can now be input into the Ffowcs Williams and Hawkings equation (Ref. [63]) in order to predict the radiated far-field spectrum, as described in the next section.

2.2.3 Sound pressure spectral density

The derivation of the expression for the spectrum of the far-field broadband noise radiation is now presented. The acoustic pressure p due to a moving elementary force $d\mathbf{F}$ (of units $\mathrm{N.m^{-2}}$) exerted by a blade surface element (of area dS_2) on the fluid is given by the Ffowcs Williams and Hawkings [63] equation as

$$p\left(r_0,\theta,\psi_0,t\right)=-\int_{S_2}\nabla\cdot\left[\frac{d\mathbf{F}\left(r,X_2,\phi_2,\tau\right)}{4\pi R_0}\right]_t dS_2\left(r,X_2,\phi_2\right), \tag{2.34}$$

where R_0 is the distance between the observer at time t and the source at time τ. The surface of the rear rotor blades is denoted by S_2 and the square brackets $[.]_t$ denote an estimation at observer time t.

As stated in Section 2.1.2, the $1/R_0$ amplitude term can be approximated by $1/r_0$ in Eq. 2.34, which reduces to

$$p\left(\mathbf{x}_0,t\right)=\frac{-1}{4\pi r_0}\int_{S_2}\nabla\cdot\left[d\mathbf{F}\left(r,X_2,\phi_2,\tau\right)\right]_t dS_2\left(r,X_2,\phi_2\right). \tag{2.35}$$

The divergence in cylindrical coordinates of the elemental force vector $d\mathbf{F}$, estimated at the source time τ, is defined by

$$\nabla\cdot d\mathbf{F}\left(r,X_2,\phi_2,\tau\right)=\frac{1}{r}\frac{\partial dF_\phi\left(r,X_2,\phi_2,\tau\right)}{\partial\phi_2}+\frac{\partial dF_x\left(r,X_2,\phi_2,\tau\right)}{\partial x_2}. \tag{2.36}$$

Since the magnitude dF of the elemental force vector is directly linked to the pressure jump over the airfoil by $dF=-\Delta p$ and using the definition of the elemental force vector (Eq. 2.4), the following expression of the divergence is derived

$$\nabla\cdot d\mathbf{F}\left(r,X_2,\phi_2,\tau\right)=-\frac{\cos\alpha_2}{r}\frac{\partial\Delta p\left(r,X_2,\phi_2,\tau\right)}{\partial\phi_2}-\sin\alpha_2\frac{\partial\Delta p\left(r,X_2,\phi_2,\tau\right)}{\partial x_2}. \tag{2.37}$$

For a single value of the scattering indices (m,n,q), differentiating Eq. 2.25 with respect to ϕ_2 gives

$$\frac{\partial\Delta p_{qmn}\left(r,X_2,\phi_2,\tau\right)}{\partial\phi_2}=-il\Delta p_{qmn}\left(r,X_2,\phi_2,\tau\right). \tag{2.38}$$

Since Eq. 2.25 has no direct dependence on x_2, the right hand term in Eq. 2.37 is expressed for a single value of (m,n,q) by using the chain-rule as

$$\frac{\partial\Delta p_{qmn}}{\partial x_2}=\frac{\partial r_0}{\partial x_2}\frac{\partial\tau}{\partial r_0}\frac{\partial\Delta p_{qmn}}{\partial\tau}, \tag{2.39}$$

where the first factor is obtained from Eq. 2.9 as $\frac{\partial r_0}{\partial x_2}=\cos\theta$ and the second factor is obtained from Eq. 2.28 as $\frac{\partial\tau}{\partial r_0}\approx\frac{\partial\tau}{\partial R_0}=\frac{-1}{c_0}$. The derivative of Δp_{qmn} (Eq. 2.25) with respect to τ is

given by

$$\frac{\partial \Delta p_{qmn}\left(r, X_2, \phi_2, \tau\right)}{\partial \tau} = \frac{i}{\left(2\pi\right)^3} \frac{\rho_0 U_{X2} B_1 B_2}{r \cos\alpha_2} f_m\left(r\right) \int_{-\infty}^{\infty}\int \left(k_X U_{X2} - \omega_{qmn}\right) \mathcal{W}\left(k_r, k_X, k_Y\right)$$
$$\times\, g\left(X_2, k_r, k_X, M_{X2}\right) e^{-i\left[l\phi_2 + k_r r - \frac{mB_1}{r}\tan\alpha_1 \cos\alpha_2 (X_2 + s_2) + (\omega_{qmn} - k_X U_{X2})\tau\right]} dk_r dk_X . \quad (2.40)$$

Note here that the derivative with respect to the source time τ has produced a k_X term on the left side of the integrand in Eq. 2.40. This k_X term cannot be taken outside of the double spatial Fourier integral and will complicate considerably the derivation of the time-domain expressions of the broadband noise radiation compared to the tonal case (see Hanson [85]). This problem has arisen because $\nabla \cdot d\mathbf{F}$ cannot be written as a direct function of the pressure jump Δp, and is directly linked to the fact that the upwash velocity is turbulent and therefore contains energy over a continuous range of wavenumber. A method to deal with this issue in the time domain has been proposed by Casper and Farassat [38] and was applied to the much simpler problem of an isolated flat airfoil in a turbulent stream.

This complication is however removed when transforming to the frequency domain. As shown in section 2.2.2, the chordwise and normal turbulent wavenumbers k_X and k_Y take the discrete values $K_{X,qmn}$ and $K_{Y,qmn}$ in the frequency domain (Eq. 2.33). Therefore, using the properties of the Fourier transform of a time derivative yields the frequency domain expression Eq. 2.40

$$\frac{\partial \Delta \hat{p}\left(r, X_2, \phi_2, \omega\right)}{\partial \tau} = i\omega \Delta \hat{p}\left(r, X_2, \phi_2, \omega\right). \quad (2.41)$$

By combining Eqs 2.37 to 2.41, the divergence of the moving point force for a single value of (m, n, q) can be derived in the frequency domain as

$$\nabla \cdot d\hat{\mathbf{F}}_{qmn}\left(r, X_2, \phi_2, \omega\right) = i\left(\frac{l}{r}\cos\alpha_2 + k_0 \sin\alpha_2 \cos\theta\right) \Delta \hat{p}_{qmn}\left(r, X_2, \phi_2, \omega\right), \quad (2.42)$$

The far-field acoustic pressure in the frequency domain, for a single value of (m, n, q), is then obtained by substituting equations 2.34 and 2.42 to give

$$\hat{p}_{qmn}\left(r_0, \theta, \psi_0, \omega\right) = -i \int_{R_{h2}}^{R_{t2}} \int_{-b_2}^{b_2} \int_{0}^{2\pi} \frac{\left(\frac{l}{r}\cos\alpha_2 + k_0 \cos\theta \sin\alpha_2\right)}{4\pi r_0} \Delta \hat{p}_{qmn}\left(r, X_2, \phi_2, \omega\right) d\phi_2 dX_2 dr, \quad (2.43)$$

where R_{h2} and R_{t2} denote the radii of the hub and the tip of the rear rotor, respectively, and where $b_2 = c_2/2$ is the half-chord length of the rear rotor blades.

The integration over ϕ_2 is derived analytically by extracting the ϕ_2-dependent part from $\Delta\hat{p}_{qmn}$ in Eq. 2.32 and evaluating the following integral

$$I_\phi = \int_0^{2\pi} e^{ik_0 r\sin\theta\cos(\phi_2-\psi_2+\psi_0)-il\phi_2} d\phi_2. \tag{2.44}$$

Making the change of variables $\phi' + \frac{\pi}{2} = -(\phi_2 - \psi + \psi_0)$ (the limits of integration are unmodified due to the periodicity of the integrand) gives

$$I_\phi = e^{il\left(\psi_0+\frac{\pi}{2}-\psi_2\right)} \int_0^{2\pi} e^{ik_0 r\sin\theta\sin\phi'-il\phi'} d\phi'. \tag{2.45}$$

The azimuthal integration can now be evaluated analytically in terms of Bessel functions using the identity (see Abramowitz and Stegun [1])

$$\int_0^{2\pi} e^{i\zeta\sin\phi'-il\phi'} d\phi' = 2\pi J_l(\zeta), \tag{2.46}$$

and substituting the definition of ψ_2 (Eq. 2.5) to give

$$I_\phi = 2\pi e^{il\left(\psi_0+\frac{\pi}{2}\right)} e^{i\frac{l}{r}\sin\alpha_2(X_2+s_2)} J_l(k_0 r\sin\theta). \tag{2.47}$$

Substituting Eqs. 2.32 into Eq. 2.43 and performing the integral over ϕ_2 according to Eq. 2.47 yields the final expression for the single frequency far-field pressure, for a single value of (m, n, q), of the form

$$\hat{p}_{qmn}(r_0, \theta, \psi_0, \omega) = \frac{-i}{8\pi^2} \frac{\rho_0 b_2 B_1 B_2}{r_0} e^{i[l(\psi_0+\pi/2)-k_0 r_0]} \int_{R_{h2}}^{R_{t2}} \left(\frac{l}{r} + k_0\cos\theta\tan\alpha_2\right) \frac{J_l(k_0 r\sin\theta)}{r}$$
$$\times f_m(r) \int_{-\infty}^{\infty} \mathcal{W}(k_r, K_{X,qmn}, K_{Y,qmn}) \mathcal{L}^{\mathrm{LE}}(k_r, K_{X,qmn}, \kappa_{qmn}) e^{i[\kappa_{qmn}(s_2-b_2)-ik_r r]} dk_r dr, \tag{2.48}$$

where $\mathcal{L}^{\mathrm{LE}}$ denotes the non-dimensional aerodynamic-acoustic coupling integral along the airfoil chord and is defined by

$$\mathcal{L}^{\mathrm{LE}}(k_r, K_{X,qmn}, \kappa_{qmn}) = \frac{1}{b_2} \int_{-b_2}^{b_2} g^{\mathrm{LE}}(X_2, k_r, K_{X,qmn}, M_{X2}) e^{i\kappa_{qmn}(X_2+b_2)} dX_2, \tag{2.49}$$

and where κ_{qmn} is the aeroacoustic coupling wavenumber given by

$$\kappa_{qmn} = k_0 \cos\alpha_2 \cos\theta + mB_1 \frac{\Omega_1 + \Omega_2}{U_{X2}} - \frac{nB_2 + q}{r} \sin\alpha_2. \tag{2.50}$$

The unsteady loading term $\mathcal{L}^{\mathrm{LE}}$ includes non-compactness effects and can be interpreted as a coupling integral between the unsteady aerodynamics and the acoustic radiation to the far-field. For a given value of k_r, maximum of $\left|\mathcal{L}^{\mathrm{LE}}\right|$ is obtained when both the vortical chordwise wavenumber $K_{X,qmn}$ and the aeroacoustic coupling wavenumber κ_{qmn} tend to zero. The expression for $\mathcal{L}^{\mathrm{LE}}$ has been derived analytically using the classical approach of Amiet [6], as described in detail in Section 2.6.

Since aerodynamic broadband noise involves stochastic quantities, such as the turbulent upwash velocity, the broadband far-field noise must be evaluated as a spectral density. The time-averaged power spectral density (PSD) of the far-field acoustic pressure can be derived from $S_{pp} = \lim_{T\to\infty} \frac{\pi}{T} \langle \hat{p}\hat{p}^* \rangle$, where the brackets $\langle . \rangle$ denote the expected value and T represents the averaging time. Its contribution from (m, n, q) and (m', n', q'), is obtained from Eq. 2.43 as

$$\begin{aligned} S_{pp,qmn,q'm'n'}(r_0, \theta, \omega) = \left(\frac{1}{4\pi r_0}\right)^2 \int_{R_{h2}}^{R_{t2}} \int_{-b_2}^{b_2} \int_{0}^{2\pi} \int_{r-\frac{\Delta L_r}{2}}^{r+\frac{\Delta L_r}{2}} \int_{-b_2}^{b_2} \int_{0}^{2\pi} S_{\Delta\Delta,qmn,q'm'n'} \\ \times \left(\frac{l'}{r'}\cos\alpha_2 + k_0 \cos\theta \sin\alpha_2\right) \left(\frac{l}{r}\cos\alpha_2 + k_0 \cos\theta \sin\alpha_2\right) dr dX_2 d\phi_2 dr' dX_2' d\phi_2', \end{aligned} \tag{2.51}$$

where $S_{\Delta\Delta,qmn,q'm'n'}$ is the modal cross-PSD of the pressure jump between two points (r, X_2, ϕ_2) and (r', X_2', ϕ_2') on the blade surface and is defined by

$$S_{\Delta\Delta,qmn,q'm'n'}(r, X_2, \phi_2, r', X_2', \phi_2', \omega) = \lim_{T\to\infty} \frac{\pi}{T} \left\langle \Delta\hat{p}^*_{qmn}(r, X_2, \phi_2, \omega)\, \Delta\hat{p}_{q'm'n'}(r', X_2', \phi_2', \omega) \right\rangle. \tag{2.52}$$

Two sources of broadband noise on a rear rotor blade can be considered uncorrelated if their radial separation is larger than the spanwise correlation length Δl_r of the unsteady blade loading. Therefore, the domain of integration of the spanwise dr' integral in Eq. 2.51 has been restricted to $\left[r - \frac{\Delta L_r}{2}, r + \frac{\Delta L_r}{2}\right]$, where ΔL_r is chosen to be sufficiently larger than Δl_r to ensure convergence of S_{pp}.

The only stochastic quantity in the expression for the pressure jump $\Delta\hat{p}$ (Eq. 2.32) is $\mathcal{W}$. As a result, all other terms can be written outside the 'expected value' in Eq. 2.52, which can be simplified using Eq. 2.13. Since the turbulence is assumed homogeneous and isotropic and since the wavenumbers $K_{X,qmn}$ and $K_{Y,qmn}$ take discrete values at each frequency, we can

write for large values of T and after some analysis (see Appendix D for detailed derivation)

$$\lim_{T\to\infty}\frac{\pi}{T}\left\langle \mathcal{W}^{*}(k_r,K_{X,qmn},K_{Y,qmn})\mathcal{W}(k_r^{'},K_{X,q'm'n'},K_{Y,q'm'n'})\right\rangle = (2\pi)^3\,U_{X2}r\cos\alpha_2 \times \delta\left[m-m'\right]\delta\left[n-n'\right]\delta\left[q-q'\right]\delta(k_r-k_r^{'})\Phi_{ww}(k_r^{'},K_{X,q'm'n'},K_{Y,q'm'n'}), \quad (2.53)$$

where $\delta\left[.\right]$ denotes the Kronecker delta function and $\delta\left(.\right)$ denotes the Dirac delta function. The turbulent velocity wavenumber spectrum Φ_{ww} is chosen to be the Von Karman spectrum for isotropic and homogeneous turbulence, given by (see for instance Ref. [6])

$$\Phi_{ww}\left(k_r,k_X,k_Y\right)=\frac{55}{36\pi^{3/2}}\frac{\Gamma\left(5/6\right)}{\Gamma\left(1/3\right)}\frac{\overline{w^2}}{k_e^5}\left(k^2-k_Y^2\right)\left[1+\left(k/k_e\right)^2\right]^{-17/6}, \quad (2.54)$$

where Γ is the Gamma function, $k=\sqrt{k_r^2+k_X^2+k_Y^2}$ is the magnitude of the turbulence wavenumber vector, $\overline{w^2}$ is the mean square turbulent velocity and k_e is defined by $k_e=\frac{\sqrt{\pi}}{L}\frac{\Gamma(5/6)}{\Gamma(1/3)}$, where L is the turbulence integral lengthscale.

In order to reduce the general expression of the PSD (Eq. 2.51) to a form that is computationally more efficient, the strip theory approximation is applied to account for the spanwise variation of aerodynamic quantities and geometry. Hence, the far-field pressure spectrum is assumed to be due to the sum of the incoherent contributions generated by a distribution of N_j spanwise blade strips whose flow and geometrical parameters are assumed to be uniform in each strip and equal to their value at the strip midspan, located radially at $r=\bar{r}$. The span of each of the N_j strips, denoted by Δr, must be chosen to be larger than a turbulence integral lengthscale L, in order to encompass the largest scale eddies. The distance ΔL_r in Eq. 2.51 is chosen to be equal to the strip length Δr, its maximum value allowed by the use of strip theory, so that the condition $\Delta L_r=\Delta r>\Delta l_r$ is satisfied in most cases.

Note that it is difficult to verify the validity of condition $\Delta r>\Delta l_r$, for the blade geometry and turbulent parameters under investigation here, since no simple expression for the correlation length Δl_r of the unsteady loading is available. However, the large span approximation made later in this model overcomes this uncertainty. Further discussion about a relevant choice for Δl_r can be found in the work of Posson et al. [127].

The spanwise separation distance $\delta r=r'-r$ is neglected in the amplitude terms of Eq. 2.48. Thus, combining the expression of the pressure jump (Eq. 2.32) and the formulation for the PSD (Eq. 2.51 to Eq. 2.53) yields the final expression of the PSD radiated by a single strip, of the form

$$S_{pp}\left(r_0,\theta,\omega\right)=\frac{1}{4}\left(\frac{B_1B_2\rho_0k_0b_2}{r_0}\right)^2U_{X2}\Delta r\sum_{q=-\infty}^{\infty}\sum_{m=-\infty}^{\infty}\sum_{n=-\infty}^{\infty}D_{ml}\left(\theta,\alpha_2,\omega\right) \times\int_{-\infty}^{\infty}\Phi_{ww}\left(k_r,K_{X,qmn},K_{Y,qmn}\right)\left|\mathcal{L}^{\mathrm{LE}}\left(k_r,K_{X,qmn},\kappa_{qmn}\right)\right|^2\frac{\sin\left(k_r\frac{\Delta r}{2}\right)}{\pi k_r}dk_r, \quad (2.55)$$

where D_{ml} is a modal polar directivity term given by

$$D_{ml}\left(\theta,\alpha_2,\omega\right)=\frac{1}{\Delta r}\int_{\bar{r}-\frac{\Delta r}{2}}^{\bar{r}+\frac{\Delta r}{2}}\frac{f_m^2\left(r\right)}{r\mathrm{cos}\alpha_2}\left(\frac{l}{k_0 r}\mathrm{cos}\alpha_2+\mathrm{cos}\theta\mathrm{sin}\alpha_2\right)^2 J_l^2\left(k_0 r\mathrm{sin}\theta\right)dr. \tag{2.56}$$

The expression for the PSD of the overall radiated noise is now reduced to a summation over N_j strips, each involving three infinite summations (over indices q, m and n) and two integrals over the strip span Δr and the spanwise wavenumber k_r. The modal behaviour of the radiated broadband noise is discussed in the next section.

The k_r integral in Eq. 2.55 must be evaluated numerically and therefore represents a significant computational burden, which can be substantially reduced by making the large span approximation. In the large-span limit, the identity

$$\lim_{\Delta r\to\infty}\frac{\sin\left(k_r\frac{\Delta r_j}{2}\right)}{\pi k_r}=\delta\left(k_r\right), \tag{2.57}$$

can be used and, therefore, only small values of k_r contribute significantly to the radiated noise. Thus, in the large-span limit, Eq. 2.57 can be substituted into Eq. 2.55 to yield the following expression

$$S_{pp}\left(r_0,\theta,\omega\right)=\frac{1}{4}\left(\frac{B_1 B_2\rho_0 k_0 b_2}{r_0}\right)^2 U_{X2}\Delta r\sum_{q=-\infty}^{\infty}\sum_{m=-\infty}^{\infty}\sum_{n=-\infty}^{\infty}D_{ml}\left(\theta,\alpha_2,\omega\right)$$
$$\times\,\Phi_{ww}\left(0,K_{X,qmn},K_{Y,qmn}\right)\left|\mathcal{L}^{\mathrm{LE}}\left(0,K_{X,qmn},\kappa_{qmn}\right)\right|^2. \tag{2.58}$$

This simplified form for the PSD of the broadband noise due to rotor-wake/rotor interaction may be used to establish the asymptotic behaviour of the noise in the low and high frequency limits. In accordance with Eq. 2.54 for Φ_{ww}, the low and high frequency asymptotic domains of Φ_{ww} are reached for $kL\ll 1$ and $kL\gg 1$, respectively. The summation over the indices q is equivalent to an integral over k_Y (see Eq. 2.24), and the 3D velocity spectrum $\Phi_{ww}\left(k_r,k_X,k_Y\right)$ therefore varies with mean square velocity $\overline{w^2}$, integral length scale L and turbulent wavenumber magnitude k as a 2D spectrum $\Phi_{ww}\left(k_r,k_X\right)$, obtained by integrating Eq. 2.54 over all k_Y to give

$$\Phi_{ww}\left(k_r,k_X\right)=\int_{-\infty}^{+\infty}\Phi_{ww}\left(k_r,k_X,k_Y\right)dk_Y=\frac{4}{9\pi}\frac{\overline{w^2}}{k_e^4}\frac{k^2}{\left(1+\left(k/k_e\right)^2\right)^{7/3}}. \tag{2.59}$$

Assuming that $k \sim \omega/U_{X2}$, scaling laws for Eq. 2.59 valid in the limits of low and high values of kL can be derived as

$$\lim_{kL\to 0} \Phi_{ww}\left(k_r, k_X\right) \sim \overline{w^2} L^4 \left(\frac{\omega}{U_{X2}}\right)^2, \tag{2.60}$$

$$\lim_{kL\to \infty} \Phi_{ww}\left(k_r, k_X\right) \sim \overline{w^2} L^{-2/3} \left(\frac{\omega}{U_{X2}}\right)^{-8/3}. \tag{2.61}$$

Since the flat plate response functions g^{LE} of Amiet [5, 7] are used in Eq. 2.49 and considering that the frequencies of interest are not too low, the scaling of the unsteady loading term $\left|\mathcal{L}^{\mathrm{LE}}\right|^2$ with flow speed and frequency can be approximated as $\left|\mathcal{L}^{\mathrm{LE}}\right|^2 \sim \omega^{-2} U_{X2}$ (see Amiet [6]). The scaling laws for the PSD of the broadband noise must also present a dependency on the half wake width b_W, due to the Fourier components f_m^2 of the wake profiles appearing in Eq. 2.56. It can be seen from equation 2.15 that the term f_m^2 scales with b_W^2, but the fact that the source term $S_{QQ,qmn}$ is summed over m yields a scaling of S_{pp} with b_W. Substituting the above scaling laws for Φ_{ww} and $\mathcal{L}^{\mathrm{LE}}$ into Eqs. 2.58 and 2.56 yields the scaling laws of the PSD of the broadband noise due to rotor-wake/rotor interaction with $\overline{w^2}$, L, b_W and ω and U_{X2} as

$$\lim_{kL\to 0} S_{pp} \sim b_W \overline{w^2} L^4 \omega^2, \tag{2.62}$$

$$\lim_{kL\to \infty} S_{pp} \sim b_W \overline{w^2} L^{-2/3} U_{X2}^{14/3} \omega^{-8/3}. \tag{2.63}$$

The high frequency scaling law in Eq. 2.63 is in agreement with the high frequency approximated expression derived by Amiet [6] (if the dependency on b_W is not considered) for predicting the broadband noise due to an isolated flat plate in a turbulent stream. Note that the validity of the low frequency scaling law of Eq. 2.62 is not as rigorous as Eq. 2.63, due to the high frequency approximation made in the term $\mathcal{L}^{\mathrm{LE}}$, as explained above. However, as shown by the author in Ref. [20], this expression still predicts reasonably well the low frequency trends of the BRWI noise within the audible frequency range.

Sound pressure levels for the BRWI noise can be computed from Eqs. 2.55 or 2.58 by use of the expression

$$\mathrm{SPL}\left(r_0, \theta, \omega\right) = 10\log_{10}\left(\frac{2S_{pp}\left(r_0, \theta, \omega\right)}{4 \times 10^{-10}}\right), \qquad \text{(dB)} \tag{2.64}$$

where the factor 2 has been introduced in order to consider only the positive frequencies of the spectrum.

Finally, the derivation of the sound power level (PWL) including the effects of a uniform mean flow is detailed in Appendix B. The final expression is given by

$$\mathrm{PWL}\left(\omega\right) = 10\log_{10}\left(\frac{2\mathcal{P}\left(\omega\right)}{10^{-12}}\right), \qquad \text{(dB)} \tag{2.65}$$

where

$$\mathcal{P}(\omega) = \frac{2\pi r_0^2}{\rho_0 c_0} \int_0^{\pi} S_{pp}\left(\breve{r}_0, \breve{\theta}, \omega\right) F(\theta, M_x) \sin\theta d\theta, \tag{2.66}$$

and where the function $F(\theta, M_x)$ is defined in Appendix B. Note that the effects of uniform flow can be neglected by setting $\breve{r}_0 = r_0$, $\breve{\theta} = \theta$ and $F(\theta, M_x) = 1$ in Eq. 2.66.

2.3 Modal behaviour of the radiated broadband noise

In this section, a method for reducing the three infinite modal summations in the analytical expression of the PSD (Eq. 2.58) is discussed. In order to identify the modes that contribute most significantly to the far-field radiation, it is essential to understand the variation of the modal PSD of the broadband noise $S_{pp,qmn} = D_{ml}\Phi_{ww}\left|\mathcal{L}^{\mathrm{LE}}\right|^2$ (from Eqs. 2.56 and 2.58), with m, n and q. In general, $S_{pp,qmn}$ varies slowly with changes in the turbulent mode order q but is highly sensitive to the value of the indices m and n. It is therefore proposed to investigate separately the behaviour of $S_{pp,qmn}$ with the indices m and n and its behaviour with the mode q.

2.3.1 Reduction of the summations over the scattering indices m and n

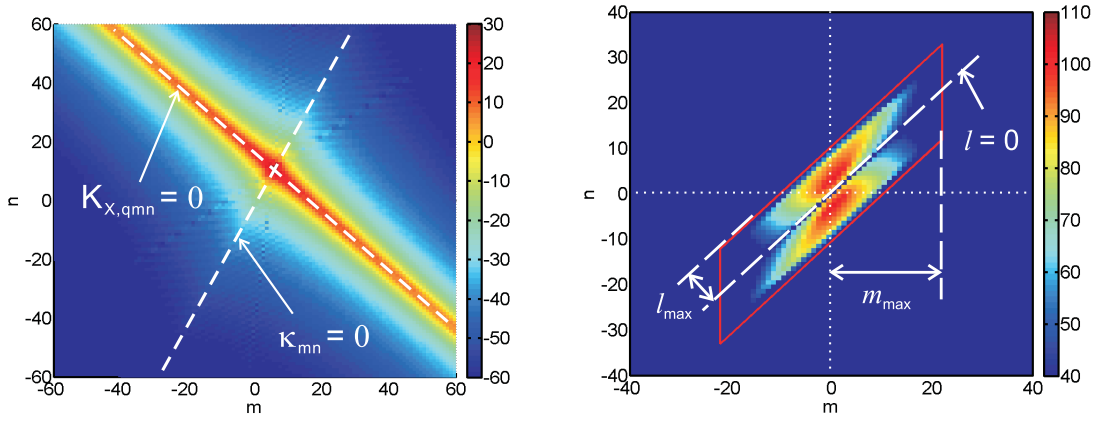

Figure 2.5: Variation of (a) the source term $S_{QQ,qmn} = \Phi_{ww}\left|\mathcal{L}^{\mathrm{LE}}\right|^2$, and (b) the radiation term D_{ml} (in dB and for a single strip) with m and n. $f = 8$kHz, $C_d = 0.1$, $q = 0$, $\theta = 90^{\mathrm{o}}$.

Figure 2.5 shows the variation of the source term $S_{QQ,qmn} = \Phi_{ww}\left|\mathcal{L}^{\mathrm{LE}}\right|^2$, and radiation term D_{ml} with the indices m and n for $q = 0$, for a single strip of the rear rotor at $\theta = 90^{\mathrm{o}}$ at $f = 8$kHz. The configuration chosen here is that of a typical full scale CROR. The source term $S_{QQ,qmn}$ can be seen to have energy distributed over a wide range of (m, n) but is mainly concentrated around the low values of the turbulent chordwise wavenumber

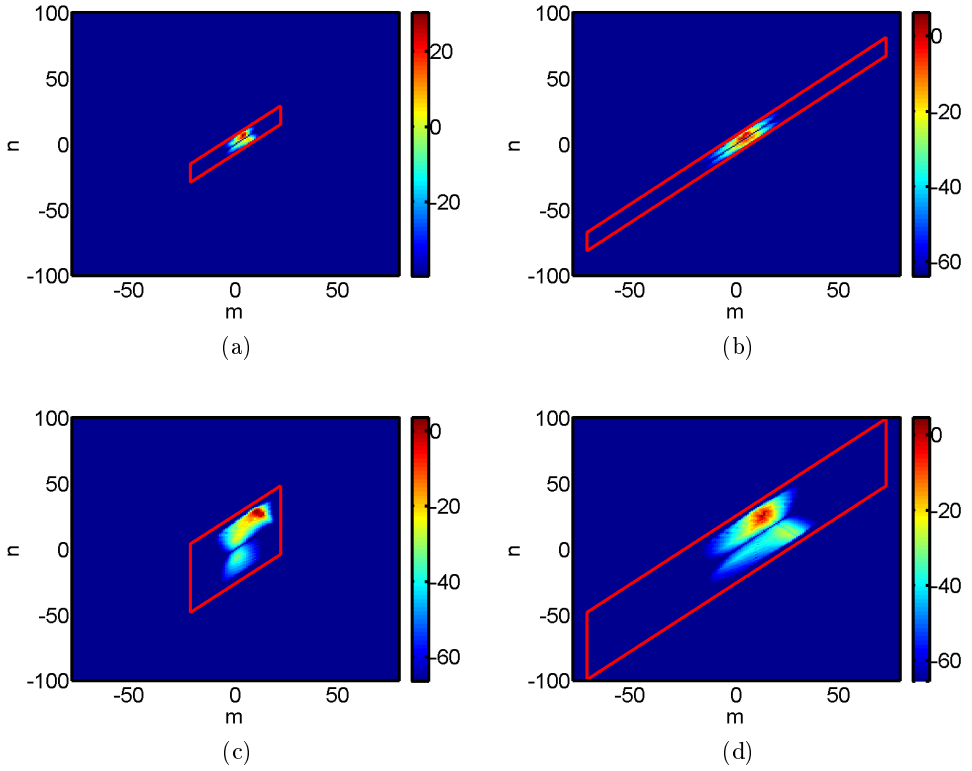

Figure 2.6: Variation of $S_{pp,qmn}$ in dB with m and n and validation of the limiting conditions l_{max} and m_{max} (red line) for a single strip, $q = 0$, $\theta = 90^o$, (a) $f = 5$kHz, $C_d = 0.1$, (b) $f = 5$kHz, $C_d = 0.02$, (c) $f = 20$kHz, $C_d = 0.1$, (d) $f = 20$kHz, $C_d = 0.02$.

($K_{X,qmn} = 0$, dashed line in Fig. 2.5). $S_{QQ,qmn}$ can be observed to exhibit a maximum level at the value of (m, n) corresponding to the smallest values of both the chordwise wavenumber of the turbulence $K_{X,qmn}$ and the aeroacoustic coupling wavenumber κ_{qmn}. This behaviour is due to a combination of the turbulent velocity spectrum Φ_{ww}, which decays rapidly with $K_{X,qmn}$, and the unsteady loading term $|L_{qmn}|^2$, which is maximum for $(K_{X,qmn}, \kappa_{qmn}) \rightarrow (0, 0)$, from Eq. 2.49 and using the flat plate response functions due to Amiet [7, 5].

As shown in Fig. 2.5 (b), the radiation term D_{ml} exhibits sharp cut-off that can be used to limit the maximum value of the m and n summations in Eq. 2.58. The two limits are specified by l_{max} and m_{max}, which are the maximum absolute values of l and m above which the acoustic radiation can be neglected. The limit l_{max} originates, mathematically, from the behaviour of the Bessel function of order l in Eq. 2.56 and is a sharp cut-off condition, whereas the condition m_{max} originates from the behaviour of the Fourier component f_m of the wake profiles of Eq. 2.15 and is a softer limiting condition.

For Bessel functions $J_l(x)$ of high order l, the value of the argument x_0 above which the Bessel function is no longer negligible can be approximated by $x_0 \approx l$. As suggested in Ref. [93] (Chapter 1), the cut-on condition $l \leq l_{max}$ can therefore be approximated by

$\xi > 1$, where $\xi = x_0/l$. Defining the circumferential phase speed of the azimuthal acoustic mode l at the strip considered as $c_l = \omega\bar{r}/l$, the cut-on condition $\xi > 1$ can therefore be satisfied at any θ only if

$$c_l > c_0. \tag{2.67}$$

Equation 2.67 confirms the well-known result that only azimuthal modes l whose azimuthal phase speed is supersonic can radiate efficiently to the far-field. Based on this argument, the maximum value of l is chosen empirically as

$$l_{max} = 1.25\frac{\omega}{c_0}\bar{r}\sin\theta + 3, \tag{2.68}$$

in order to take into account every significant mode l at all frequencies. The Fourier components of the wake profile f_m (Eq. 2.15) are defined by a Gaussian function of m with 'standard deviation' $\sigma = \frac{\bar{r}\sqrt{2a}}{B_1 b_W}$. The width of a Gaussian function is proportionally related to the standard deviation σ and, therefore, the maximum value of m that must be included in the modal summation of Eq. 2.58 must be related to σ and is set to be

$$m_{max} = 4\sigma = 4\frac{\bar{r}\sqrt{2a}}{B_1 b_W}, \tag{2.69}$$

which includes more than 99.99% of the 'energy' distribution over m, according to the '68-95-99.7% rule' for Gaussian functions.

Figure 2.6 shows the variation of $S_{pp,qmn}$ on m and n, for $q = 0$ and $\theta = 90^o$, due to a single strip of the rear rotor. The limits l_{max} and m_{max} are represented by the parallelogram in Fig 2.6. These limits are therefore set conservatively, since a number of non-significant indices m and n are included in the summations, especially at low C_d (which yields low b_W) and high frequency, due to the definition of m_{max}. Note also that the computational cost of the model will be low at high blade numbers B_1 and B_2, since $m_{max} \sim 1/B_1$ (Eq. 2.69) and since fewer l modes are needed if B_1 and B_2 are large (Eq. 2.26).

2.3.2 Reduction of the summation over the azimuthal mode order q

The identification of clear limits involved in the sum over q is more difficult than for the sums over m and n. The limits l_{max} and m_{max} have been defined in Section 2.3.1 for a single given mode q, and therefore the contribution $S_{pp,q}$ of each mode order q to the radiated broadband noise must be expressed $after$ summation over indices m and n, as $S_{pp,q} = \sum_m \sum_n S_{pp,qmn}$. Contrary to that observed for the reduction of the sums over m and n, the behaviour of $S_{pp,q}$ exhibits no clear cut-off condition. A large number of modes q therefore contributes significantly to the far-field noise. Thus, the sum over q can become an important computational burden, especially at high frequencies where many (m, n) modes are significant. This problem has been partly overcome by using an adaptive integration

scheme (adaptive Simpson quadrature) to compute the sum over q at medium and high frequencies. Using this numerical method makes the computation significantly faster, although some care must be taken in its implementation so that all the contributions of the modes q are well captured. $S_{pp,q}$ is generally a smooth well behaved function of q but may exhibit strong oscillatory behaviour in the limit of low frequency and high blade number, which yields strong blade-to-blade correlation as explained in Section 2.4.1. In this case, experience has shown that the adaptive integration should be avoided, and the summation over q should therefore be performed exactly over a sufficiently large range of q to ensure convergence.

In the next section, a simplified model is presented where the rear rotor blade-to-blade interaction is neglected and where the potential issue of finding the limits to the summation over the turbulent azimuthal modes of order q is overcome.

2.4 A simplified BRWI model: approximation of zero correlation between Δp of adjacent blades

In this section, an approximate BRWI model is presented that is a fast alternative to the general model described in Section 2.2. The motivation for investigating a simplified BRWI model came from the observation that the PWL predicted by the general model (Eq. 2.58) generally scales as $B_1 \times B_2$, as presented first below (also presented in Blandeau and Joseph [20]). A simplified expression for the PSD of the BRWI noise is then derived by making the assumption of zero correlation between the pressure jump Δp of adjacent blades. This simplified model is much faster to compute and simpler to implement than the general model because the summation over the mode orders q in Eq. 2.58 (that is treated numerically, see Section 2.3.2) is removed. Finally, a comparison of the simplified and general BRWI models is presented. Predictions of PWL by both models are shown to agree within 1dB if $2b_W/d_2 < 1$, which is verified for most practical CROR configurations.

2.4.1 Motivations for a simplified model: scaling of the PWL as $B_1 \times B_2$

The effects of variations in B_1 and B_2 on the BRWI noise predicted by Eq. 2.58 are investigated for a typical CROR configuration by 'freezing' all other aerodynamic and geometrical parameters. The baseline configuration chosen for this study is that of a typical full scale CROR and the predictions are performed for a single representative spanwise strip of the rotors located at the midspan. The details of the configuration of the CROR and the noise levels are confidential at the time of writing and, therefore, only relative levels of broadband noise are presented in this subsection, without any loss of generality.

Figure 2.7 illustrates the effects of blade number variation on the predicted PWL (in dB) of the BRWI noise. Contour plots of PWL are presented for three representative frequencies

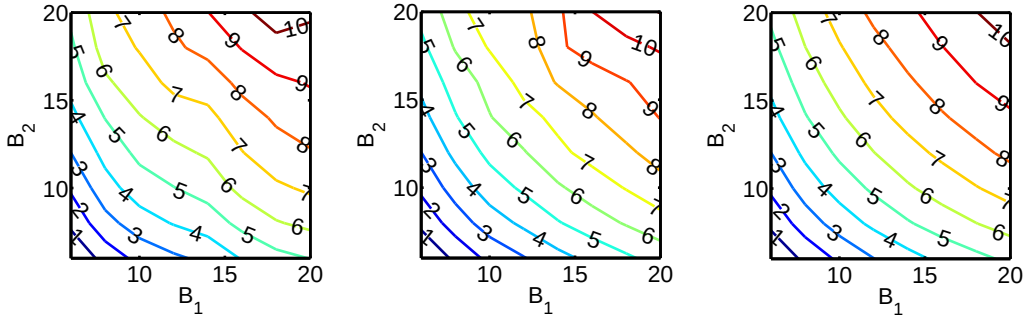

(a) $f = 500$Hz (b) $f = 1$kHz (c) $f = 10$kHz

Figure 2.7: Effects of blade number on PWL $-$ PWL($B_1 = B_2 = 6$) (in dB).

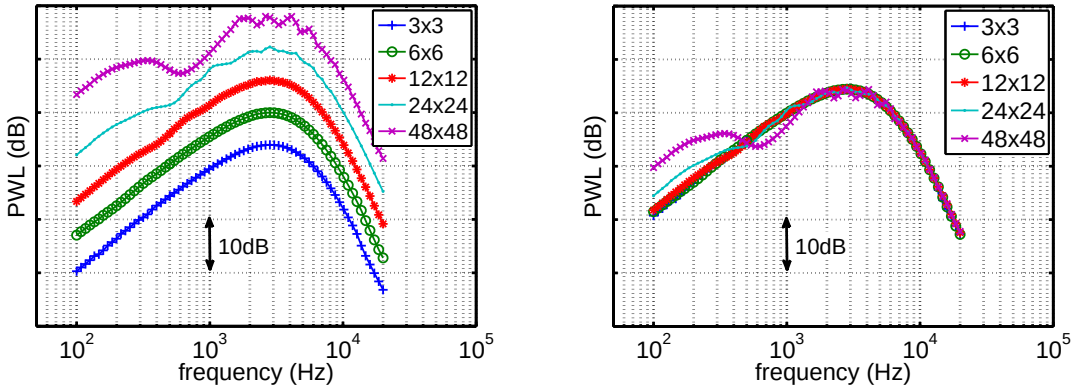

(a) (b)

Figure 2.8: Effects of blade number on PWL(f) (a) without and (b) with normalisation by $B_1 \times B_2$.

and for blade numbers $B_1 = B_2 = 6$ to 20 (with a step of 2). The variation of the contours of PWL, relative to their value at $B_1 = B_2 = 6$, is shown. The contours of PWL exhibit strong symmetry with respect to B_1 and B_2, with small deviations for large values of B_1 and B_2 in Fig. 2.7 (a) and (b). This symmetry indicates that the PWL of the BRWI noise scales as $B_1 \times B_2$. It should be noted, however, that a more complex sensitivity of PWL with the number of blades B_1 and B_2 would be expected if the engine power and solidity were kept constant. Such a parameter study, which represents more closely realistic engineering problems, is presented in Section 4.3.3.

Figure 2.8 shows predicted PWL spectra for $B_1 = B_2 = 3$ to 48, with and without normalisation by $B_1 \times B_2$. As shown in Fig. 2.8(b), the PWL spectra normalised by $B_1 \times B_2$ collapse within 1dB for $f > 6$kHz, at all configurations. At lower frequencies, a collapse within 2dB is observed for low blade numbers configurations ($B_1 = B_2 = 3$ to 12), whereas large oscillations in the PWL spectra are observed for high blade numbers configurations ($B_1 = B_2 = 24$ and 48). These oscillations correspond to the small deviations from the symmetry observed in Fig. 2.7(a) and (b), for large values of B_1 and B_2, and are attributed to blade-to-blade

correlation effects. Blade-to-blade correlation effects for high solidity fans have been first discussed by Mani [109] and Homicz and George [88] (for noise due to turbulence ingestion into a rotor), and occur when the time scale for eddies to be convected past a given point in the rotor plane is smaller than the blade passage time. In this case, peaks occur at frequencies corresponding to the interaction tone frequencies, i.e. at $\omega_{mn} = |mB_1\Omega_1 - nB_2\Omega_2|$ (where $m > 0$ and $n > 0$).

The excellent collapse observed in Fig. 2.8 (b) denotes a clear scaling of the PWL with $B_1 \times B_2$ and suggests that there should exist a fast approximate model, similar to that of Eq. 2.58, in which the correlation between the pressure jump Δp of adjacent blades is neglected. This simplified model is derived in the next section.

2.4.2 Derivation of the simplified model

This section presents the analytical formulation of a simplified model for predicting the BRWI noise, based on the general model presented in Section 2.2.

First, it can be noted that the combination $(nB_2 + q)$ appears in every instance in which the indices n and q appear in Sections 2.2.2 and 2.2.3, except in the definition of $K_{Y,qmn}$ (Eq. 2.33) which is a function of $(nB_2 + q)$ and q. Setting $B_2 = 1$ therefore allows a change of variable to be performed on the scattering index n as $h = n + q$ in Eq. 2.25, to give the pressure jump in the time domain on a *single rear rotor blade* as

$$\Delta p\left(r, X_2, \phi_2, \tau\right) = \frac{1}{\left(2\pi\right)^3} \frac{\rho_0 U_{X2} B_1}{r\cos\alpha_2} \sum_{q=-\infty}^{\infty} \sum_{m=-\infty}^{\infty} \sum_{h=-\infty}^{\infty} f_m\left(r\right) \int_{-\infty}^{\infty}\int \mathcal{W}\left(k_r, k_X, k_Y\right)$$
$$\times\, g^{\mathrm{LE}}\left(X_2, k_r, k_X, M_{X2}\right) e^{-i\left[l\phi_2 + k_r r - \frac{mB_1}{r}\tan\alpha_1\cos\alpha_2\left(X_2+s_2\right)+\left(\omega_{mh}-k_X U_{X2}\right)\tau\right]} dk_r dk_X, \quad (2.70)$$

where $\omega_{mh} = mB_1\Omega_1 + h\Omega_2$ and $l = mB_1 - h$.

Assuming now that a noise source on a blade does not correlate with itself, i.e. that a single rear rotor blade does not 'cut' twice the same eddy, it is possible to write the reciprocal of Eq. 2.24 as

$$\frac{1}{r\cos\alpha_2} \sum_{q=-\infty}^{\infty} \rightarrow \int_{-\infty}^{\infty} dk_Y. \quad (2.71)$$

Substituting Eq. 2.71 into Eq. 2.70 and integrating over all k_Y values yields

$$\Delta p\left(r, X_2, \phi_2, \tau\right) = \frac{1}{\left(2\pi\right)^3} \rho_0 U_{X2} B_1 \sum_{m=-\infty}^{\infty} \sum_{h=-\infty}^{\infty} f_m\left(r\right) \int_{-\infty}^{\infty}\int \mathcal{W}\left(k_r, k_X\right)$$
$$\times\, g^{\mathrm{LE}}\left(X_2, k_r, k_X, M_{X2}\right) e^{-i\left[l\phi_2 + k_r r - \frac{mB_1}{r}\tan\alpha_1\cos\alpha_2\left(X_2+s_2\right)+\left(\omega_{mh}-k_X U_{X2}\right)\tau\right]} dk_r dk_X, \quad (2.72)$$

Following then the same derivation as Eqs. 2.28 to 2.58 and introducing a factor B_2, to account for the contribution of all rear rotor blades, yields the final expression of the simplified model for the PSD of the acoustic pressure radiated to the far-field as

$$S_{pp}\left(r_0,\theta,\omega\right)=\frac{B_2}{4}\left(\frac{B_1\rho_0 k_0 b_2}{r_0}\right)^2 U_{X2}\Delta r\sum_{m=-\infty}^{\infty}\sum_{h=-\infty}^{\infty}D_{ml}^{'}\left(\theta,\alpha_2,\omega\right)\\ \times\Phi_{ww}\left(0,K_{X,mh}\right)\left|\mathcal{L}^{\mathrm{LE}}\left(0,K_{X,mh},\kappa_{mh}\right)\right|^2, \quad (2.73)$$

where the 2D Von Karman velocity spectrum $\Phi_{ww}\left(k_r,k_X\right)$ is defined in Eq. 2.54 and $D_{ml}^{'}$ is a modal polar directivity term given by

$$D_{ml}^{'}\left(\theta,\alpha_2,\omega\right)=\frac{1}{\Delta r}\int_{\bar{r}-\frac{\Delta r}{2}}^{\bar{r}+\frac{\Delta r}{2}}f_m^2\left(r\right)\left(\frac{l}{k_0 r}\mathrm{cos}\alpha_2+\mathrm{cos}\theta\mathrm{sin}\alpha_2\right)^2 J_l^2\left(k_0 r\mathrm{sin}\theta\right)dr. \quad (2.74)$$

The final expression of the simplified model for the PSD of the acoustic pressure, given by Eqs. 2.73 and 2.74, is very similar to that of the general model (Eqs. 2.58 and 2.56). However, the summation over the turbulence azimuthal mode orders q is absent in the simplified model, which is therefore much faster than the general model. In addition, the simplified model is much easier to implement than the general model, since it avoids the difficulty of performing numerically the summation over q as discussed in Section 2.3.2.

2.4.3 Validity of the simplified model for the prediction of CROR broadband noise

In this section, a study of the validity of the simplified BRWI model is presented. The simplified model (Eq. 2.73) is compared to the general model (Eq. 2.58) for CROR configurations where the rear blade number B_2 varies while all other geometrical and flow parameters are kept constant. The agreement between the two models is expected to be linked to the level of correlation between noise sources on adjacent rear rotor blades and hence to the ratio $\frac{2b_W}{d_2}=\frac{b_W B_2}{\pi\bar{r}}$ of the mean wake width over the azimuthal blade separation distance.

Predictions from the two models are compared for a single strip of width $\Delta r=0.2$m and chord $c_2=0.3$m, centred at $\bar{r}=1$m. The front blade number is set equal to $B_1=10$ while the rear blade number B_2 varies. The front and rear stagger angles are set equal to $\alpha_1=\alpha_2=45°$. The two rotor speeds are $\Omega_1=\Omega_2=170\mathrm{rad.s}^{-1}$, the relative gust speed is $U_{X2}=240\mathrm{m.s}^{-1}$ and the turbulent wake parameters are $L=0.04$m and $w_{\mathrm{rms}}/U_{X2}=2\%$. According to Eq. 2.78, the half-wake width is set equal to $b_W=0.095$m. This configuration corresponds to a hypothetical, but realistic CROR, with a highly loaded front rotor, hence the particularly large half-wake width b_W. Figure 2.9 presents the PWL predicted by both models for $B_2=5\,\mathrm{to}\,80$, which corresponds to values of $2b_W/d_2=0.15\,\mathrm{to}\,2.4$. For low $2b_W/d_2$ configurations ($B_2=5\,\mathrm{and}\,10$), excellent agreement of less than 1dB is observed at

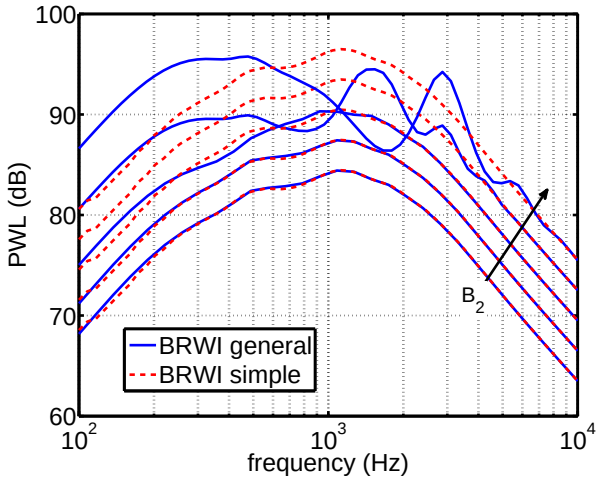

Figure 2.9: PWL of simplified and general BRWI models for $B_2 = 5$, 10, 20, 40, 80, which corresponds to $2b_W/d_2 = 0.15$, 0.3, 0.6, 1.2, 2.4.

all frequencies between the simplified and the general models. For $2b_W/d_2 > 1$ configurations ($B_2 = 40$ and 80), the agreement at high frequencies is good but the agreement at low and medium frequencies is poor, since the PWL spectra predicted by the general model exhibit large oscillations that are not predicted by the simplified model. These differences are attributed to the fact that the simplified model fails to capture the effects of blade-to-blade correlation, which becomes significant for $2b_W/d_2 > 1$. These observations are confirmed in Fig. 2.10, where directivity plots are shown for the SPL (in dB, with relative levels) predicted by both the simplified and general models for $B_2 = 10$, 20 and 40 and for $f = 220$Hz, 1500Hz and 10000Hz.

Figure 2.11 presents overall sound power levels (OAPWL) predicted by both models as a function of $2b_W/d_2$, varying $B_2 = 5$ to 320 and for $L = 0.02$, 0.04 and 0.08 (L is related to b_W by Eq. 2.78). The agreement in terms of OAPWL between the two models is excellent (less than 0.5dB) for $2b_W/d_2 < 1$ but is only fair for $2b_W/d_2 > 1$ (difference up to 3dB). Moreover, both models predict a clear scaling of the OAPWL with B_2 for $2b_W/d_2 < 1$, whereas the general model predicts a scaling of the OAPWL with B_2^2 for $2b_W/d_2 \gtrsim 4$. This B_2^2 scaling represents the fact that noise sources on adjacent blades are strongly correlated for large values of $2b_W/d_2$. However, the B_2^2 scaling of OAPWL is obtained for unrealistically high values of B_2 and is only of academic interest. For realistic CROR configurations, the ratio $2b_W/d_2$ is generally less than 1 and the simplified model can, therefore, be used instead of the general model in most practical cases.

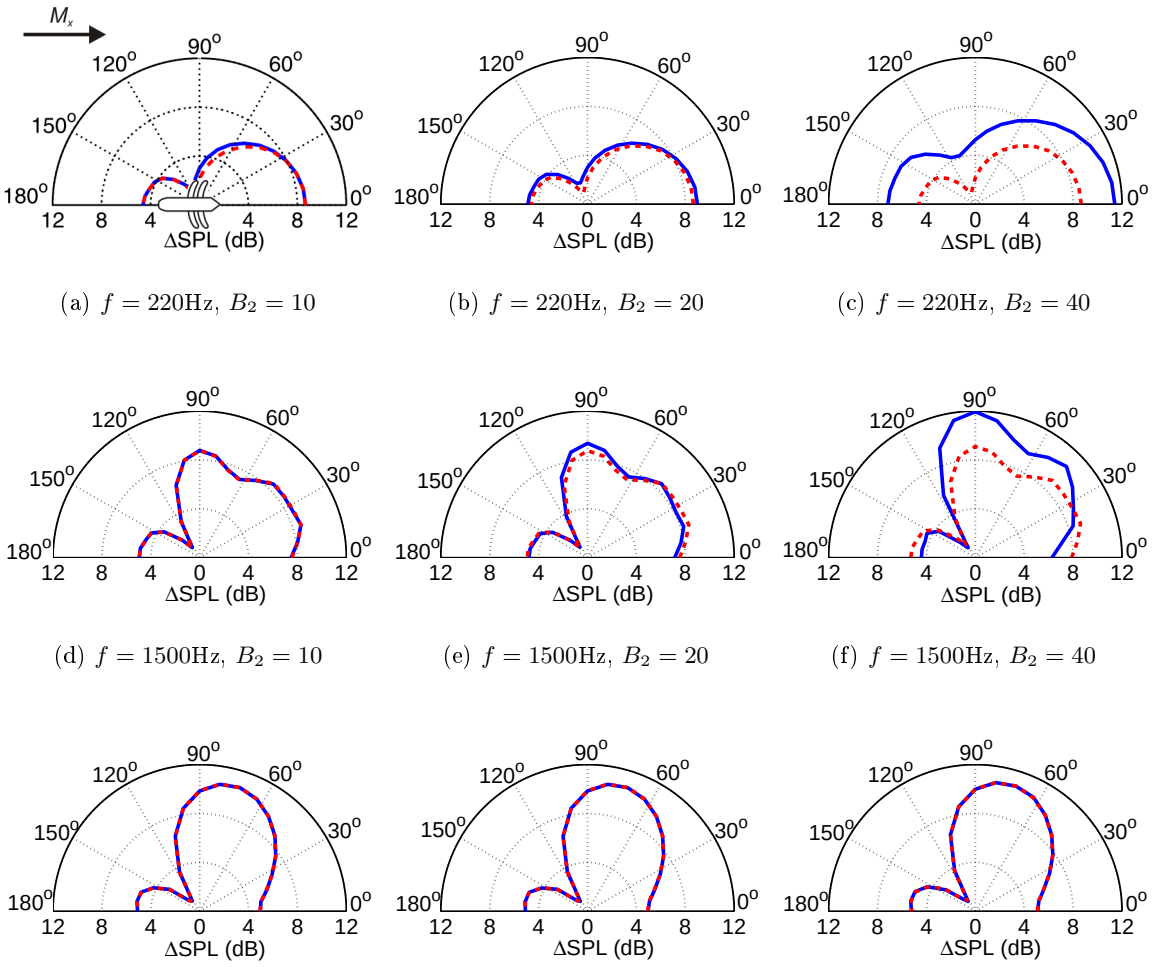

(a) $f = 220$Hz, $B_2 = 10$ (b) $f = 220$Hz, $B_2 = 20$ (c) $f = 220$Hz, $B_2 = 40$

(d) $f = 1500$Hz, $B_2 = 10$ (e) $f = 1500$Hz, $B_2 = 20$ (f) $f = 1500$Hz, $B_2 = 40$

(g) $f = 10000$Hz, $B_2 = 10$ (h) $f = 10000$Hz, $B_2 = 20$ (i) $f = 10000$Hz, $B_2 = 40$

Figure 2.10: Relative SPL as a function of θ from the simplified (−−) and general (−) BRWI models for $B_2 = 10$, 20 and 40 and for $f = 220$Hz, 1500Hz and 10000Hz.

2.5 An empirical model for mean and turbulent wake parameters

The mean and turbulent wake parameters (see Section 2.2.1) are amongst the aerodynamic inputs to which the BRWI noise model presented in this chapter is most sensitive. Their precise values must be known in order to predict broadband noise emissions with accuracy. Since no measurements from the front rotor wake of CRORs were available at the time of this study, the mean and turbulent wake parameters are predicted here using the empirical correlations described in this section. Gliebe et al. [77] established correlations for the half-wake width b_W and the centreline velocity deficit u_0, based on hot-wire measurements in the near-wake region downstream of the front fan of a model-scale turbofan engine, which

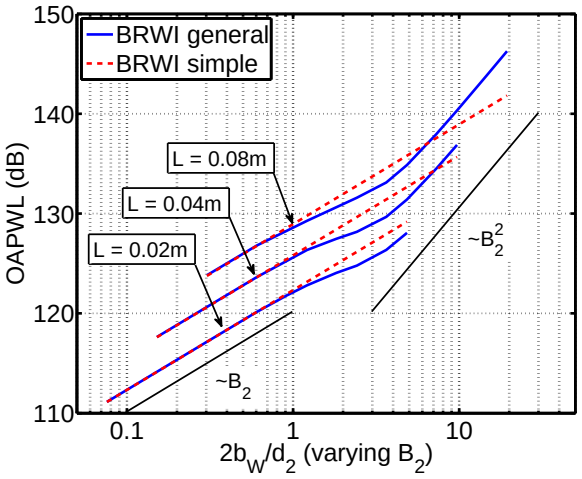

Figure 2.11: OAPWL of simplified and general BRWI models as a function $2b_W/d_2$, varying $B_2 = 5$ to 320 and for $L = 0.02$m, 0.04m and 0.08m.

are given by

$$\left(\frac{b_W}{\Theta_1}\right)^2 = 0.158X_\Theta + 2.494 \text{ and } \left(\frac{U_{X1}}{u_0}\right)^2 = 0.2133X_\Theta + 7.458, \text{ for } X_\Theta < 65, \quad (2.75)$$

where X_Θ is the normalised helical convection distance of a rotor wake, which is the helical convection distance X_η normalised on the momentum thickness Θ_1 (close to the trailing edge) of the front rotor blades, $X_\Theta = X_\eta/(2\Theta_1)$. The helical convection distance X_η is the helical distance in the direction $\mathbf{e}_{X1}$ (see Fig. 2.1) between the front rotor trailing edge and the rear rotor leading edge[2] and is given by

$$X_\eta \cos\alpha_1 = \eta - \left(\frac{c_1}{2} + s_1\right)\cos\alpha_1 - \left(\frac{c_2}{2} - s_2\right)\cos\alpha_2, \quad (2.76)$$

where η is the axial distance between the midchord of the two rotors disks at the hub. The momentum thickness Θ_1 is approximated by Gliebe et al. [77] by $\Theta_1 \approx C_d c_1/2$. Despite the fact that the measurements of Gliebe et al. were performed in the near-wake region (for $X_\Theta < 65$), the predictions of b_W and u_0, given by Eq. 2.75, have been shown to follow closely the classical far-wake scaling laws of Wygnanski et al. [155] and can, therefore, be used with accuracy also in the far-wake region. However, the near-wake correlations proposed by Gliebe et al. for the turbulence integral lengthscale L and the root-mean-square turbulence velocity $w_{rms} = \sqrt{\overline{w^2}}$, given by

$$\frac{L}{\Theta_1} = 0.03084X_\Theta + 1.3591 \text{ and } \frac{w_{rms}}{u_0} = 0.004417X_\Theta + 0.1402, \text{ for } X_\Theta < 65, \quad (2.77)$$

must be replaced by more accurate correlations, as explained below.

[2]Note that Gliebe et al. [77] refer to X_η as the 'axial distance from the rotor blade trailing edge'. This choice of words might be confusing for the reader since their empirical correlations are not defined as a function of the distance in the direction of the fan axis, but rather as a function of the 'helical convection distance' of the turbulent wakes (i.e. in the direction of the chord of the front rotor blades).

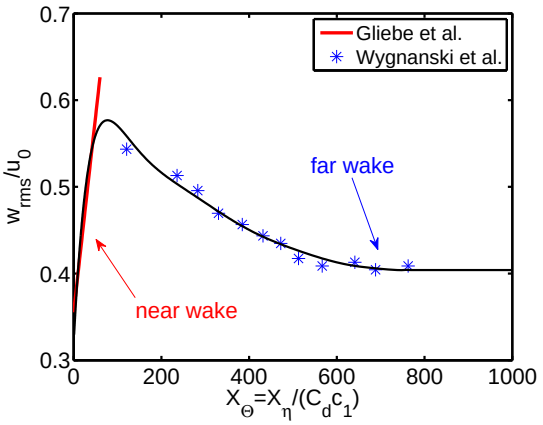

Figure 2.12: Prediction of w_{rms}/u_0 by polynomial curve-fit of order 9 of near and far-wake hot-wire measurements.

First, it can be observed in Eq. 2.77 that the integral lengthscale L is predicted to scale as X_Θ, whereas the half-wake width b_W is predicted to scale as $\sqrt{X_\Theta}$ in Eq. 2.75. If Eq. 2.77 is used in the far-wake region (large values of X_Θ), it can predict the physically unreasonable result that $L > b_W$, i.e. that the large turbulent scales are too large to be contained in the wake. This conclusion would be in contradiction with the results of, for instance, Ganz and al [67] or, more recently, Jurdic et al. [97], who showed that L must be smaller than b_W and that their ratio is generally constant at about 0.4 along the rotor span (except very close to the hub and tip). In the current study, it is therefore chosen to estimate L according to Jurdic et al. [97] as

$$L = 0.42 b_W. \tag{2.78}$$

Moreover, Eq. 2.77 predicts that the ratio w_{rms}/u_0 increases linearly with X_Θ. As for L, this near-wake correlation cannot be extended to the far-wake region since w_{rms}/u_0 must eventually decrease with distance, as shown in the measurements of Wygnanski et al. [155] performed on 2D turbulent wakes downstream of a stationary symmetrical airfoil. It is therefore proposed in this work to predict w_{rms} by combining the near-wake correlation of Gliebe et al. [77], valid for $X_\Theta \leq 65$, and the far-wake measurements of Wygnanski et al. [155], obtained at $X_\Theta \geq 120$. A polynomial curve-fit of order 9, given in Table 2.1 is used to predict the range $65 < X_\Theta < 120$ where no measurements are available, as shown by Fig. 2.12. According to Wygnanski et al. [155], the ratio w_{rms}/u_0 tends asymptotically, in the limit of large X_Θ, to a value independent of X_Θ. Therefore, w_{rms}/u_0 is set arbitrarily to 0.404 for configurations where X_Θ is larger than the maximum value plotted in Fig 2.12 (i.e. for $X_\Theta > 762$ here).

P_0	P_1	P_2	P_3	P_4
0.3200	0.0097	-1.4016×10^{-4}	1.0125×10^{-6}	-4.3311×10^{-9}

P_5	P_6	P_7	P_8	P_9
1.1567×10^{-11}	-1.9492×10^{-14}	2.0145×10^{-17}	-1.1662×10^{-20}	2.8959×10^{-24}

Table 2.1: Coefficients P_j for $w_{rms}/u_0 = \sum_{j=0}^{9} P_j X_\Theta^j$ (for $X_\Theta \leq 762$).

2.6 Response of a flat plate encountering a turbulent gust

This section presents the method used to predict the response function of an isolated unloaded flat plate airfoil, without sweep, to the impingement of a single wavenumber vortical gust and, therefore, to estimate the coupling integral $\mathcal{L}^{\mathrm{LE}}$, given by Eq. 2.49. This problem has been extensively studied since the 1930s (see a brief literature review in Section 1.3.2). A closed-form solution which is uniformly valid at all frequency is not in existence. It has been chosen in this study to follow the formulation of Amiet, detailed in Ref. [13], which is based on the work of Sears [140], Landahl [103] and others.

The 2D problem of a gust at normal incidence ($k_r = 0$) is first considered here. The similarity rules of Graham are then used to extend this solution to the 3D problem of a gust at incidence ($k_r \neq 0$). Note that the subscript $(.)_i$, denoting a quantity associated with the i^{th} rotor (i =1 or 2) in previous sections, has been omitted in this section for the sake of brevity.

2.6.1 Gusts at normal incidence ($k_r = 0$)

Adopting the solution due to Amiet [6], the flat plate response function g^{LE}, introduced in Eq. 2.49, takes two forms depending on the value of a chord-based acoustic reduced frequency $\mu_a = \frac{k_X M_X b}{\beta_X^2}$, which is related to the hydrodynamic reduced frequency $\mu_h = \frac{k_X b}{\beta_X^2} = \mu_a / M_X$. If $\mu_a < \pi/4$, the following flat plate response function, introduced in Ref. [5], is used:

$$g_{low}^{\mathrm{LE}}\left(X, 0, k_X, M_X\right) = \frac{1}{\pi \beta_X} \sqrt{\frac{1 - X/b}{1 + X/b}} S\left(\mu_h\right) e^{i\left(\mu_a M_X X/b + \mu_h f(M_X)\right)}, \tag{2.79}$$

where S is the Sears function defined in terms of Hankel functions of the second kind $H_0^{(2)}$ and $H_1^{(2)}$ as

$$S\left(\mu_h\right) = \frac{2}{\pi \mu_h} \frac{1}{H_0^{(2)}\left(\mu_h\right) - i H_1^{(2)}\left(\mu_h\right)}. \tag{2.80}$$

The phase term $f(M_X) = (1-\beta_X)\ln M_X + \beta_X \ln(1+\beta_X) - \ln 2$ in Eq. 2.79 was introduced by Amiet [5] to correct the solution due to Osborne [118].

If $\mu_a > \pi/4$, the following high frequency response function due to Amiet [7] is used

$$g_{high}^{\mathrm{LE}}(X,0,k_X,M_X) = g_1(X,0,k_X,M_X) + g_2(X,0,k_X,M_X), \tag{2.81}$$

where the functions g_1 and g_2 represent the leading edge scattering and the trailing edge back-scattering of the sound, respectively, and are given by

$$g_1(X,0,k_X,M_X) = \frac{1}{\pi\sqrt{\pi(1+M_X)k_X(b+X)}} e^{-i\left(\mu_a(1-M_X)(1+X/b)-k_X b+\frac{\pi}{4}\right)}, \tag{2.82}$$

$$g_2(X,0,k_X,M_X) = \frac{(1+i)E^*(2\mu_a(1-X/b))-1}{\pi\sqrt{2\pi(1+M_X)k_X b}} e^{-i\left(\mu_a(1-M_X)(1+X/b)-k_X b+\frac{\pi}{4}\right)}, \tag{2.83}$$

where $E^*(\zeta)$ is the conjugate of the Fresnel integral defined by

$$E^*(\zeta) = \frac{1}{\sqrt{2\pi}} \int_0^{\zeta} \frac{e^{-iz}}{\sqrt{z}} dz. \tag{2.84}$$

Note that a different definition for the Fresnel integral is given in Abramowitz and Stegun [1] and implemented in the software MATLAB.

2.6.2 Gusts at incidence ($k_r \neq 0$)

Graham [80] showed that the general problem of a skewed (i.e. 3D) compressible gust encountering a flat plate can be split into two simpler problems depending on the value of the spanwise phase speed $V = U_X/\sin\zeta$ of the gust at the leading edge (cf. Fig 2.13) or, equivalently, the value taken by the Graham number $\Theta_G = k_X M_X/k_r\beta_X$. If V is supersonic ($\Theta_G > 1$), there is similarity to the 2D problem of a compressible gust at normal incidence ($\zeta = 0°$ in Fig. 2.13). If V is subsonic ($\Theta_G < 1$), there is similarity to the 3D problem of an incompressible gust at oblique incidence ($\zeta > 0°$ in Fig. 2.13).

The similarity rule of Graham [80] states that the 3D solution may be obtained from the 2D solution by

$$g^{\mathrm{LE}}(X,k_r,k_X,M_X) = \frac{\beta_{X\infty}}{\beta_X} g^{\mathrm{LE}}(X,0,k_{X\infty},M_{X\infty})\, e^{i\frac{k_r^2}{k_X}X}, \tag{2.85}$$

where the following notations are introduced

$$\beta_{X\infty}^2 = \beta_X^2\left(1+k_r^2/k_X^2\right), \qquad M_{X\infty}^2 = M_X^2 - \beta_X^2 k_r^2/k_X^2, \tag{2.86}$$

$$k_{X\infty} = \frac{\beta_{X\infty}^2}{\beta_X^2} k_X, \qquad \mu_{a\infty} = \frac{k_{X\infty}M_{X\infty}b}{\beta_{X\infty}^2} = \sqrt{\mu_a^2 - \left(\frac{k_r b}{\beta_X}\right)^2}. \tag{2.87}$$

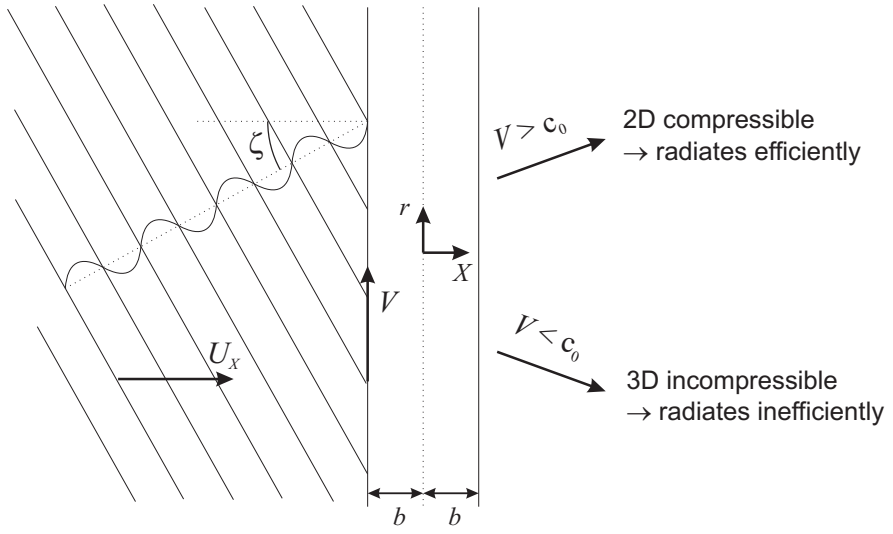

Figure 2.13: Graham's similarity principle for a skewed gust impinging on the leading edge of a flat plate.

Note that the hydrodynamic reduced frequency is unchanged by Graham's similarity rule, since $\mu_{h\infty} = \frac{k_{X\infty} b}{\beta^2_{X\infty}} = \frac{k_X b}{\beta^2_X} = \mu_h$.

Adopting the solution of Amiet [13] for skewed gusts, the flat plate response function g^{LE} takes two forms depending on the value of the acoustic reduced frequency $\mu_{a\infty}$, corrected for the effects of skewed gust. If $\mu_{a\infty} < \pi/4$, substituting Eq. 2.79 into Eq. 2.85 yields,

$$g^{\mathrm{LE}}_{low}\left(X, k_r, k_X, M_X\right) = \frac{1}{\pi\beta_X}\sqrt{\frac{1-X/b}{1+X/b}}S\left(\mu_h\right)e^{i(\mu_a M_X X/b + \mu_h f(M_{X\infty}))}. \tag{2.88}$$

If $\mu_{a\infty} > \pi/4$, substituting Eq. 2.81 to 2.83 into Eq. 2.85 yields,

$$g^{\mathrm{LE}}_{high}\left(X, k_r, k_X, M_X\right) = g_1\left(X, k_r, k_X, M_X\right) + g_2\left(X, k_r, k_X, M_X\right), \tag{2.89}$$

where

$$g_1\left(X, k_r, k_X, M_X\right) = \frac{1}{\pi\sqrt{\pi\left(1+M_{X\infty}\right)k_X\left(b+X\right)}}e^{-i\left((\mu_{a\infty}-\mu_a M_X)(1+X/b)-k_X b+\frac{\pi}{4}\right)}, \tag{2.90}$$

$$g_2\left(X, k_r, k_X, M_X\right) = \frac{(1+i)\,E^*\left(2\mu_{a\infty}\left(1-X/b\right)\right)-1}{\pi\sqrt{2\pi\left(1+M_{X\infty}\right)k_X b}}e^{-i\left((\mu_{a\infty}-\mu_a M_X)(1+X/b)-k_X b+\frac{\pi}{4}\right)}. \tag{2.91}$$

The non-dimensional aerodynamic-acoustic coupling integral $\mathcal{L}^{\mathrm{LE}}$ can now be obtained for the whole range of $\mu_{a\infty}$ by substituting Eqs. 2.88 and 2.89 into Eq. 2.49 and performing analytically the integral over the chord distance X. For low acoustic reduced frequency

$\mu_{a\infty} < \pi/4$, $\mathcal{L}^{\mathrm{LE}}$ is given by

$$\mathcal{L}^{\mathrm{LE}}_{low}\left(k_r, k_X, \kappa\right) = \frac{1}{\beta_X} S\left(\mu_h\right) e^{i\mu_h f(M_{X\infty})} \left(J_0\left(\mu_a M_X - \kappa b\right) - i J_1\left(\mu_a M_X - \kappa b\right)\right). \tag{2.92}$$

For high acoustic reduced frequencies $\mu_{a\infty} > \pi/4$, $\mathcal{L}^{\mathrm{LE}}$ is given by

$$\mathcal{L}^{\mathrm{LE}}_{high}\left(k_r, k_X, \kappa\right) = \mathcal{L}_1\left(k_r, k_X, \kappa\right) + \mathcal{L}_2\left(k_r, k_X, \kappa\right), \tag{2.93}$$

where $\mathcal{L}_1$ and $\mathcal{L}_2$ are defined by

$$\mathcal{L}_1\left(k_r, k_X, \kappa\right) = \frac{\sqrt{2}}{\pi\beta_X\sqrt{\mu_h\left(1+M_{X\infty}\right)\Theta_1}} E^*\left(2\Theta_1\right) e^{i\Theta_2}, \tag{2.94}$$

and

$$\begin{aligned}\mathcal{L}_2\left(k_r, k_X, \kappa\right) = \frac{e^{i\Theta_2}}{\pi\Theta_1\beta_X\sqrt{2\pi\mu_h\left(1+M_{X\infty}\right)}} \Big\{ & i\left(1 - e^{-2i\Theta_1}\right) \\ & + (1-i)\left[E^*\left(4\mu_{a\infty}\beta^2_{X\infty}\right) - \sqrt{\frac{2\mu_{a\infty}}{\Theta_3}} e^{-2i\Theta_1} E^*\left(2\Theta_3\right)\right]\Big\},\end{aligned} \tag{2.95}$$

where the following notation has been introduced for the sake of brevity

$$\begin{cases} \Theta_1 = \mu_{a\infty} - \mu_a M_X + \kappa b \\ \Theta_2 = \beta^2_X \mu_h + \kappa b - \frac{\pi}{4} \\ \Theta_3 = \mu_{a\infty} + \mu_a M_X - \kappa b \end{cases}. \tag{2.96}$$

Equations 2.94 and 2.95 can also be expressed using the error function $\mathrm{erf}\left(\zeta\right)$, which is related to $E^*\left(\zeta\right)$ by $E^*\left(\zeta\right) = \frac{1}{\sqrt{2i}}\mathrm{erf}\left(\sqrt{i\zeta}\right)$ (see Eq. 2.84), as

$$\mathcal{L}_1\left(k_r, k_X, \kappa\right) = \frac{\mathrm{erf}\left(\sqrt{2i\Theta_1}\right) e^{i\Theta_2}}{\pi\beta_X\sqrt{i\mu_h\left(1+M_{X\infty}\right)\Theta_1}}, \tag{2.97}$$

and

$$\begin{aligned}\mathcal{L}_2\left(k_r, k_X, \kappa\right) = \frac{ie^{i\Theta_2}}{\pi\Theta_1\beta_X\sqrt{2\pi\mu_h\left(1+M_{X\infty}\right)}} \Bigg\{ & 1 - \mathrm{erf}\left(2\sqrt{i\mu_{a\infty}\beta^2_{X\infty}}\right) \\ & - e^{-2i\Theta_1}\left(1 - \sqrt{\frac{2\mu_{a\infty}}{\Theta_3}}\mathrm{erf}\left(\sqrt{2i\Theta_3}\right)\right)\Bigg\}.\end{aligned} \tag{2.98}$$

Note that the above expressions for $\mathcal{L}^{\mathrm{LE}}$ (Eqs. 2.92 to 2.98) are valid only when $M_{X\infty} = \sqrt{M_X^2 - \beta_X^2 k_r^2/k_X^2} > 0$, i.e. for supercritical gusts ($\Theta_G > 1$). Expressions for subcritical gusts ($\Theta_G < 1$) are readily deduced from the above expressions by setting $M_{X\infty} = \sqrt{\beta_X^2 k_r^2/k_X^2 - M_X^2}$ in Eqs. 2.86 and 2.87.

Equations 2.97 and 2.98 have to be evaluated a large number of times in order to predict BRWI noise emissions using Eqs. 2.55 or 2.58. The computational effort associated with

the evaluations of error functions $\mathrm{erf}(\zeta)$ with complex argument is particularly high at high frequency, where a large number of indices q, m and n must be computed (see Section 2.3.1). However, this effort can be reduced by replacing, when appropriate, the function $\mathrm{erf}(\zeta)$ by its asymptotic expansion (see Abramowitz and Stegun [1]) defined by

$$\mathrm{erf}(\zeta) \to 1 - \frac{e^{-\zeta^2}}{\zeta\sqrt{\pi}}\left(1 - \frac{1}{2\zeta^2} + \mathcal{O}\left(\frac{1}{\zeta^4}\right)\right), \text{ for } |\zeta| \gg 1 \text{ and } |\arg(\zeta)| < \frac{3\pi}{4}. \tag{2.99}$$

Chapter 3

A model for rotor trailing edge broadband noise

In this chapter a semi-analytical model for the broadband noise due to the interaction of the boundary layer turbulence on each rotor blade with its trailing edge is described. This noise source is referred to here as Broadband noise from Rotor Trailing Edge (BRTE), or 'rotor self-noise', and represents the broadband noise that would be emitted by each rotor if no interaction occurred between the two rotors. The frequency domain noise model presented in this chapter follows an approach similar to Kim and George [100], who assumed that the noise source was a compact point dipole and applied the theory of Ffowcs Williams and Hawkings [64] for the noise from rotating dipole sources to rotor trailing-edge noise predictions. In the present analysis, however, the effects of source non-compactness are fully taken into account. The unsteady loading of the front and rear rotor blades is modelled using classical isolated flat-plate airfoil theory. The flat plate response function due to Amiet [8, 11] is used here and has been chosen because of its similarity to the leading edge noise model used in Chapter 2. The main aerodynamic input to the present BRTE noise model is the surface pressure spectrum close to the trailing edge, for which many semi-empirical models are available in the literature. Predictions from several of these semi-empirical models for the surface pressure spectrum are compared with measurements of Garcia Sagrado [68], in order to identify the most suitable model for BRTE noise prediction. Boundary layer parameters close to the trailing edge of each rotor blade, which are input to the models for the surface pressure spectrum, are predicted using the panel method code XFOIL (Drela [55]). The boundary layer parameters obtained from XFOIL are also validated against measurements by Garcia Sagrado.

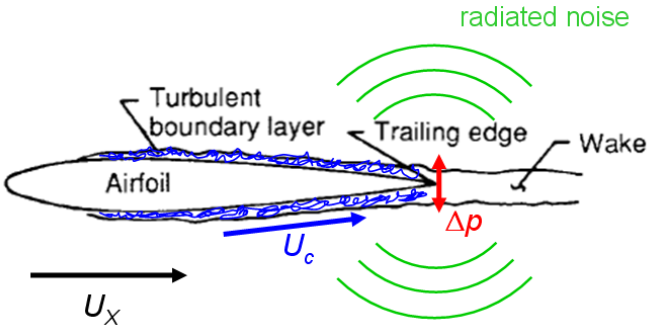

Figure 3.1: Mechanism of broadband noise emission due to trailing edge interaction. Reproduced from Brooks et al. [36].

3.1 Analytical formulation

In this chapter, the expression for the PSD of the BRTE noise is derived in the coordinate systems of the rear rotor, which are presented in Section 2.1. However, the final result can be directly applied to both rotors independently, since the self-noise is by definition independent of any interaction between the rotors. The subscripts $(.)_i$, where $i = 1 \text{ or } 2$, used in Chapter 2 to denote quantities associated to the front and rear rotor, are therefore omitted in this chapter.

Note that, as in the BRWI model derived in Chapter 2, the medium of sound radiation is assumed to be at rest in the present analysis. As for the BRWI model, the effects of uniform flow on the BRTE sound radiation can be taken into account by means of simple corrections derived by Chapman [41], for example, and presented in Appendix B.

3.1.1 Unsteady loading of the rotor blades due to trailing edge interaction

Each rotor blade undergoes a stochastic unsteady pressure difference Δp (or 'pressure jump') when the turbulence in its boundary layer interacts with its trailing edge, as shown in Fig 3.1, thus resulting in broadband noise emission. Following the approach of Amiet [8], the boundary layer turbulence is assumed to be statistically stationary as it is convected past the trailing edge (Taylor's hypothesis) at a velocity U_c. This assumption makes possible the derivation of an expression for the pressure jump from the convecting surface pressure that would exist along the airfoil in the absence of a trailing edge. Including the amplitude correction of Amiet's trailing edge noise formulation due to Moreau and Roger [112, 131], the pressure jump Δp due to a single wavenumber component of the boundary layer turbulence *on one side of the blade* near the trailing edge is given by

$$\Delta p\left(r, X, k_r, k_X, \tau\right) = 2P\left(k_r, k_X\right) g^{\mathrm{TE}}\left(X, k_r, k_X, M_c\right) e^{-i\left(k_r r - k_X U_c \tau\right)}, \tag{3.1}$$

where $M_c = \omega/U_c$. The eddy convection speed is set here equal to $U_c = 0.8U_X$ according to Amiet [8]. The flat plate airfoil response function $g^{\mathrm{TE}}(X, k_r, k_X, M_c)$ in Eq. 3.1 between the incident boundary layer pressure and the pressure jump is chosen to be that derived by Amiet [8, 11]. The term $P(k_r, k_X)$ in Eq. 3.1 represents the surface pressure disturbance near the trailing edge in the wavenumber domain and is obtained by Fourier transforming its spatial counterpart $P(r, X)$ as

$$P(k_r, k_X) = \int_{-R}^{R}\int P(r, X)\, e^{i(k_r r + k_X X)} dr dX, \tag{3.2}$$

where $R = TU_c$ is a large but finite number. Generalising Eq. 3.1, the pressure jump $\Delta\tilde{p}$ due to the interaction of the turbulent boundary layer with the trailing edge is obtained, in the rotating airfoil-bound reference frame, by integrating Eq. 3.1 over all wavenumber components as

$$\Delta\tilde{p}(r, X, \tau) = \frac{2}{(2\pi)^2}\int_{-\infty}^{\infty}\int P(k_r, k_X)\, g^{\mathrm{TE}}(X, k_r, k_X, M_c)\, e^{-i(k_r r - k_X U_c \tau)} dk_r dk_X. \tag{3.3}$$

Since the boundary layer pressures on each blade are uncorrelated, the expression for the pressure jump Δp in the engine-bound reference frame is derived for a single rotating blade, and the 2π azimuthal periodicity of the rotation is introduced as

$$\Delta p(r, X, \phi, \tau) = \Delta\tilde{p}(r, X, \tau) \sum_{l=-\infty}^{\infty} \delta(\phi - \Omega\tau - 2\pi l). \tag{3.4}$$

Substituting Eq.3.3 into 3.4 yields

$$\Delta p(r, X, \phi, \tau) = \frac{2}{(2\pi)^3}\sum_{l=-\infty}^{\infty}\int_{-\infty}^{\infty}\int P(k_r, k_X)\, g^{\mathrm{TE}}(X, k_r, k_X, M_c) \times e^{-i(k_r r - l\phi - (k_X U_c - l\Omega)\tau)} dk_r dk_X, \tag{3.5}$$

where l denotes the azimuthal acoustic mode since it appears in the term $e^{il\phi}$ in Eq. 3.5. The pressure jump estimated at observer time t is obtained by substituting the retarded time Eq. 2.28 in Eq. 3.6, to give

$$\Delta p(r, X, \phi, t) = \frac{2}{(2\pi)^3}\sum_{l=-\infty}^{\infty}\int_{-\infty}^{\infty}\int P(k_r, k_X)\, g^{\mathrm{TE}}(X, k_r, k_X, M_c)\, e^{-i(k_r r - l\phi)} \times e^{i\frac{k_X U_c - l\Omega}{c_0}[c_0 t - r_0 + (X+s)\cos\alpha\cos\theta + r\sin\theta\cos(\phi - \psi + \psi_0)]} dk_r dk_X. \tag{3.6}$$

Fourier transforming Eq. 3.6 with respect to t yields the expression of pressure jump in the frequency domain

$$\Delta\hat{p}\left(r,X,\phi,\omega\right)=\frac{2}{\left(2\pi\right)^{2}U_{c}}\sum_{l=-\infty}^{\infty}\int_{-\infty}^{\infty}P\left(k_{r},K_{X,l}\right)g^{\mathrm{TE}}\left(X,k_{r},K_{X,l},M_{c}\right)$$
$$\times e^{-i(k_{r}r-l\phi)}e^{-ik_{0}[r_{0}-(X+s)\cos\alpha\cos\theta-r\sin\theta\cos(\phi-\psi+\psi_{0})]}dk_{r}, \tag{3.7}$$

where the chordwise turbulent wavenumber $K_{X,l}$ is given by

$$K_{X,l}=\frac{\omega_{l}}{U_{c}}, \tag{3.8}$$

where $\omega_{l}=\omega+l\Omega$ is the Doppler shifted frequency of the l^{th} azimuthal acoustic mode.

Equation 3.7 can now be input into the Ffowcs Williams and Hawkings equation (Ref. [63]) in order to predict the radiated far-field spectrum, as described in the next section.

3.1.2 Sound pressure spectral density of rotor trailing edge noise

The derivation of the PSD of the BRTE noise is presented in this section. Using Eq. 3.7 to describe the unsteady blade loading and following a derivation similar to Eqs. 2.34 to 2.51, the contribution of two azimuthal acoustic modes l and l' to the PSD of the self noise due to a B bladed rotor is derived as

$$S_{pp,ll'}\left(r_{0},\theta,\omega\right)=B\left(\frac{1}{4\pi r_{0}}\right)^{2}\int_{R_{h}}^{R_{t}}\int_{-b}^{b}\int_{0}^{2\pi}\int_{r-\frac{\Delta L_{r}}{2}}^{r+\frac{\Delta L_{r}}{2}}\int_{-b}^{b}\int_{0}^{2\pi}S_{\Delta\Delta,ll'}(r,X,\phi,r',X',\phi',\omega)$$
$$\times\left(\frac{l}{r}\cos\alpha_{2}+k_{0}\cos\theta\sin\alpha_{2}\right)\left(\frac{l'}{r'}\cos\alpha_{2}+k_{0}\cos\theta\sin\alpha_{2}\right)drdXd\phi dr'dX'd\phi', \tag{3.9}$$

where $S_{\Delta\Delta,ll'}$ is the modal cross-PSD of the pressure jump between two points between two points (r,X,ϕ) and (r',X',ϕ') on the surface of a reference blade, due to mode orders l' and l, and is defined by

$$S_{\Delta\Delta,ll'}(r,X,\phi,r',X',\phi',\omega)=\lim_{T\to\infty}\frac{\pi}{T}\left\langle\Delta\hat{p}_{l}^{*}(r,X,\phi,\omega)\Delta\hat{p}_{l'}(r',X',\phi',\omega)\right\rangle, \tag{3.10}$$

where the brackets $\langle.\rangle$ denote the expected value, T represents the averaging time and $\Delta\hat{p}_{l}$ is given by Eq. 3.7 for a single mode order l. Two point sources of broadband noise on a rotor blade can be considered uncorrelated if their radial separation distance is larger than the spanwise correlation length Δl_{r}. Therefore, the domain of integration of the spanwise dr' integral in Eq. 3.9 has been restricted to $\left[r-\frac{\Delta L_{r}}{2},r+\frac{\Delta L_{r}}{2}\right]$, where ΔL_{r} is chosen to be sufficiently larger than Δl_{r} to ensure convergence of S_{pp}.

The only stochastic quantity in the expression for the pressure jump $\Delta\hat{p}$ (Eq. 3.7) is $P(k_r, K_{X,l})$. As a result, every other term can be written outside the expected value in Eq. 3.10. Assuming local homogeneity of the boundary layer turbulence and after some analysis (see Appendix D for detailed derivation), the surface pressure cross-spectrum can be written as

$$\lim_{T\to\infty}\frac{\pi}{T}\left\langle P^*(k_r, K_{X,l})P(k_r^{'}, K_{X,l'})\right\rangle = (2\pi)^2\, U_c\delta\left[l-l'\right]\delta(k_r-k_r^{'})S_{qq}(k_r^{'}, k_X^{'}), \tag{3.11}$$

where S_{qq} is the wavenumber spectral density of the surface pressure cross-spectrum, which is obtained following the approach of Roger and Moreau [130] and Zhou [158], based on the classical model of Corcos [47], as

$$S_{qq}(k_r, k_X) = \frac{1}{\pi}l_r(k_X U_c, k_r)\Phi_{pp}(k_X U_c), \tag{3.12}$$

where $\Phi_{pp}(\omega)$ is the surface pressure spectral density close to the trailing edge (see Section 3.2.1) and the spanwise correlation length l_r is given by

$$l_r(\omega, k_r) = \frac{l_2(\omega)}{\pi}\frac{1}{1+l_2^2(\omega)\,k_r^2}, \tag{3.13}$$

where $l_2 = \frac{\zeta_2 U_c}{\omega}$ and ζ_2 is an adjustable empirical constant. Different values of ζ_2 have been measured by different authors depending on the type of airfoil studied, the angle of attack and the flow velocities, as reviewed by Garcia Sagrado [68] for example. In the present study, it is set equal to $\zeta_2 = 1.6$, as measured by Brooks and Hodgson [35] on a NACA0012 airfoil at zero angle of attack. Note that, since the boundary layer turbulence on both sides of a blade are statistically independent, the contribution to the BRTE noise of the turbulent boundary layers on both sides of the rotor blades can readily be included by replacing Φ_{pp} in Eq. 3.12 by the sum of the surface pressure spectra Φ_{pp} from each side of the reference blade.

In order to reduce the general expression of the PSD (Eq. 3.9) to a form that is computationally more efficient, strip theory is applied in an identical way to the BRWI model, in Section 2.2.3, by dividing the blade span into N_j segments of width Δr, centred at $r = \bar{r}$ and by setting $\Delta L_r = \Delta r$ in Eq. 3.9.

It is assumed that the spanwise separation $\delta r = r' - r$ across a correlation length Δl_r is much smaller than the blade span $R_t - R_h$, and can thus be neglected in amplitude terms in Eq. 3.9. Combining the expression of the pressure jump (Eq. 3.7) and the formulation for the PSD (Eq. 3.9 to Eq. 3.11) yields the final expression of the PSD radiated by a single

strip as

$$S_{pp}\left(r_0,\theta,\omega\right)=\frac{B}{2\pi}\left(\frac{k_0 b}{r_0}\right)^2\Delta r\sum_{l=-\infty}^{\infty}D_l\left(\theta,\alpha,\omega\right)$$
$$\times\int_{-\infty}^{\infty}\left|\mathcal{L}^{\mathrm{TE}}\left(k_r,K_{X,l},\kappa_l\right)\right|^2 S_{qq}\left(k_r,K_{X,l}\right)\frac{\sin\left(k_r\frac{\Delta r}{2}\right)}{\pi k_r}dk_r, \tag{3.14}$$

where D_l is a polar directivity term associated with the l^{th} azimuthal acoustic mode given by

$$D_l\left(\theta,\alpha,\omega\right)=\frac{1}{\Delta r}\int_{\bar{r}-\frac{\Delta r}{2}}^{\bar{r}+\frac{\Delta r}{2}}\left(\frac{l}{k_0 r}\mathrm{cos}\alpha+\mathrm{cos}\theta\mathrm{sin}\alpha\right)^2 J_l^2\left(k_0 r\mathrm{sin}\theta\right)dr. \tag{3.15}$$

The term $\mathcal{L}^{\mathrm{LE}}$ in Eq. 3.14 denotes the non-dimensional aerodynamic-acoustic coupling integral along the airfoil chord and is defined by

$$\mathcal{L}^{\mathrm{TE}}\left(k_r,K_{X,l},\kappa_l\right)=\frac{1}{b}\int_{-b}^{b}g^{\mathrm{TE}}\left(X,k_r,K_{X,l},M_X\right)e^{i\kappa_l(X+b)}dX, \tag{3.16}$$

where the aeroacoustic coupling wavenumber κ_l is given by

$$\kappa_l=\frac{l}{r}\mathrm{sin}\alpha-k_0\mathrm{cos}\alpha\mathrm{cos}\theta. \tag{3.17}$$

Making the large span approximation it follows that $k_r=0$, as in Section 2.2.3, and Eq. 3.14 becomes

$$S_{pp}\left(r_0,\theta,\omega\right)=\frac{B}{2\pi}\left(\frac{k_0 b}{r_0}\right)^2\Delta r\sum_{l=-\infty}^{\infty}D_l\left(\theta,\alpha,\omega\right)\left|\mathcal{L}^{\mathrm{TE}}\left(0,K_{X,l},\kappa_l\right)\right|^2 S_{qq}\left(0,K_{X,l}\right). \tag{3.18}$$

The chordwise integral in Eq. 3.16 can be solved analytically using the response function g^{TE} due to Roger and Moreau [130], who extended the earlier work of Amiet [8, 11] to take into account the effects of skewed gusts, to give

$$\mathcal{L}^{\mathrm{TE}}\left(k_r,k_X,\kappa\right)=\frac{e^{2i\Theta_b}}{i\Theta_b}\left\{e^{-2i\Theta_b}\sqrt{\frac{\Theta_a}{\Theta_a-\Theta_b}}\mathrm{erf}\left[\sqrt{2i\left(\Theta_a-\Theta_b\right)}\right]-\mathrm{erf}\left[\sqrt{2i\Theta_a}\right]+1\right\}, \tag{3.19}$$

where the following notation has been introduced for the sake of brevity

$$\begin{cases}\Theta_a=b\left(k_X+\mu_{a\infty}+\mu_a M_X\right)\\ \Theta_b=b\left(k_X+\kappa\right)\end{cases}, \tag{3.20}$$

and where $\mu_a=k_X M_c b/\beta_X^2$, $\mu_{a\infty}=\sqrt{\mu_a^2-\left(k_r b/\beta_X\right)^2}$ for supercritical gusts (i.e. $\frac{k_X M_c}{k_r\beta_X}>$

1) and $\mu_{a\infty} = \sqrt{(k_r b/\beta_X)^2 - \mu_a^2}$ for subcritical gusts (i.e. $\frac{k_X M_c}{k_r \beta_X} < 1$). Note that Eq. 3.19 neglects the effects of back-scattering by the leading edge and, therefore, neglects most of the effects of finite chord. Moreover, because of the infinite summation over l in Eq. 3.19, the wavenumber $K_{X,l}$ can now take negative values. In order to prevent non-physical discontinuities, the factor $1/\Theta_b = 1/(bk_X + b\kappa)$ at the front of Eq. 3.19, must be replaced by $1/\Theta_b = 1/(b|k_X| + b|\kappa|)$.

A correction term to g^{TE}, in Eq. 3.16, that includes the effects of leading edge back-scattering was derived by Roger and Moreau [130], who showed that this term is significant only at low reduced frequency ($\omega c/c_0 < 1$) and low values of M_X. This correction is not included in the present analysis, since realistic CROR applications often present relatively high values of M_X (generally, $0.4 < M_X < 1$) and since the relation $\omega c/c_0 > 1$ is often verified for frequencies in the audible range.

An alternative expression to Eq. 3.18, in which the effects of rotation are treated approximately, was derived by Amiet [10] and has been widely used for rotor trailing edge noise predictions since. A detailed study of the validity of Amiet's model for rotor trailing edge noise is presented in Chapter 5.

Note that the sound pressure level (SPL) and the sound power level (PWL) of the BRTE noise are computed by substituting Eq. 3.18 into Eqs. 2.64 and 2.65, respectively.

3.2 Models of the surface pressure spectrum Φ_{pp}

3.2.1 Modelling the surface pressure beneath a turbulent boundary layer

In order to use the BRTE noise model given by Eq. 3.18, an accurate evaluation of the surface pressure spectrum Φ_{pp} is required. When no measurements or accurate CFD computations of Φ_{pp} are available, semi-empirical models of Φ_{pp} are needed in order to predict the BRTE noise. Many semi-empirical models of Φ_{pp} are available in the literature and reviews of some of them have been presented by Graham [81], Hwang et al. [94], Rozenberg [133] and others. The main physical characteristics of the surface pressure spectrum Φ_{pp} are described in this section.

It is difficult to establish semi-empirical models for Φ_{pp} that are valid for any airfoil shape and flow conditions since Φ_{pp} is generally sensitive to variations in pressure gradient, and since no universal scaling of the surface pressure spectrum Φ_{pp} exists. Normalisation is usually performed based on parameters associated with one of the following three sets of pressure scales and time scales:

- The *inner variables*, with the wall shear stress τ_w as the pressure scale and ν/u_τ^2 as the time scale ($u_\tau = \sqrt{\tau_w/\rho_0}$ being the friction velocity).

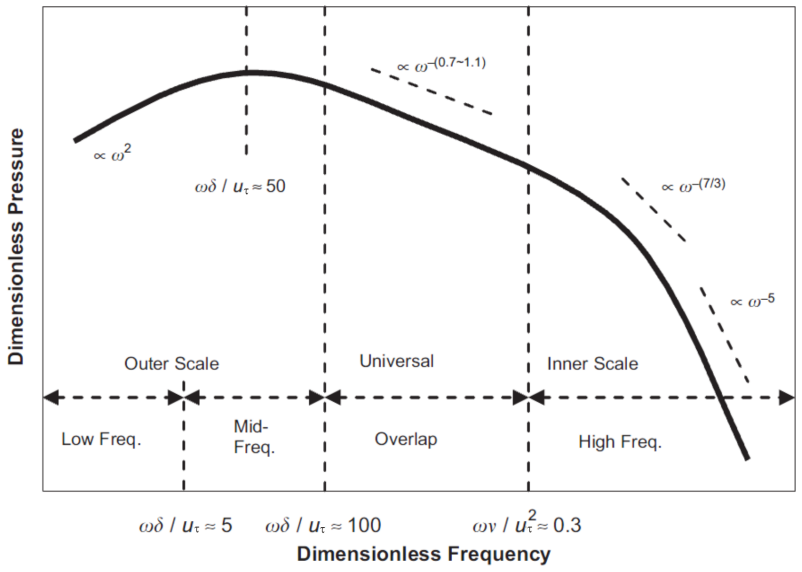

Figure 3.2: General spectral characteristics of Φ_{pp} as a function of non-dimensional frequency. Reproduced from Hwang et al. [94].

- The *outer variables*, with the dynamic pressure $\frac{1}{2}\rho_0 U_X^2$ as the pressure scale and δ^*/U_X as the time scale.
- The *mixed variables*, with the wall shear stress τ_w as the pressure scale and δ^*/U_X as the time scale.

The general spectral characteristics of Φ_{pp} as a function of non-dimensional frequency are shown in Fig. 3.2. Three main frequency regions of Φ_{pp} can be observed: a low frequency range where Φ_{pp} scales with ω^2, a high frequency range where Φ_{pp} scales with ω^{-5} and an overlap range where Φ_{pp} decays as approximately ω^{-1}. The existence of the overlap range was first postulated by Bradshaw [34] and its frequency bandwidth has been observed to increase with Reynolds number.

Keith et al. [99], Goody [78] and others have studied the impact of the choice of normalisation on the collapse of the surface pressure spectra Φ_{pp} measured on flat surfaces (i.e. no pressure gradient) by several authors. They observed that using the inner variables τ_w and ν/u_τ^2 and the outer variable $\frac{1}{2}\rho_0 U_X^2$ and δ^*/U_X provides a good collapse of the data in the high and low frequency range, respectively. Both the inner and outer variables provide reasonable agreement in the overlap range. However, it is generally agreed (Goody [78], Rozenberg [133]) that the use of the mixed variables τ_w and δ^*/U_X for normalising Φ_{pp} provides the best overall collapse of the measured data, and should therefore be used when developing semi-empirical models.

A short review of several semi-empirical models for Φ_{pp} commonly used for trailing edge noise predictions is now presented. A distinction is made in this review between the semi-empirical

models based on surface pressure measurements on unloaded flat plates (zero pressure gradient) and on airfoils (non-zero pressure gradients). Note that all the expressions presented here for $\Phi_{pp}(\omega)$ are *double-sided* spectra, following the convention $\overline{p^2} = \int_{-\infty}^{\infty} \Phi_{pp}(\omega)\, d\omega$. Thus, a factor 1/2 has been included in the models that were initially expressed as *single-sided* spectra.

3.2.2 Flat plate models

Willmarth-Roos-Amiet

Amiet [8] proposed an expression for the surface pressure spectrum Φ_{pp} by curve-fitting the measurements of Willmarth and Roos [152] of the pressure fluctuation beneath the turbulent boundary layer of a flat plate. Amiet chose to normalise Φ_{pp} with outer variables and obtained the expression

$$\frac{\Phi_{pp}(\omega)\, U_X}{\left(\frac{1}{2}\rho_0 U_X^2\right)^2 \delta^*} = \frac{2 \times 10^{-5}}{(1 + \bar{\omega} + 0.217\bar{\omega}^2 + 0.00562\bar{\omega}^4)} \quad \text{for } 0.1 < \bar{\omega} < 20, \tag{3.21}$$

where $\bar{\omega} = \omega\delta^*/U_X$.

This model was a used by Schlinker and Amiet [138] to predict the trailing edge noise of helicopter rotor blades and showed reasonable agreement in overall level but poor agreement in terms of spectrum shape. The main theoretical drawbacks of this model are that the outer variables are used for normalising Φ_{pp} and that the physical asymptotic trends shown in Fig. 3.2 are not captured.

Chase-Howe

Howe [90] proposed an expression for Φ_{pp} based on the model of Chase [44] which is given by

$$\frac{\Phi_{pp}(\omega)\, U_X}{\tau_w^2 \delta^*} = \frac{\bar{\omega}^2}{(\bar{\omega}^2 + 0.0144)^{1.5}}. \tag{3.22}$$

The Chase-Howe model uses mixed variables for normalisation. Unlike the Willmarth-Roos-Amiet model of Eq. 3.21, it captures the scaling of Φ_{pp} with ω^2 in the low frequency limit and with ω^{-1} in the high frequency limit, which corresponds to the overlap frequency region (see Section 3.2.1). However, the ω^{-5} behaviour observed at high frequencies is not included in the Chase-Howe model.

Goody

More recently, Goody [78] proposed a semi-empirical model which takes into account the effects of the Reynolds number on the size of the overlap frequency region. Goody extends the Chase-Howe model by considering an extensive data set of surface pressure spectra gathered from the work of seven different research teams. He achieves a reasonable match to the data set using the expression

$$\frac{\Phi_{pp}(\omega)\,U_X}{\tau_w^2\delta} = \frac{1}{2}\frac{3.0\,(\omega\delta/U_X)^2}{\left[(\omega\delta/U_X)^{0.75}+0.5\right]^{3.7}+\left[1.1R_T^{-0.57}\,(\omega\delta/U_X)\right]^7}, \tag{3.23}$$

where the ratio R_T of outer-to-inner timescales has been introduced as

$$R_T = (\delta/U_X)\,/\left(\nu/u_\tau^2\right) = (u_\tau\delta/\nu)\sqrt{C_f/2}, \tag{3.24}$$

and where $C_f = \tau_w/\left(0.5\rho_0 U_X^2\right)$ is the skin friction coefficient.

The main improvements of this model to the Chase-Howe model are the following:

1. The ω^{-5} scaling of Φ_{pp} in the high frequency limit is predicted by the inclusion of a term in the denominator.
2. The rate of decay with frequency of the overlap region is now $\omega^{-0.7}$, which is in better agreement with the measurements collated by Goody than the theoretical ω^{-1} rate, introduced by Bradshaw [34].
3. The introduction of the ratio of outer-to-inner timescales R_T in Eq. 3.23 allows the model to capture the effects of Reynolds number on the width of the overlap region.

Note that, contrary to the all other models considered here, Goody chose to use as a lengthscale the boundary layer thickness δ instead of the displacement thickness δ^*. This choice was motivated by the fact that the largest coherent structure in the boundary layer are of order δ and this modification yields a slightly better collapse of the experimental data collated by Goody.

3.2.3 Airfoil models

Kim-George

Kim and George [100] proposed an empirical expression for Φ_{pp} by curve-fit of the experimental data of both Brooks and Hodgson [35] and Yu and Joshi [156] measured on a

NACA0012 airfoil, which is given by

$$\frac{\Phi_{pp}(\omega)\,U_X}{\left(\frac{1}{2}\rho_0 U_X^2\right)^2\delta^*} = \frac{1}{2}\frac{1.732\times10^{-3}\bar{\omega}}{1-5.489\bar{\omega}+36.74\bar{\omega}^2+0.1505\bar{\omega}^5} \quad \text{for } \bar{\omega}<0.06, \tag{3.25}$$

$$\frac{\Phi_{pp}(\omega)\,U_X}{\left(\frac{1}{2}\rho_0 U_X^2\right)^2\delta^*} = \frac{1}{2}\frac{1.4216\times10^{-3}\bar{\omega}}{0.3261+4.1837\bar{\omega}+22.818\bar{\omega}^2+0.0013\bar{\omega}^3+0.0028\bar{\omega}^5} \quad \text{for } 0.06\leq\bar{\omega}\leq20. \tag{3.26}$$

Some of the effects of adverse pressure gradient are included in this formulation because the data fitted were obtained by measurements on a NACA0012 airfoil. However, the low and high frequency asymptotic trends shown in Fig. 3.2 are not captured and outer variables have been used rather than mixed variables for normalising Φ_{pp}.

Rozenberg

Rozenberg [133] proposed a model based on Goody's model (Eq. 3.23) that includes the effects of an adverse (positive) pressure gradient. His approach differs from that of Goody due to the fact that the Strouhal number $\bar{\omega}$ used is based on displacement thickness δ^* (using the relation $\delta = 8\delta^*$), rather than the boundary layer thickness δ used in Goody's model, and that an additional term C is introduced. Rozenberg's final expression is given by

$$\frac{\Phi_{pp}(\omega)\,U_X}{\tau_w^2\delta^*} = \frac{1}{2}\frac{C\bar{\omega}^2}{\left[\bar{\omega}^{0.75}+0.105\right]^{3.7}+\left[3.76R_T^{-0.57}\bar{\omega}\right]^7}. \tag{3.27}$$

The factor $C = 0.78\,(1.8\Pi\beta_c + 6)$ is introduced to capture the effects of the pressure gradient on the surface pressure spectrum. It is a function of Coles' wake law parameter Π and Clauser's pressure gradient parameter β_c, respectively given by the expressions

$$2\Pi - \ln(1+\Pi) = \kappa U_X/u_\tau - \ln\left(\delta^* U_X/\nu\right) - 5.1\kappa - \ln\kappa, \tag{3.28}$$

$$\beta_c = (\Theta/\tau_w)\,(dp/dx)\,, \tag{3.29}$$

where dp/dx is the pressure gradient along the chord and $\kappa = 0.41$ is the Von Karman constant. Note that if $dp/dx = 0$ and if the relation $\delta = 8\delta^*$ is assumed to be valid, Eq. 3.27 reduces exactly to Eq. 3.23.

We note the following three issues concerning the application of Rozenberg's model:

- Rozenberg provides little detail about how to compute dp/dx in Eq. 3.29. In the current analysis, dp/dx is computed as the average gradient of the pressure coefficient C_p between the 50% and 85% of the chord.

- The factor C in Eq. 3.27 has been introduced to take into account the effects of the adverse pressure gradient ($dp/dx > 0$) that occurs on the suction side of an airfoil at angle of attack. However, this model has not been designed to predict the effects of favorable pressure gradient ($dp/dx < 0$) that occurs on the pressure side of the airfoil. Setting $dp/dx < 0$ may yield negative predicted values of Φ_{pp}, which is not physically correct. For configurations with favorable pressure gradients, it is therefore chosen to neglect the effects of pressure gradient by setting $dp/dx = 0$ in Eq. 3.27.
- The term R_T (eq. 3.24) is still expressed as a function of the boundary layer thickness δ in Rozenberg's model, rather than the displacement δ^* which is used in the Strouhal number $\bar{\omega}$. In the current study, the relation $\delta = 8\delta^*$ is also used in R_T (Eq. 3.24), for consistency.

Rozenberg's semi-empirical model is more detailed than the other 'Corcos-based' models presented previously and is intended to be more robust to variations in airfoil configurations. It should also be able to predict some of the effects of airfoil camber and thickness on the aerodynamic input, for it takes into account the effects of pressure gradient. However, it has been so far validated against few test cases and, according to Rozenberg [133], this model would need to be refined further by comparing it to a larger set of experimental data.

Glegg-Jochault

Glegg and Jochault [76] proposed an alternative model to Eq. 3.12 for computing S_{qq}. Using the classical formulation of Amiet [8] for predicting the PSD $S_{pp,0}$ of the trailing edge noise due to a stationary flat plate airfoil in a flow, they proposed to deduce the wavenumber cross-spectrum of the surface pressure S_{qq} from $S_{pp,0}$ as

$$S_{qq}\left(0, k_X\right) = \frac{S_{pp,0}\left(r_0, \theta, \omega\right)}{8D\left(r_0, \theta, \omega, 0, k_X\right)}, \tag{3.30}$$

where, following the approach by Amiet [8], $D\left(\mathbf{x}_0, \omega, 0, k_X\right)$ is a directivity factor given by

$$D\left(r_0, \theta, \omega, k_r, k_X\right) = \Delta r \left(\frac{k_0 b}{2\pi r_0 \left(1 - M_X^2 \sin^2\theta\right)}\right)^2 \left|\mathcal{L}^{\mathrm{TE}}\left(k_r, K_{X,0}, \kappa_0\right)\right|^2,$$

where $\left|\mathcal{L}^{\mathrm{TE}}\right|^2$ is given by Eq. 3.19, $K_{X,0}$ and κ_0 are deduced from Eqs. 3.8 and 3.17 with $l = 0$.

Note that, contrary to all the 'Corcos based' semi-empirical models for Φ_{pp} described previously, this formulation avoids the need for modelling the spanwise correlation length l_r(in Eq. 3.12), since it is already included in S_{qq}. In the current study, as in Ref. [76], $S_{pp,0}$ is evaluated using the semi-empirical prediction model of Brooks et al. [36], which has been widely used and validated. Note that a factor of 1/2 has been introduced in Eq. 3.30 to

consider a *double-sided* spectrum and a factor of 1/4 has been introduced as a correction term for Amiet's model, as suggested by Moreau and Roger [131]. This method should capture accurately variations in Strouhal number, chord length and angle of attack, as these parameters are included in the semi-empirical prediction scheme due to Brooks et al. [36] The main limitation of this model is that it is only strictly applicable to NACA0012 airfoils, since the prediction scheme of Brooks et al. is valid only for symmetrical NACA0012 profiles.

3.3 Comparison of predictions of Φ_{pp} with surface pressure measurements on a NACA0012 airfoil

Surface pressure and boundary layer measurements were performed by Garcia Sagrado [68] on a NACA0012 airfoil of chord $c = 0.3$m for two different flow speeds, $U_X = 10\text{m.s}^{-1}$ and 20m.s^{-1} (corresponding respectively to chord-based Reynolds numbers equal to $Re_c = 2 \times 10^5$and 4×10^5), and for three different effective angles of attack $AoA = 0°$, 6.25°and 8° (corrected to take into account the deflection of the jet by the airfoil). Both sides of the airfoil include a trip wire at 12.7% of the chord in order to force the transition of the boundary layer. The data considered were obtained on a slightly blunt airfoil with a thickness at the trailing edge of 1.6mm. A small contribution of vortex-shedding to the surface pressure spectrum has been observed very close to the trailing edge at zero angle of attack at frequencies close to 550Hz for $Re_c = 2\times10^5$ and close to 1100Hz for $Re_c = 4\times10^5$. Very little contribution of the vortex-shedding was observed at $AoA = 6.25°$ and 8°.

The code XFOIL, due to Drela [55], is used to obtain the turbulent boundary layer parameters close to the trailing edge, required in all the models for Φ_{pp} described in Sections 3.2.2 and 3.2.3. XFOIL is a panel method code for the viscous or inviscid analysis of isolated airfoils in subsonic steady flows. It incorporates the effects of compressibility via a Karman-Tsien correction factor. The boundary layer is modelled using a two-equation integral formulation (for the momentum thickness and the kinetic energy shape parameter, as presented in Drela and Giles [56]) which allows XFOIL to model moderate boundary layers separation and transitional separation bubbles. The presence of a trip wire to force the transition of the turbulent boundary layer can be included in XFOIL.

In this section, the boundary layer measurements of Garcia Sagrado [68] are used to validate the predictions of XFOIL. The surface pressure models described in Sections 3.2.2 and 3.2.3 are then compared to Garcia Sagrado's [68] surface pressure measurements.

3.3.1 Comparison of XFOIL predictions with measurements

In this section, a comparison between the boundary layer measurements of Garcia Sagrado [68] on the suction side of a NACA0012 airfoil (pressure side measurements are not available)

and numerical predictions of the panel method code XFOIL [55] is presented for the displacement thickness δ^*, the skin friction coefficient C_f , the pressure coefficient C_p and the average pressure gradient dp/dx between 50% and 85% of the chord. The six airfoil configurations studied by Garcia Sagrado are considered here, i.e. $AoA = 0°$, 6.25°and 8° and $Re_c = 2 \times 10^5$and 4×10^5. Note however that these Reynolds numbers are significantly lower than those encountered in realistic CRORs (about $Re_c \approx 3 \times 10^6$ to 6×10^6 at take-off, for the configuration presented in Section 4.2.1.1).

Figure 3.3 presents the comparison between the measured and predicted values of the displacement thickness δ^*. Note that for the $AoA = 8°$ case, measured data are available for only three chordwise points, but the comparison is still shown here for the sake of completeness. For $AoA = 0°$, a good agreement is observed between predictions and measurements, but δ^* is systematically underpredicted for $AoA = 6.25°$ and 8°. This discrepancy may be due to a lack of accuracy in the estimation of the angle of attack in the measurements due to the deflection of the jet by the airfoil, which is fairly strong in Garcia Sagrado's experiments. The *effective* angles of attack ($AoA = 6.25^o$ and 8^o) have been deduced from the *actual* angles ($AoA = 12.6^o$ and 16^o, respectively) using the empirical wind tunnel correction scheme by Brooks et al.[36]. An error of only 1^o for $AoA = 6.25°$ and 2° for $AoA = 8°$ would be enough to justify the discrepancy shown in Fig.3.3 (c) to (f).

An accurate estimation of the friction coefficient $C_f = \tau_w / \left(0.5\rho_0 U_X^2\right)$ is also important since several Φ_{pp} models in Section 3.2 use the wall shear stress τ_w as an input. A comparison of the predicted and measured values of C_f is presented in Fig. 3.4. The agreement between the measurements and the predictions is good for all configurations, although the XFOIL predictions underestimate slightly the measurements at $Re_c = 2 \times 10^5$ and $AoA = 0°$.

As stated in Section 3.2.3, since the average pressure gradient between 50% and 85% of the chord is used as input into Rozenberg's model for Φ_{pp}, an accurate estimation of the pressure coefficient C_p is required. Figure 3.5 shows a comparison between the measured and predicted values of C_p along the airfoil chord. Good agreement is observed, even if all the predictions underestimate slightly the measurements. The peak of C_p observed in the measurements at approximately 13% of the chord is due to the trip used to force the transition of the boundary layer (located at 12.7%). The presence of this trip is taken into account in the predictions of XFOIL but does not generate the large disturbance observed in the measurements in Fig 3.5.

Garcia Sagrado [68] provides an averaged value of the pressure gradient (between 25% and 85% of the airfoil chord) in terms of the non-dimensional pressure gradient parameter $K = \frac{\nu}{U_X^2}\frac{dU_X}{dx}$. The number K can be related to the pressure gradient dp/dx and the Clauser parameter β_c (Eq. 3.29), used in the Rozenberg model, using the Bernoulli equation as

$$K = -\frac{\nu}{\rho U_X^3}\frac{dp}{dx} = \frac{\nu}{\Theta U_X}\left(\frac{u_\tau}{U_X}\right)^2 \beta_c. \tag{3.31}$$

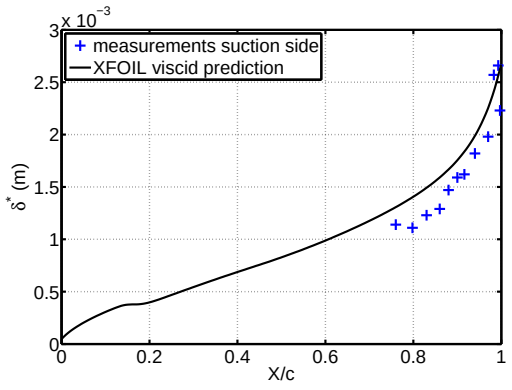

(a) $Re_c = 2 \times 10^5$, $AoA = 0°$

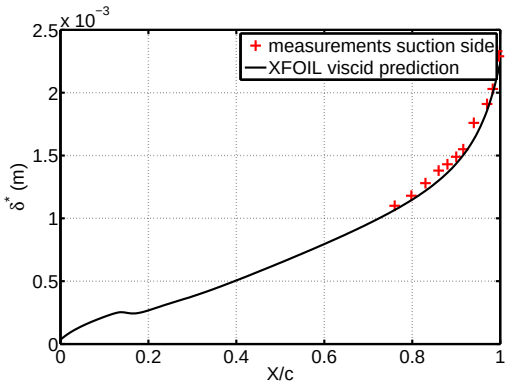

(b) $Re_c = 4 \times 10^5$, $AoA == 0°$

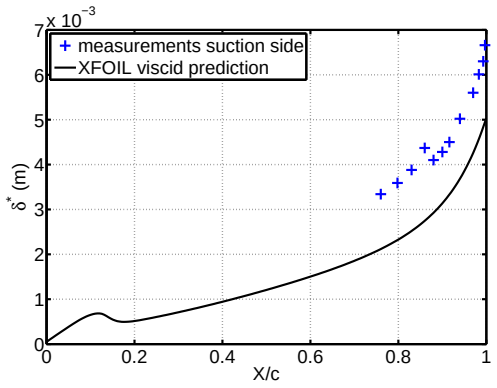

(c) $Re_c = 2 \times 10^5$, $AoA = 6.25°$

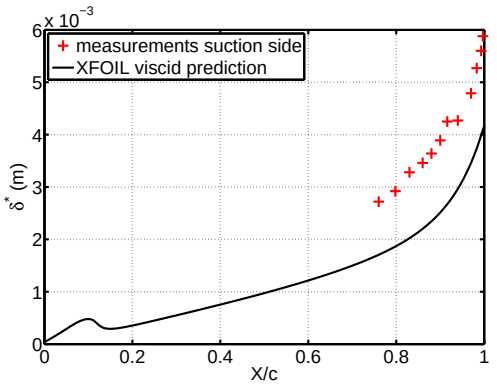

(d) $Re_c = 4 \times 10^5$, $AoA = 6.25°$

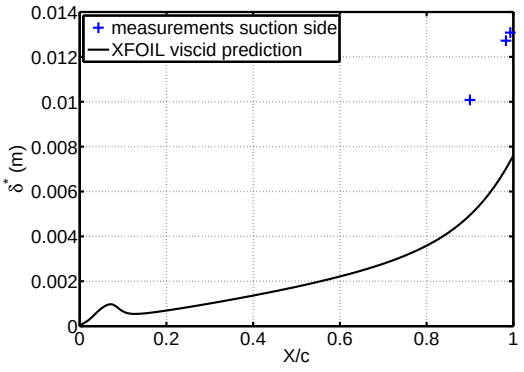

(e) $Re_c = 2 \times 10^5$, $AoA = 8°$

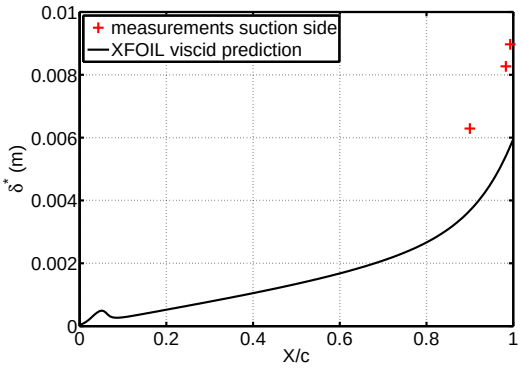

(f) $Re_c = 4 \times 10^5$, $AoA = 8°$

Figure 3.3: Comparison of measured and predicted (XFOIL) values of δ^*.

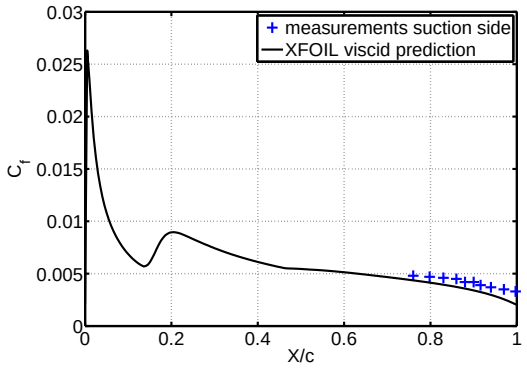

(a) $Re_c = 2 \times 10^5$, $AoA = 0°$

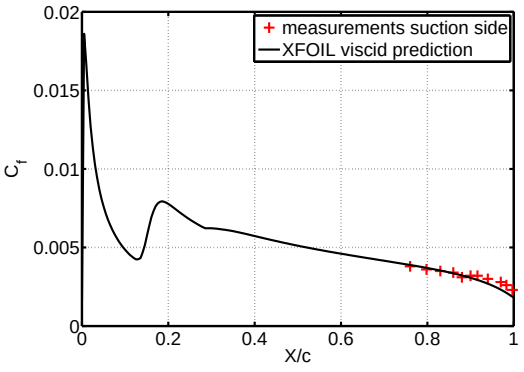

(b) $Re_c = 4 \times 10^5$, $AoA = 0°$

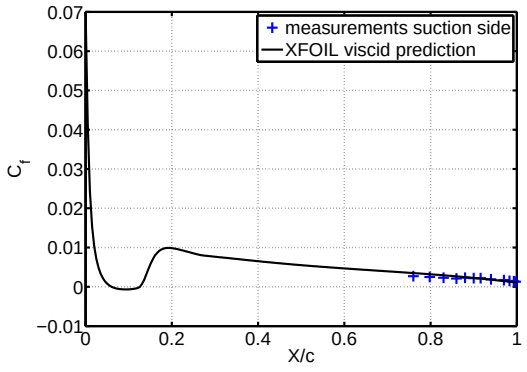

(c) $Re_c = 2 \times 10^5$, $AoA = 6.25°$

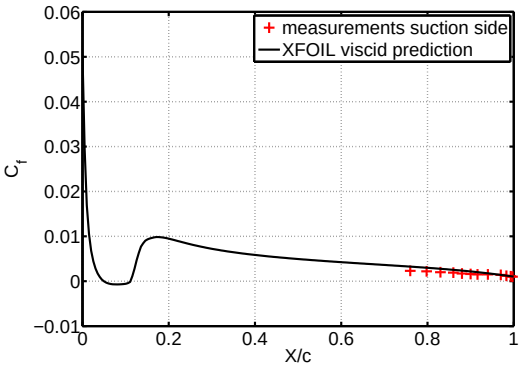

(d) $Re_c = 2 \times 10^5$, $AoA = 6.25°$

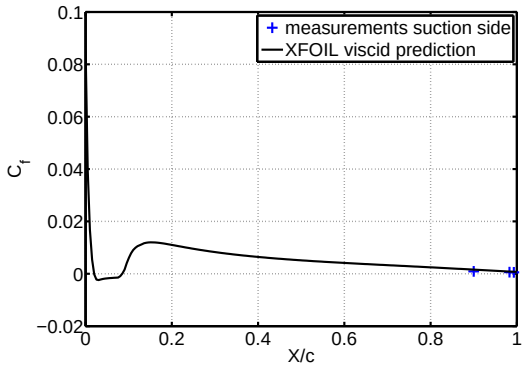

(e) $Re_c = 2 \times 10^5$, $AoA = 8°$

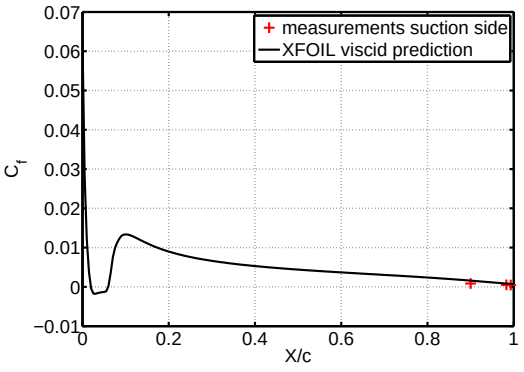

(f) $Re_c = 4 \times 10^5$, $AoA = 8°$

Figure 3.4: Comparison of measured and predicted (XFOIL) values of C_f.

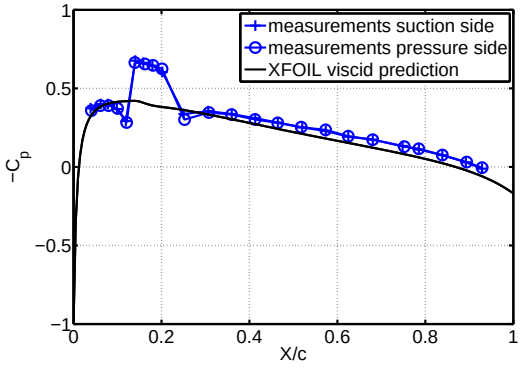

(a) $Re_c = 2 \times 10^5$, $AoA = 0°$

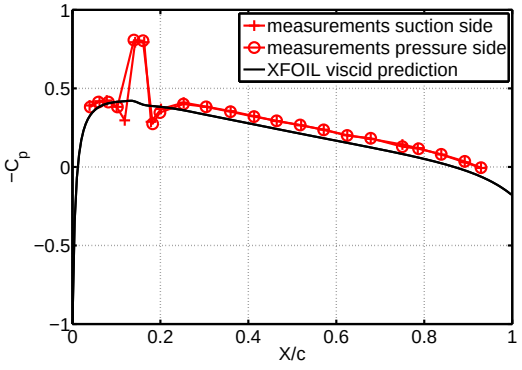

(b) $Re_c = 4 \times 10^5$, $AoA = 6.25°$

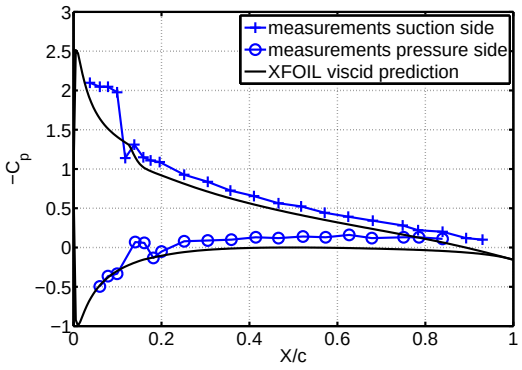

(c) $Re_c = 2 \times 10^5$, $AoA = 0°$,

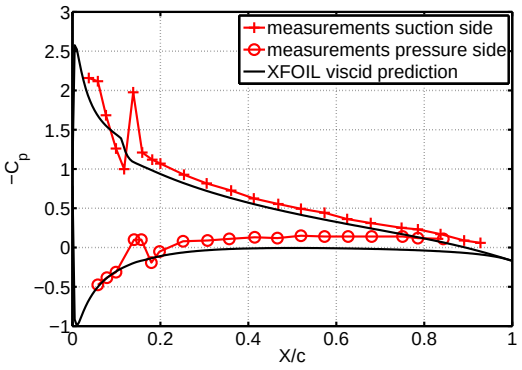

(d) $Re_c = 4 \times 10^5$, $AoA = 6.25°$

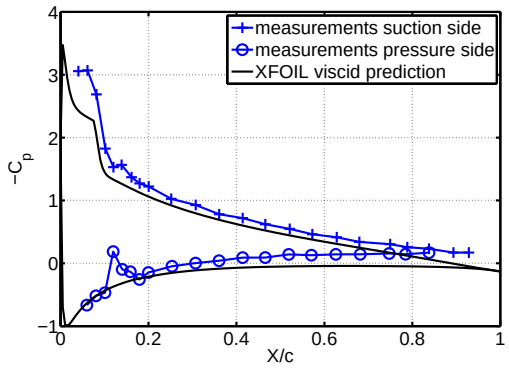

(e) $Re_c = 2 \times 10^5$, $AoA = 8°$

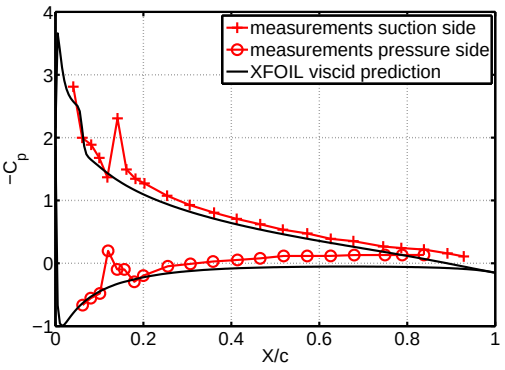

(f) $Re_c = 4 \times 10^5$, $AoA = 8°$

Figure 3.5: Comparison of measured and predicted (XFOIL) values of C_p

$\frac{dp}{dx}$ measured [kg.m^{-2}.s^{-2}]	$AoA = 0°$		$AoA = 6.25°$		$AoA = 8°$	
	suction	pressure	suction	pressure	suction	pressure
$Re_c = 2 \times 10^5$	43.40	43.40	78.12	-5.373	82.67	-26.87
$Re_c = 4 \times 10^5$	181.87	181.87	327.36	-19.84	367.04	-95.89

$\frac{dp}{dx}$ XFOIL [kg.m^{-2}.s^{-2}]	$AoA = 0°$		$AoA = 6.25°$		$AoA = 8°$	
	suction	pressure	suction	pressure	suction	pressure
$Re_c = 2 \times 10^5$	35.79	35.78	79.44	-1.864	91.67	-10.92
$Re_c = 4 \times 10^5$	143.20	143.15	320.62	-7.341	374.90	-43.69

Table 3.1: Comparison of measured and predicted (XFOIL) values of the average pressure gradient dp/dx between 50% and 85% of the airfoil chord, on the suction and pressure sides.

The values of dp/dx obtained from Garcia Sagrado's measurements of K and Eq. 3.31 are given in Table 3.1 and compared to the values predicted by XFOIL. For $AoA = 0°$, the agreement between the pressure gradients predicted by XFOIL and the measurements is reasonable (within 80%). For non-zero angles of attack, the agreement is very good for the suction side (within 98%) but is poor for the pressure side (less than 30%). However, this discrepancy does not affect the predictions of Rozenberg's model since the effects of negative (favorable) pressure gradient are not included, as explained in Section 3.2.3. Note that the values of dp/dx provided by Garcia Sagrado (through the number K) are in disagreement by a factor 2 with the pressure gradients deduced graphically from her measurements of static pressure (showed in Fig 3.5). It has been assumed here that this was an error and the values of K provided has therefore been divided by 2.

For the configurations considered in this section, the predictions of XFOIL for the boundary layer parameters agree reasonably well with the measurements of Garcia Sagrado [68]. The code XFOIL is therefore used in the rest of this study to provide boundary layer parameters to the semi-empirical models described in Sections 3.2.2 and 3.2.3. A comparison between some of these models and measurements is presented in the next section.

3.3.2 Choice of a model for Φ_{pp}

This section presents a comparison between the semi-empirical models for the surface pressure spectrum Φ_{pp}, presented in Sections 3.2.2 and 3.2.3, and the measurements by Garcia Sagrado [68] performed on the suction side of a NACA0012 airfoil. Since the model due to Glegg and Jochault (Eq. 3.30) predicts directly S_{qq} rather than Φ_{pp}, Eq. 3.30 is substituted into Eq. 3.12 and the value $l_r = 1.5U_c/\omega$ is used (as measured by Garcia Sagrado)

to allow comparison with the other models and measurements. Note that, at $AoA = 0°$, vortex-shedding has been observed to be significant at 550Hz for $Re_c = 2.10^5$ and 1100Hz for $Re_c = 4.10^5$. Since the models for Φ_{pp} do not take into account the effects of vortex-shedding, measurements and predictions at $AoA = 0°$ are only compared at frequencies away from these frequencies.

Figure 3.6 presents a comparison between the measured and predicted values of Φ_{pp}. The boundary layer parameters measured at 2mm upstream of the trailing edge are used as inputs to the semi-empirical models. Strong disparities are observed between the predictions of the different models. Rozenberg's model generally achieves the best agreement in terms of spectrum shape, although it systematically underpredicts the measured data (by up to 3dB at $AoA = 0°$, away from the vortex-shedding frequencies, and up to 10dB at non-zero AoA). For non-zero AoA, it also achieves a much better agreement in level than Goody's model, from which it was derived. This may suggests that the effects of adverse pressure gradient on the surface pressure spectrum can be significant and should be taken into account in the modelling of Φ_{pp}. The model due to Glegg and Jochault generally achieves the best fit in level in the range $\omega\delta^*/U_X = 0.5$ to 10, but fails to capture the asymptotic behaviour of Φ_{pp} (see Section 3.2.1) at lower and higher frequencies. It also tends to exhibit non-realistic oscillations in the spectrum, which originates from the use of the directivity function in Eq. 3.30. Both the Willmarth-Roos-Amiet and the Chase-Howe models tend to underpredict Φ_{pp} at low frequencies and overpredict Φ_{pp} at high frequencies. However, the agreement in level of the Willmarth-Roos-Amiet model is much better than the Chase-Howe model, especially at non-zero AoA where the latter can underpredict Φ_{pp} by up to 15dB. The model due to Kim and George is generally in fair agreement with the measurements at low frequencies, but overpredicts significantly Φ_{pp} at medium to high frequencies, for all configurations.

The two models for Φ_{pp} that achieve the best agreement with the experiments are those due to Rozenberg (Eq 3.27) and Glegg-Jochault (Eq. 3.30). Good agreement in level between Garcia Sagrado's measurements and the Glegg-Jochault model is not expected to sustain when airfoils other that a NACA0012 are considered, as explained in Section 3.2.3. By contrast, the Rozenberg model has the advantage of being theoretically applicable to any airfoil geometry, including airfoils with camber such as the ones used in CRORs. However, this model is still in early stages of development and would need some refinements, according to Rozenberg [133]. Note also that the generally good agreement in level of the Glegg-Jochault model with the measurements can be seen as an element of validation of the factor introduced by Moreau and Roger [112] to correct the formulation of Amiet and used in the BRTE noise model presented in this chapter (introduced here in Eq. 3.1).

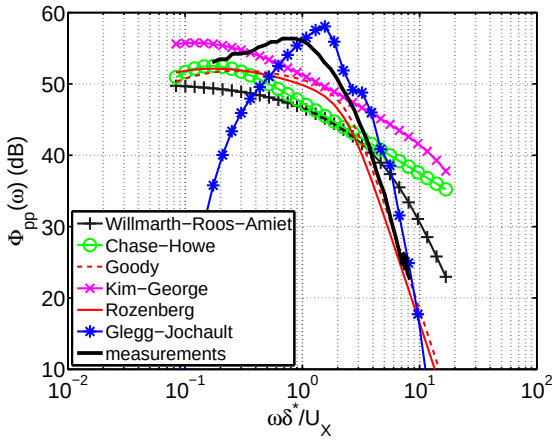

(a) $Re_c = 2 \times 10^5$, $AoA = 0°$

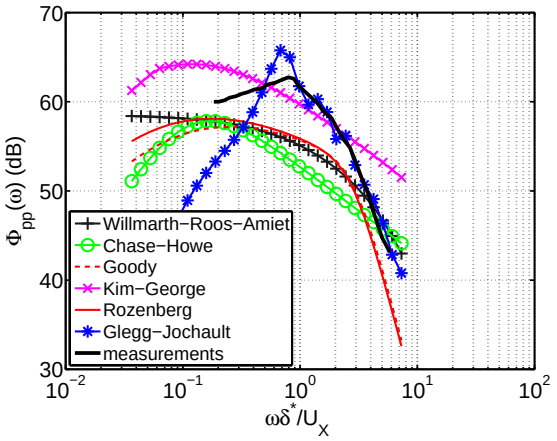

(b) $Re_c = 4 \times 10^5$, $AoA = 0°$

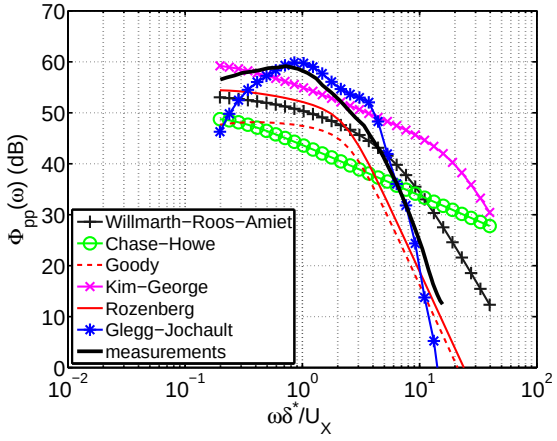

(c) $Re_c = 2 \times 10^5$, $AoA = 6.25°$

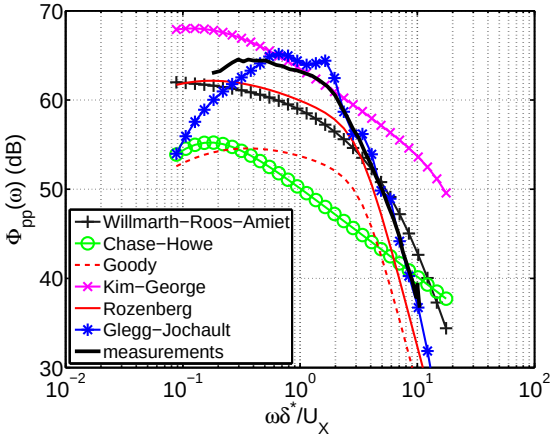

(d) $Re_c = 4 \times 10^5$, $AoA = 6.25°$

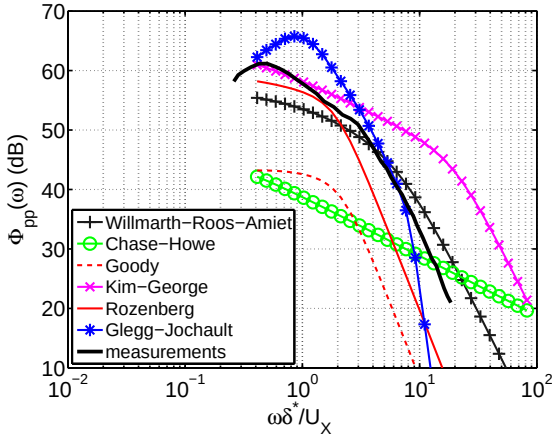

(e) $Re_c = 2 \times 10^5$, $AoA = 8°$

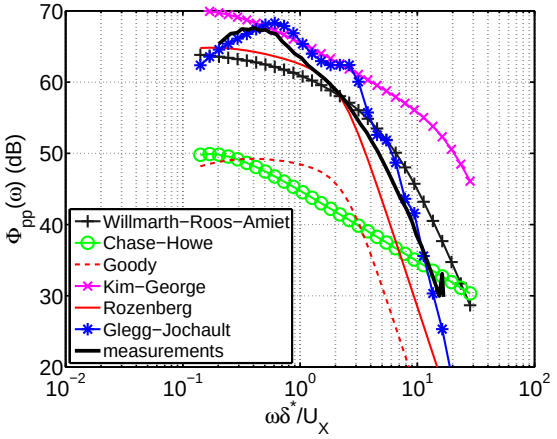

(f) $Re_c = 4 \times 10^5$, $AoA = 8°$

Figure 3.6: Comparison of measured and predicted surface pressure spectrum Φ_{pp} on the suction side of a NACA0012 airfoil.

Chapter 4

Application of models; comparison with measurements and parameter study

In this chapter, the BRWI and BRTE noise models (see Chapters 2 and 3, respectively) are compared against experimental data obtained from a $1/6^{\text{th}}$ scale CROR rig, which is described here. Good agreement is observed between the broadband noise predictions and the measured CROR broadband noise. The relative importance of the BRWI and BRTE noise sources is also investigated for a hypothetical, but realistic, full-scale CROR configuration at three operating conditions. This configuration is used as a baseline for a parameter study by which the effects of rotor-rotor separation distance (or 'rotor-rotor gap'), rotor speed and blade number are investigated at constant engine power, equal torque split and constant solidity. Strategies for CROR broadband noise reduction are then proposed.

4.1 Comparison of broadband noise predictions with measurements

4.1.1 Experimental setup

Noise and aerodynamic measurements were undertaken by Rolls-Royce on a $1/6^{\text{th}}$ scale CROR rig (referred to as RIG145) in the large open jet wind tunnel of DNW, Netherlands, as part of the FP7 European project DREAM [54]. The facility is a closed circuit, atmospheric, continuous low-speed wind tunnel with a 6x8m rectangular nozzle, which is shown in Fig. 4.1. A number of in-flow and out-of-flow microphone arrays, including a phased array, were used to acquire the noise data. The two contra-rotating rotors were driven by two independently controlled electric motors, so that their rotation speeds could be modified independently.

Figure 4.1: Experimental setup of Rolls-Royce's RIG145 in DNW, Netherlands.

The pitch of each blade was adjusted between test runs, thus simulating a full-scale variable pitch CROR. A number of rotor blade designs and CROR configurations were tested. Single rotor tests, in which the rear rotor was removed, were also conducted. The radius of the rear rotor is less than that of the front rotor, so that the tip-vortex shed from the front rotor does not impinge onto the rear rotor. Note that, although an upstream pylon is present in the configuration shown in Fig. 4.1, the broadband noise data considered in this section were measured on an *uninstalled* CROR configuration in which the pylon is absent.

The levels of broadband noise emissions were extracted from the measured data using a median filtering technique, in order to remove the contribution of the tonal component of the noise. Due to the presence of the turbulent shear layer of the rectangular jet, the noise spectra from the out-of-flow microphones revealed spectral broadening of the tonal components, or 'haystacking'. The haystacking effect on tone levels is small at low frequencies, e.g. at the first few harmonics of rotor alone and interaction tones, and can be corrected. With increasing frequency, haystacking becomes progressively stronger, making it difficult to identify and separate tones when the haystack frequency bandwidth covers more than one tonal component. In this case, haystacking may also obscure the true level of broadband noise. Spectra from the in-flow (nose-cone) microphones do not exhibit any detectable haystacking effects but these measurements suffer the disadvantages of possible near-field effects and are still being analysed at the time of writing. For these reasons, only out-of-flow, far-field measurements are considered here.

There are usually numerous facility effects and scaling effects associated with a rig mounted in an open jet wind-tunnel that would not be present on a full-scale engine in operation. CFD simulations, produced specifically for the geometry of this $1/6^{\text{th}}$ scale rig mounted in the DNW wind-tunnel, have been used in order generate the most representative aerodynamic inputs to the broadband noise models, such as the drag coefficient C_d of the front rotor blades and the blades angles of attack. The CFD results were produced by Colin [46] as part of the FP7 European project DREAM. These CFD results are confidential at the time of writing and are not presented here.

4.1.2 Validation of the BRTE noise model

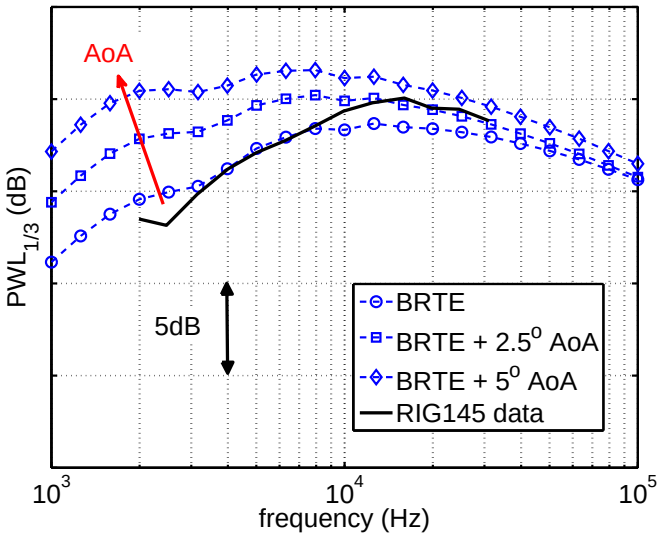

Figure 4.2: Validation of BRTE noise model against RIG145 measurements for no correction of AoA, $AoA + 2.5°$ and $AoA + 5°$.

Single rotor noise measurements (rear rotor removed) were performed during the RIG145 tests in order to investigate the significance of rotor self-noise in CRORs. Figure 4.2 presents a comparison between predicted (using the BRTE noise model presented in Chapter 3) and measured third-octave $\mathrm{PWL}_{1/3}$ for the single rotor RIG145 test. The predictions are made using Eq. 3.18 for 10 spanwise strips. In order to assess the sensitivity of the BRTE noise predictions to angle of attack, three blades angles of attack are considered: AoA, $AoA + 2.5°$ and $AoA + 5°$, where AoA denotes the value of angle of attack obtained from CFD simulations. Note that the $\mathrm{PWL}_{1/3}$ spectra are plotted in Fig 4.2 for the frequency range $1\mathrm{kHz} < f < 100\mathrm{kHz}$, which corresponds to $167\mathrm{Hz} < f < 16.7\mathrm{kHz}$ at full-scale.

Good agreement with the RIG145 single-rotor measurements and the BRTE noise predictions is observed in Fig. 4.2 for the predictions with no correction of AoA, both in terms of spectral shape and level (less than 2dB). As expected from previous studies (see for example George and Chou [69]), increasing the angle of attack of the rotor blades by 5° yields a significant increase of the BRTE noise predictions at low frequencies ($\approx +6.0$dB at 1kHz) and small increase at high frequencies ($\approx +0.9$dB at 100kHz).

Note that, due to confidentiality reasons at the time of writing, the model for the surface pressure spectrum Φ_{pp} used in the BRTE predictions cannot be identified here. This model was chosen to be the one which provided the best agreement of BRTE predictions with the RIG145 measurements of Fig. 4.2 amongst the different models presented in Section 3.2. This model is retained for the validation of the full CROR broadband noise predictions presented in the next section.

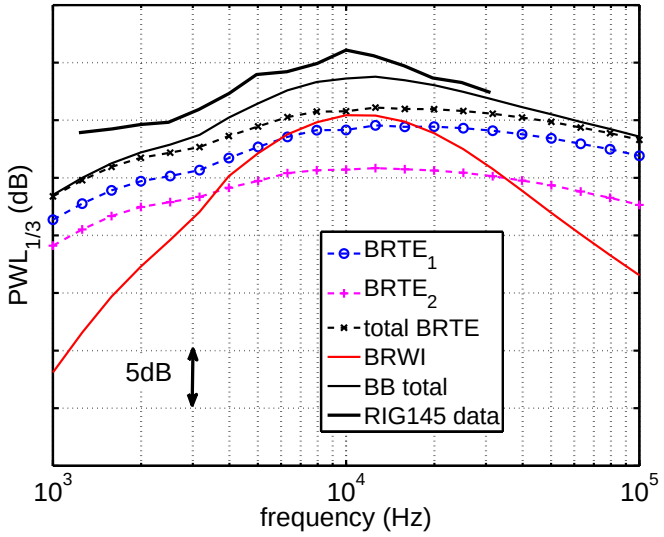

Figure 4.3: Validation of the total CROR broadband noise models (BRWI and BRTE) against RIG145 data.

4.1.3 Validation of the total CROR broadband noise model

A comparison between the total CROR broadband noise model, predicting the BRWI noise and the BRTE noise from each of the rotors, against measured RIG145 data is presented in this section. The CROR configuration chosen for the validation corresponds to a typical take-off configuration and is the same as that of Section 4.1.2, except that both rotors are now present.

A fast approximate BRWI model was introduced in Section 2.4 (Eq.2.73) as an alternative to the computationally demanding general BRWI model (Eq.2.58). The approximations made in this simple BRWI model are shown in Section 2.4.3 to be valid only if the ratio $2b_W/d_2$ of the wake width over the interblade separation distance is less than 1. For the current CROR configuration, the ratio $2b_W/d_2$ ranges from 0.04 to 0.12 and, therefore, this condition is satisfied. The BRTE noise of the front and rear rotors, denoted respectively by BRTE_1 and BRTE_2, is predicted using the same surface pressure spectrum model as in the previous section.

Figure 4.3 presents a comparison between predictions and measurements of the broadband noise in terms of the third-octave PWL. The contribution of each source of broadband noise to the total $\text{PWL}_{1/3}$ prediction is given. Good agreement in spectral shape and level (less than 2.5dB at spectrum peak) is observed. For the CROR configuration considered, the total BRTE noise dominates the total broadband noise emissions at low and high frequencies, and the BRWI source contributes significantly to the total broadband noise emissions in the frequency range 2kHz $< f <$ 60kHz only, which is equivalent to the range 300Hz $< f <$ 10kHz at full scale. Note also that the front rotor was run faster than the rear rotor in this

particular configuration and, therefore, the BRTE_1 noise predictions are higher than the BRTE_2 noise predictions.

4.2 Relative importance of broadband noise sources for a baseline CROR configuration

This section presents a study of the relative importance of the BRTE and BRWI noise sources for a realistic, but hypothetical, CROR configuration at three different operating conditions. The CROR configuration and the spanwise distribution of the main inputs to the broadband noise models are described in detail for the three operating conditions considered. The model for the surface pressure Φ_{pp} due to Rozenberg [133] is used for BRTE noise predictions in this section because of its reasonable agreement with the surface pressure measurements of Garcia Sagrado [68], as shown in Fig. 3.6, and because of its ability to capture the asymptotic trends of Φ_{pp} in the low and high frequency limits, as discussed in Section 3.2.1.

4.2.1 CROR configuration and input parameters to broadband noise models

4.2.1.1 CROR baseline configuration

The baseline hypothetical, but realistic, CROR configuration used in this study is described in this section. It consists of a 10x9 bladed CROR, of which the tip radius of the front and rear rotors are $R_{t1} = 2\text{m}$ and $R_{t2} = 1.8\text{m}$, respectively, and the hub radius is equal to $R_h = 0.67\text{m}$ for both rotors. The axial distance between the two rotors disks (i.e. the axial distance between the mid-chord points of the front and rear rotors, at the hub) is chosen to be $\eta = 1\text{m}$. The baseline rotor tip Mach number is chosen to be the same for all the operating conditions considered and equal to $M_{t1} = M_{t2} = 0.5$. Equal torque split between the two rotors is assumed.

	Take-off	Cruise	Approach
flight Mach number M_x	0.25	0.7	0.25
thrust	86000 N	21700 N	19600N
engine power	12000 kW	6000 kW	2000 kW

Table 4.1: Flight Mach number, thrust and engine power of the hypothetical CROR configuration considered, at assumed take-off, cruise and approach-type conditions.

The relative importance of the BRWI and the BRTE noise sources is studied for three different flight conditions that represent, approximately, take-off, cruise and approach operations. In practice, because there is a wide range of aircraft weights and sizes and a variety of ways in which an aircraft can be operated and flown, the precise definitions of such flight conditions can vary quite substantially. The values of engine power, thrust and flight Mach number presented in Table 4.1 have been chosen here as rough approximations to those of a typical short-haul, 150-seat, aircraft with two engines. These definitions are used throughout this paper, but it needs to be emphasised that the operating conditions of future open rotors may vary significantly from those assumed here.

The geometry and flow parameters are assumed to vary slowly along the span of the rotor blades and, therefore, they are assumed to be constant over each of the 10 spanwise blade sections (or 'strips') of the rotors considered in this chapter. The desired torque split, engine power, blade numbers and rotor speeds are input to a CROR 2D design code, which gives as output the spanwise distribution of the blade chord c_i, the stagger angles α_i, the mean flow velocities U_{Xi} relative to the rotor blades and the angles of attack AoA_i of the blades for both rotors. This design code is based on the measured lift and drag distribution of a NACA16 airfoil, and neglects the effects of sweep and of three dimensional flows. It is assumed here that the broadband noise predictions are not significantly affected by these approximations. Note that the solidity of the rotors is kept constant and, therefore, the spanwise variation of chord length c_i varies only if the blade numbers B_i are modified.

Figure 4.4 presents the spanwise variation of c_i, α_i, U_{Xi}, AoA_i and front rotor drag coefficient C_d for the baseline CROR configuration at the three operating conditions considered. As expected, the distribution of chord c_i is unchanged for the different operating conditions, unlike the variation of α_i, U_{Xi}, AoA_i and C_d. At a given operating condition, the spanwise variations of α_i and AoA_i take comparable values for both rotors, whereas the relative mean-flow velocity U_{X2} is always larger than U_{X1} at all operating conditions (but more significantly at assumed take-off). Note that the distribution of AoA_i is between -2.2^o and 1.7^o at assumed cruise and approach, and between 7.1^o and 11.6^o at assumed take-off. Similarly, the values of C_d predicted at assumed take-off are much larger (up to 0.2) than the values predicted at assumed cruise and approach (less than 0.01). Note also that sudden increases in the spanwise distribution of C_d are observed at $r = 1$m and $r = 1.9$m in Fig. 4.4(e) at assumed take-off. This may result from a separation of the boundary layer at these radial locations since the rotors are operating at high loading at assumed take-off for the CROR configuration chosen.

4.2.1.2 Main input parameters to the broadband noise models

The broadband noise models described in Chapters 2 and 3 require as input the turbulent boundary layer parameters over both sides of the front and rear rotor blades (for the BRTE model) and the characteristics of the turbulent wakes shed from the front rotor (for the

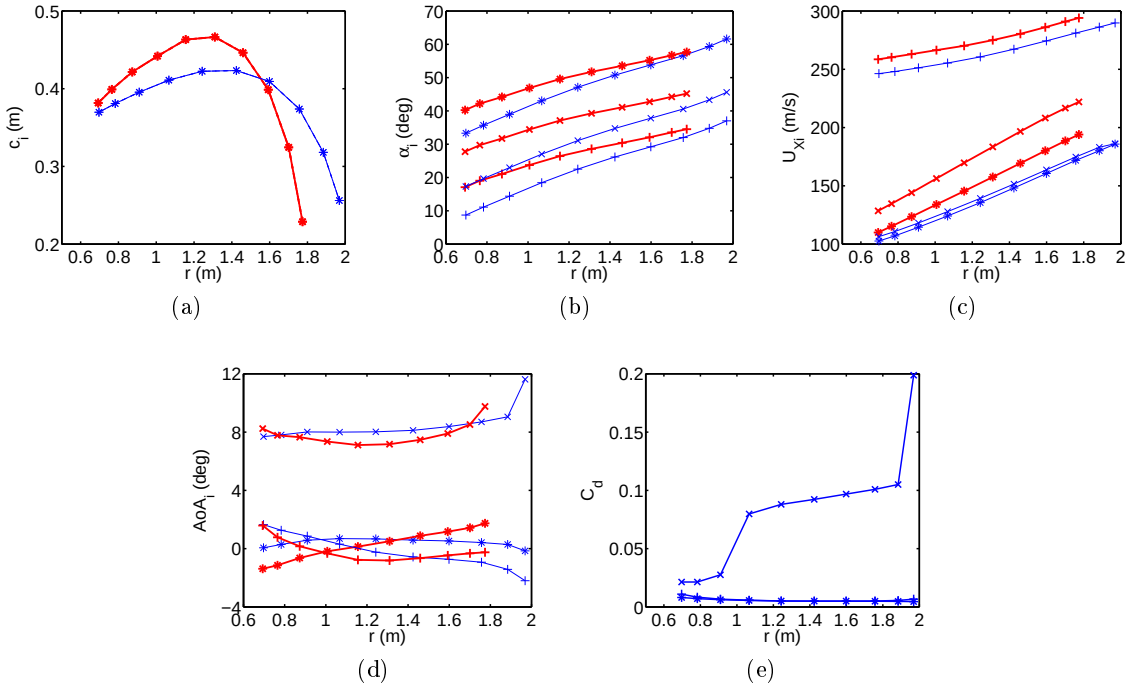

Figure 4.4: Spanwise variation of (a) chord c_i, (b) stagger angle α_i, (c) relative mean-flow velocity U_{Xi}, (d) angle of attack AoA_i and (e) drag coefficient C_d of the front rotor blades. Quantities related to the front and rear rotor are plotted in thin blue ($-$) and thick red (-) lines, respectively. Assumed take-off, cruise and approach are denoted by ($\times$), ($+$) and ($*$), respectively.

BRWI model). Predictions of the spanwise variation of these input parameters for the configurations considered are presented in this section.

Turbulent boundary layer parameters for BRTE model

The turbulent boundary layer is modelled by means of the panel method code XFOIL, developed by Drela [55] and presented briefly in Section 3.3. A standard NACA0012 profile is assumed for this study. The values of the chord length c_i, mean flow chordwise velocity U_{Xi} and angle of attack AoA_i are input to XFOIL, which gives as output the turbulent boundary layer parameters required by the BRTE noise model.

Figure 4.5 presents the spanwise variation of the displacement thickness δ_i^*, normalised by the chord c_i; this is the boundary layer parameter to which the surface pressure spectrum Φ_{pp} is most sensitive (see Eq. 3.27, for Rozenberg's model). The values of δ_i^*/c_i are generally similar for both rotors and generally varies smoothly along the span, except at assumed take-off where δ_i^*/c_i increases suddenly at the last strip of the front rotor. This is consistent with the sudden increase in C_d at the last strip at assumed take-off observed in Fig. 4.4(e) and may be due to boundary layer separation at the blade tip. The spanwise variation of δ_i^*/c_i for the three operating conditions follows closely the trends of the spanwise variation

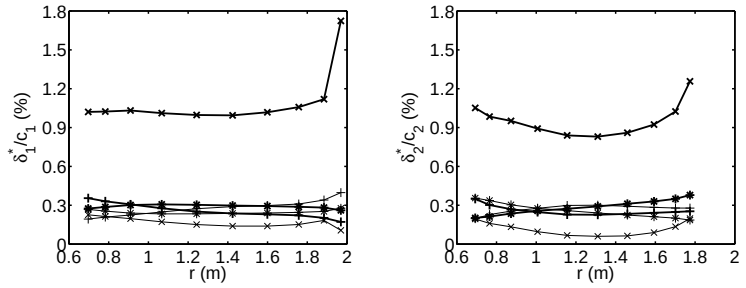

Figure 4.5: Predicted spanwise variation of normalised displacement thickness δ_i^*/c_i on the suction side (-) and the pressure side $(-)$ of (a) the front rotor blades and (b) the rear rotor blades. Assumed take-off, cruise and approach configurations are denoted by $(\times)$, $(+)$ and $(*)$, respectively.

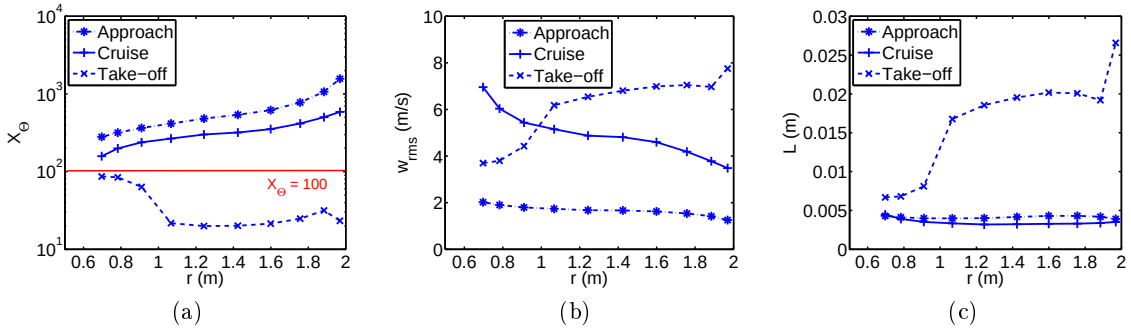

Figure 4.6: Predicted spanwise variation of (a) the normalised helical path X_Θ, (b) the root-mean-square turbulent velocity $w_{rms} = \sqrt{\overline{w^2}}$ and (c) the turbulence integral lengthscale L at the leading edge of the rear rotor.

of AoA_i, shown in Fig. 4.4(d). The predicted values of δ_i^*/c_i on the suction side of the rotor blades are significantly larger at assumed take-off than at assumed cruise and approach. The PWL spectrum of BRTE noise can therefore be expected to peak at much lower frequencies at assumed take-off than at assumed cruise and approach, as verified later in Section 4.2.2.

Turbulent wake parameters for BRWI model

The mean and turbulent wake parameters are predicted from the chordwise flow speed U_{X1} and the non-dimensional helical path distance $X_\Theta \approx X_\eta/(C_d c_1)$ using the empirical model described in Section 2.5. In this section, the range $X_\Theta < 100$, where w_{rms}/u_0 is increasing with increasing X_Θ in Fig. 2.12, is referred to as the 'near-wake region', whereas the range $X_\Theta > 100$, where w_{rms}/u_0 is decreasing (and eventually constant) with increasing X_Θ, is referred to as the 'far-wake region'.

Figure 4.6 presents the predicted spanwise variation of X_Θ, L and w_{rms} at the leading edge of the rear rotor. As shown in Fig. 4.6(a), the leading edge of the rear rotor can be

considered to lie in the near-wake region ($X_\Theta < 100$) at assumed take-off and in the far-wake region ($X_\Theta > 100$) at assumed cruise and approach. The root-mean-square turbulent velocity w_{rms} is predicted (using the polynomial curve-fit shown in Fig. 2.12) to increase along the span at assumed take-off and to decrease along the span at assumed cruise and approach. The spanwise variation of L follows closely the trends of the spanwise variation of C_d (Fig. 4.4(e)). Therefore, small values of L ($L < 0.5$cm) are predicted at assumed cruise and approach whereas large values of L ($0.6\text{cm} < L < 2.7\text{cm}$) are predicted along most of the rotor span at assumed take-off. Note that, at assumed take-off, both w_{rms} and L exhibit a sudden increase in value at $r = 1$m and at $r = 1.9$m, which result from similar increases of C_d at these radial locations, as shown in Fig. 4.4(e).

4.2.2 Relative importance of broadband noise sources

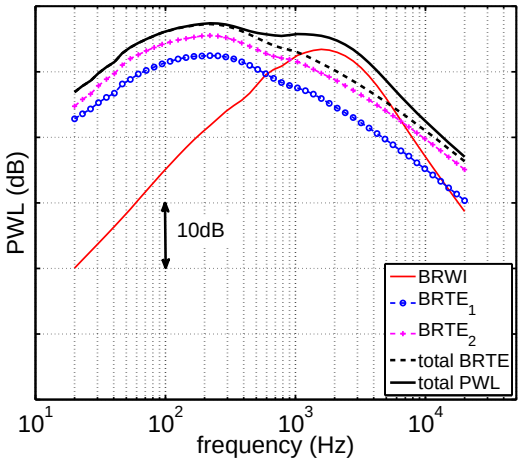

(a) Take-off, OAPWL = $\text{OAPWL}_{\text{ref}}$

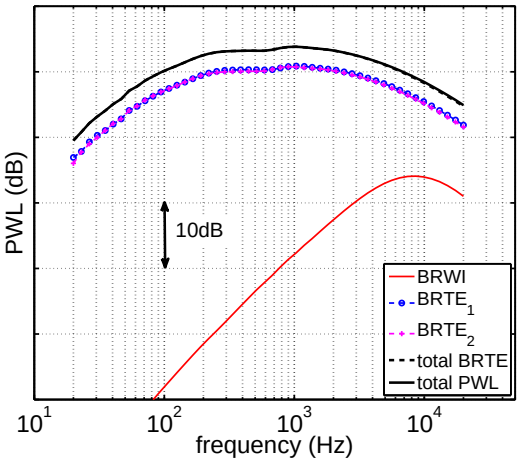

(b) Cruise, OAPWL = $\text{OAPWL}_{\text{ref}} + 0.4$dBA

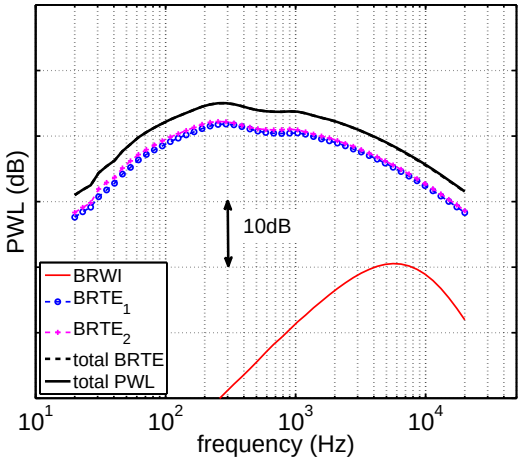

(c) Approach, OAPWL = $\text{OAPWL}_{\text{ref}} - 11.2$dBA

Figure 4.7: Predicted PWL for the baseline CROR configuration at assumed (a) take-off, (b) cruise and (c) approach.

Figure 4.7 presents sound power level predictions (PWL) for the baseline CROR configuration presented in Section 4.2.1.1 at assumed take-off, cruise and approach. The BRTE noise from each rotor and the BRWI noise are computed separately using the input parameters presented in Section 4.2.1.2, for the three operating conditions. Values of the total OAPWL (in dBA), relative to the value at assumed take-off, are also provided for each operating conditions.

According to the predictions shown in Fig. 4.7, the predicted levels of BRTE broadband noise are significantly greater than those of BRWI broadband noise at assumed cruise and approach, but are of comparable levels at assumed take-off. At take-off, the BRWI noise dominates both BRTE noise sources in the mid-frequency range (600Hz $< f <$ 6kHz) and the BRTE noise of both rotors dominates at low and high frequencies outside of this frequency range. This is due to the fact that the drag of the front rotor blade is much higher at assumed take-off than at assumed cruise and approach (see Fig. 4.4(e)), which yields deeper and wider turbulent wakes and, therefore, higher levels of BRWI noise emissions at assumed take-off than at assumed cruise and approach. On the other hand, BRTE noise appears to be much less sensitive to operating conditions and, therefore, dominates the total broadband noise emissions at assumed cruise and approach. Note also that the OAPWL of the total broadband noise is predicted to be similar at assumed take-off and cruise but more than 11dBA lower at assumed approach, as shown in Fig. 4.7.

Figure 4.8 presents directivity plots of the sound pressure level (SPL) of each source of broadband noise at $f = 100$Hz, $f = 1$kHz and $f = 10$kHz at assumed take-off, cruise and approach. Directivity plots of the BRWI noise are shown only at assumed take-off since this sound source is not significant compared to BRTE noise at assumed cruise and approach, as shown in Fig. 4.7. It appears that, for all configurations and frequencies considered, the BRTE broadband noise peaks in the forward arc, whereas the BRWI broadband noise peaks in the rear arc. This is consistent with the fact that the trailing edge noise and the leading edge noise of an isolated airfoil generally peak in the forward arc and the rear arc, respectively (see, for instance, Moreau and Roger [111]). Thus, the overall directivity of the broadband noise is fairly omnidirectional when both the BRWI noise and the total BRTE noise are roughly of equal significance, as is predicted to occur at assumed take-off (see Fig. 4.7(a)). The directivity pattern of the BRTE noise is also observed to be significantly different at assumed cruise and approach, which is explained by the fact that the stagger angles α_i are much smaller at assumed cruise than at assumed approach.

4.3 Parameter study

This section presents a parameter study in which the effects of rotor-rotor gap, rotor speed and blade number on CROR broadband noise are investigated at constant engine power, constant solidity and equal torque split between the rotors. This study is based on the

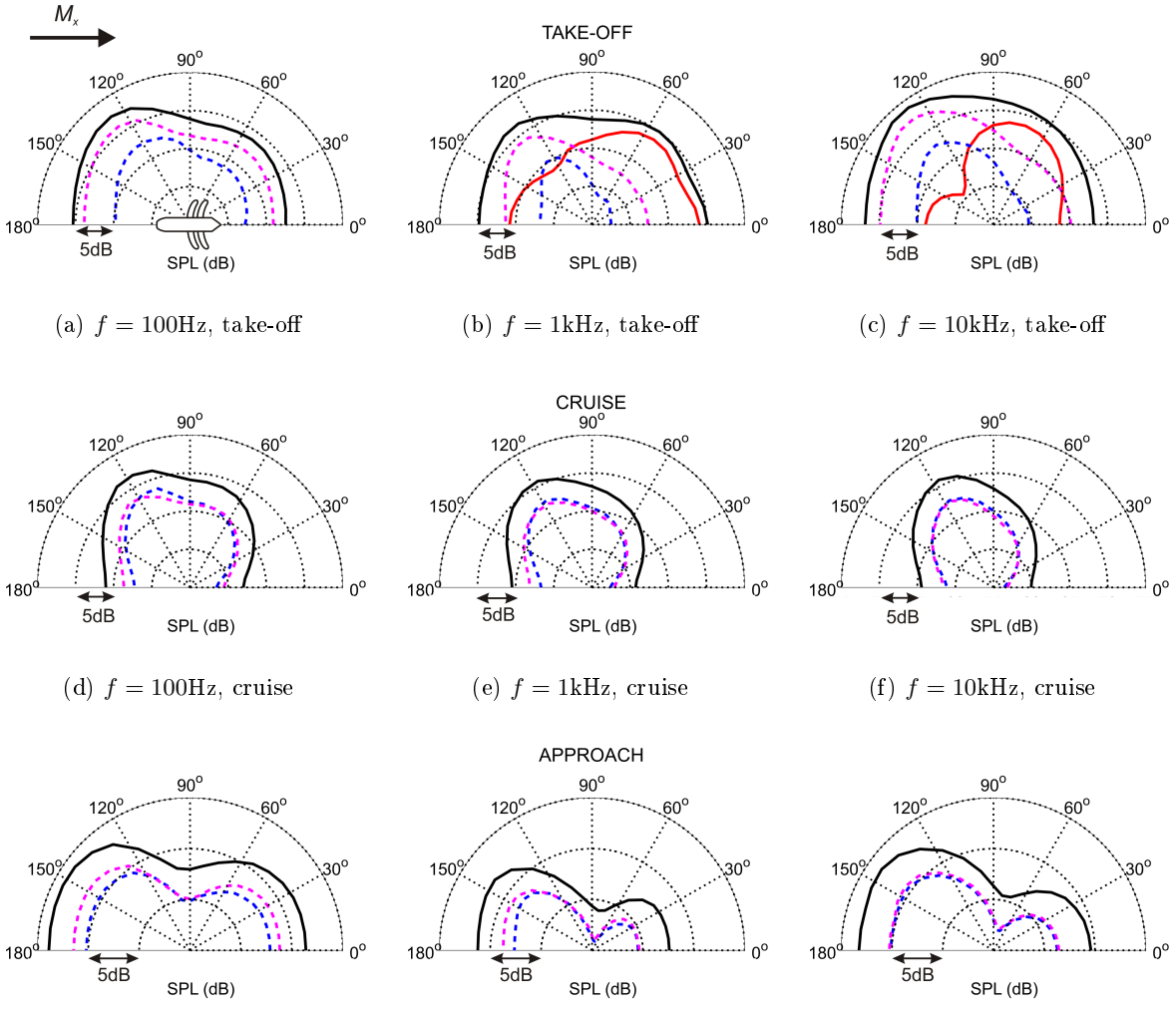

(a) $f = 100$Hz, take-off (b) $f = 1$kHz, take-off (c) $f = 10$kHz, take-off

(d) $f = 100$Hz, cruise (e) $f = 1$kHz, cruise (f) $f = 10$kHz, cruise

(g) $f = 100$Hz, approach (h) $f = 1$kHz, approach (i) $f = 10$kHz, approach

Figure 4.8: Directivity plots of BRTE_1 noise (−−), BRTE_2 noise (−−), BRWI noise (−) and total broadband noise (−) at assumed take-off, cruise and approach and for f =100Hz, 1kHz and 10kHz.

baseline configuration presented in Section 4.2 at the same three flight conditions (assumed take-off, cruise and approach). Similarly to Section 4.2, the BRTE noise is predicted using Eq. 3.18 and Rozenberg's model for the surface pressure spectrum, and the BRWI noise is predicted using the simplified model given by Eq. 2.73. Ten spanwise rotor strips are used to take into account the spanwise variation of geometry and aerodynamic parameters. The variation of broadband noise emissions over the parameter space are studied in terms of sound power level (PWL, in dB) and overall sound power level (OAPWL, in dBA). Strategies for broadband noise reduction are then proposed. Note that the simple BRWI model (Eq. 2.73) is used in this parameter study since the ratio $2b_W/d_2$ is always much less than one ($\max(2b_W/d_2) = 0.26$ for the cases considered).

4.3.1 Effects of rotor-rotor gap

The variation of the rotor-rotor axial gap η is assumed to have a much larger impact on the BRWI noise than on the BRTE noise. This section therefore presents the effects of η (with $\eta = 0.5$ to 1.5m) on the BRWI noise only. The variation of the aerodynamic inputs to the BRWI model are investigated separately at assumed cruise and approach (where the front rotor drag is low) and at assumed take-off (where the front rotor drag is high). The effects of η on the BRWI noise predictions and on the total broadband noise predictions are then presented.

4.3.1.1 Input parameters

Assumed cruise and approach

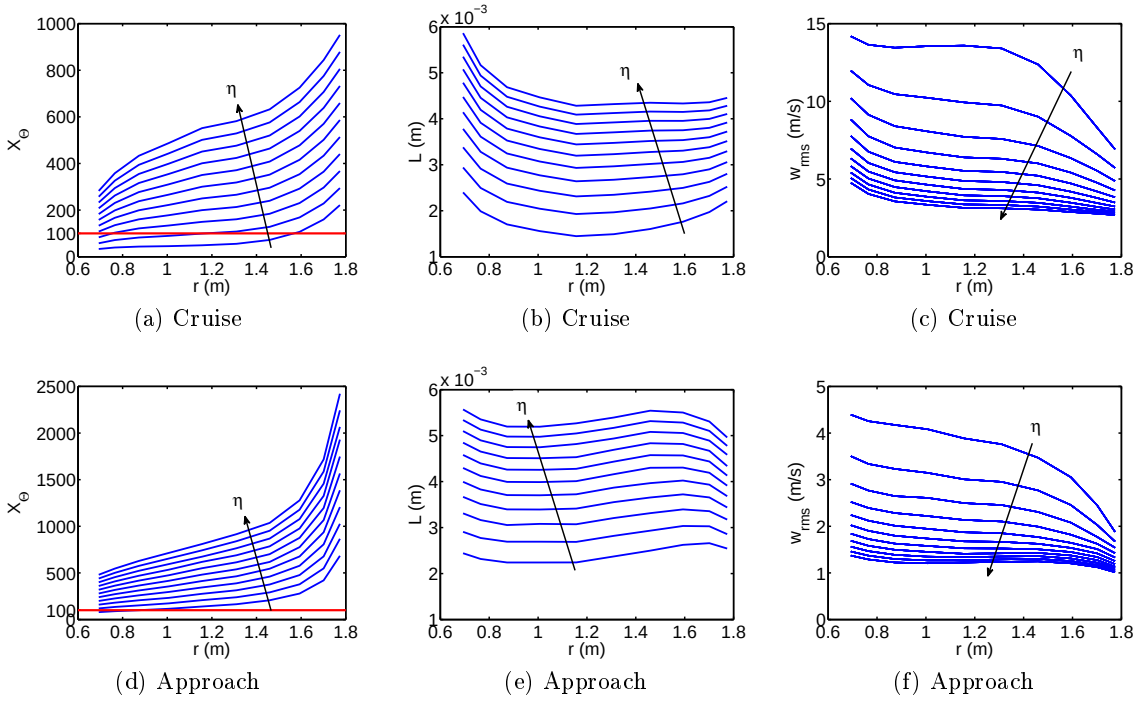

(a) Cruise (b) Cruise (c) Cruise

(d) Approach (e) Approach (f) Approach

Figure 4.9: Variation with rotor-rotor gap η = 0.5m to 1.5m (step of 0.1m) of (a)(d) the normalised helical path length X_Θ, (b)(e) the integral length scale L and (c)(f) the root-mean-square turbulent velocity w_{rms} along the span of the rear rotor blades, at assumed cruise and approach.

Figures 4.9 (a) to (f) present the variation with η of the normalised helical path length of the wakes $X_\Theta \approx X_\eta/(C_d c_1)$, the wake turbulence integral lengthscale L and the root-mean-square turbulent velocity w_{rms} at the leading edge of the rear rotor blades at assumed cruise and approach. The spanwise distribution of the drag coefficient C_d is constant with η and, therefore, L and w_{rms} are only affected by variations in the helical path length X_η. The integral lengthscale L is observed in Figs. 4.9(b) and (e) to increase with increasing

η, due to wake spreading. Figure 4.9(a) and (d) show that $X_\Theta > 100$ for most of the configurations considered, which implies (see Section 4.2.1.2) that the leading edge of the rear rotor generally lies in the far-wake region, where the ratio of w_{rms} over the velocity deficit u_0 decreases with increasing X_Θ, as seen in Fig. 2.12. This explains the decay of w_{rms} with increasing η observed in Figs. 4.9(c) and (f).

Assumed take-off

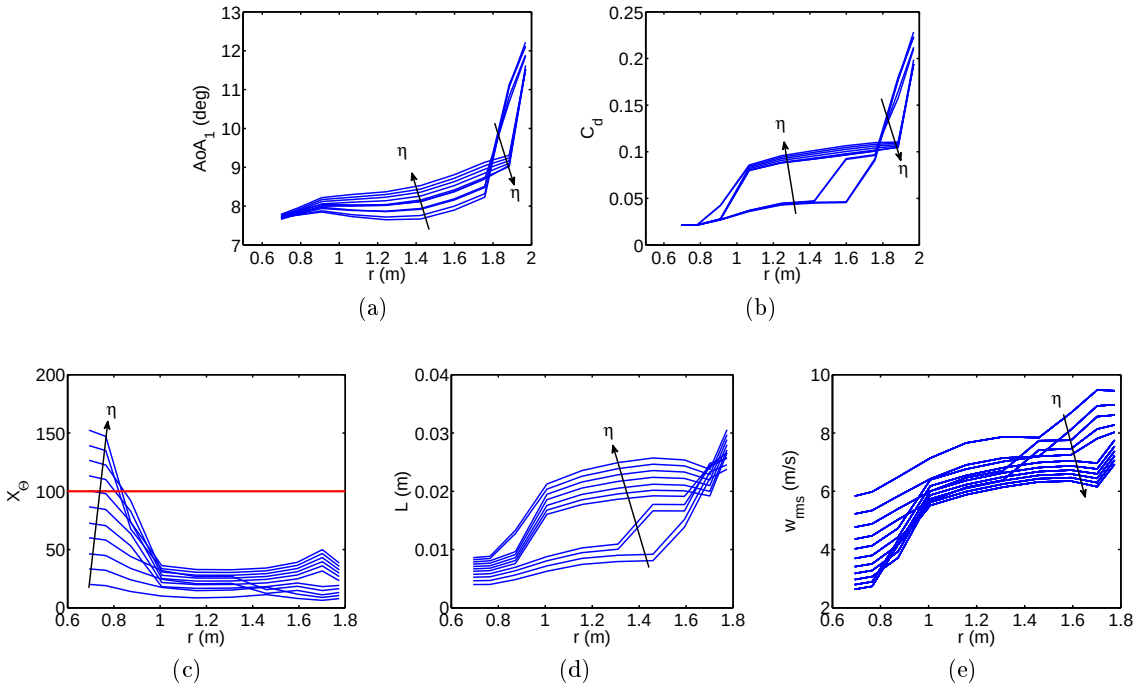

Figure 4.10: Variation with rotor-rotor gap η of (a) the angle of attack AoA_1, (b) the drag coefficient C_d, (c) the normalised helical path length X_Θ, (d) the integral length scale L and (e) the root-mean-square turbulent velocity w_{rms} along the span of the rear rotor blades, at assumed take-off.

Figures 4.10 (a) to (e) present the variation with η of the angle of attack AoA_1, the drag coefficient C_d of the front rotor blades along the span of the front rotor blades, and the variation X_Θ, L and w_{rms} at the leading edge of the rear rotor blades at assumed take-off. Unlike at assumed cruise and approach, the 2D CROR design code predicts small variations in angle of attack AoA_1 with η at assumed take-off, which predicts sudden increases in the spanwise distribution of C_d when certain values of η are reached (see Fig. 4.10(b)). These variations in C_d can be attributed to flow separation over the blades due to the fact that the front rotor is highly loaded at assumed take-off. Thus, the variation of X_Θ, L and w_{rms} with η is affected not only by the change in helical path length X_η but also by the sudden variations of C_d with η. Moreover, it appears that $X_\Theta < 100$ for most of the gap values considered (except close to the hub), which means (see Section 4.2.1.2) that the leading edge of the rear rotor generally lies in the near-wake region, where w_{rms}/u_0 increases with

increasing X_Θ, as seen in Fig. 2.12. However, it appears that the variation of L and w_{rms} with η at assumed take-off still generally follows the trends observed at assumed cruise and approach (i.e. L increases and w_{rms} decreases with η, although not monotonically) but the decrease in w_{rms} is generally milder at assumed take-off than at assumed cruise and approach.

4.3.1.2 Broadband noise predictions

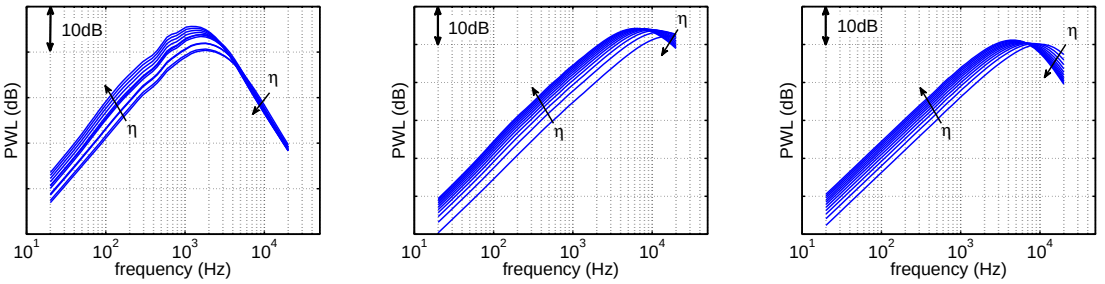

(a) Take-off (b) Cruise (c) Approach

Figure 4.11: Effect of rotor-rotor gap on PWL at assumed take-off, cruise and approach.

Figure 4.11 presents the effects of η on the PWL predicted by the BRWI model, at assumed take-off, cruise and approach. The general trends are that the PWL increases with η at low frequencies and decreases with η at high frequencies. The effects of rotor-rotor gap on PWL presented in this section differ from those reported by the authors in Ref. [20], where a much stronger increase (≈+30dB) of the PWL with η was predicted at low frequency and an increase (≈+4dB) was predicted at high frequency. This difference is because the near-wake empirical correlations of Gliebe et al. [77] used in Ref. [20] predict a nearly linear increase of w_{rms} with increasing η whereas, in the current study, a more realistic model was used for w_{rms} (described in Section 2.5) which predicts a decrease of w_{rms} with increasing η over most strips, as observed in Figs. 4.9(c), (f) and Fig. 4.10(e).

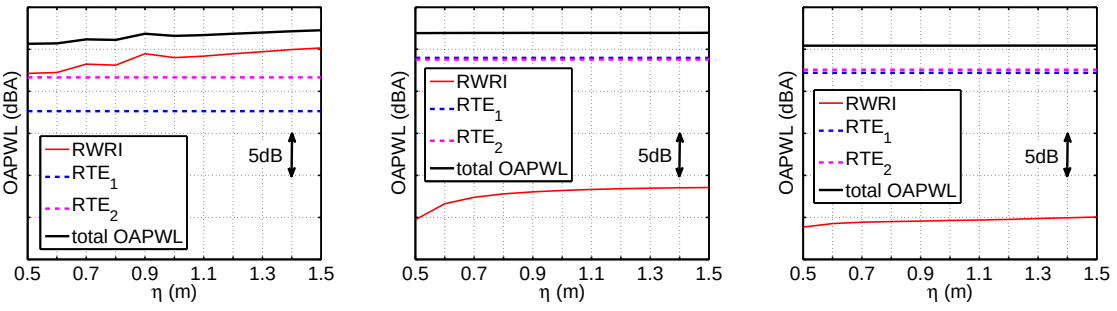

(a) Take-off (b) Cruise (c) Approach

Figure 4.12: Effects of rotor-rotor gap on predicted OAPWL (in dBA) at assumed take-off, cruise and approach.

Figure 4.12 presents the variation of OAPWL (in dBA) with η at assumed take-off, cruise and approach. The variation of η from 0.5m to 1.5m results in an increase in the OAPWL of the BRWI noise of 3.1dBA at assumed take-off, 3.9dBA at assumed cruise and 1.2dBA at assumed approach. Considering the contribution of the BRTE noise, increasing η from 0.5m to 1.5m yields an increase in the total OAPWL of only 1.6dBA at assumed take-off, while the total broadband noise emissions are unchanged at assumed cruise and approach, where the BRTE noise dominates the BRWI noise. The effects of rotor-rotor gap length η on the total broadband noise emissions of CRORs can therefore be considered as being small at assumed take-off and negligible at assumed cruise and approach.

4.3.2 Effects of rotor speed

In this section the effects of rotor speeds on both the BRWI noise and the BRTE noise are studied for constant engine power and torque split. The tip Mach number of the front and rear rotors range from $M_{ti} = 0.4$ to 0.7. The stagger angles α_i are adjusted as M_{ti} varies so that the engine power and the torque split are kept constant and equal to the baseline values described in Section 4.2. The variation with M_{ti} of the main input parameters to the noise models are presented for a representative strip located at 80% of the rear rotor radius, although the contribution of all strips is included in the broadband noise predictions. Similarly to Section 4.3.1, the input parameters for the low rotor drag (assumed cruise and approach) and the high rotor drag operating conditions (assumed take-off) are presented separately. The variation of the boundary layer displacement thickness δ^* is shown for the suction side only for the sake of brevity, but the values of δ^*on both sides of the rotor blades are taken into account in the broadband noise predictions. The effects of M_{ti} on the broadband noise emissions are then discussed.

4.3.2.1 Input parameters

Assumed cruise and approach

Figures 4.13 and 4.14, (a) to (g), present the variation with M_{ti} of X_Θ, U_{X1}, U_{X2}, L, w_{rms}, δ_1^*/c_1 and δ_2^*/c_2, evaluated at $r/R_{t2} = 80\%$ at assumed cruise and approach, respectively. The angles of attack of the rotor blades AoA_i are almost constant (and close to zero) with M_{ti} at assumed cruise and approach, and are therefore not plotted here. As expected, the wake turbulence parameters L and w_{rms} are highly sensitive to variations in M_{t1} and weakly sensitive to variations in M_{t2}. The non-dimensional helical path length X_Θ of the wakes increases significantly with increasing M_{t1}, due to the associated increase of stagger angle α_1 in order to maintain constant engine power. The turbulence integral lengthscale L therefore increases with increasing M_{t1}, at both assumed cruise and approach. The root-mean-square turbulent velocity w_{rms} varies little for $M_{t1} < 0.5$ and then increases for $0.5 < M_{t1} < 0.7$. The normalised boundary layer displacement thicknesses (on the suction side) δ_1^*/c_1 and

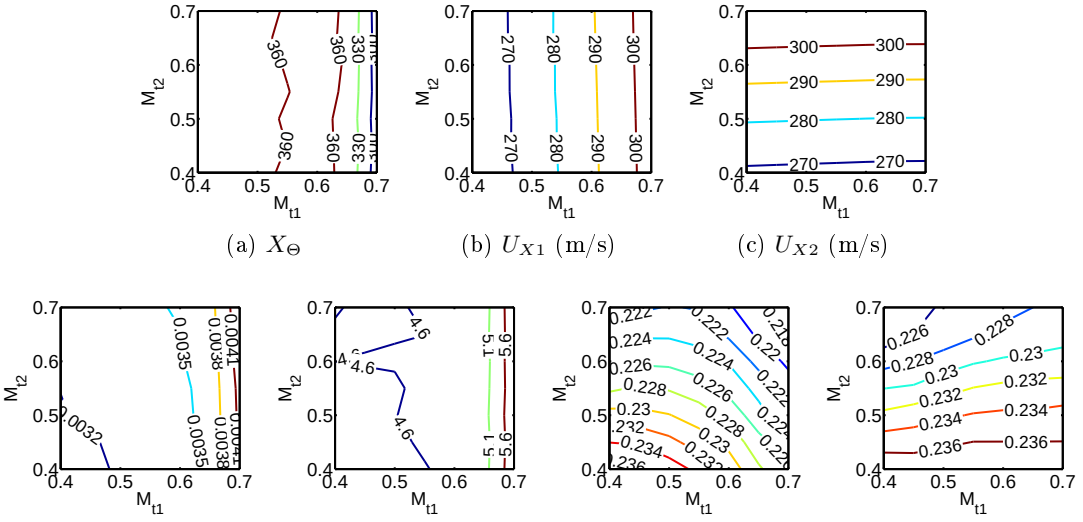

(a) X_Θ (b) U_{X1} (m/s) (c) U_{X2} (m/s)

(d) L (m) (e) w_{rms} (m/s) (f) $\delta_1^*/c_1 \times 100$ (g) $\delta_2^*/c_2 \times 100$

Figure 4.13: Variation with rotor speed of X_Θ, U_{X1}, U_{X2}, L, w_{rms}, δ_1^*/c_1 and δ_2^*/c_2 at assumed cruise.

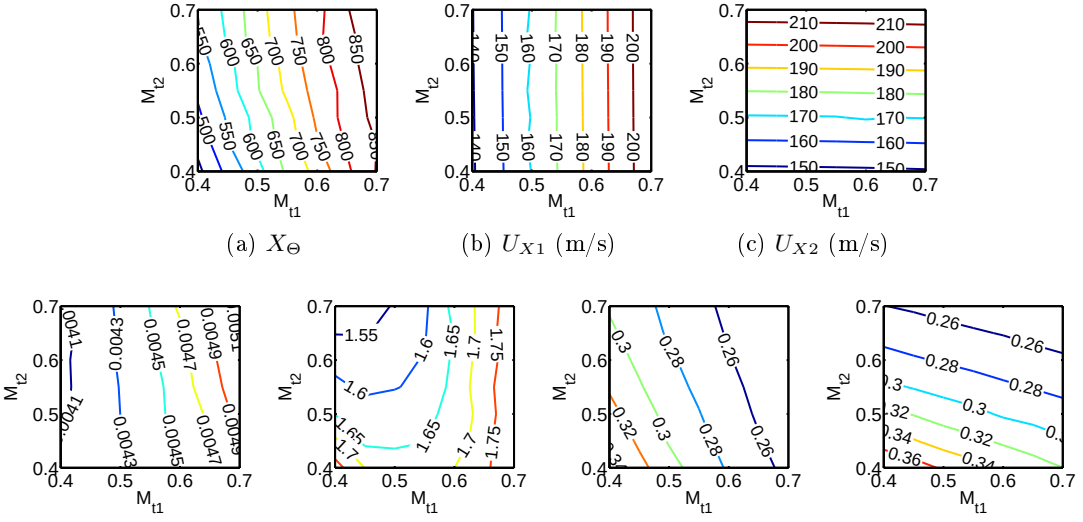

(a) X_Θ (b) U_{X1} (m/s) (c) U_{X2} (m/s)

(d) L (m) (e) w_{rms} (m/s) (f) $\delta_1^*/c_1 \times 100$ (g) $\delta_2^*/c_2 \times 100$

Figure 4.14: Variation with rotor speed of X_Θ, U_{X1}, U_{X2}, L, w_{rms}, δ_1^*/c_1 and δ_2^*/c_2 at assumed approach.

δ_2^*/c_2 tend to decrease with M_{t1} and M_{t2}, respectively, at assumed approach, whereas very little variation of δ_i^*/c_i is observed at assumed cruise.

Assumed take-off

Figure 4.15 presents the variation with M_{ti} of AoA_1, AoA_2, X_Θ, U_{X1}, U_{X2}, L, w_{rms}, δ_1^*/c_1 and δ_2^*/c_2, evaluated at $r/R_{t2} = 80\%$ at assumed take-off. The variation of these parameters with M_{ti} at assumed take-off exhibits a completely different behaviour than at

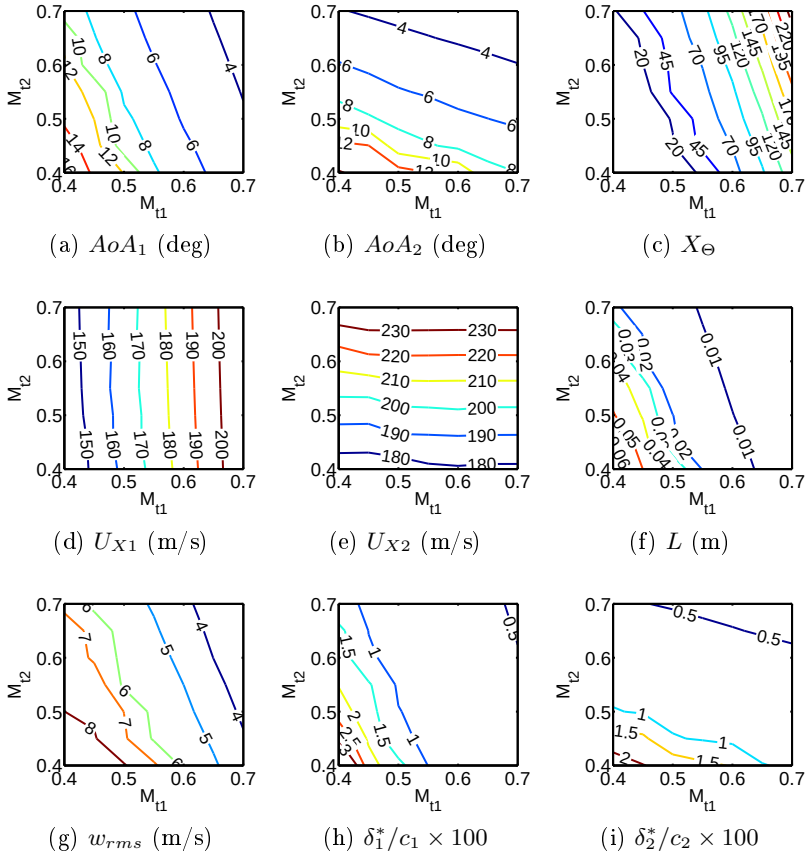

(a) AoA_1 (deg) (b) AoA_2 (deg) (c) X_Θ

(d) U_{X1} (m/s) (e) U_{X2} (m/s) (f) L (m)

(g) w_{rms} (m/s) (h) $\delta_1^*/c_1 \times 100$ (i) $\delta_2^*/c_2 \times 100$

Figure 4.15: Variation with rotor speed of AoA_1, AoA_2, X_Θ, U_{X1}, U_{X2}, L, w_{rms}, δ_1^*/c_1 and δ_2^*/c_2 at assumed take-off.

assumed cruise and approach. First, a significant variation of AoA_i with M_{ti} is observed at assumed take-off, while none was observed at assumed cruise and approach. The angles of attack are predicted here to vary from $AoA_i \approx 3^o$ at $M_{t1} = M_{t2} = 0.7$, to $AoA_i \approx 15^o$ at $M_{t1} = M_{t2} = 0.4$. This effect modifies significantly the normalised helical path length X_Θ and, therefore, the turbulent wake parameters L and w_{rms} which become significantly larger at low rotor speeds. The boundary layer parameters δ_1^*/c_1 and δ_2^*/c_2 follow closely the trends of AoA_1 and AoA_2, respectively, and therefore take much larger values at low rotor speeds than at high rotor speeds.

4.3.2.2 Broadband noise predictions

Figure 4.16 presents the variation of OAPWL (in dBA) with M_{t1} and M_{t2} at assumed take-off, cruise and approach. The levels have been normalised on the total OAPWL of the quietest configuration, which is $M_{t1} = M_{t2} = 0.4$ at approach. Over the whole parameter space, the BRTE noise dominates significantly the BRWI noise at assumed cruise and approach, while both noise sources are significant at assumed take-off. The BRTE noise increases fairly symmetrically with M_{t1} and M_{t2} at assumed cruise (maximum variation:

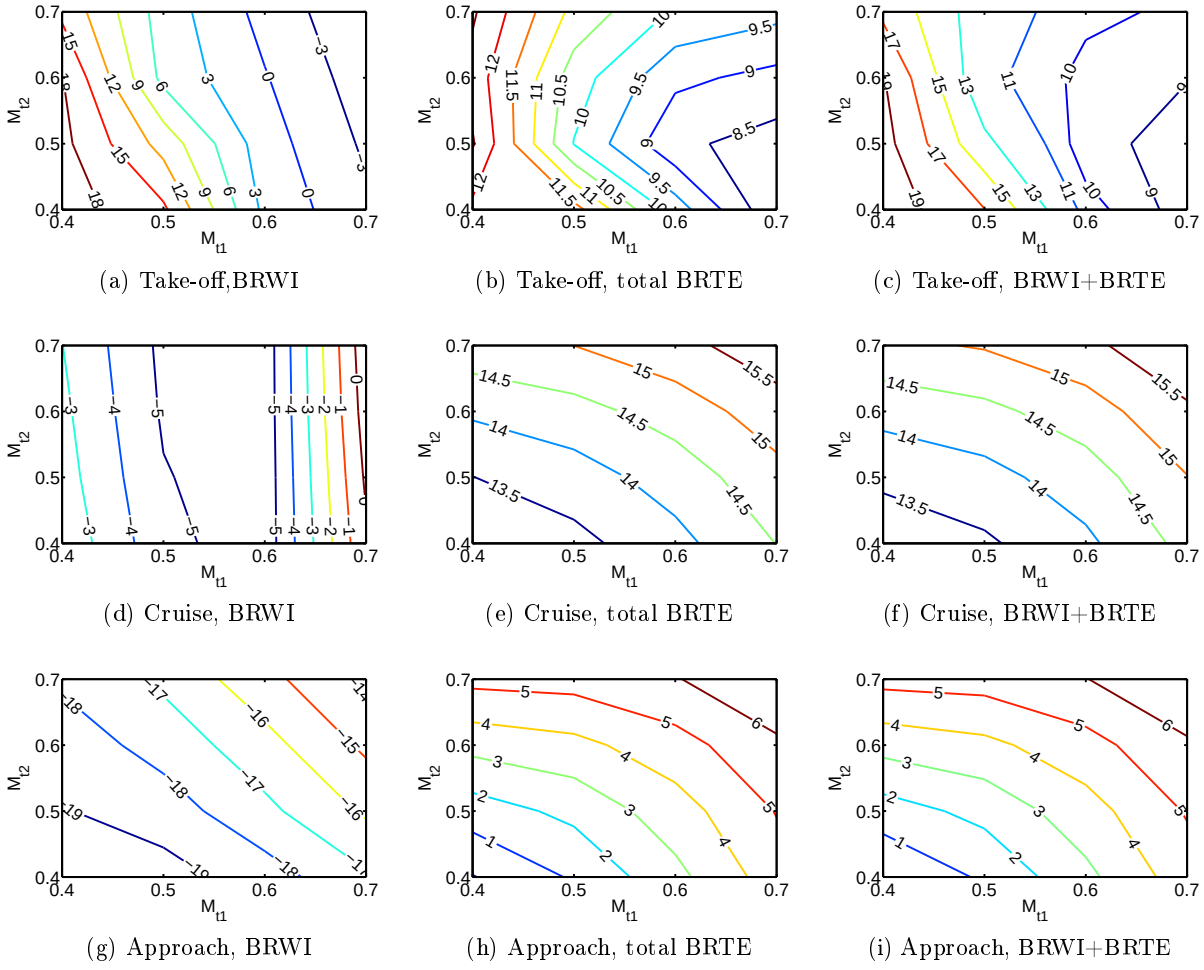

(a) Take-off,BRWI (b) Take-off, total BRTE (c) Take-off, BRWI+BRTE

(d) Cruise, BRWI (e) Cruise, total BRTE (f) Cruise, BRWI+BRTE

(g) Approach, BRWI (h) Approach, total BRTE (i) Approach, BRWI+BRTE

Figure 4.16: Effects of rotor speed on the variation of OAPWL (in dBA) of the BRWI noise, the BRTE noise and the total broadband noise at assumed take-off, cruise and approach. The levels are normalised on the total OAPWL of the quietest configuration, which is $M_{t1} = M_{t2} = 0.4$ at approach.

+2.8dBA) and approach (maximum variation: +6.8dBA) configurations. This is due to the fact that the variation of δ^* is weak at assumed cruise and approach (see Fig. 4.3.2.1) and, therefore, the effects of U_{X1} and U_{X2} are dominating significantly the variation of the BRTE noise. A different trend is observed at assumed take-off, where the total OAPWL varies little with M_{t2} but decreases significantly when M_{t1} increases (maximum variation: -11.7dBA). This trend is also observed for both the BRWI noise and the BRTE noise but is much more significant for the BRWI noise.

Further detail of the balance between BRWI noise and BRTE noise at assumed take-off is shown in Fig. 4.17, where the effects of rotor speed on PWL are presented by fixing successively $M_{ti} = 0.4$ and $M_{ti} = 0.7$. Increasing M_{t2}, for $M_{t1} = 0.4$ and 0.7, yields a reduction in the broadband noise at low frequencies and an increase at high frequencies, for both sources of noise. Increasing M_{t1}, for $M_{t2} = 0.4$ and 0.7, yields a reduction of both sources of broadband noise at all frequencies, but this reduction is much larger for the

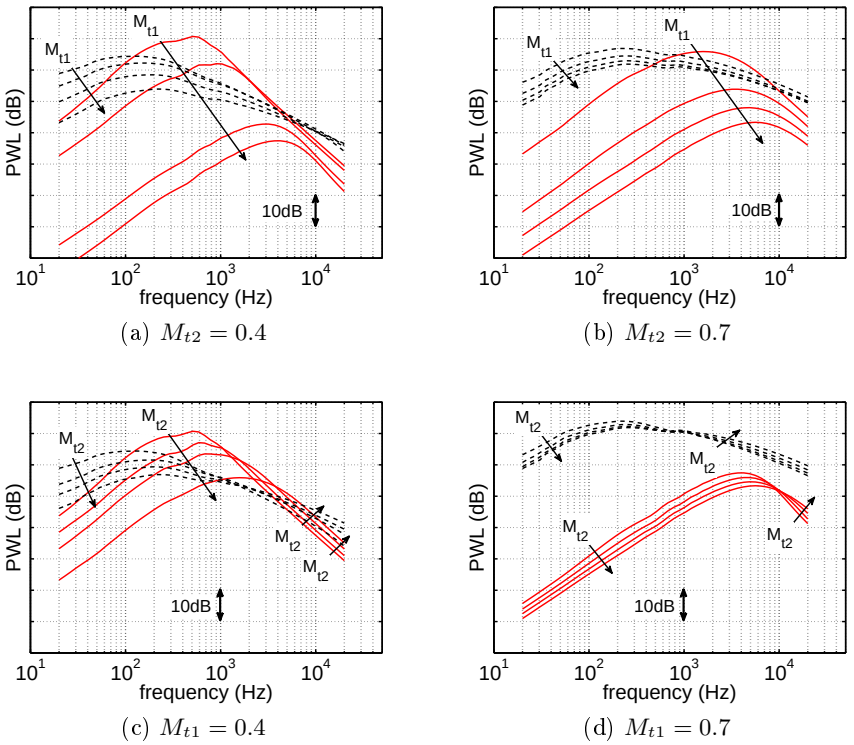

(a) $M_{t2} = 0.4$ (b) $M_{t2} = 0.7$

(c) $M_{t1} = 0.4$ (d) $M_{t1} = 0.7$

Figure 4.17: Effects of rotor speed ($M_{t1,2} = 0.4$ to 0.7, with a step of 0.1) on the PWL of (−) BRWI noise and (−−) total BRTE noise at assumed take-off.

BRWI noise (up to 40dB at low frequency) than for the BRTE noise (up to 15dB at low frequency).

Thus, according to the predictions, the effects of rotor speeds on the broadband noise emissions in CRORs are different if the front rotor is highly or weakly loaded. For CROR configurations where the front rotor loading is low (e.g. at assumed cruise and approach), the BRTE dominates. In this case, increasing the rotor speed at constant engine power and equal torque split yields a slight increase in broadband noise emissions. However, for CROR configurations where the front rotor loading is high (e.g. at assumed take-off), a significant reduction in broadband noise emissions can be achieved by increasing the front rotor speed, which yields a reduction in the width of the turbulent wakes and, therefore, in the contribution of BRWI noise.

4.3.3 Effects of blade number at constant solidity

In this section, the effects of blade number on the broadband noise emissions in CRORs are investigated at constant engine power, equal torque split and constant solidity. The blade numbers range from $B_i = 7$ to 15. The front and rear chord lengths c_i vary with the blade numbers B_i (to keep the solidity constant) but are independent of the operating conditions. The only aerodynamic parameters affected by the change in blade number B_i

(and, therefore, by the change in c_i) are the normalised helical path length X_Θ, the turbulent wake parameters L and w_{rms} and the turbulent boundary layer parameters. In a similar manner to the rotor speed study presented in Section 4.3.2, the main aerodynamic inputs to the broadband noise models are presented below for a representative spanwise strip located at 80% of the rear rotor radius, but the broadband noise predictions are computed from the contributions of all strips. The predicted values of δ_i^*/c_i are presented for the suction side of the rotor blades only, for the sake of brevity, both the values of δ^* from both sides of the rotor blades are used to compute the BRTE noise predictions.

4.3.3.1 Input parameters

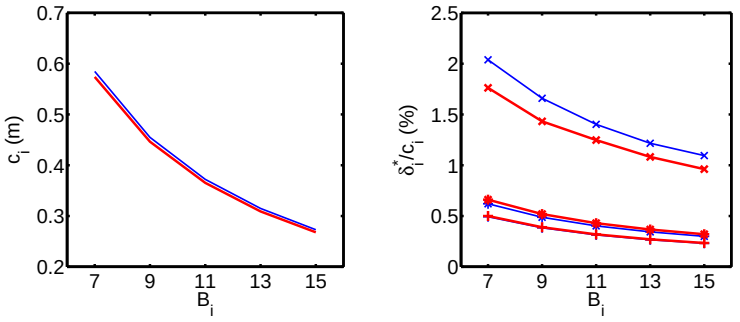

(a) (b)

Figure 4.18: Variation of (a) the chord length c_i and (b) the normalised displacement thickness δ_i^*/c_i on the suction side with B_i. Quantities related to the front and rear rotor are plotted in thin blue ($-$) and thick red (-) lines, respectively. Assumed take-off, cruise and approach are denoted by ($\times$), ($+$) and ($*$), respectively.

The variation of c_i and δ_i^*/c_i with the associated blade number B_i is shown in Fig. 4.18, for the representative strip. Due to the constant solidity assumption, the distribution of c_i decreases as B_i^{-1} and, therefore, the total wetted area of the blades of the rotor is kept constant. The predicted values of δ_i^*/c_i are also decreasing as B_i^{-1} at assumed cruise and approach and at a slightly lower rate ($\approx B_i^{-0.6}$) at assumed take-off. The normalised displacement thickness δ_i^*/c_i is also much larger at assumed take-off than at assumed cruise and approach, due to the higher angles of attack of the rotor blades.

Figure 4.19 presents the variation of the wake parameters X_Θ, L and w_{rms} with B_i at assumed take-off, cruise and approach. Contrary to that observed for the rotor speed study (Section 4.3.2), the contours of the variation of the wake parameters are very similar in shape for all operating conditions. The reason why the wake parameters are affected by the variation of B_1 is due to the associated change in c_1 (since solidity is kept constant), which modifies significantly the drag of the front rotor blades. As a result, the wake turbulence parameters L and w_{rms} decrease as B_1 is increased. A small variation of these parameters with B_2 is also observed, which is due to the small effect of the associated variation in c_2 on

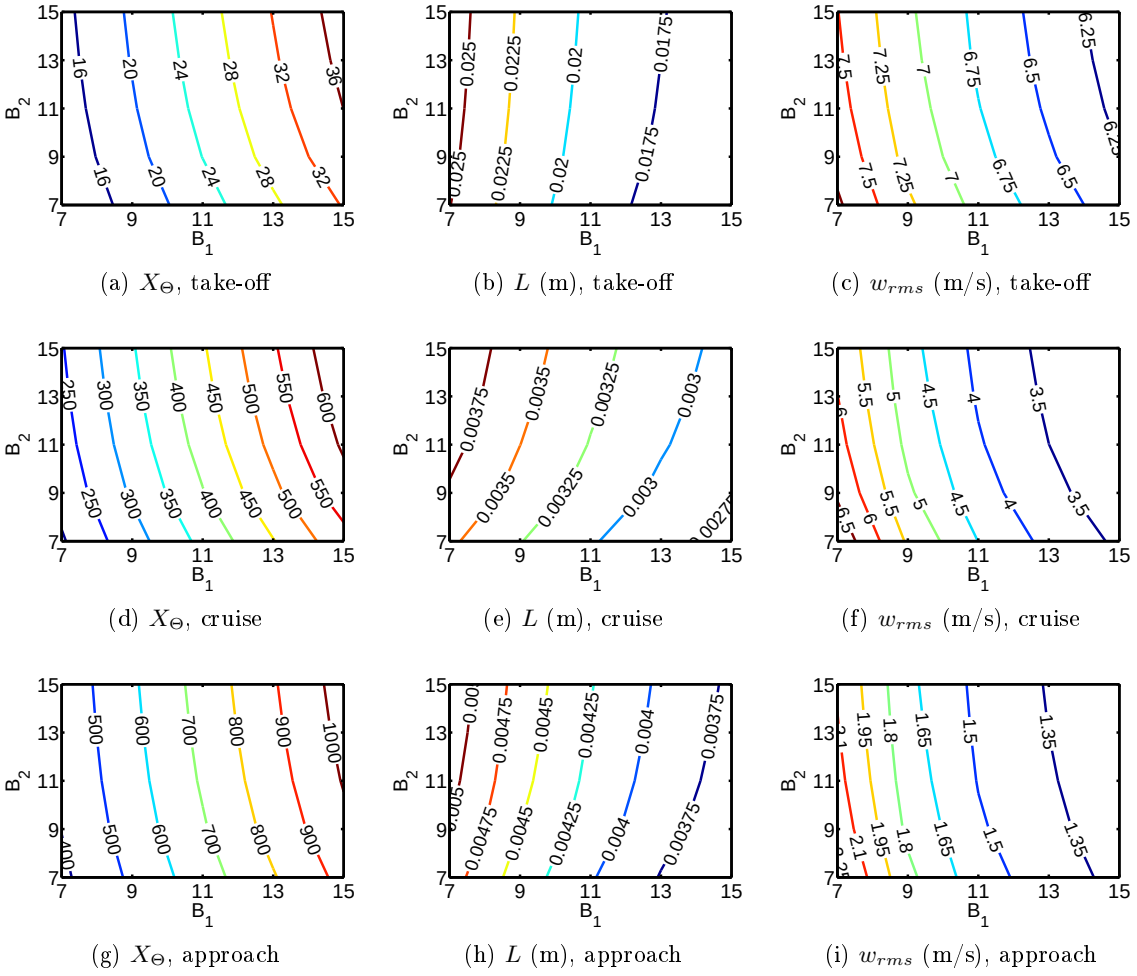

(a) X_Θ, take-off (b) L (m), take-off (c) w_{rms} (m/s), take-off

(d) X_Θ, cruise (e) L (m), cruise (f) w_{rms} (m/s), cruise

(g) X_Θ, approach (h) L (m), approach (i) w_{rms} (m/s), approach

Figure 4.19: Variation of X_Θ, L and w_{rms} with B_1 and B_2 at assumed (a-c) take-off, (d-f) cruise and (g-i) approach.

the separation distance η between the trailing edge of the front rotor blades and the leading edge of the rear rotor blades.

If the aerodynamic input parameters δ_i^*, L and w_{rms} were unchanged by the variation of B_1 and B_2, the total BRTE noise would scale with $B_1 + B_2$ and the BRWI with $B_1 \times B_2$ (as shown in Section 2.4.1). However, the increase in broadband noise due to an increase in B_1 and B_2 is balanced here by an associated reduction in the values of δ_i^*, L and w_{rms} due to the reduction in c_1 and c_2, as shown in this section. In the next section, broadband noise predictions are presented to establish whether the increasing sound power due to increasing B_i is negated by the reduction in sound power due to reduced chord, for the three operating conditions considered.

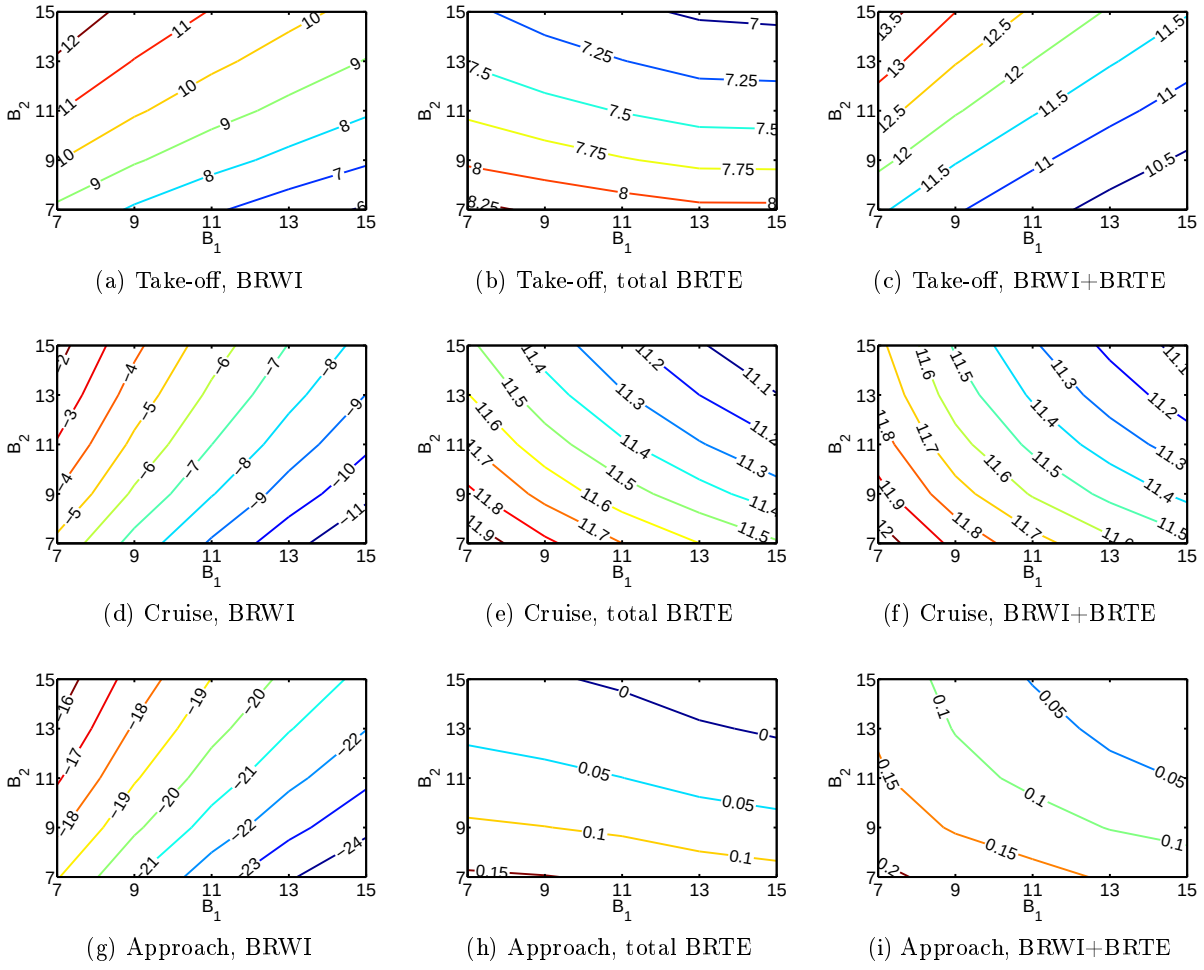

(a) Take-off, BRWI (b) Take-off, total BRTE (c) Take-off, BRWI+BRTE

(d) Cruise, BRWI (e) Cruise, total BRTE (f) Cruise, BRWI+BRTE

(g) Approach, BRWI (h) Approach, total BRTE (i) Approach, BRWI+BRTE

Figure 4.20: Effects of blade number on the OAPWL (in dBA) of the BRWI noise, the BRTE noise and the total broadband noise at assumed take-off, cruise and approach. The levels are normalised on the total OAPWL of the quietest configuration, which is $B_1 = B_2 = 15$ at approach.

4.3.3.2 Broadband noise predictions

Figure 4.20 presents the variation of OAPWL (in dBA) with B_1 and B_2 at assumed take-off, cruise and approach, normalised on the value of the quietest configuration, which is $B_1 = B_2 = 15$ at approach. In a similar manner to the input parameters presented in Section 4.3.3.1, the shape of the predicted broadband noise contours is very similar for all operating conditions. The BRWI noise increases with B_2 and decreases with B_1, with a maximum variation in total OAPWL of approximately 3.7dBA at assumed take-off. The total BRTE noise, however, is very weakly affected by the variation in blade number, with a maximum variation in total OAPWL of 1.25 dBA at assumed take-off and less than 1dBA at assumed cruise and approach. As shown previously, the BRTE noise also dominates significantly the BRWI noise at assumed cruise and approach.

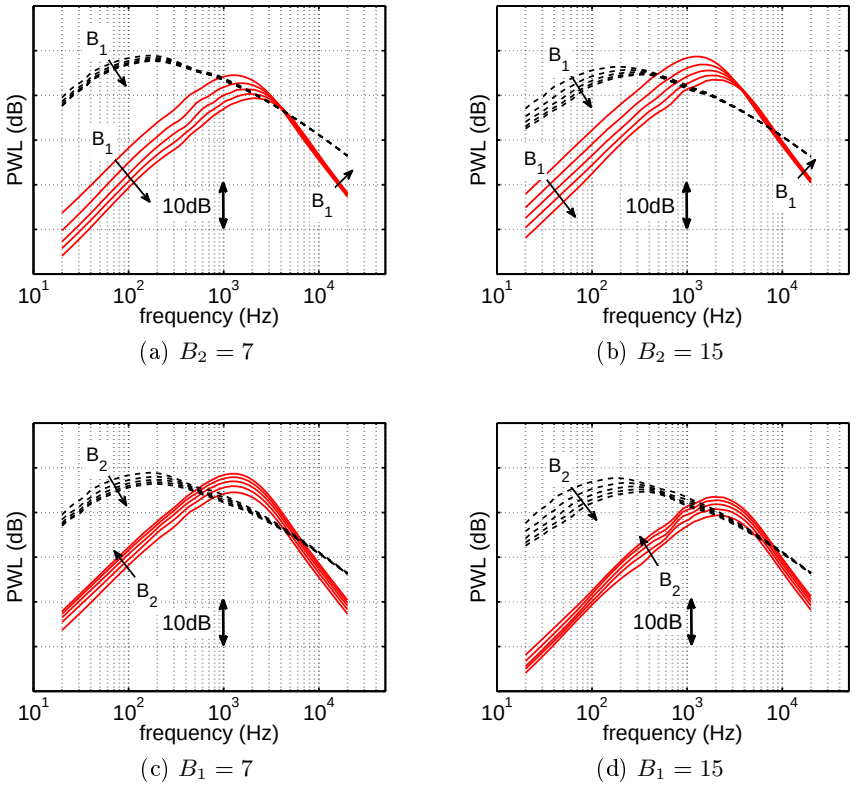

(a) $B_2 = 7$ (b) $B_2 = 15$

(c) $B_1 = 7$ (d) $B_1 = 15$

Figure 4.21: Effects of blade number ($B_{1,2} = 7$ to 15) on the PWL of (−) BRWI noise and (−−) total BRTE noise at assumed take-off.

further details of the balance between BRWI noise and BRTE noise at assumed take-off are shown in Fig. 4.21, where the effects of blade number on PWL are presented by fixing successively $B_i = 7$ and $B_i = 15$. Blade number variations appear to have a significant effect on the BRTE noise only at low frequencies, where the PWL is reduced as B_i is increased. The PWL of the BRWI noise increases with B_2 at all frequencies, whereas increasing B_1 yields a significant decrease in the PWL at low frequencies (up to 10dB) and a small rise in PWL at high frequencies (approximately 1dB).

The effects of blade number at constant solidity are significantly different for highly or weakly loaded front rotor configurations, as for the effects of rotor speed presented in Section 4.3.2. For CROR configurations where the front rotor loading is low (e.g. at assumed cruise and approach), the total broadband noise emissions are dominated by BRTE noise, which is almost completely unaffected by the variation in blade number at constant solidity. However, for CROR configurations where the front rotor loading is high (e.g. at assumed take-off here), the contribution of the BRWI noise to the OAPWL becomes significant. Thus, a significant reduction in broadband noise emissions can be achieved by reducing B_2 and increasing B_1. This is due to the fact that, since the solidity is kept constant, c_1 decreases when B_1 increases which yields a significant decrease of the turbulent wake parameters L

and w_{rms} and, therefore, a reduction of the BRWI noise. In addition, the BRWI noise is weakly affected by small changes in c_2 and, therefore, increases with B_2.

4.3.4 Summary of the results of the parameter study

Assuming that BRWI and BRTE are the two main sources of broadband noise in uninstalled CRORs, the main conclusions of the parameter study presented in this section are that:

- Total broadband noise emissions are significantly dominated by the BRTE noise at assumed cruise and approach (when the front rotor loading is low) whereas both BRTE and BRWI noise contribute significantly to the total CROR broadband noise emissions at assumed take-off (when the front rotor loading is high).
- Varying the rotor-rotor gap can have a significant effect on BRWI noise emissions but generally has a weak effect on total broadband noise emissions. The maximum variation of OAPWL was predicted here to be 1.6dBA at assumed take-off. This result was not expected since the tonal component of CROR noise (in particular the contribution of the potential field interaction) can generally be very sensitive to variations of rotor-rotor gap.
- Increasing the front rotor speed yields a significant broadband noise reduction at assumed take-off (up to -11.7dBA here).
- Reducing the speed of both rotors yields a significant broadband noise reduction at assumed approach (up to -6.8dBA here) and a small broadband noise reduction at assumed cruise (up to -2.8dBA here).
- Increasing the front rotor blade number at constant solidity (i.e. adding blades to the front rotor but reducing their chord) can yield a broadband noise reduction at assumed take-off (up to -3.7dBA here).
- Broadband noise emissions at assumed cruise and approach are almost completely unaffected by variations in blade number at constant solidity. The maximum variation in total OAPWL was predicted to be less than 1dBA.

According to the parameter study presented in this chapter, the BRWI noise is generally more sensitive to variations in design parameters and operating conditions than the BRTE noise in CRORs. Significant broadband noise reductions can therefore be achieved more easily at assumed take-off, where the BRWI is usually significant, than at assumed cruise and approach, where the BRTE noise from each rotor dominates. Note also that, since BRTE noise reduction in CRORs appears to be generally difficult to achieve by modifying design parameters and operating conditions, other noise reduction techniques should be considered for this source of broadband noise, such as active or passive trailing edge treatments for example.

Chapter 5

Validity of Amiet's approximate model for rotor trailing edge noise

5.1 Introduction

In order to deal with the computational cost associated with the use of the FW-H equation for rotating broadband noise sources, which was considered high at the time, Amiet [9, 10] proposed a simplified alternative approach which has been widely used since. This approach consists of approximating the noise from an airfoil in rotating motion by the average over angular position of the noise from the translating airfoil. In other words, the circular motion is approximated by a series of translations over an infinitesimal distance, as shown in Fig 5.1. Amiet stated in Ref. [10] that this approach is valid at high frequencies and low rotor speed, where the effects of rotation on the noise are weak. Amiet's method has been first applied to the leading-edge rotor noise by Paterson and Amiet [125] and to trailing edge rotor noise by Schlinker and Amiet [138]. This formulation has been used extensively in recent years to predict the leading-edge and trailing edge broadband noise of low-speed fans (see for instance Rozenberg et al. [134], Roger et al. [132], Fedala et al. [61]), helicopter rotors (Amiet et al. [14], Amiet [13]), wind turbines (Glegg et al. [73]) and open propellers (Pagano et al. [119]).

To the knowledge of the author, there has been no published work on the validity of the approximations made in Amiet's model. In an attempt to understand better the range of validity of Amiet's model, the aim of this chapter is to compare Amiet's BRTE noise model to the equivalent FW-H based BRTE noise model presented in Chapter 3, in which the effects of circular motion are treated exactly. The present study focuses on rotor *trailing edge* noise only, because in the case of leading-edge noise Amiet's formulation requires substantial modifications to capture the effects of blade-to-blade correlation due to turbulence ingestion (as explained in Ref. [13]).

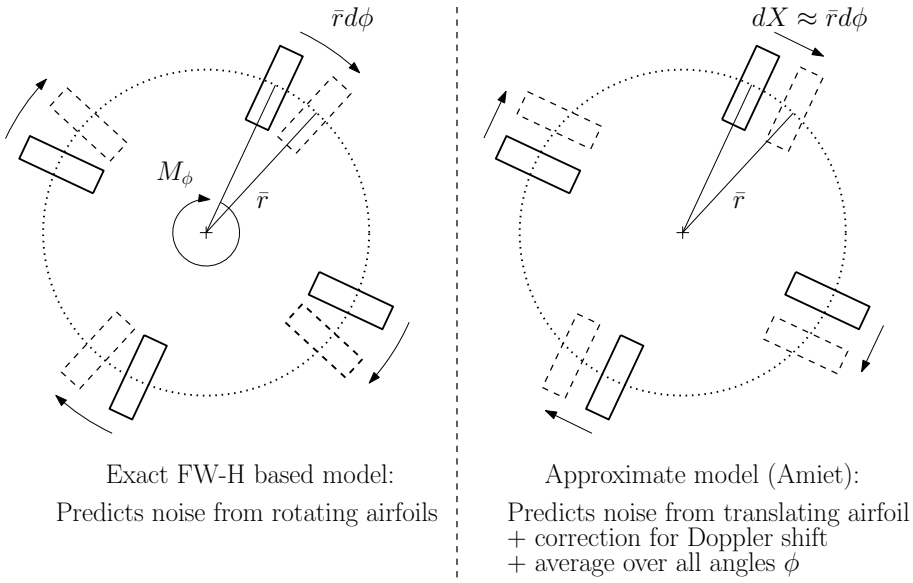

Figure 5.1: Physical description of the exact FW-H based model and the approximate model due to Amiet.

The expressions used to predict the unsteady blade loading in the present study are very fast and, therefore, Amiet's approximate model for deducing the noise of a rotating airfoil from the noise of a translating airfoil saves only little computational time compared to the exact FW-H based formulation. However, if more complex blade response models were used, such as a CFD-based airfoil response function, for instance, Amiet's rotor model would save significant computational time. This brings further motivation to the understanding of the general principles and limitations of Amiet's model for treating the effects of rotation on airfoil noise radiation.

In this chapter, Amiet's BRTE noise model is first described in detail. A comparative study is then presented between the analytical FW-H formulation and the approximate Amiet model. Criteria for the validity of Amiet's model are then proposed. Finally, according to these criteria, the validity of Amiet's model is tested for three practical applications : an open propeller, a model cooling fan and a wind turbine.

5.2 Amiet's model for rotor trailing edge broadband noise

The starting point of Amiet's model is the observation from the work of Lowson [106] that the effect of rotation on noise generation by rotating source is weak if the ratio of angular frequency over rotor speed is high (i.e. $\omega/\Omega \gg 1$). This has been confirmed by the work of Morfey and Tanna [114]. This condition of validity of Amiet's model will be significantly revised in Section 5.3.2.1. Amiet's trailing edge noise model for an isolated airfoil in translation (see Ref. [8]) is applied by considering a rotating motion to be a series of translations over an infinitesimal distance. Furthermore, Amiet also introduces corrections

to take into account the main effects of rotation. He argued that a rotating blade segment (centred radially at $r = \bar{r}$ and of width Δr) moving alternatively away from and towards the observer can be taken into account by, first, substituting the angular frequency ω by a Doppler-shifted frequency ω_ϕ given by

$$\frac{\omega_\phi}{\omega} = 1 + M_\phi \cos\phi \sin\theta, \tag{5.1}$$

where $M_\phi = \bar{r}\Omega/c_0$ is the rotation Mach number, θ is the observer angle and ϕ is the azimuthal location of the blade section, as in previous sections (see Fig. 2.3). Then, since the Doppler-shifted frequency ω_ϕ now varies with the azimuthal location $\phi = \Omega t$ of the airfoil, an averaging of the pressure spectrum over ϕ needs to be performed. With these corrections included, the PSD of the acoustic pressure radiated to the far-field by B blades can be written, using Amiet's notation, as

$$S_{pp,Amiet}\left(r_0, \psi_0, \theta, \omega\right) = \frac{B}{2\pi} \int_0^{2\pi} \left(\frac{\omega}{\omega_\phi}\right)^2 S_{pp,\phi}\left(r_0, \psi_0, \theta, \omega_\phi\right) d\phi. \tag{5.2}$$

The term $S_{pp,\phi}$ in Eq. 5.2 corresponds to the expression for the PSD of the trailing edge noise due to a translating rectangular blade segment centered at a radius $\bar{r}$. It can be expressed in the airfoil bound coordinate system $\left(\left(r - \bar{r}\right), X, Y\right)$ from Refs. [8, 11], and including the amplitude correction due to Moreau and Roger [112, 131], as

$$S_{pp,\phi}\left(r_0, \psi_0, \theta, \omega_\phi\right) = \frac{1}{2\pi} \left(\frac{\omega_\phi b Y}{c_0 \sigma^2}\right)^2 \Delta r \left|\mathcal{L}^{\mathrm{TE}}\left(0, K_{X,\phi}, \kappa_\phi\right)\right|^2 S_{qq}\left(0, K_{X,\phi}\right), \tag{5.3}$$

where the unsteady loading term $\mathcal{L}^{\mathrm{TE}}$ is given by Eq. 3.19, $\sigma^2 = X^2 + \beta_X^2\left(\left(r - \bar{r}\right)^2 + Y^2\right)$, $\beta_X = \sqrt{1 - M_X^2}$, and the effects of skewed gusts are neglected (i.e. $k_r = 0$) by making the large span approximation, although this is not an essential requirement for the validity of Eq. 5.2. In this study, the semi-empirical model for Φ_{pp} due to Goody [78] is used in Eq. 3.12 to estimate the wavenumber cross-spectrum S_{qq} of the surface pressure. The subscript $(.)_\phi$ denotes a quantity dependent on the azimuthal location ϕ of the blade segment. The chordwise turbulence wavenumber and the aeroacoustic coupling wavenumber are respectively given by

$$K_{X,\phi} = \frac{\omega_\phi}{U_c} \quad \text{and} \quad \kappa_\phi = \frac{k_0}{\beta_X^2}\left(M_X - X/\sigma\right). \tag{5.4}$$

Schlinker and Amiet [138] assume *a priori* that the broadband self-noise radiated to the far-field is independent of the azimuthal observer azimuthal coordinate ψ_0, which is equivalent to assuming that the observer is located in the (x, z) plane (cf. Fig 2.3). The relation between the airfoil-bound coordinates $\left(\left(r - \bar{r}\right), X, Y\right)$ and the polar observer coordinates (r_0, θ), that includes the effect of stagger angle α and azimuthal angle ϕ, can be obtained

from

$$\begin{bmatrix} r-\bar{r} \\ X \\ Y \end{bmatrix} = \mathcal{M}_\alpha \mathcal{M}_\phi \begin{bmatrix} r_0 \cos\theta \\ 0 \\ r_0 \sin\theta \end{bmatrix}, \tag{5.5}$$

where the rotation matrices $\mathcal{M}_\alpha$, and $\mathcal{M}_\phi$ are defined by

$$\mathcal{M}_\alpha = \begin{bmatrix} 1 & 0 & 0 \\ 0 & -\sin\alpha & \cos\alpha \\ 0 & \cos\alpha & \sin\alpha \end{bmatrix}, \quad \mathcal{M}_\phi = \begin{bmatrix} 0 & \cos\phi & \sin\phi \\ 0 & -\sin\phi & \cos\phi \\ 1 & 0 & 0 \end{bmatrix} \tag{5.6}$$

The effects of mean flow convection are neglected in the comparison between the two models, i.e. $\beta_X = 1$ in Eqs. 5.3 and 5.4, without any loss of generality. The final expression of the far-field PSD of the BRTE noise, as predicted by Amiet's model, can therefore be obtained by substituting Eqs. 5.3 to 5.6 into Eq. 5.2 to give

$$S_{pp,Amiet}\left(r_0,\theta,\omega\right) = \frac{B}{2\pi}\left(\frac{k_0 b}{r_0}\right)^2 \frac{\Delta r}{2\pi} \int_0^{2\pi} D_\phi\left(\theta,\alpha\right) \left|\mathcal{L}\left(0,K_{X,\phi},\kappa_\phi\right)\right|^2 S_{qq}\left(0,K_{X,\phi}\right) d\phi, \tag{5.7}$$

where

$$K_{X,\phi} = \frac{\omega_\phi}{U_c} \text{ and } \kappa_\phi = k_0\left(\sin\theta\sin\alpha\cos\phi - \cos\theta\cos\alpha\right). \tag{5.8}$$

The convection velocity U_c is related to the chordwise flow velocity by $U_c = 0.8U_X$ (according to Amiet [8] and as in Section 3) and a directivity term D_ϕ is introduced in Eq. 5.7 as

$$D_\phi\left(\theta,\alpha\right) = \left(\cos\theta\sin\alpha + \sin\theta\cos\alpha\cos\phi\right)^2. \tag{5.9}$$

Note that in the expression of κ_ϕ (Eq. 5.8), the acoustic wavenumber $k_0 = \omega/c_0$ is a function of the observer frequency ω rather than the Doppler shifted frequency ω_ϕ. To the knowledge of the author, this point is not explicitly made in Amiet's original work (see for instance Ref. [13]) and this might lead the reader to use in error $k_0 = \omega_\phi/c_0$ instead of $k_0 = \omega/c_0$ in Eq. 5.8. The wavenumber κ_ϕ appears in the term $\mathcal{L}^{\mathrm{TE}}\left(k_r,k_X,\kappa\right)$ as a coupling term between the wavenumber of the turbulent gust $K_{X,\phi}$ and the acoustic wavenumber k_0 of the sound radiation, and only the former can be affected by a Doppler shift resulting from rotation.

5.3 Comparative study

5.3.1 Equivalence of the directivity functions D of both models

Amiet's simplified model and the general FW-H based model of Chap. 3, in which the effects of rotation are treated exactly, have been expressed in the previous sections in a form that facilitates their comparison. From Eqs. 5.7 and 3.18, the two models can be expressed in similar forms. However, three fundamental differences can be identified and are listed below:

1. The directivity terms in the two models (D_l and D_ϕ, see Eqs. 3.15 and 5.9 respectively) differ. The exact model includes a Bessel function of the first kind and an integral over the strip span, which are not appearing in Amiet's model.
2. The exact model presents an infinite sum over the azimuthal acoustic mode orders l whereas Amiet's model involves an integral over the blade azimuth ϕ.
3. The expressions of the turbulent chordwise wavenumber K_X and the aeroacoustic coupling wavenumber κ are different in each model (see Eqs. 5.8, 3.8 and 3.17).

As a first step, both models are compared in terms of their directivity terms only. For this purpose, the third point above is neglected and the source terms $|\mathcal{L}|^2$ and S_{qq} can therefore be taken outside of the integral and the summation in Eqs. 5.7 and 3.18, respectively. In this case, the only difference between the final expressions of the two models lies in the directivity functions $D_{exact} = \sum_{l=-\infty}^{\infty} D_l$ and $D_{Amiet} = \frac{1}{2\pi}\int_0^{2\pi} D_\phi d\phi$ of the exact model and of Amiet's model, respectively.

The directivity function D_{Amiet} of Amiet's model is obtained from Eq. 5.9 as

$$\begin{aligned} D_{Amiet} &= \frac{1}{2\pi}\int_0^{2\pi} D_\phi\left(\theta,\alpha\right) d\phi \\ &= \cos^2\theta \sin^2\alpha + \frac{1}{2}\sin^2\theta\cos^2\alpha, \end{aligned} \tag{5.10}$$

whereas the directivity function D_{exact} of the exact model is deduced directly from Eq. 3.15 as

$$\begin{aligned} D_{exact} &= \sum_{l=-\infty}^{\infty} D_l\left(\theta,\alpha,\omega\right) \\ &= \frac{1}{\Delta r}\sum_{l=-\infty}^{\infty} \int_{\bar{r}-\frac{\Delta r}{2}}^{\bar{r}+\frac{\Delta r}{2}} \left(\cos\theta\sin\alpha + \frac{l}{k_0 r}\cos\alpha\right)^2 J_l^2\left(k_0 r \sin\theta\right) dr. \end{aligned} \tag{5.11}$$

The directivity function D_{exact} can alternatively be written by developing the parenthesis in Eq. 5.11 as

$$D_{exact} = \frac{1}{\Delta r} \int_{\bar{r}-\frac{\Delta r}{2}}^{\bar{r}+\frac{\Delta r}{2}} (D_1 + D_2 + D_3)\, dr, \tag{5.12}$$

where

$$\begin{aligned} D_1 &= (\cos\theta \sin\alpha)^2 \sum_{l=-\infty}^{\infty} J_l^2 (k_0 r \sin\theta), \\ D_2 &= \frac{2}{k_0 r} \cos\theta \cos\alpha \sin\alpha \sum_{l=-\infty}^{\infty} l J_l^2 (k_0 r \sin\theta), \\ D_3 &= \left(\frac{\cos\alpha}{k_0 r}\right)^2 \sum_{l=-\infty}^{\infty} l^2 J_l^2 (k_0 r \sin\theta). \end{aligned} \tag{5.13}$$

The infinite summations of Eq. 5.13 converge, for any real argument ζ, to

$$\begin{aligned} \sum_{l=-\infty}^{\infty} J_l^2 (\zeta) &= 1, \\ \sum_{l=-\infty}^{\infty} l J_l^2 (\zeta) &= 0, \\ \sum_{l=-\infty}^{\infty} l^2 J_l^2 (\zeta) &= \frac{\zeta^2}{2}, \end{aligned} \tag{5.14}$$

as proved below.

The first identity of Eq. 5.14 can be proved from Neumann's addition theorem for Bessel functions of the first kind (from Eq. 9.1.75 in Ref.[1]), which states that

$$\sum_{l=-\infty}^{\infty} J_{\nu \mp l} (u)\, J_l (v) = J_l (u \pm v), \tag{5.15}$$

for any integer ν and any reals u and v. Setting $u = v = \zeta$, $\nu = 0$ in Eq. 5.15 and noting that $J_0 (0) = 1$ yields

$$\sum_{l=-\infty}^{\infty} J_l^2 (\zeta) = 1. \tag{5.16}$$

The second identity of Eq. 5.14 comes from the property of Bessel functions of the first kind stating that $J_{-l}^2 (\zeta) = J_l^2 (\zeta)$, for any real argument ζ, which yields the identity

$$\sum_{l=-\infty}^{\infty} l J_l^2 (\zeta) = 0. \tag{5.17}$$

The third identity of Eq. 5.14 can be proved from Gegenbauer's addition theorem for Bessel functions of the first kind (Eq. 9.1.80 in Ref.[1]), which states that

$$2^{\nu}\Gamma(\nu)\sum_{l=0}^{\infty}(\nu+l)\frac{J_{\nu+l}(u)}{u^{\nu}}\frac{J_{\nu+l}(v)}{v^{\nu}}C_l^{(\nu)}(\cos\alpha)=\frac{J_{\nu}(w)}{w^{\nu}}, \tag{5.18}$$

where ν is any positive, non-zero integer, u and v are any reals, $w=\sqrt{u^2+v^2-2uv\cos\alpha}$ and $C_l^{(\nu)}(z)$ is Gegenbauer's polynomial. Setting $\nu=1$, $u=v=\zeta$, $\alpha=0$ and using the fact that $C_l^1(1)=1+l$ and $\lim_{w\to 0}J_1(w)/w=1/2$ yields

$$2\sum_{l=0}^{\infty}(l+1)^2J_{l+1}^2(z)=\frac{\zeta^2}{2}, \tag{5.19}$$

which can be extended to negative l values as

$$\sum_{l=-\infty}^{\infty}l^2J_l^2(\zeta)=\frac{\zeta^2}{2}. \tag{5.20}$$

Substituting Eqs. 5.14 into 5.12 yields

$$D_{exact}=\cos^2\theta\sin^2\alpha+\frac{1}{2}\sin^2\theta\cos^2\alpha, \tag{5.21}$$

and thus (from Eq. 5.10)

$$D_{exact}=D_{Amiet}. \tag{5.22}$$

The above analysis shows that, in the case of equivalent source terms, the directivity functions of Amiet's model and the exact model are *identical*. This equivalence does not seem to have been recognised elsewhere and was unexpected considering the fact that, unlike the exact FW-H based model, Amiet's model is not based on an exact acoustic formulation for rotating sources. Moreover, Amiet developed his model based on physical considerations and was unaware[1] of the mathematical equivalence shown in the present section.

However, even though this result reinforces the confidence in the validity of Amiet's model, it does not prove equivalence between the two methods since the source terms $\mathcal{L}$ and S_{qq} in each model cannot be considered equivalent, as discussed later in Sections 5.3.2 and 5.3.3.

5.3.2 Comparison of Amiet's model and the exact model at low frequency

5.3.2.1 Estimation of the low frequency limit f_{low} of validity of Amiet's model

As mentioned in Section 5.2, Amiet [10] stated that his model should be valid at frequencies well above the shaft frequency of the rotor so that the effects of rotation on the generation of sound can be neglected. Thus, over an acoustic period $2\pi/\omega$, the angular displacement

[1] from private communication with Dr. Roy K. Amiet, 25 May 2010.

of the blade can be neglected and, therefore, Amiet gave an estimate of the low frequency limit f_{low} of validity of his model as

$$f_{low} \approx f_{shaft} = \frac{\Omega}{2\pi}. \tag{5.23}$$

A more accurate estimation of the low frequency f_{low} of the validity of Amiet's model is proposed in this section, based on the differences of the two models in predicting the directivity of the broadband noise at low frequencies.

It has been shown in Section 5.3.1 that the directivity functions of both models are equivalent if the source terms $|\mathcal{L}|^2$ and S_{qq} are assumed to be the same in both models. This assumption was made as a first step in the comparison of the two models but must be relaxed to allow a complete comparison.

From the properties of the function D_l (Eq. 3.15), the exact model predicts that only the $l = 0$ azimuthal acoustic mode contributes to the radiated noise in the low frequency limit. The second term in Eq. 5.9, which represents the contribution to the noise of the component of the unsteady blade loading in the *torque* direction (i.e. the azimuthal direction), must therefore vanish in the low frequency limit. Thus, the exact model predicts that the BRTE noise is controlled only by the component of the unsteady blade loading in the *thrust* direction (i.e. the axial direction) at frequencies where only the azimuthal acoustic mode of order $k = 0$ contributes to the radiated noise. This behaviour cannot be captured by Amiet's model since, from Eq. 5.9, both the thrust and torque components of the unsteady blade loading contribute significantly to the noise in the low frequency limit. Amiet's model must, therefore, differ from the exact model at frequencies lower than the cut-off frequency f_{low} of the first azimuthal mode of order $k = 1$, which is given by

$$f_{low} = \frac{c_0}{2\pi\bar{r}\sin\theta}. \tag{5.24}$$

This revised estimate of the low frequency limit f_{low} of validity of Amiet's model is significantly different from Amiet's estimate, given in Eq. 5.23. Both conditions represent a critical frequency below which the effects of rotation can be considered important, but the effects of rotation are quantified differently, i.e. in terms of the rotor angular frequency Ω in Eq. 5.23 and in terms of the radial location $\bar{r}$ in Eq. 5.24. Moreover, unlike Eq. 5.23, the improved estimation of f_{low} presents a dependency on the observer angle. From Eq. 5.24, the low frequency condition $f > f_{low}$ of validity of Amiet's model can be alternatively rewritten as $2\pi\bar{r}\sin\theta > \lambda$ (where $\lambda = c_0/f$ is the acoustic wavelength). This physically means that Amiet's model must be valid for acoustic wavelengths smaller than the distance $2\pi\bar{r}$ covered by the blade segment during one rotation, projected in the direction of the observer.

Figure 5.2 presents a comparison between sound pressure levels (at 1m) predicted by Amiet's model and the exact model for $\theta = 45^o$, 75^o and 90^o. The configuration used is a single spanwise strip of the model cooling fan described in Section 5.4.1. It appears from these plots

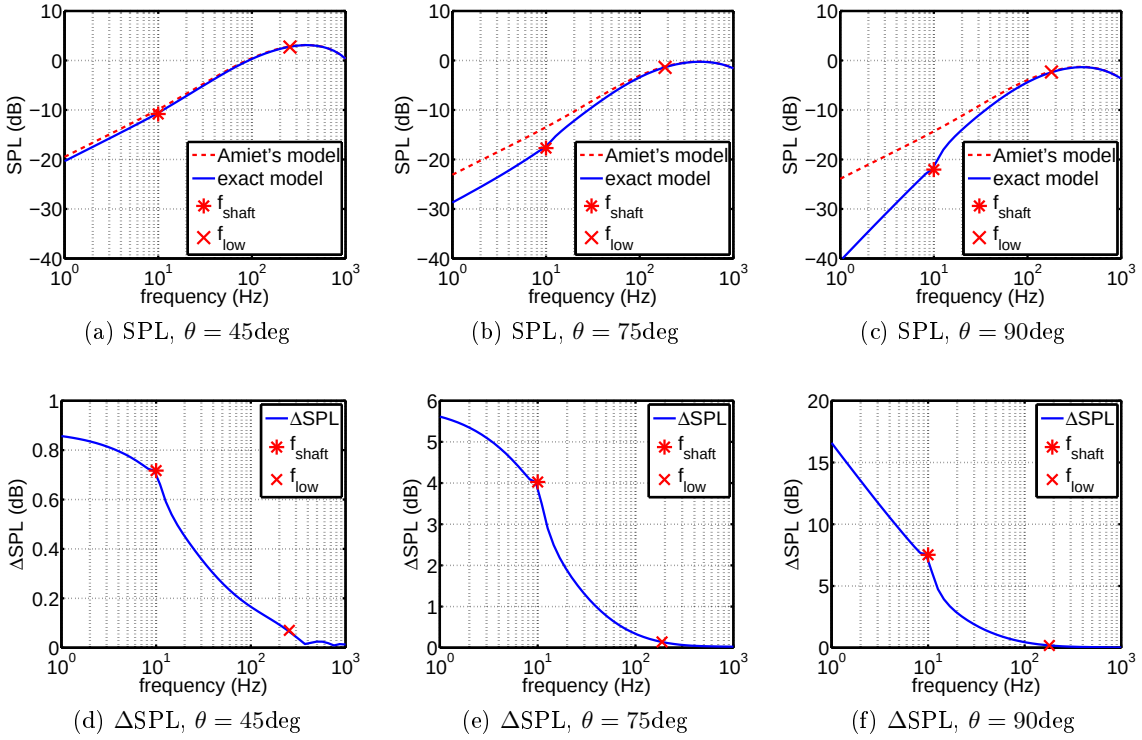

(a) SPL, $\theta = 45$deg (b) SPL, $\theta = 75$deg (c) SPL, $\theta = 90$deg

(d) ΔSPL, $\theta = 45$deg (e) ΔSPL, $\theta = 75$deg (f) ΔSPL, $\theta = 90$deg

Figure 5.2: SPL predicted by Amiet's model and the exact model and ΔSPL for the observer angles $\theta = 45^o$, 75^o, 90^o.

that the expression of f_{low} introduced in this section (Eq. 5.24) predicts more accurately the low frequency limit of validity of Amiet's model than the condition $f_{low} \approx f_{shaft}$ (Eq. 5.23), introduced by Amiet in Ref. [10]. Note that the ratio $\Delta SPL = 10\log_{10}(S_{pp,Amiet}/S_{pp,exact})$ between the predictions of Amiet's model and the exact model tends in the low frequency limit to a value independent of frequency, denoted here by $\Delta SPL_{low} = \lim_{f/f_{low}\to 0}\Delta SPL$, except for $\theta = 90^o$. An estimate for ΔSPL_{low} is given in the next section.

5.3.2.2 Estimation of the low frequency error ΔSPL_{low} of Amiet's model

An estimate for the error of Amiet's model ΔSPL_{low} in the low frequency limit is now derived. Noting from Eq. 3.19 that $\lim_{f\to 0}\mathcal{L}^{\mathrm{TE}} = 1/\left(\frac{c}{2}|k_X| + \frac{c}{2}|\kappa|\right)$ and that $\Phi_{pp}(\omega)$ is proportional to ω^2 in the low frequency limit (from Eq. 3.23), an exact value of the low frequency error of Amiet's model can be obtained from Eqs. 3.18 and 5.7 as

$$\lim_{f/f_{low}\to 0}\frac{S_{pp,Amiet}}{S_{pp,exact}} = \frac{1}{2\pi}\int_0^{2\pi}\frac{(1+M_c|\cos\theta\cos\alpha|)^2\left(1+\frac{\tan\theta}{\tan\alpha}\cos\phi\right)^2(1+M_\phi\sin\theta\cos\phi)}{(1+M_\phi\sin\theta\cos\phi+M_c|\sin\alpha\sin\theta\cos\phi-\cos\theta\cos\alpha|)^2}d\phi. \tag{5.25}$$

The integral in Eq. 5.25 does not seem to have a simple analytical solution valid for all values of θ, α, M_ϕ and M_c. However, a simple solution of Eq. 5.25 exists in the low Mach

number limit (i.e. $(M_\phi, M_c) \ll 1$), which gives the following approximate expression for ΔSPL_{low} (in dB):

$$\lim_{(M_\phi, M_c)\to 0} \Delta SPL_{low} = 10\log_{10}\left\{1 + \frac{1}{2}\left(\frac{\tan\theta}{\tan\alpha}\right)^2\right\}. \tag{5.26}$$

Figure 5.3 shows the variation of the exact (Eq. 5.25) and low Mach number (Eq. 5.26) estimates of ΔSPL_{low}, as a function of the observer angle θ and for $M_\phi = 0.1$, 0.45 and 0.8, and $\alpha = 30°$, 45° and 60°. For any configuration, ΔSPL_{low} is zero for an observer on the rotor axis ($\theta = 0°$ and $\theta = 180°$) and tends to infinity for an observer located in the rotor plane ($\theta = 90°$). This result can be explained by noting, from Section 5.3.2.1, that ΔSPL_{low} must be large if the component of the unsteady blade loading in the torque direction is large compared to the component in the thrust direction. However, according to Eqs. 3.15 and 5.9, the thrust component vanishes when the observer is in the rotor plane ($\theta = 90°$) whereas the torque component vanishes when the observer is on the rotor axis ($\theta = 0°$ and $\theta = 180°$), thus explaining the shape of ΔSPL_{low} shown in Fig.5.3. Note also that ΔSPL_{low} is weakly affected by changes in M_ϕ and is higher for small stagger angles α for any given observer angle $\theta \neq 90°$. These results confirm the behaviour observation in Fig. 5.2.

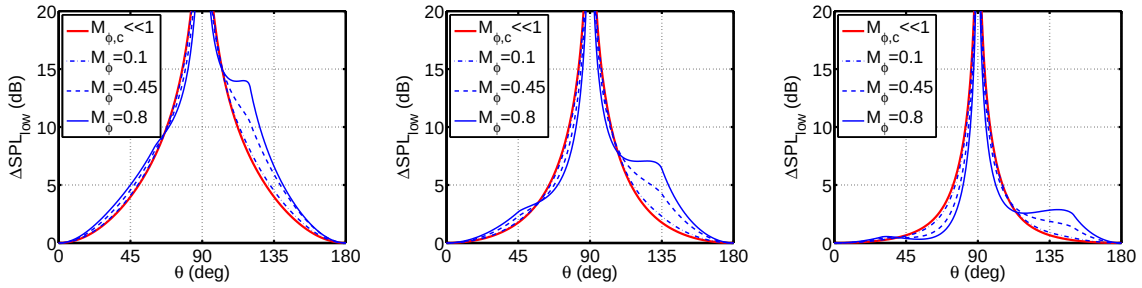

(a) $\alpha = 30$deg (b) $\alpha = 45$deg (c) $\alpha = 60$deg

Figure 5.3: Variation of ΔSPL_{low} with θ for (a) $\alpha = 30°$, (b) $\alpha = 45°$, (c) $\alpha = 60°$, and $M_\phi = 0.1$, 0.45, 0.8.

5.3.3 Comparison of Amiet's model and the exact model at high frequency

5.3.3.1 Estimation of the high frequency limit f_{high} of validity of Amiet's model

In both the exact and the approximated models, the streamwise turbulence wavenumber k_X is Doppler shifted in order to capture the effects of source rotation (see Eqs. 3.8 and 5.8). The expressions for those Doppler shifts are different in both models, but the range of shifted frequencies as ϕ varies is approximately the same. Thus, the maximum value of the Doppler shift for Amiet's model is obtained for $\phi = 0$ whereas the maximum value of

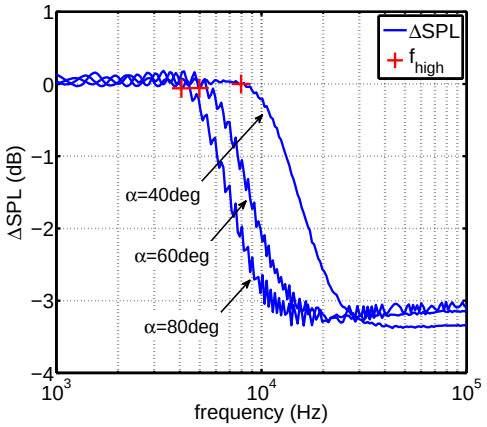

Figure 5.4: Validation of f_{high} for $\alpha = 40°$, $60°$ and $80°$, $M_\phi = 0.6$ and $\theta = 90°$.

the Doppler shift for the exact model is obtained for $l_{max} \approx k_0 \bar{r} \sin\theta$ (from the property of Bessel functions of the first kind), which yields

$$\frac{\omega_l}{\omega}\Big|_{max} = 1 + l_{max}\Omega/\omega \approx 1 + M_\phi \sin\theta = \frac{\omega_\phi}{\omega}\Big|_{max}. \tag{5.27}$$

Since the range of shifted frequencies is not exactly the same, a small error exists between the two models, and this error must become significant in regions where the boundary layer pressure spectrum scales with k_X to a high power. This typically occurs in the high frequency limit, where the surface pressure spectrum Φ_{pp} scales with k_X^{-5} (see Fig. 3.2). It is therefore proposed to associate the critical frequency f_{high} with the 'turning point' where Φ_{pp} enters its high frequency asymptotic region. Assuming that this 'turning point' is accurately predicted by the model for Φ_{pp} proposed by Goody [78], an estimate for f_{high} can be identified from Eq. 3.23 as the frequency above which the second term in the denominator becomes dominant compared to the first term:

$$f_{high} \approx 3.0 \frac{U_X R_T^{0.57}}{2\pi\delta}, \tag{5.28}$$

where R_T is introduced in Eq. 3.24 and deduced from the turbulent boundary layer parameters on the suction side of the airfoil, and where the factor 3.0 has been set empirically.

Figure 5.4 presents a validation of Eq. 5.28 by plotting the difference in sound pressure level $\Delta SPL = SPL_{Amiet} - SPL_{exact}$ predicted by each model. The rotation Mach number M_ϕ is kept constant while ΔSPL is estimated at several stagger angles α, and therefore several values of f_{high} (since $U_X = M_\phi c_0 / \sin\alpha$), are evaluated. The observer angle is set to $\theta = 90°$, so that the effects of the Doppler shifts are maximum. The baseline configuration chosen here consists of a single blade segment ($B = 1$) of chord $c = 0.4$m, span $\Delta r = 0.6$m and stagger angle $\alpha = 60°$, rotating at $M_\phi = 0.6$ and located radially at $\bar{r} = 1$m from the centre of rotation. The main turbulent boundary layer parameters required in the surface pressure spectrum used here (Eq. 3.23) are the boundary layer thickness and the friction coefficient, set to $\delta = 5$cm and $C_f = 10^{-5}$ respectively. This configuration has been chosen arbitrarily,

without any loss of generality, so that the high frequency error of Amiet's model appears clearly in Fig. 5.4. Practical applications to realistic rotor configurations are presented in Section 5.4.1.

The estimate for f_{high} given in Eq. 5.28 predicts accurately the high frequency limit at which Amiet's model starts to deviate from the exact model in Fig. 5.4. Note also in Fig. 5.4 that ΔSPL converges to a value, denoted here by ΔSPL_{high}, that is independent of frequency and weakly dependent on stagger angle. An estimate for ΔSPL_{high} is given in the next section.

5.3.3.2 Estimation of the high frequency error ΔSPL_{high} of Amiet's model

Due to the complexity of Eqs. 3.18 and 5.7, it is difficult to establish an exact analytical expression for the high frequency error ΔSPL_{high} between Amiet's model and the exact model. However, it has been observed that ΔSPL_{high} varies mostly as a function of $M_\phi \sin\theta$, which corresponds to the main term of the Doppler shifts responsible for the high frequency error of Amiet's model (see Eq. 5.27). Figure 5.5 presents plots of ΔSPL_{high} as a function of θ for different values of M_ϕ, for the configuration described in Section 5.3.3.1. These plots were obtained at the unrealistically high frequency of $f = 100$kHz, where ΔSPL_{high} has converged to a value independent of frequency (as shown in Fig. 5.4). An empirical estimate of ΔSPL_{high} is obtained by curve fitting the exact value to give

$$\Delta SPL_{high} \approx A \log_{10} \left\{ 1 - (M_\phi \sin\theta)^6 \right\}, \tag{5.29}$$

where A is an arbitrary constant set equal to $A = 160$.

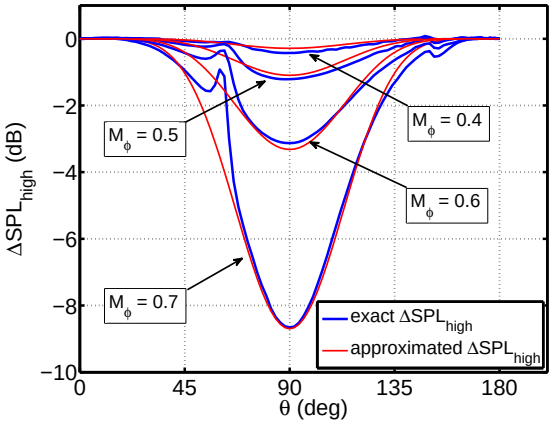

Figure 5.5: Variation of the high frequency error ΔSPL_{high} of Amiet's model with M_ϕ and θ.

Reasonable agreement is shown in Fig. 5.5 between the approximated ΔSPL_{high} of Eq. 5.29 and the exact value of ΔSPL_{high}. Equation 5.29 can therefore be used as an estimate of

the high frequency error between Amiet's model and the exact model, when the frequency is above the high frequency limit of validity f_{high}, given in Eq. 5.28.

5.4 Applications and discussion of the domain of validity of Amiet's model

5.4.1 Applications

The results presented in section 5.3 show that Amiet's model and the exact model for propeller trailing edge noise agree better than 0.1dB over a frequency range bounded by the frequencies f_{low} and f_{high} (Eqs. 5.24 and 5.28). Approximate estimates of the low and high frequency error ΔSPL_{low} and ΔSPL_{high} of Amiet's model, beyond these critical frequencies, have also been proposed in this chapter (Eqs. 5.26 and 5.29).

The criteria defining the validity of Amiet's model are now applied to different realistic industrial fans and rotors. Three different applications are chosen on the basis that they all have been the subject of published studies of trailing edge noise. They consist of an open propeller [120, 119] (at take-off and cruise conditions), a model cooling fan [134] and a wind turbine [116]. Note that the trailing edge noise model due to Amiet, assessed in this chapter, was in fact used in these references to predict the broadband noise of the open propeller [120, 119] and the model cooling fan [134], whereas the semi-empirical method of Brooks et al. [36] was used for predicting the broadband noise from the wind turbine [116].

In this section, Amiet's model and the exact model are compared, for all rotor configurations, by predicting the trailing edge noise directivity and PWL spectrum of a representative blade section located at 3/4 of the tip radius (i.e. $\bar{r} = 0.75R_t$). The span of the blade section considered is set to be equal to a third of its radial location (i.e. $\Delta r = \bar{r}/3$). The panel method software XFOIL is used to obtain the boundary layer parameters required for the trailing edge broadband noise models. Since no blade geometry is provided in the references (except for the cooling fan in Ref. [134]) and since the interest is in comparing the trailing edge noise models, rather than producing highly accurate noise predictions, a NACA0012 airfoil geometry is used as input into the XFOIL code for all the rotor configurations. It is also assumed, without any loss of generality, that the angle of attack is zero in all configurations.

The main geometry and aerodynamic parameters used in this study are given in Table 5.1. The tip radius of the open propeller is not provided in Refs. [120, 119] and is therefore set arbitrarily to $R_t = 1.8$m, which is a typical value for open propellers. Note that the stagger angle α is the only parameter modified between the take-off and the cruise conditions, for the open propeller configuration. An approximate value of the chord length c of the open propeller and the wind turbine, at 75% of R_t, has been deduced graphically from the sketches provided in Refs. [120, 119] and Ref. [116], respectively.

	Model cooling fan	Open propeller	Wind Turbine
R_t	0.4m	1.8m (typical)	29m
α	56^o	73^o(take-off), 52^o(cruise)	80^o
c	0.13m	0.31m (estimated)	2m (estimated)
B	2	6	3
Ω	62.83rad.s^{-1}	188.5rad.s^{-1}	2.618rad.s^{-1}
M_ϕ	0.0525	0.748	0.165

Table 5.1: Main input parameters used for the applications considered.

	f_{shaft}	f_{low} ($\theta = 90^O$)	ΔSPL_{low} ($\theta = 60^O$)	f_{high}	ΔSPL_{high} ($\theta = 90^O$)
model cooling fan	10Hz	180Hz	1dB	500Hz	$\approx$ 0dB
propeller (cruise)	30Hz	40Hz	3dB	2.3×10^5Hz	-13dB
propeller (take-off)			1dB	1.7×10^5Hz	
wind turbine	0.42Hz	2.5Hz	$<$ 1dB	6520Hz	$\approx$ 0dB

Table 5.2: Estimates of the validity of Amiet's model applied to the four configurations considered.

The main criteria for the validity of Amiet's model, introduced in section 5.3, are applied to the three cases considered and are summarised in Table 5.2. The maximum values of f_{low} and ΔSPL_{high} (i.e. at $\theta = 90^o$) are shown and an estimate of ΔSPL_{low} is given at $\theta = 60^O$ using Eq. 5.26. Figure 5.6 presents predictions of PWL using both the exact model and Amiet's model, for the four configurations considered. Agreement better than 0.5dB is generally observed between the two models for frequencies above f_{low}. The low frequency error ΔSPL_{low} and the low frequency limit f_{low} of Amiet's model agree well with the values predicted in Table 5.2. Moreover, the high frequency error ΔSPL_{high} of Amiet's model is either negligible (for the cooling fan and the wind turbine) or significant (for the open propeller) but only at frequencies $f > f_{high}$ well above the audible frequency range, as shown in Table 5.2.

Figure 5.7 presents directivity patterns predicted by both methods for the four rotor configurations considered at $f = 10$Hz, $f = 100$Hz and $f = 10$kHz. In these directivity plots, Amiet's model and the exact model differ only at very low frequencies ($f = 10$Hz), as already observed for PWL in Fig. 5.6. At frequencies $f = 100$Hz and $f = 10$kHz, which are within the audible range, the agreement of these directivity plots is excellent and the difference in SPL between the two models is within 1dB.

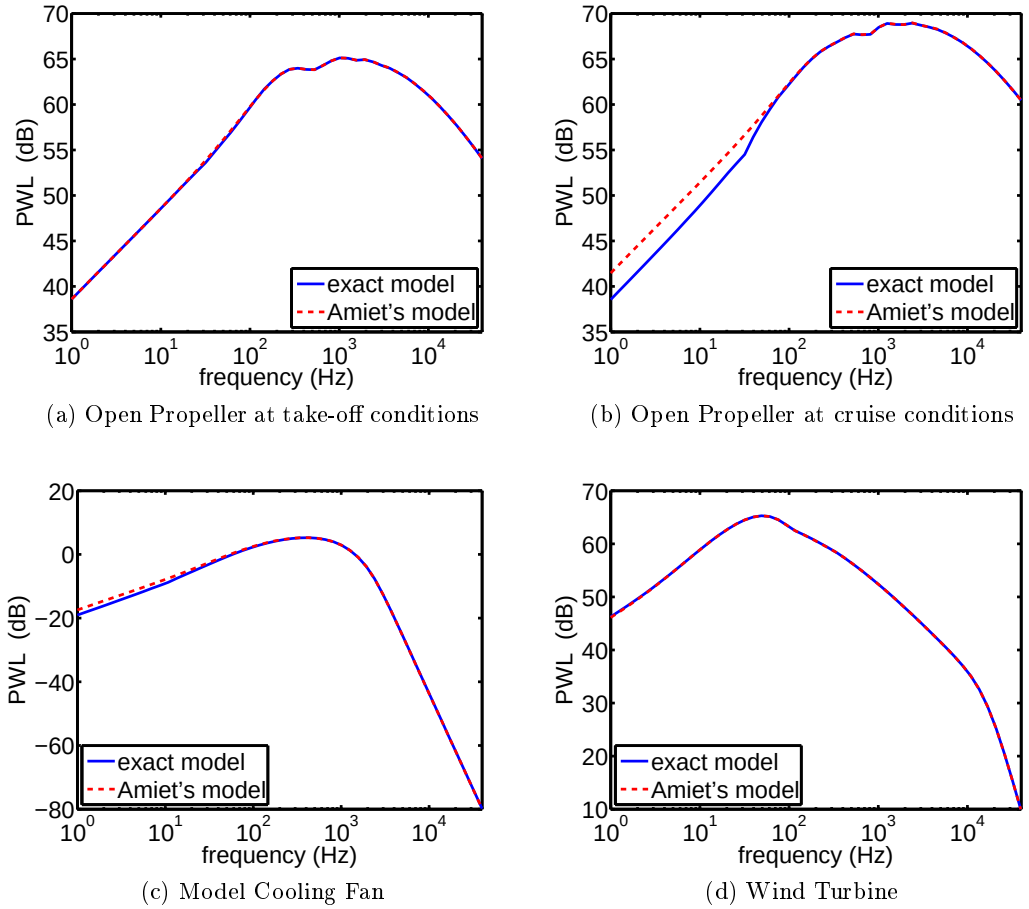

(a) Open Propeller at take-off conditions

(b) Open Propeller at cruise conditions

(c) Model Cooling Fan

(d) Wind Turbine

Figure 5.6: PWL predictions, using Amiet's model and the exact model, of the trailing edge noise due to a single strip of an open propeller at (a) take-off and (b) cruise conditions, (c) a model cooling fan and (d) a wind turbine.

5.4.2 Discussion of the validity of Amiet's model

Despite the important theoretical differences presented in section 5.3, the approximations made in Amiet's model for the noise due to a rotating blade section seem to impact very little on the noise predictions over the audible frequency range. For the configurations studied, both models provide predictions of PWL and directivity which differ by less than 0.5dB and 1dB, respectively. It has been shown that the error of Amiet's model can become significant, but the frequencies at which this occurs are generally either too low or too high to be of significance in evaluating subjective indicators of noise, such as EPNLdB. Thus, the study presented in this chapter formally establishes the validity of Amiet's assumption [10] that, over most of the audible frequency range, the effects of rotation on rotor broadband noise can be included by means of averaging over the angular position of a locally translating airfoil, as shown in Fig. 5.1.

As mentioned in Section 5.1, the difference in computational time between the two models compared in this study is not significant, since the analytical isolated flat-plate response

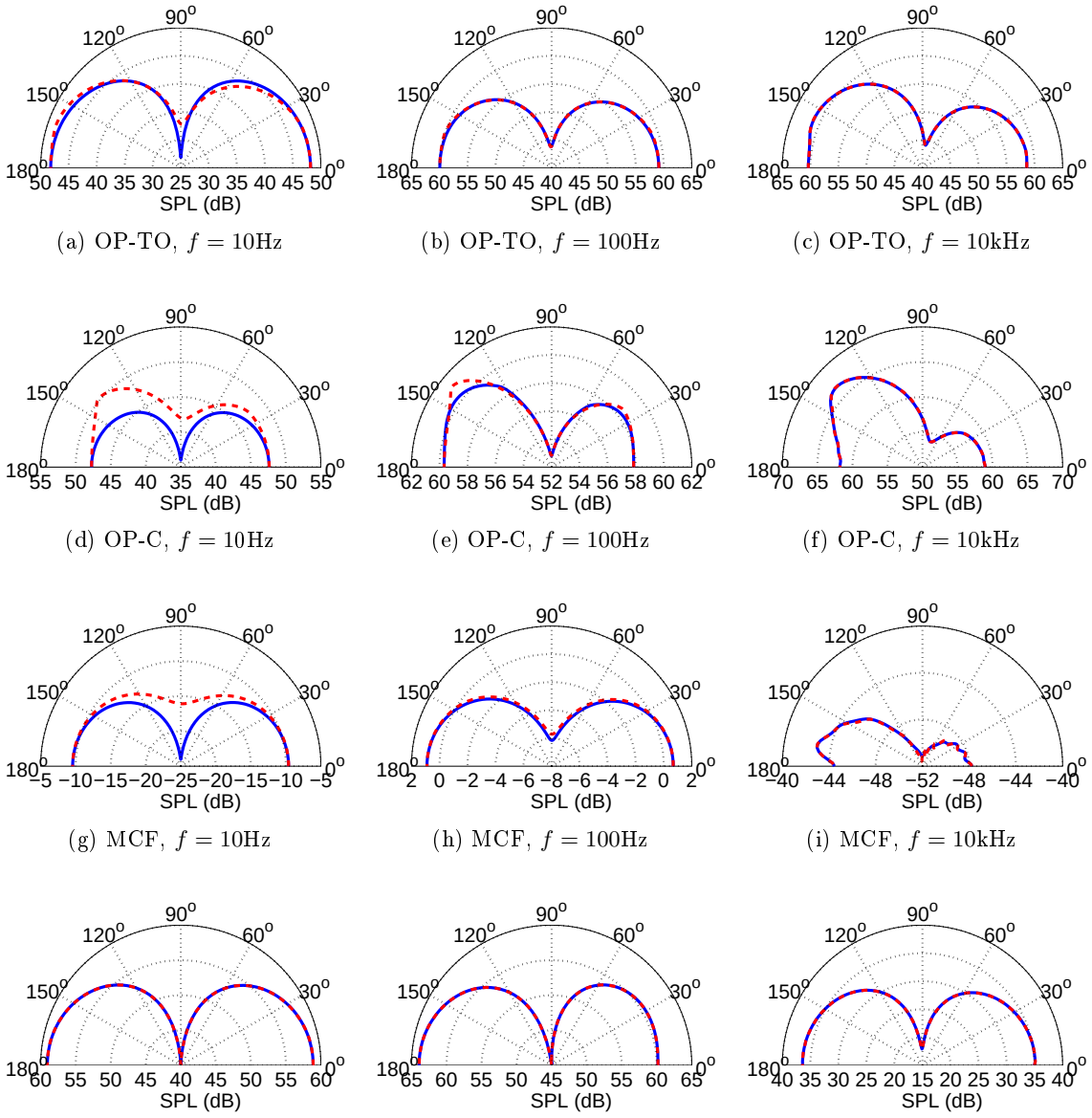

(a) OP-TO, $f = 10$Hz (b) OP-TO, $f = 100$Hz (c) OP-TO, $f = 10$kHz

(d) OP-C, $f = 10$Hz (e) OP-C, $f = 100$Hz (f) OP-C, $f = 10$kHz

(g) MCF, $f = 10$Hz (h) MCF, $f = 100$Hz (i) MCF, $f = 10$kHz

(j) WT, $f = 10$Hz (k) WT, $f = 100$Hz (l) WT, $f = 10$kHz

Figure 5.7: Directivity of SPL (at 1m) predicted by Amiet's model (−−) and the exact model (−), for the Open Propeller at (a-c) take-off (OP-TO) and (d-f) cruise (OP-C), (g-i) the Model Cooling Fan (MCF) and (j-l) the Wind Turbine (WT), at $f = 10$Hz, $f = 100$Hz and $f = 10$kHz.

functions used in this chapter (Eq. 3.19) are fast to compute. However, Amiet's approach for deducing the noise of rotating airfoils from translating airfoils noise models may save significant computational time if more complex models are used for the blade response functions, than the comparatively simple models investigated here. The very good agreement observed in this study between the approximate model and the exact model indicate that applications of Amiet's model to response models such as, for instance, CFD-based models that can take into account realistic airfoil geometries (see for instance Sandberg and Sandham [136]), may be feasible and should be investigated in subsequent work.

Chapter 6

Comparison of sound power from isolated airfoils and cascades

6.1 Introduction

The accurate modelling of the broadband noise due to the interaction between turbulent flow and a cascade of airfoils is of interest in a number of aerospace applications, such as the prediction of open rotors BRWI noise (see Chapter 2) but also the prediction of rotor/stator interaction broadband noise in turbofans. An approach commonly taken to predict the latter has been to calculate the acoustic response due to an impinging single wavenumber vortical gust in the form of upstream and downstream propagating acoustic modes that are generated in the gap between adjacent blades, and to simulate the turbulent wake by Fourier synthesis. The solution to this problem for a high wavenumber gust is generally formulated in terms of an integral equation, which can be solved either numerically using the co-location technique (see Smith [143] and Whitehead [149]), or analytically by the use of the Wiener-Hopf procedure (see Peake [126] and Glegg [72], for example). In both cases, the solution can be time consuming, particularly for broadband calculations in which, at each frequency, the radiation is synthesised from a broad continuum of turbulence wavenumber components.

To overcome the computational overhead and the complexity associated with the use of the cascade response function, the blade response is often computed using isolated airfoil theory (see, for example, Chapter 2 for BRWI noise in CRORs and de Gouville et al. [49] for turbofan noise) in which the acoustic interaction between adjacent blades is neglected (see Fig. 6.1). The blade response in this case is much simpler and faster to compute than using the cascade approach. However, little work has been undertaken on quantifying the validity of this isolated airfoil approximation in the context of turbulence-multiblade interaction problems.

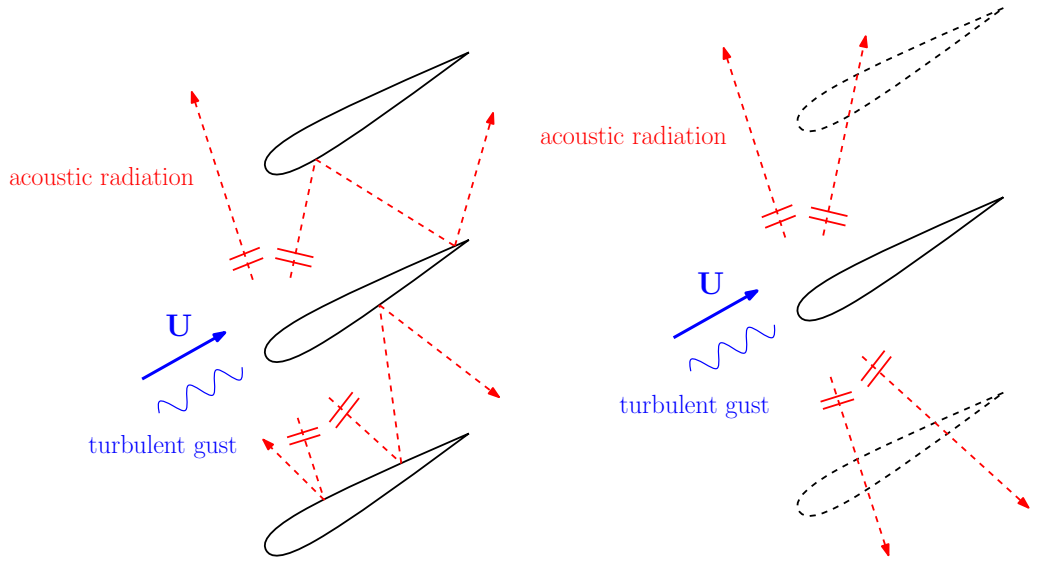

(a) Cascade model (b) Isolated airfoil model

Figure 6.1: Schematic representation of (a) a cascade model and (b) an isolated airfoil model

The aim of this chapter is to validate the use of isolated airfoil theory for the prediction of CROR interaction noise by comparison of an isolated airfoil model and a cascade model for sound power radiation. An analytical model is presented for the sound power radiation (per unit span) due to an isolated flat plate airfoil in a 2D isotropic, homogeneous, turbulent flow at zero angle of attack. The upstream and downstream sound powers, with respect to the fan axis, are computed for arbitrary stagger angle to allow comparisons with the sound power radiated from a cascade of flat plate airfoils interacting with the same 2D turbulent flow. Asymptotic solutions are given for the upstream and downstream sound power that are valid in the high and low frequency limits, for arbitrary Mach number and stagger angle. The isolated airfoil calculation is shown to be in excellent agreement (less than 1dB) with the cascade calculation at frequencies greater than the critical frequency identified by Cheong et al. [45]. At frequencies below the critical frequency, agreement will be shown to be poor for cascades with high solidity (which are typical of turbofan stator vanes) but reasonable for cascades with low solidity, which are typical of open rotors.

Note that the restriction of the analysis to 2D turbulent gusts and the subsequent use of 2D blade response functions incurs no loss of generality as it is well known that the 3D problem can be formulated as a special case of the 2D formulation depending upon whether the gust is sub-critical or super-critical (see, for example, Section 2.6.2 for single airfoils and Lloyd and Peake [105] for cascades).

The problem of predicting the sound pressure radiated by isolated airfoils in a turbulent stream has been addressed by many authors since the classical work of Amiet [6] in the 1970s. However, there is little work focused on the behavior of *sound power* radiation from single airfoils in turbulent flows. To the author's knowledge, only Atassi et al. [16] have

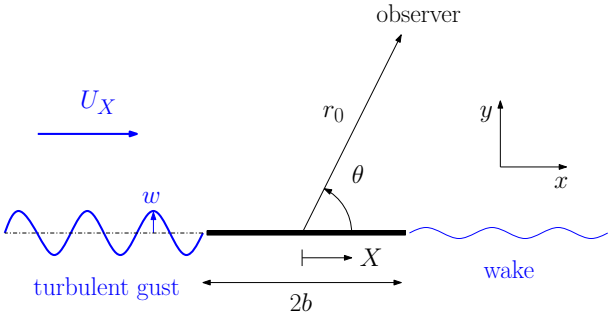

Figure 6.2: Configuration of the problem of turbulence-flat plate interaction noise.

addressed this problem by deriving an expression for the sound power of the broadband noise radiated from an isolated airfoil in a turbulent stream in which the unsteady pressure jump across a flat plate airfoil was computed using a linearised Euler solver. Atassi et al. studied the effects of frequency and Mach number on the directivity of the acoustic pressure and intensity. The validity of the approximation of compact source for the total sound power was also investigated. New results for the sound power radiation are presented in the current chapter by using analytical expressions for the unsteady pressure jump across the flat plate airfoil (described in Section 2.6), by considering the effects of stagger angle on the sound power radiated upstream and downstream relative to a hypothetical fan axis and by deriving closed-form asymptotic expressions for the upstream and downstream sound powers that are valid in the limit of low and high reduced frequency.

6.2 Pressure spectral density due to a flat plate in a 2D turbulent flow

This section presents an expression for the pressure PSD of the broadband noise due a flat plate airfoil of infinite span in a 2D turbulent flow, based on the classical approach of Amiet [6]. First, the homogeneous and isotropic turbulent velocity field is assumed to be a 'frozen' velocity pattern as it passes the leading edge of the flat plate. The upwash turbulent velocity can, therefore, be expressed in the reference frame moving with the gust as

$$w\left(X,t\right)=\frac{1}{2\pi}\int_{-\infty}^{\infty}\mathcal{W}\left(k_X\right)e^{-ik_X\left(X-U_Xt\right)}dk_X, \tag{6.1}$$

where $\mathcal{W}$ is the upwash velocity in the wavenumber domain and is defined in a frame moving with the base flow as

$$\mathcal{W}\left(k_X\right)=\int_{-\infty}^{\infty}\tilde{w}\left(X\right)e^{ik_XX}dX, \tag{6.2}$$

where $\tilde{w}\left(X-U_Xt\right)=w\left(X,t\right)$.

For a single harmonic vortical gust, with upwash velocity of the form $w_0 e^{-ik_X(X-U_X t)}$, the pressure jump Δp is given by (Ref. [6])

$$\Delta p\left(X,t\right) = 2\pi\rho_0 U_X w_0 g^{\mathrm{LE}}\left(X,k_X,M_X\right) e^{ik_X U_X t}, \tag{6.3}$$

where $M_X = U_X/c_0$ and $g^{\mathrm{LE}}\left(X,k_X,M_X\right)$ is the non-dimensional transfer function between the turbulent upwash velocity and the pressure jump across the flat plate airfoil. In this study, the flat plate response functions g^{LE} derived by Amiet [7, 5] are used following the same approach as in Section 2.6, but the spanwise wavenumber k_r is set equal to zero in order to consider a gust at normal incidence. The final expression of the unsteady pressure jump, in the time domain, is obtained by combining Eqs. 6.1 and 6.3 as

$$\Delta p\left(X,t\right) = \rho_0 U_X \int_{-\infty}^{\infty} \mathcal{W}\left(k_X\right) g^{\mathrm{LE}}\left(X,k_X,M_X\right) e^{ik_X U_X t} dk_X. \tag{6.4}$$

The unsteady pressure jump in the frequency domain can be deduced by Fourier transform of Eq. 6.4 with respect to t, to give

$$\begin{aligned}\Delta\hat{p}\left(X,\omega\right) &= \int_{-\infty}^{\infty} \Delta p\left(X,t\right) e^{-i\omega t} dt, \\ &= 2\pi\rho_0 \mathcal{W}\left(K_X\right) g^{\mathrm{LE}}\left(X,K_X,M_X\right),\end{aligned} \tag{6.5}$$

where $K_X = \omega/U_X$.

By use of the Kirchhoff-Helmholtz integral theorem and considering that the surface of the flat plate is rigid, the radiated acoustic pressure due to the unsteady pressure jump Δp is given by

$$p\left(x,y,t\right) = \frac{-1}{2\pi} \int_{-\infty}^{\infty}\int_{-b}^{b} \Delta\hat{p}\left(X,\omega\right) \frac{\partial G}{\partial y}\left(x,y,X,\omega\right) e^{i\omega t} dX d\omega., \tag{6.6}$$

where the $G\left(x,y,X,\omega\right)$ is the 2D time harmonic Green's function, with effects of mean flow included, given by

$$G\left(x,y,X,\omega\right) = \frac{-i}{4\beta_X} H_0^{(2)}\left(\frac{k_0}{\beta_X^2}\sqrt{\left(x-X\right)^2 + \beta_X^2 y^2}\right) e^{ik_0 M_X (x-X)/\beta_X^2}, \tag{6.7}$$

and where $k_0 = \omega/c_0$, $\beta_X = \sqrt{1-M_X^2}$ and $H_0^{(2)}$ is the Hankel function of the second kind and of order 0. The derivative of Eq. 6.7 with respect to y is given by

$$\frac{\partial G}{\partial y}\left(x,y,X,\omega\right) = \frac{iy e^{ik_0 M_X (x-X)/\beta_X^2}}{4\beta_X\sqrt{\left(x-X\right)^2 + \beta_X^2 y^2}} H_1^{(2)}\left(\frac{k_0}{\beta_X^2}\sqrt{\left(x-X\right)^2 + \beta_X^2 y^2}\right). \tag{6.8}$$

Assuming that the observer is in the far-field, the Hankel function $H_1^{(2)}$ and the flow-corrected distance between source and observer $(x-X)^2+\beta_X^2 y^2$ can be approximated, respectively, as

$$H_1^{(2)}(\zeta) \approx \sqrt{\frac{2}{\pi\zeta}} e^{-i\zeta+i3\pi/4}, \tag{6.9}$$

$$(x-X)^2+\beta_X^2 y^2 \approx \sigma - \frac{Xx}{\sigma}, \tag{6.10}$$

where $\sigma = \sqrt{x^2+\beta_X^2 y^2}$. Considering that the second term of Eq. 6.10 can be neglected in amplitude terms, substituting Eqs. 6.9 and 6.10 into Eq. 6.8 leads to the far-field approximation

$$\frac{\partial G}{\partial y}(x,y,X,\omega) \approx \frac{iy}{4}\sqrt{\frac{2k_0}{\pi\sigma^3}} e^{-i\frac{k_0}{\beta_X^2}[\sigma - Xx/\sigma - M_X(x-X)]+i\frac{3\pi}{4}}. \tag{6.11}$$

The PSD of the acoustic pressure is defined by

$$S_{pp}(x,y,\omega) = \int_{-\infty}^{\infty} \langle p^*(x,y,t)\, p(x,y,t+\tau)\rangle\, e^{-i\omega\tau} d\tau, \tag{6.12}$$

where the brackets $\langle . \rangle$ represent the ensemble average.

Substituting Eq. 6.6 into 6.12 yields after some algebra

$$\begin{aligned} S_{pp}(x,y,\omega) = \frac{1}{2\pi}\int_{-\infty}^{\infty}\int_{-b}^{b} & S_{QQ}(X_1,X_2,\omega_1,\omega_2)\, e^{i(\omega_1-\omega_2)t}\delta(\omega-\omega_2) \\ & \times \frac{\partial G^*}{\partial y}(x,y,X_1,\omega_1)\frac{\partial G}{\partial y}(x,y,X_2,\omega_2)\, dX_1 dX_2 d\omega_1 d\omega_2, \end{aligned} \tag{6.13}$$

where S_{QQ} is the cross-spectrum of the unsteady pressure jump between two points X_1 and X_2 along the chord of the flat plate, at frequencies ω_1 and ω_2, and is written as

$$\begin{aligned} S_{QQ}(X_1,X_2,\omega_1,\omega_2) &= \langle \Delta\hat{p}^*(X_1,\omega_1)\, \Delta\hat{p}(X_2,\omega_2)\rangle, \\ &= (2\pi\rho_0)^2 g^{\mathrm{LE}*}(X_1,K_{X1},M)\, g^{\mathrm{LE}}(X_2,K_{X2},M)\, \langle \mathcal{W}^*(K_{X1})\, \mathcal{W}(K_{X2})\rangle, \end{aligned} \tag{6.14}$$

where $K_{X1} = \omega_1/U$ and $K_{X2} = \omega_2/U$.

Assuming homogeneous turbulence, setting $X_2 - X_1 = \delta X$ and using the definition of the upwash velocity wavenumber spectrum (Eq. 6.2), the turbulence velocity cross-spectrum can be written as

$$\begin{aligned} \langle \mathcal{W}^*(K_{X1})\, \mathcal{W}(K_{X2})\rangle &= 2\pi\delta(K_{X1}-K_{X2}) \int_{-\infty}^{\infty} \langle w(X_1)\, w(X_1+\delta X)\rangle\, e^{iK_{X2}\delta X} d\delta X, \\ &= 2\pi\delta(K_{X1}-K_{X2})\, \Phi_{ww}(K_{X2}). \end{aligned} \tag{6.15}$$

The term $\Phi_{ww}(k_X)$ in Eq. 6.15 is the 1D velocity spectrum of the turbulent upwash velocity, for which the Liepmann model is used for consistency with the model of Cheong et al. [45], against which the current model is compared in Section 6.6. The 2D Liepmann turbulence velocity spectrum is given in Ref. [45] by

$$\Phi_{ww}(k_X, k_Y) = \frac{\overline{w^2}L^2}{4\pi} \frac{1 + L^2\left(4k_X^2 + k_Y^2\right)}{\left(1 + L^2\left(k_X^2 + k_Y^2\right)\right)^{5/2}}, \tag{6.16}$$

where k_Y is the wavenumber component of the turbulence in the direction normal to the chord of the flat plate, $\overline{w^2}$ is the mean square turbulent upwash velocity and L is the turbulence integral lengthscale. The 1D velocity spectrum, used in Eq. 6.15, is obtained by integrating Eq. 6.16 over all k_Y values, to give

$$\Phi_{ww}(k_X) = \frac{\overline{w^2}L}{2\pi} \frac{1 + 3k_X^2L^2}{\left(1 + k_X^2L^2\right)^2}. \tag{6.17}$$

The final expression for the PSD of the acoustic pressure radiated to the far-field is obtained by substituting Eqs. 6.11, 6.14 and 6.15 into Eq. 6.13. In polar coordinates (r_0, θ), this expression is given by

$$S_{pp}(r_0, \theta, \omega) = \frac{\pi\rho_0^2 b^2 \sin^2\theta U_X k_0}{2r_0 A(\theta, M)^3} \Phi_{ww}(K_X) \left|\mathcal{L}^{\mathrm{LE}}(\theta, K_X)\right|^2, \tag{6.18}$$

where the notation $A(\theta, M_X) = \sqrt{1 - M_X^2 \sin^2\theta}$ has been introduced for the sake of brevity. The unsteady loading term $\mathcal{L}^{\mathrm{LE}}$ is given by

$$\mathcal{L}^{\mathrm{LE}}(\theta, K_X, \kappa) = \frac{1}{b} \int_{-b}^{b} g^{\mathrm{LE}}(X, K_X, M_X)\, e^{i\kappa(X+b)} dX, \tag{6.19}$$

where κ is the aeroacoustic coupling wavenumber given by

$$\kappa = \frac{k_0}{\beta_X^2} \left(\frac{\cos\theta}{A(\theta, M_X)} - M_X \right). \tag{6.20}$$

The chordwise integral in Eq. 6.19 can be derived analytically, as presented in Section 2.6, and two different expressions are obtained depending on the value of the acoustic reduced frequency $\mu_a = \frac{\omega b}{c_0 \beta_X^2}$ by setting $k_r = 0$ and substituting Eq. 6.20 into Eqs. 2.92 to 2.95. If $\mu_a < \pi/4$, the flat plate response function introduced in Ref. [5] is used and Eq. 6.19 becomes

$$\mathcal{L}^{\mathrm{LE}}_{low}(\theta, K_X, \kappa) = \frac{S(\mu_h)}{\beta_X} e^{i\mu_h f(M_X)} \left\{ J_0\left(\mu_a \frac{\cos\theta}{A(\theta, M_X)}\right) - iJ_1\left(\mu_a \frac{\cos\theta}{A(\theta, M_X)}\right) \right\}, \tag{6.21}$$

where $f(M_X) = (1 - \beta_X)\ln M_X + \beta_X \ln(1 + \beta_X) - \ln(2)$, J_0 and J_1 are Bessel functions of the first kind and S is the well known Sears [140] function (see Eq. 2.80), which is expressed as a function of the chord-based hydrodynamic reduced frequency $\mu_h = \frac{\omega b}{U_X \beta_X^2} = \frac{\mu_a}{M_X}$.

If $\mu_a > \pi/4$, the high frequency response function due to Amiet [7] is used and Eq. 6.19 becomes

$$\mathcal{L}^{\mathrm{LE}}_{high}\left(\theta, K_X, \kappa\right) = \mathcal{L}_1\left(\theta, K_X, \kappa\right) + \mathcal{L}_2\left(\theta, K_X, \kappa\right), \tag{6.22}$$

where the functions $\mathcal{L}_1$ and $\mathcal{L}_2$ represent the leading edge scattering and the trailing edge back-scattering of the sound, respectively, and are given by

$$\mathcal{L}_1\left(\theta, K_X, \kappa\right) = \frac{\sqrt{2}}{\pi\beta_X\sqrt{\mu_h\left(1+M_X\right)\Theta_1}} E^*\left(2\Theta_1\right) e^{i\Theta_2}, \tag{6.23}$$

$$\begin{aligned}\mathcal{L}_2\left(\theta, K_X, \kappa\right) = \frac{e^{i\Theta_2}}{\pi\Theta_1\beta_X\sqrt{2\pi\mu_h\left(1+M_X\right)}} \Big[& i\left(1-e^{-i2\Theta_1}\right) + (1-i) \\ & \times \left[E^*\left(4\mu_a\beta_X^2\right) - \sqrt{\frac{2}{1+\frac{\cos\theta}{A(\theta,M_X)}}} e^{-i2\Theta_1} E^*\left(2\Theta_3\right)\right]\Big],\end{aligned} \tag{6.24}$$

and where the following notation has been introduced for the sake of brevity

$$\Theta_1 = \mu_a\left(1 - \frac{\cos\theta}{A\left(\theta, M_X\right)}\right), \tag{6.25}$$

$$\Theta_2 = \beta_X^2\mu_h + \mu_a\left(M_X - \frac{\cos\theta}{A\left(\theta, M_X\right)}\right) - \frac{\pi}{4}, \tag{6.26}$$

$$\Theta_3 = \mu_a\left(1 + \frac{\cos\theta}{A\left(\theta, M_X\right)}\right). \tag{6.27}$$

The above solution for $\mathcal{L}^{\mathrm{LE}}$ assumes that the low and high frequency solutions are continuous at $\mu_a = \pi/4$. However, large differences in values have been observed at this frequency, especially for small observer angle θ. As explained in Appendix E, this issue has been resolved in this chapter by splitting the solution for $\mathcal{L}^{\mathrm{LE}}$ into the three frequency regimes:

$$\mathcal{L}^{\mathrm{LE}}_{low} \qquad \text{for } \mu_a < \frac{\pi}{4}, \tag{6.28}$$

$$\mathcal{L}^{\mathrm{LE}}_{high} \approx \mathcal{L}_1 \qquad \text{for } \frac{\pi}{4} < \mu_a < \frac{\pi}{4\left(1-\frac{\cos\theta}{A(\theta,M)}\right)}, \tag{6.29}$$

$$\mathcal{L}^{\mathrm{LE}}_{high} \approx \mathcal{L}_1 + \mathcal{L}_2 \qquad \text{for } \mu_a > \frac{\pi}{4\left(1-\frac{\cos\theta}{A(\theta,M)}\right)}. \tag{6.30}$$

6.3 Analytical formulation for sound power

In the prediction of fan broadband noise from aircraft engines, it is generally of interest to predict separately the sound power radiated upstream $\mathcal{P}^+$ and downstream $\mathcal{P}^-$ of the engine axis. In this section, an analytical expression is derived for the total sound power

$\mathcal{P} = \mathcal{P}^+ + \mathcal{P}^-$, from which the expressions for the sound power radiated upstream and downstream of the fan axis are deduced.

The general definition of the time averaged acoustic intensity vector $\bar{\mathbf{I}}$ in an isentropic potential flow with uniform velocity is given by (Morfey [113])

$$\bar{\mathbf{I}} = \overline{p\mathbf{u}} + \frac{\mathbf{M}}{\rho_0 c_0}\overline{p^2} + \mathbf{M}\overline{p\,(\mathbf{u}.\mathbf{M})} + \rho_0 c_0 \overline{\mathbf{u}\,(\mathbf{u}.\mathbf{M})}, \tag{6.31}$$

where $\mathbf{M} = \mathbf{U}/c_0$ is the Mach number vector of the mean flow, p is the instantaneous acoustic pressure, $\mathbf{u}$ is the instantaneous acoustic particle velocity vector and the upper bar denotes the time average.

The sound intensity $\overline{I_r}$ in the direction of the observer from the infinite span airfoil at a single frequency ω, can be deduced from Eq. 6.31 as

$$\overline{I_r}\,(r_0,\theta,\omega) = \frac{1}{2}\mathrm{Re}\left\{\hat{p}\hat{u}_r^* + \frac{M\cos\theta}{\rho_0 c_0}\,|\hat{p}|^2 + M^2\cos\theta\hat{p}\hat{u}_x^* + M\rho_0 c_0 \hat{u}_r\hat{u}_x^*\right\}, \tag{6.32}$$

where $\hat{u}_r$ and $\hat{u}_x$ are the frequency domain components of the acoustic particle velocity in the radial and streamwise directions, respectively. The coordinate dependence (r_0,θ,ω) has been omitted in the right hand side of Eq. 6.32 for the sake of brevity.

The acoustic particle velocities $\hat{u}_r$ and $\hat{u}_x$ can be expressed as a function of the acoustic pressure $\hat{p}$ by, first, considering the velocity potential defined as

$$p\,(r_0,\theta,t) = -\rho_0\left(\frac{\partial}{\partial t} + U_X\frac{\partial}{\partial x}\right)\Phi\,(r_0,\theta,t)\,, \tag{6.33}$$

which gives at a single frequency

$$\hat{p}\,(r_0,\theta,\omega) = -i\rho_0 c_0\left(k_0 - iM_X\frac{\partial}{\partial x}\right)\Phi\,(r_0,\theta,\omega)\,. \tag{6.34}$$

Equation 6.34 can be rewritten by use of the chain rule ($\frac{\partial\Phi}{\partial x} = \frac{\partial\Phi}{\partial r_0}\frac{\partial r_0}{\partial x} + \frac{\partial\Phi}{\partial\theta}\frac{\partial\theta}{\partial x}$), and after some algebra, as

$$\hat{p}\,(r_0,\theta,\omega) = -i\rho_0 c_0 k_0\frac{A\,(\theta,M_X) - M_X\cos\theta}{\beta_X^2 A\,(\theta,M_X)}\Phi\,(r_0,\theta,\omega)\,. \tag{6.35}$$

The acoustic particle velocity in the radial and polar directions can be obtained from Φ by

$$\hat{u}_r\,(r_0,\theta,\omega) = \frac{\partial\Phi\,(r_0,\theta,\omega)}{\partial r_0}, \tag{6.36}$$

$$\hat{u}_\theta\,(r_0,\theta,\omega) = \frac{1}{r_0}\frac{\partial\Phi\,(r_0,\theta,\omega)}{\partial\theta}, \tag{6.37}$$

from which the acoustic particle velocity in the axial direction is given by

$$\hat{u}_x\,(r_0,\theta,\omega) = \hat{u}_r\,(r_0,\theta,\omega)\cos\theta - \hat{u}_\theta\,(r_0,\theta,\omega)\sin\theta. \tag{6.38}$$

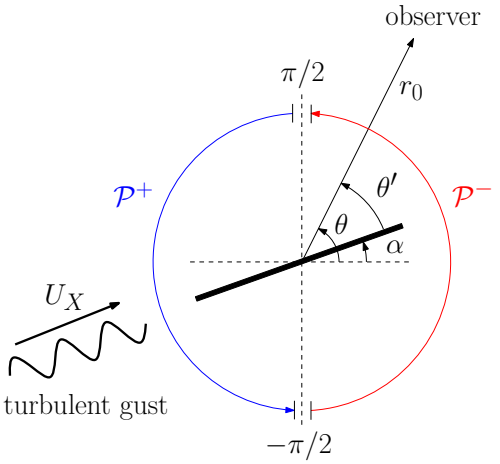

Figure 6.3: Configuration for the upstream and downstream power due to an isolated airfoil with stagger angle α.

Substituting Eq. 6.35 into Eqs. 6.36 to 6.38 and considering only the solutions of order $O\left(1/r_0\right)$ yields the direct relations between acoustic particle velocities and pressure

$$\hat{u}_r\left(r_0,\theta,\omega\right) = A\left(\theta,M_X\right)\frac{\hat{p}\left(r_0,\theta,\omega\right)}{\rho_0 c_0}, \tag{6.39}$$

$$\hat{u}_x\left(r_0,\theta,\omega\right) = \left(A\left(\theta,M_X\right)\cos\theta - M_X\sin^2\theta\right)\frac{\hat{p}\left(r_0,\theta,\omega\right)}{\rho_0 c_0}. \tag{6.40}$$

The single frequency expression for the time averaged sound intensity in the direction of the observer is then obtained by substituting Eq. 6.39 and Eq. 6.40 into 6.32 to give

$$\overline{I_r}\left(r_0,\theta,\omega\right) = \frac{\left|\hat{p}\left(r_0,\theta,\omega\right)\right|^2}{2\rho_0 c_0}F\left(\theta,M_X\right), \tag{6.41}$$

where the function $F\left(\theta,M_X\right)$ is the non-dimensional power factor given by

$$F\left(\theta,M_X\right) = \frac{\beta_X^4 A\left(\theta,M_X\right)}{\left(A\left(\theta,M_X\right) - M_X\cos\theta\right)^2}. \tag{6.42}$$

Note that, in the limit of vanishing Mach number M_X, $F \to 1$ and Eq. 6.32 reduces to the classical expression for the far-field intensity in a quiescent medium.

For continuous spectra, the pressure spectral density $S_{pp}\left(r_0,\theta,\omega\right)$ replaces $\left|\hat{p}\left(r_0,\theta,\omega\right)\right|^2$ in Eq. 6.41. The total sound power per unit span from the infinite-span flat plate is obtained by integrating Eq. 6.41 over the surface of a cylinder of unit height centred on $\left(r_0,\theta\right) = \left(0,0\right)$,

$$\mathcal{P}\left(\omega\right) = \frac{r_0}{2\rho_0 c_0}\int_0^{2\pi} S_{pp}\left(r_0,\theta,\omega\right)F\left(\theta,M_X\right)d\theta. \tag{6.43}$$

Substituting Eq. 6.18 into 6.43 yields the final expression for the total sound power spectrum per unit span as

$$\mathcal{P}(\omega) = \frac{\pi}{4}\beta_X^4 M_X k_0 \rho_0 b^2 \Phi_{ww}(K_X) \int_0^{2\pi} \frac{\left|\mathcal{L}^{\mathrm{LE}}(\theta, K_X)\right|^2 \sin^2\theta}{A(\theta, M_X)^2 \left(A(\theta, M_X) - M_X \cos\theta\right)^2} d\theta. \tag{6.44}$$

One of the objectives of the current study is to predict separately the sound power radiated upstream and downstream of the (hypothetical) fan axis, denoted respectively by $\mathcal{P}^+$ and $\mathcal{P}^-$, so that the current isolated airfoil model can be compared to the 2D cascade noise model due to Cheong et al. [45]. However, unlike the total sound power radiation $\mathcal{P}$, the sound power components $\mathcal{P}^+$ and $\mathcal{P}^-$ are sensitive to variations in stagger angle α. Equation 6.44 can be decomposed into power components $\mathcal{P}^+$ and $\mathcal{P}^-$, that include the effects of stagger angle α, by introducing the change of variable $\theta' = \theta - \alpha$ and then integrating over the front and rear arcs respectively, as shown in Fig. 6.3, to give

$$\mathcal{P}^{\pm}(\omega) = \frac{\pi}{4}\beta_X^4 M_X k_0 \rho_0 b^2 \Phi_{ww}(K_X) \int_{\mp\pi/2}^{\pm\pi/2} \frac{\left|\mathcal{L}^{\mathrm{LE}}(\theta', K_X)\right|^2 \sin^2\theta'}{A(\theta', M_X)^2 \left(A(\theta', M_X) - M_X \cos\theta'\right)^2} d\theta. \tag{6.45}$$

The total sound power level in dB due to a flat plate of span Δr, as a one-sided function of angular frequency, can therefore be computed as

$$\mathrm{PWL}^{\pm}(\omega) = 10\log_{10}\left(\frac{2\mathcal{P}^{\pm}(\omega)\,\Delta r}{10^{-12}}\right), \tag{6.46}$$

where a factor of 2 is introduced to take into account the negative frequencies.

6.4 High and low frequency asymptotic expressions for sound power

In this section, asymptotic expressions for the upstream, downstream and total sound power are derived from Eq. 6.45 in the limits of low and high frequency. We start by noting that the blade loading term $\left|\mathcal{L}^{\mathrm{LE}}\right|^2$ (Eqs. 2.92 and 2.93) exhibits the following asymptotic behaviour in the limits of low and high acoustic reduced frequency μ_a,

$$\lim_{\mu_a \to 0} \left|\mathcal{L}^{\mathrm{LE}}\right|^2 = \frac{1}{\beta_X^2} \left|S(\mu_h)\right|^2, \tag{6.47}$$

$$\lim_{\mu_a \to \infty} \left|\mathcal{L}^{\mathrm{LE}}\right|^2 = \frac{1}{\beta_X^2 \pi^2 \mu_h \mu_a (1 + M_X)\left(1 - \frac{\cos\theta}{A(\theta, M_X)}\right)}. \tag{6.48}$$

Note that Eq. 6.48 is only valid for $\theta \neq 0°$.

From the definition of the Sears function (Eq. 2.80), we have $\lim_{\mu_h \to 0} S(\mu_h) = 1$. Noting that $\mu_a < \mu_h$, for any $M_X < 1$, and substituting Eqs. 6.47 and 6.48 into 6.45 yields

$$\lim_{\mu_h \to 0} \mathcal{P}^{\pm} = \frac{\pi}{4} \beta_X^2 M_X \rho_0 k_0 b^2 \Phi_{ww}(K_X) \oint_{\pm\pi/2}^{\mp\pi/2} d_{low}(\theta', M_X)\, d\theta, \tag{6.49}$$

$$\lim_{\mu_a \to \infty} \mathcal{P}^{\pm} = \frac{\beta_X^6 M_X \rho_0}{4\pi K_X} \Phi_{ww}(K_X) \oint_{\pm\pi/2}^{\mp\pi/2} d_{high}(\theta', M_X)\, d\theta, \tag{6.50}$$

where

$$d_{low}(\theta, M_X) = \frac{\sin^2\theta}{A^2 (A - M_X \cos\theta)^2}, \tag{6.51}$$

$$d_{high}(\theta, M_X) = \frac{\sin^2\theta}{A^2 (A - M_X \cos\theta)^2 (1 + M_X)\left(1 - \frac{\cos\theta}{A}\right)}, \tag{6.52}$$

and where $A(\theta, M_X)$ has been abbreviated to A for the sake of brevity.

The functions d_{low} and d_{high} represent the directivity of the acoustic intensity in the low and high reduced frequency limits, respectively. These functions tend in the low Mach number limit to

$$\lim_{M_X \to 0} d_{low} = \sin^2\theta, \tag{6.53}$$

$$\lim_{M_X \to 0} d_{high} = \sin^2\frac{\theta}{2}, \tag{6.54}$$

which recovers classical results (see, for example, Paterson and Amiet [123]). Substituting Eqs. 6.51 and 6.52 into Eqs. 6.49 and 6.50, the integrals over d_{low} and d_{high} can be computed analytically to give the final asymptotic expressions for the upstream and downstream power at low and high reduced frequency:

$$\lim_{\mu_h \to 0} \mathcal{P}^{\pm} = \frac{\pi \rho_0 k_0 b^2}{2 M_X \beta_X^2} \Phi_{ww}(K_X)\, f_{low}^{\pm}(\alpha, M_X), \tag{6.55}$$

$$\lim_{\mu_a \to \infty} \mathcal{P}^{\pm} = \frac{\rho_0 M_X}{2\pi K_X} \Phi_{ww}(K_X)\, f_{high}^{\pm}(\alpha, M_X), \tag{6.56}$$

where $f_{low}^{\pm}$ and $f_{high}^{\pm}$ are non-dimensional functions given by

$$f_{low}^{\pm}(\alpha, M_X) = \frac{\pi}{2}(1 - \beta_X) \mp \sin^{-1}(M_X \cos\alpha) \pm M_X \cos\alpha \sqrt{1 - M_X^2 \cos^2\alpha}, \tag{6.57}$$

$$f_{high}^{\pm}(\alpha, M_X) = \pi H(\mp 1) \pm \cos^{-1}(M_X \cos\alpha) \mp \cos\alpha \sqrt{1 - M_X^2 \cos^2\alpha}. \tag{6.58}$$

These functions quantify the effects of stagger angle α on $\mathcal{P}^{\pm}$. In equation 6.58, $H(\mp 1)$ is the Heaviside step function of argument ∓ 1, which is thus equal to 0 in the upstream case and 1 in the downstream case.

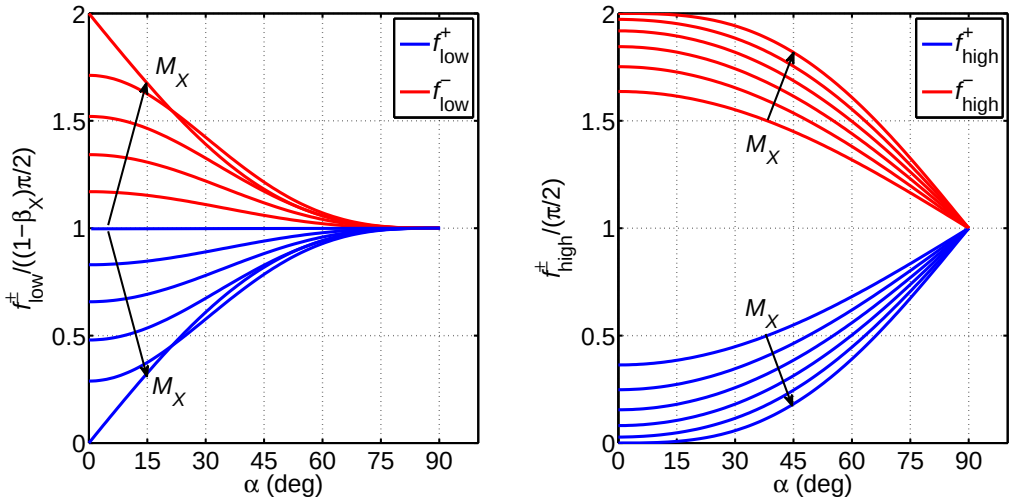

Figure 6.4: Variation of (a) $f^{\pm}_{low}/\left(\frac{\pi}{2}\left(1-\beta_X\right)\right)$ and (b) $f^{\pm}_{high}/\frac{\pi}{2}$ with α, for $M_X = 0$, 0.2, 0.4, 0.6, 0.8 and 1.

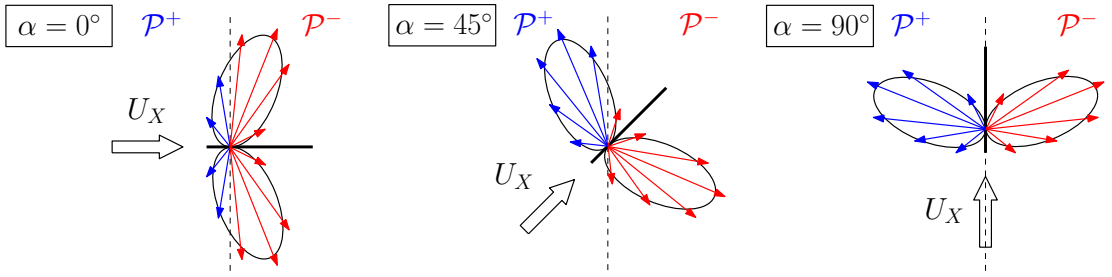

Figure 6.5: Schematic representation of the effects of stagger angle on the upstream and downstream sound power radiated by an isolated flat plate.

Figure 6.4 shows the variation with stagger angle α of the functions $f^{\pm}_{low}$ and $f^{\pm}_{high}$ normalised by their value at $\alpha = 90°$, given by $\left(f^{+}_{low} + f^{-}_{low}\right)/2 = \frac{\pi}{2}\left(1-\beta_X\right)$ and $\left(f^{+}_{high} + f^{-}_{high}\right)/2 = \frac{\pi}{2}$, for a range of Mach numbers between 0 and 1. It appears that the difference between the upstream and downstream expression of $f^{\pm}_{low}$ and $f^{\pm}_{high}$ lessens with α, tending to zero as $\alpha \to 90°$. Figure 6.5 presents a schematic representation of the effects of stagger angle α on $\mathcal{P}^+$ and $\mathcal{P}^-$, which illustrates the behaviour of $f^{\pm}_{low}$ and $f^{\pm}_{high}$ shown in Fig. 6.4. This behaviour is due to the fact that the directivity of the interaction noise is symmetrical with respect to the chord of the flat plate airfoil. Note also that, as expected, all the sound power is predicted by $f^{\pm}_{low}$ and $f^{\pm}_{high}$ to be radiated downstream when $\alpha = 0$ and $M_X = 1$.

Figure 6.6 presents a comparison, for $M_X = 0.2$ and 0.8 and $\alpha = 0°$, 30° and 60°, of the general expression given in Eq. 6.45 for the upstream and downstream sound powers with the asymptotic expressions given in Eqs. 6.55 and 6.56. The input parameters used are the same as in Amiet [6], i.e. an airfoil with a span $\Delta r = 53.34$cm, half-chord $b = 22.86$cm, flow speed $U_X = 31.4\text{m.s}^{-1}$, turbulent integral lengthscale $L = 3.175$cm and turbulent intensity

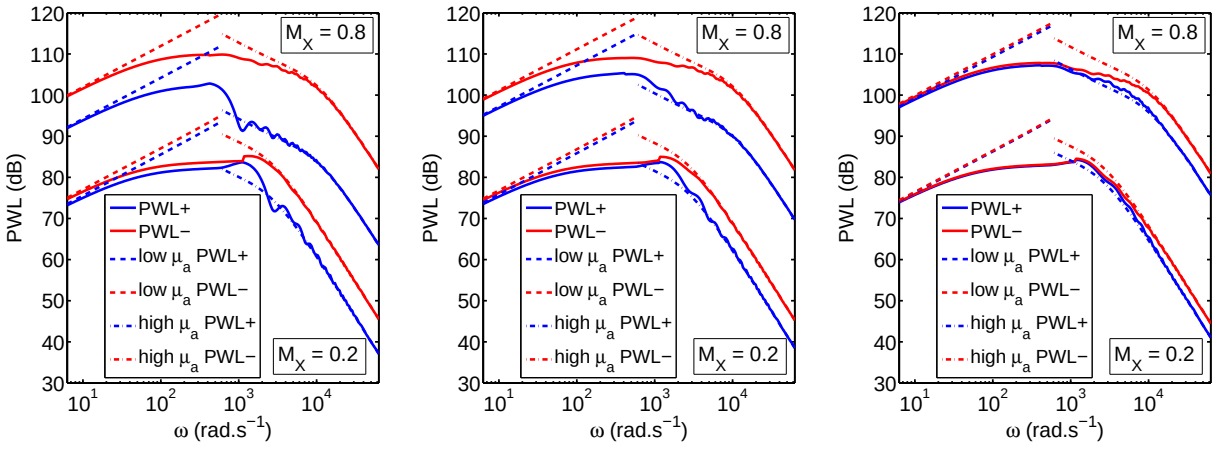

Figure 6.6: Predicted upstream and downstream PWL and low and high frequency asymptotes for $M_X = 0.2$, 0.8 and (a) $\alpha = 0^o$, (b) $\alpha = 30^o$ and (c) $\alpha = 60^o$.

$I_t = \sqrt{\overline{w^2}}/U_X = 4.4\%$. The fluid density and speed of sound are set to $\rho_0 = 1.2\text{kg.m}^{-3}$ and $c_0 = 340\text{m.s}^{-1}$. As expected, the asymptotic expressions for $\mathcal{P}^{\pm}$ agree well with the predictions made using the exact expression of Eq. 6.45 in the low and high frequency limits.

The asymptotic expressions for sound power radiation given in Eqs. 6.55 and 6.56 can be simplified further by using the asymptotic expressions of the 1D Liepmann turbulent velocity spectrum Φ_{ww} (Eq. 6.17) valid in the limits of low and high $k_X L$, given by

$$\lim_{k_X L \to 0} \Phi_{ww}(k_X) = \frac{\overline{w^2} L}{2\pi}, \tag{6.59}$$

$$\lim_{k_X L \to \infty} \Phi_{ww}(k_X) = \frac{\overline{w^2} L}{2\pi} \frac{3}{(k_X L)^2}. \tag{6.60}$$

Substituting Eqs. 6.59 and 6.60 into Eqs. 6.55 and 6.56 yields the following asymptotic expressions for the upstream and downstream sound power:

$$\lim_{(K_X L, \mu_h) \to 0} \mathcal{P}^{\pm} = \frac{\rho_0 c_0^2 k_0 b^2 M_X I_t^2 L}{4\beta_X^2} f_{low}^{\pm}(\alpha, M_X), \tag{6.61}$$

$$\lim_{(K_X L, \mu_a) \to \infty} \mathcal{P}^{\pm} = \frac{3\rho_0 c_0^2 M_X^3 I_t^2}{4\pi^2 L K_X^3} f_{high}^{\pm}(\alpha, M_X). \tag{6.62}$$

The corresponding asymptotic expressions for the *total* sound power $\mathcal{P} = \mathcal{P}^+ + \mathcal{P}^-$ can be obtained from Eqs. 6.61 and 6.62 to give

$$\lim_{(K_X L, \mu_h) \to 0} \mathcal{P} = \frac{\rho_0 c_0^2 k_0 b^2 M_X I_t^2 L \pi (1 - \beta_X)}{4\beta_X^2}, \tag{6.63}$$

$$\lim_{(K_X L, \mu_a) \to \infty} \mathcal{P} = \frac{3\rho_0 c_0^2 M_X^3 I_t^2}{4\pi L K_X^3}. \tag{6.64}$$

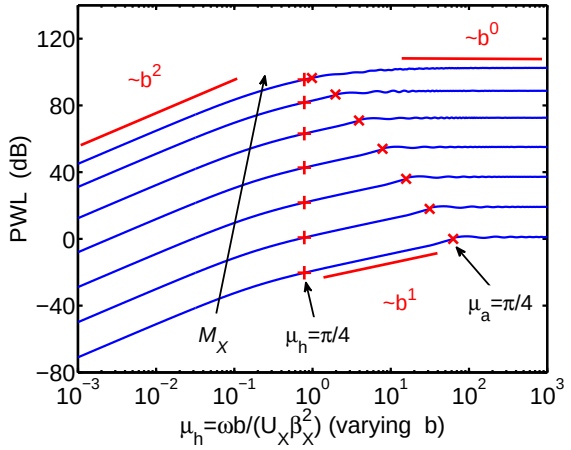

Figure 6.7: Effect of chord length on PWL for $M_X = 0.0125$, 0.025, 0.05, 0.1, 0.2, 0.4 and 0.8. $\mu_h = \frac{\pi}{4}$ is marked by '+' and $\mu_a = \frac{\pi}{4}$ is marked by '×'.

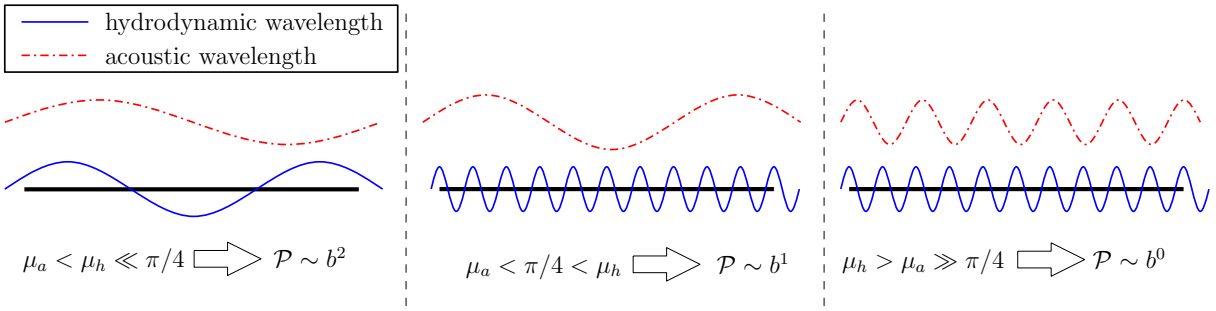

Figure 6.8: Physical representation of the low, medium and high reduced frequency ranges of the effects of chord length.

Equation 6.63 tends in the limit of $M_X \to 0$ to the low Mach number asymptotic expression for sound power derived by Atassi et al. [16] (where ρ_0, b and Φ_{ww} were set equal to unity). However, the present result is more general than the expression of Atassi et al., since it is valid for all $M_X < 1$.

6.5 Effects of chord length on sound power

The effects of chord length on sound power level are controlled only by the term $\mathcal{L}^{\mathrm{LE}}$ (Eq 6.19), which is a function of the acoustic and hydrodynamic reduced frequencies, $\mu_a = \frac{\omega b}{c_0 \beta^2}$ and $\mu_h = \frac{\omega b}{U \beta^2}$. Figure 6.7 presents the variation of PWL with μ_h, by varying b, keeping ω fixed and for a range of Mach numbers. The same input parameters listed in Section 6.4 are used. The scaling of PWL with the (half) chord b is observed to fall into three distinct ranges of reduced frequency μ_h, whose physical meaning is represented in Fig. 6.8 and described below:

1. $(\mu_h, \mu_a) \ll \pi/4$

In this low reduced frequency range, both the wavelength of the vortical gust (i.e. the hydrodynamic wavelength) and the acoustic wavelength are large compared to a quarter of the chord of the flat plate. The noise sources on the flat plate surface can, therefore, be considered as compact dipoles which radiate coherently along the chord, hence the scaling of the power with b^2 observed in Fig. 6.7. This behaviour is proved mathematically in Section 6.4, where the low frequency asymptotic expression of sound power (Eq. 6.63) is shown to scale with b^2.

2. $(\mu_h, \mu_a) \gg \pi/4$

   In this high reduced frequency range, both the hydrodynamic and the acoustic wavelength are small compared to a quarter of the the chord of the flat plate. The response of a flat plate of finite chord can, therefore, be approximated by the response of a semi-infinite flat plate. Thus, the effects of finite chord length are negligible in the limit of high hydrodynamic and acoustic reduced frequencies and PWL is therefore independent of b, as observed in Fig. 6.7. This behaviour is also proved mathematically in Section 6.4, where the high frequency asymptotic expressions of sound power (Eq. 6.64) is shown to be independent of b.

3. $\mu_a < \pi/4 < \mu_h$

   In this reduced frequency sub-range, which becomes increasingly large at low flow speeds, the hydrodynamic wavelength is smaller than a quarter of the chord ($\mu_h > \pi/4$), whereas the acoustic wavelength is larger than a quarter of the chord ($\mu_a < \pi/4$). This phenomenon leads to a scaling of PWL with b^1 only, as shown in Fig. 6.8. This scaling law arises from equations E.1 and E.3 (in Appendix E), which both show that $\left|\mathcal{L}^{\mathrm{LE}}\right|^2 \sim b^{-1}$ in the sub-range $\mu_a < \pi/4 < \mu_h$.

Note that the low and high frequency scaling laws (items 1. and 3. above) of leading edge noise with chord have first been reported by Amiet [12], for the case of turbulence ingestion into a rotor for the noise on the rotor axis. The present results confirm those findings using analytic asymptotic expressions for sound power. However, to the knowledge of the author, the existence of a mid-frequency band (item 3.) where the sound power scales with b is presented here for the first time.

6.6 Comparison between isolated airfoil model and cascade model

This section presents a comparison between the predicted power radiation from an isolated airfoil, presented in Sections 6.2 and 6.3, and the predicted radiation from a rectilinear cascade, using the model due to Cheong et al. [45]. This model, which is briefly described below, provides an expression for the sound power spectrum radiated upstream and downstream

of a two-dimensional rectilinear cascade of flat plate airfoil interacting with homogeneous, isotropic turbulence.

In the cascade model due to Cheong et al., the unsteady loading of the flat plates in a cascade is computed using a numerical co-location technique (from the work of Smith [143] and Whitehead [149]). This model therefore requires a significantly larger computational effort than the isolated airfoil model, where closed-form expressions are used to estimate the unsteady flat plate loading (see Section 6.2). Another important difference between the cascade model due to Cheong et al.[45] and the single airfoil power analysis given above, is that the turbulent wavenumbers in the direction parallel to the face of the cascade are assumed to be 2π-periodic, as would be the case if the cascade was rolled up into a duct.

Following Cheong et al.[45], the final expression for the acoustic power radiated upstream and downstream of the cascade is in the form of a summation of modes of order l given by

$$\mathcal{P}^{\pm}(\omega) = \frac{2\pi\rho_0 M}{\cos\alpha} \sum_{l=-\infty}^{\infty} Q_l^{\pm}(K_X) \sum_{n=-\infty}^{\infty} \Phi_{ww}(K_X, k_{Y,l+Bn}), \tag{6.65}$$

where B is the number of blades of the cascade, l denotes the azimuthal acoustic mode order, n denotes the cascade scattering index and k_Y is the turbulence wavenumber component in the direction normal to the surface of the flat plates. The quantity $Q_l^{\pm}$ in Eq. 6.65 is a non-dimensional modal power response function given by

$$Q_l^{\pm}(K_X) = \left|R_l^{\pm}\left(K_X, k_{Y,\mathrm{mod}(l,B)}\right)\right|^2 \frac{\mathrm{Re}\left\{-\alpha_l^{\pm} + M_x\left(k_0 + M_x\alpha_l^{\pm} + M_y\beta_l\right)\right\}}{\left|k_0 + M_x\alpha_l^{\pm} + M_y\beta_l\right|^2}, \tag{6.66}$$

where the axial and azimuthal flow Mach numbers are given by $M_x = U_X\cos\alpha/c_0$ and $M_y = U_X\sin\alpha/c_0$, respectively, and $\mathrm{mod}(l, B)$ is the remainder when l is divided by B. The axial and azimuthal wavenumbers of the acoustic modes radiated from the cascade, denoted by $\alpha_l^{\pm}$ and β_l respectively, are given by

$$\alpha_l^{\pm} = \frac{M_x\left(k_0 + M_y\beta_l\right) \pm \sqrt{\left(k_0 + M_y\beta_l\right)^2 - \left(1 - M_x^2\right)\beta_l^2}}{1 - M_x^2}, \tag{6.67}$$

$$\beta_l = k_X\sin\alpha + k_Y\cos\alpha - \frac{2\pi l}{d}, \tag{6.68}$$

where $d = 2\pi\bar{r}/B$ is the azimuthal distance (or 'gap') between adjacent blades and $\bar{r}$ is the spanwise location of the strip on a blade of the cascade. In the work of Cheong et al. [45], the modal cascade response functions $R_l^{\pm}$ are computed using the numerical code LINSUB, developed by Whitehead [149].

Figure 6.9 presents comparisons between the upstream and downstream PWL, per blade, predicted by the cascade model of Eq. 6.65 and the isolated airfoil model of Eq. 6.45 for four cascade configurations, denoted by (a), (b), (c) and (d). For all configurations, a single strip of span $\Delta r = 1$m is considered, whose midspan is located at a spanwise radius equal to

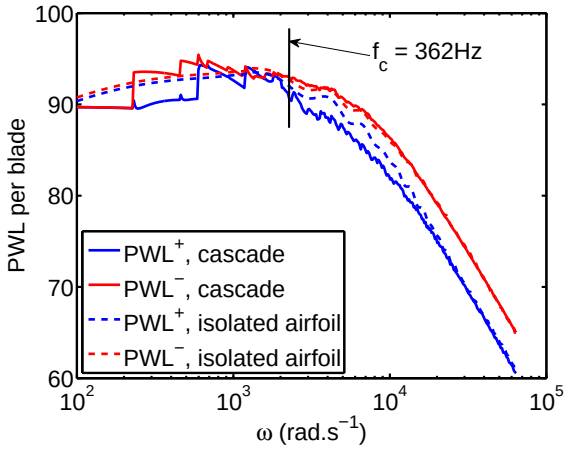

(a) $B = 10$, $\alpha = 60°$, $c = 0.335$m, $d/c = 1.5$

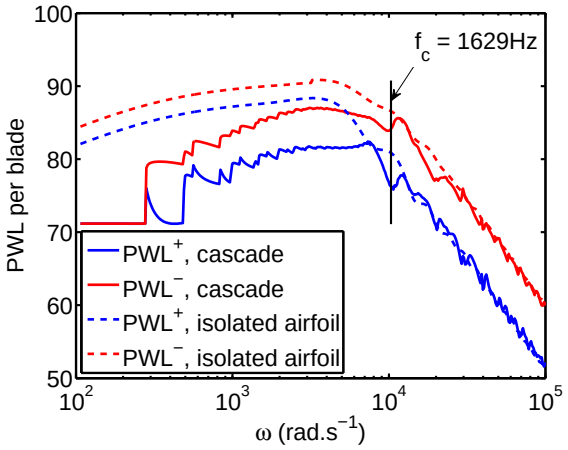

(b) $B = 45$, $\alpha = 30°$, $c = 0.125$m, $d/c = 0.89$

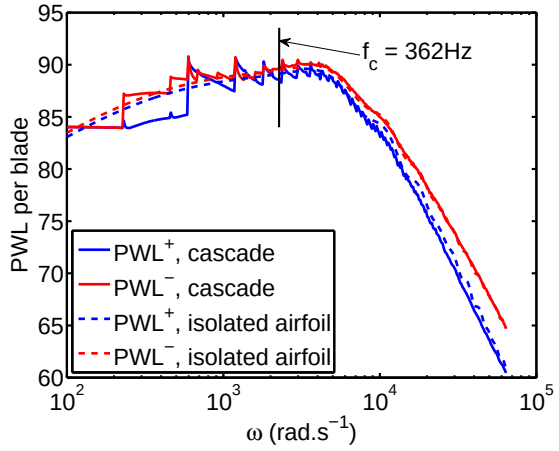

(c) $B = 10$, $\alpha = 60°$, $c = 0.125$m, $d/c = 4.0$

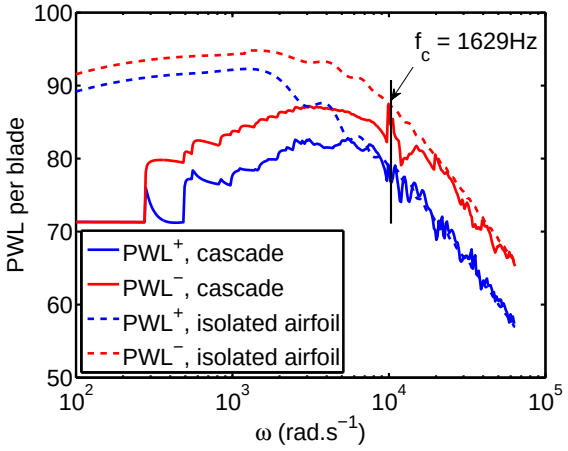

(d) $B = 45$, $\alpha = 30°$, $c = 0.335$m, $s/c = 0.33$

Figure 6.9: Upstream and downstream PWL per blade predicted by the cascade model and by the isolated airfoil model for four cascade configurations.

$\bar{r} = 0.8$m. The flow parameters are $M_X = 0.5$, $L = 0.028$m and $I_t = 2\%$. The values of chord and blade number are chosen so that the configurations (a) and (c) are low solidity cascades ($d/c > 1$) and (b) and (d) are high solidity cascades ($d/c < 1$). The configurations (a) and (b) are typical of CRORs and of turbofan stator vanes, respectively. The configurations (c) and (d) have the same number of blades as in (a) and (b), respectively, but the values of the chord length are interchanged in order to consider more extreme values of d/c.

In all cases, agreement between the sound power predictions of both models is excellent for frequencies above the critical frequency f_c, defined by Cheong et al. [45], at which the first interblade acoustic mode (or 'cascade mode') cuts on, and given by

$$f_c = \frac{1 - M_X^2}{(1 - M_x^2)^{1/2} + M_y} \frac{Bc_0}{2\pi\bar{r}}. \tag{6.69}$$

The agreement between the two models for frequencies below f_c is generally poor for the high solidity cascade configurations (b) and (d), as expected. However, the agreement is reasonable ($<$ 3dB) for the low solidity cascade configurations (a) and (c), even though the details of the cascade spectra at low frequency, due to individual 'duct modes', cannot be captured by the single airfoil prediction.

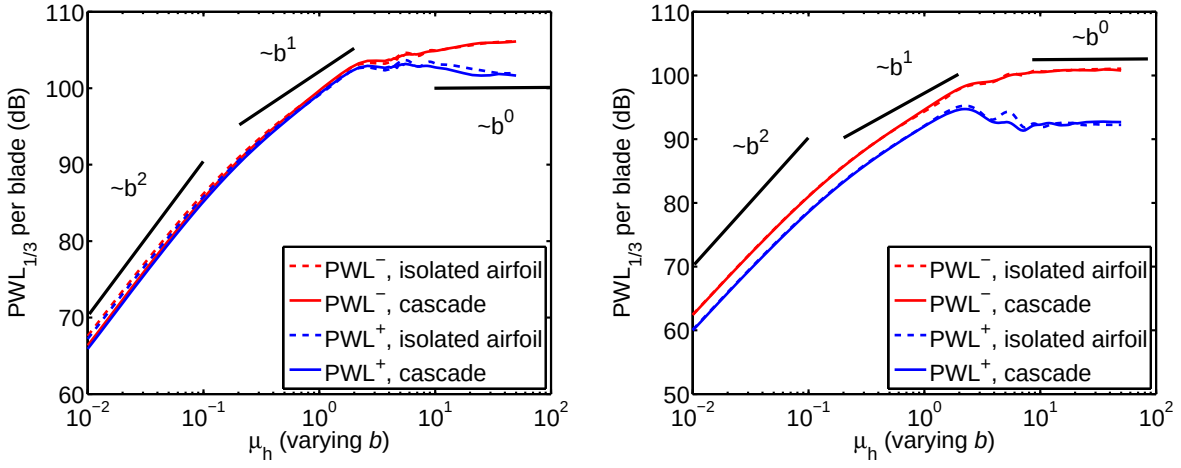

(a) $B = 10$, $\alpha = 60°$ (b) $B = 45$, $\alpha = 30°$

Figure 6.10: Effects of chord length on the total $\mathrm{PWL}_{1/3}$ per blade predicted by the cascade model and by the isolated airfoil model, for (a) the CROR and (b) the turbofan stator vanes configurations.

Figure 6.10 presents a comparison of the effects of chord length on the upstream and downstream sound power predicted by the two models for the CROR and turbofan cascade configurations, defined in Fig. 6.9 (a) and (b). The sound power is integrated over a 1/3-octave frequency band well above the critical frequency f_c (band centered at 7.5kHz for the CROR configuration and at 15kHz for the turbofan configuration). The reduced frequency μ_h varies between 0.01 to 50 (at the center frequency of the 1/3-octave band), which corresponds to a variation of the chord $c = 2b$ between 5.32×10^{-5}m and 0.266m. Excellent agreement (less than 1.5dB) is observed between the two predictions for both configurations. Moreover, the two predictions follow well the scaling laws with b described in Fig. 6.7.

Figure 6.11 presents a comparison of the effects of stagger angle on the sound power radiated upstream and downstream predicted by the cascade model, the isolated model and the analytical asymptotic expression given by Eq. 6.58 (valid at high μ_a), for the same configurations as in Fig. 6.10. Values of $f^{\pm}_{high}$ are deduced using Eq. 6.56 from the sound power $\mathcal{P}^{\pm}$, predicted by both models, which is integrated over the same 1/3-octave frequency bands used in Fig. 6.10. The agreement between the two models and the analytical high frequency expression is excellent (within 1dB) for most stagger angles α of practical interest. A large discontinuity is observed in the predictions of the cascade model for values of α close to $\pi/2$, i.e. $\alpha > 89°$ for Fig. 6.11 (a) and $\alpha > 84°$ for Fig. 6.11 (b), which have been attributed to numerical issues in the LINSUB code.

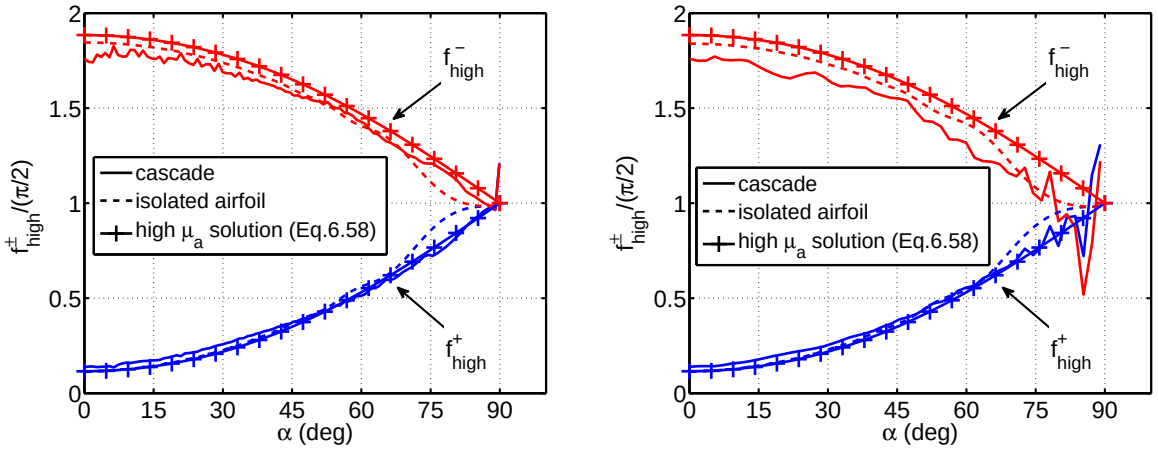

(a) $B = 10$, $c = 0.335$m (b) $B = 45$, $c = 0.125$m

Figure 6.11: Comparison of the variation of $f^{\pm}_{high}$ with α (linear scale) predicted by the cascade mode, the isolated airfoil model and the asymptotic expression of Eq. 6.58, for (a) the CROR and (b) the turbofan stator vanes configurations.

Note that the cascade PWL predictions shown in Figs. 6.9, 6.10 and 6.11 have been performed by Gareth Jenkins, research student at the Institute of Sound and Vibration Research, as part of a joint study.

6.7 Validity of the isolated airfoil model for CROR broadband noise

The results shown in Figs. 6.9, 6.10 and 6.11 indicate that isolated airfoil models can be used in place of cascade models at $f > f_c$ without significant loss of accuracy. This can provide a significant computational time reduction, since fan broadband noise predictions using cascade models are generally time consuming, particularly at high frequencies. As shown in Figs. 6.9 (a) and (c), the isolated airfoil model also agrees reasonably well with the cascade model at low frequencies ($f < f_c$) for cascade configurations with non-overlapping blades ($d/c > 1$). The precise condition for which the cascade sound pressure radiation approximates closely to that of a single airfoil requires further study.

The isolated airfoil approximation is made in the model for BRWI noise in CRORs presented in Chapter 2. This model is used in the parameter study presented in Section 4.3, where the effects of rotor-rotor gap, rotor speed and blade number on CROR broadband noise are investigated at constant engine power, torque split and solidity. In this parameter study, the value of the critical frequency f_c (Eq. 6.69), above which the isolated airfoil approximation is considered valid, ranges between 2.5Hz and 898Hz for all the 10 spanwise strips and all the CROR configurations considered. Moreover, the solidity of the rear rotor d_2/c_2 always exceeds 1 ($1.26 < \frac{d_2}{c_2} < 5.41$ from the hub to the tip, for all configurations studied in

Section 4.3). The present work suggests that the isolated airfoil approximation made in the BRWI model is acceptable for all the configurations studied in the parameter study in Section 4.3, i.e. for most realistic uninstalled CROR configurations.

The study of the effects of cascade presented in this chapter considers only leading edge interaction noise, with application to the BRWI noise in CRORs or the rotor-stator interaction noise in turbofans for example. This study should be, however, extended in future work to rotor trailing edge noise, in order to understand the validity of the isolated airfoil approximation made in the BRTE noise model.

Chapter 7

Conclusion and recommendations for future work

7.1 Conclusions

This research constitutes the first investigation of broadband noise emissions from uninstalled contra-rotating open rotors (CRORs). As presented in the introduction, the broadband component of the noise from CRORs can contribute significantly to the total noise emissions, according to noise measurements on a scaled model CROR, hence the necessity of the present work.

It has been assumed in this work that the two most significant sources of broadband noise in uninstalled CRORs are the broadband rotor-wake/rotor interaction noise (BRWI) and the broadband rotor tailing edge noise (BRTE). Semi-analytical prediction methods for these two sources of broadband noise have been developed and show good agreement with experimental data.

The main conclusions of this research are presented below.

7.1.1 Relative importance of BRWI and BRTE noise

The relative importance of the BRWI and the BRTE noise sources have been studied for a realistic CROR configuration at three different flight conditions, which correspond approximately to values of thrust and flight speed of a typical short-haul, 150-seat, aircraft with two engines at assumed take-off, cruise and approach-type conditions.

Predictions have shown that the BRTE noise emissions are significantly greater than the BRWI noise emissions at assumed cruise and approach, whereas both sources of broadband noise are significant at assumed take-off. This result is due to the fact that the loading of

the front rotor blades is high at assumed take-off and low at assumed cruise and approach. Therefore, wide wakes with a high turbulence intensity are shed from the front rotor at assumed take-off, resulting in high BRWI noise emissions, whereas thin wakes with a low turbulence intensity are shed from the front rotor at assumed cruise and approach, resulting in low BRWI noise emissions. BRTE noise emissions have been predicted to be less sensitive to operating conditions than BRWI noise emissions, hence the observed difference in the balance of the two sources of broadband noise between assumed cruise and approach (low rotor loading) and assumed take-off (high rotor loading).

7.1.2 Results of the parameter study

A parameter study has been conducted in order to investigate strategies for the reduction of CROR broadband noise. The effects on broadband noise emissions of variations in rotor-rotor axial gap, rotor speed and blade number have been studied at constant engine power, torque split and solidity. The main conclusions of this parameter study are the following:

- Rotor-rotor gap effects: Increasing the rotor-rotor gap generally yields an increase in the overall sound power level (OAPWL) of BRWI noise emissions, but has no impact on the BRTE noise assuming that the aerodynamics of each rotor is unchanged. Therefore, rotor-rotor gap effects on total CROR broadband noise emissions were predicted to be only small at assumed take-off (at which both BRWI and BRTE noise sources are significant) and negligible at assumed cruise and approach (at which the BRTE noise sources dominate).

- Rotor speed effects: At assumed cruise and approach, increasing the speed of each rotor yields an increase in the total OAPWL of the broadband noise emissions. However, at assumed take-off, increasing the speed of the front rotor was predicted to yield a large reduction in total OAPWL, whereas variations in rear rotor speed were predicted to have a lesser impact on total OAPWL predictions.

- Blade number effects: Variations in the blade numbers of the front and rear rotors (at constant solidity) were predicted to have a significant impact on BRWI noise emissions but a very small impact on BRTE noise emissions. Therefore, the total OAPWL of the broadband noise emissions at assumed cruise and approach, which is dominated by the BRTE noise, was predicted to be almost independent of variations in blade number. At assumed take-off, however, increasing the blade number of the front rotor was predicted to yield a decrease in OAPWL, whereas increasing the blade number of the rear rotor was predicted to yield an increase in OAPWL.

7.1.3 Validity of Amiet's model for BRTE noise

The BRTE noise model developed in this work, which treats the effects of blade rotation exactly, has been compared to the widely used BRTE noise model of Amiet, in which the effects of rotation are treated approximately. These two models have been analytically expressed in a form that facilitates their comparison. Equivalence of their directivity functions has been shown. Amiet's model exhibits excellent agreement with the exact model over the mid-frequency range but diverges in the low and high frequency limits. Criteria for the low and high frequency limits of validity of Amiet's model have been established. Estimates of the error of Amiet's model in the low and high frequency limits have been provided. The two trailing edge noise models have been applied to practical rotor configurations, including an open aircraft propeller, a model cooling fan and a wind turbine. It has been shown that the domain of validity of Amiet's model covers most of the domain of frequencies of interest, for the configurations studied.

7.1.4 Validity of isolated airfoil approximation for turbulence-cascade interaction noise

The sound power radiated from isolated airfoils and from blade cascades in a turbulent stream has been compared, in order to assess the validity of the isolated airfoil approximation in prediction methods for turbulence-cascade interaction noise, such as the BRWI noise in CRORs.

For this purpose, an analytical model of the sound power radiated from a flat plate airfoil in a 2D turbulent flow has been derived. The effects of stagger angle on the radiated sound power are included so that the sound power radiated upstream and downstream relative to a hypothetical fan axis can be predicted. This isolated airfoil model has then been compared to an existing cascade model, in which the effects of acoustic scattering due to adjacent flat plates are taken into account. Excellent agreement is observed at frequencies above a critical frequency, suggesting that isolated airfoil theory may be used in models of fan broadband noise at high frequencies. Reasonable agreement is also observed at low frequency for fans with sufficiently low solidity (such as CRORs). However, agreement at low frequency is poor for cascade with high solidity (such as turbofan stator vanes). This study suggests that the isolated airfoil approximation made in the BRWI model (see Chapter 2), to reduce the large computational effort associated with the use of cascade response functions, is acceptable for most realistic uninstalled CROR configurations.

7.2 Recommendations for future work

Recommendations and suggestions for future work are listed below:

1. In the introduction to this thesis, noise measurements of a scaled model CROR were shown to exhibit a significant contribution of the broadband noise to the total noise emissions. However, a more complete study is required to analyse the relative importance of tonal and broadband noise emissions in CRORs, for a range of configurations and operating conditions. Such a parameter study could be performed using the fast CROR broadband noise prediction methods developed in this research and existing prediction methods for CROR tonal noise (see Section 1.3.3).

2. In the present work, the mean and turbulent wake parameters input to the BRWI noise model are deduced from empirical correlations. A more accurate description of these aerodynamic input parameters is required and could be obtained from either hot-wire measurements of the front rotor wake turbulence or from high-fidelity CFD results.

3. The response function of the rotor blades is approximated, in both the BRWI and the BRTE noise models, by that of unloaded flat plates. It is suggested to study and quantify the effects of real blade geometry (thickness, camber, angle of attack, etc.) on CROR broadband noise predictions.

4. Further improvement of the BRWI and BRTE noise models could be to include the effects of lean, sweep, anisotropy and inhomogeneity of the turbulent inputs and to quantify these effects for CROR broadband noise predictions.

5. The comparison of sound power predictions using single airfoil models and cascade models presented in this thesis for interaction noise (see Chapter 6) could be extended to trailing edge noise, in order to assess the validity of using isolated airfoil models for BRTE noise predictions.

6. It is suggested to develop prediction methods for other sources of broadband noise in CRORs, such as the turbulent tip-vortex interaction noise, the pylon-wake/rotor interaction noise and the turbulence ingestion noise. The relative importance of these additional sources of broadband noise in CRORs compared to the BRWI and the BRTE noise sources could then be studied.

7. Installation effects, such as the scattering of the broadband noise by the fuselage, the centre body, the wing, etc. could be studied and quantified.

Appendix A

Poisson's summation formula for rotor-wake/rotor interaction model

Poisson's summation formula is applied in Chapters 2 and 3 to include the azimuthal periodicity of both the rotor blades and the turbulent wakes into the noise models. The detailed application of this formula to the modelling of the rotor wakes (Section 2.2.1) is presented in this appendix.

Poisson's summation formula relates the Fourier coefficients of the periodic extension $f\left(x+kT_0\right)$ (of period T_0) of a function $f\left(x\right)$ to its Fourier transform $\hat{f}$ as

$$\sum_{k=-\infty}^{\infty} f\left(x+kT_0\right) = \frac{1}{T_0}\sum_{m=-\infty}^{\infty} e^{-i2\pi\frac{m}{T_0}x}\hat{f}\left(\frac{m}{T_0}\right). \tag{A.1}$$

First, the function f in Eq. A.1 is to be equal to the argument of the summation in Eq. 2.12 as

$$f\left(x-kd_1\right) = \exp\left\{-\frac{a}{b_W^2}\left(x+kd_1\right)^2\right\}, \tag{A.2}$$

where $x = \left(\tilde{\mathbf{X}}_2 - \mathbf{W}\tau\right).\left(\mathbf{e}_{\phi 1} - \mathbf{e}_{x1}\tan\alpha_1\right)$ has been introduced for the sake of brevity.

The following Fourier transform is then performed

$$\hat{f}\left(\frac{m}{d_1}\right) = \int_{-\infty}^{\infty} f\left(\zeta\right) e^{i2\pi\frac{m}{d_1}\zeta} d\zeta, \tag{A.3}$$

to give

$$\hat{f}\left(\frac{m}{d_1}\right) = b_W\sqrt{\frac{\pi}{a}}\exp\left\{-\left(\frac{b_W\pi m}{d_1\sqrt{a}}\right)^2\right\}. \tag{A.4}$$

Substituting Eq. A.4 into Eq. A.1 yields

$$f_W(x) = \sum_{k=-\infty}^{\infty} f(x + kd_1) = \frac{1}{d_1} b_W \sqrt{\frac{\pi}{a}} \sum_{m=-\infty}^{\infty} \exp\left\{ -\left(\frac{b_W \pi m}{d_1 \sqrt{a}} \right)^2 \right\} e^{-i2\pi \frac{m}{d_1} x}. \tag{A.5}$$

The train of Gaussian wake profiles f_W can therefore be expressed in terms of its Fourier components f_m by setting $x = \left(\tilde{\mathbf{X}}_2 - \mathbf{W}\tau \right) . (\mathbf{e}_{\phi 1} - \mathbf{e}_{x1} \tan\alpha_1)$ and $d_1 = \frac{2\pi r}{B_1}$ in Eq. A.5, to give

$$f_W\left(\tilde{\mathbf{X}}_2, \tau \right) = \sum_{m=-\infty}^{\infty} f_m(r)\, e^{-i \frac{mB_1}{r} (\tilde{\mathbf{X}}_2 - \mathbf{W}\tau) . (\mathbf{e}_{\phi 1} - \mathbf{e}_{x1} \tan\alpha_1)}, \tag{A.6}$$

where the function f_m, given by

$$f_m(r) = \frac{1}{\sigma\sqrt{2\pi}} \exp\left\{ -\frac{1}{2} \left(\frac{m}{\sigma} \right)^2 \right\}, \tag{A.7}$$

is a Gaussian function of the scattering index m, centred at the value $m = 0$ and of 'standard deviation' $\sigma = \frac{r\sqrt{2a}}{B_1 b_W}$.

Appendix B

Correction for the effects of uniform flow on sound power radiation

The expressions for the far-field pressure spectral density derived in Sections 2.2.3 and 3.1.2 assume that the medium of acoustic radiation is at rest. This assumption is generally reasonable at low subsonic flight speeds, but the effects of the uniform mean flow, of Mach number M_x, must be included in the final expression for sound power level (PWL). The pressure spectrum with mean flow $\breve{p}$ may be deduced from the no-flow solution p by Lorentz transformation (note that the convention $\hat{(.)}$ denoting a frequency domain quantity has been dropped for the sake of clarity). According to the work of Chapman [41], the results of this transform can be generalised in a simple form as

$$\breve{p}\left(r_0, \theta, \psi_0, \omega\right) = p\left(\breve{r}_0, \breve{\theta}, \psi_0, \omega\right) e^{ik_0 r_0 M_x \cos\theta/\beta^2}, \tag{B.1}$$

where $\beta_x = \sqrt{1 - M_x^2}$ and the equivalent flow corrected radiation distance $\breve{r}_0$ and angle $\breve{\theta}$ may be obtained from their no-flow values as

$$\breve{r}_0 = \frac{r_0}{\beta_x^2}\sqrt{1 - M_x^2 \sin^2\theta}, \;\; \cos\breve{\theta} = \frac{\cos\theta}{\sqrt{1 - M_x^2\sin^2\theta}} \;\text{ and }\; \sin\breve{\theta} = \frac{\beta_x \sin\theta}{\sqrt{1 - M_x^2\sin^2\theta}}. \tag{B.2}$$

The notation $\breve{(.)}$ is used to represent a quantity expressed following Chapman's similarity rule. This approach is applied here to the derivation of the far-field sound power predicted by the BRWI model described in Chapter 2. Note that the same approach can be applied to correct for the effects of mean flow on the sound power predictions of the BRTE noise model, described in Chapter 3.

Substituting Eq. 2.48 into Eq. B.1 allows the effects of a uniform mean flow to be included into the expression for the modal pressure spectrum radiated to the far-field

$$\breve{p}_{qmn}\left(r_0,\theta,\psi_0,\omega\right)=\frac{-i}{8\pi^2}\frac{\rho_0 b_2 B_1 B_2}{\breve{r}_0}e^{i[l(\psi_0+\pi/2)-k_0 r_0 S(\theta,M_x)]}\int_{R_{h2}}^{R_{t2}}\left(\frac{l}{r}+k_0\cos\breve{\theta}\tan\alpha_2\right)\frac{J_l\left(k_0 r\sin\breve{\theta}\right)}{r}$$
$$\times f_m\left(r\right)\int_{-\infty}^{\infty}\mathcal{W}\left(k_r,K_{X,qmn},K_{Y,qmn}\right)\mathcal{L}^{\mathrm{LE}}\left(k_r,K_{X,qmn},\breve{\kappa}_{qmn}\right)e^{i\breve{\kappa}_{qmn}(s_2-b_2)}e^{-ik_r r}dk_r dr, \tag{B.3}$$

where the aeroacoustic coupling wavenumber $\breve{\kappa}_{qmn}$ has been transformed accordingly from Eqs. 2.33 and 2.50, and where $S\left(\theta,M_x\right)=\left(\sqrt{1-M_x^2\sin^2\theta}-M_x\cos\theta\right)/\beta_x^2$.

The same procedure as in Chapter 6 is now used to derive the time averaged sound intensity, in the direction of the observer, to give

$$\bar{I}_r\left(r_0,\theta,\psi_0,\omega\right)=\frac{\left|\breve{p}\left(r_0,\theta,\psi_0,\omega\right)\right|^2}{2\rho_0 c_0}F\left(\theta,M_x\right), \tag{B.4}$$

where the function $F\left(\theta,M_x\right)$ is given by

$$F\left(\theta,M_x\right)=\frac{\beta_x^4\sqrt{1-M_x^2\sin^2\theta}}{\left(\sqrt{1-M_x^2\sin^2\theta}-M_x\cos\theta\right)^2}. \tag{B.5}$$

For continuous spectra, independent of the coordinate ψ_0, the pressure spectral density $S_{pp}\left(\breve{r}_0,\breve{\theta},\omega\right)$ replaces $\left|\breve{p}\left(r_0,\theta,\psi_0,\omega\right)\right|^2$ in Eq. 6.41. The final expression for sound power is obtained by integrating Eq. B.4 over the surface of a sphere, which gives (noting that S_{pp} is axisymmetric with axis $\theta=0$)

$$\mathcal{P}\left(\omega\right)=\frac{2\pi r_0^2}{\rho_0 c_0}\int_0^{\pi}S_{pp}\left(\breve{r}_0,\breve{\theta},\omega\right)F\left(\theta,M_x\right)\sin\theta d\theta. \tag{B.6}$$

Note that an approach similar to that presented in this appendix has been used by Sinayoko et al. [142] to compute the sound power radiated from a semi-infinite duct with uniform flow.

Appendix C

Correction for the effects of fly-over on sound pressure radiation

The BRWI and BRTE noise models derived in Chapter 2 and 3, respectively, assume that the observer is stationary with respect to the CROR engine, as would be the case in a wind-tunnel. However, an aircraft trajectory is generally required to produce perceived noise level predictions and, therefore, the effects of relative motion between the engine and the observer (or 'fly-over effects') must be taken into account in the predictions. Simple corrections can be applied to the final expressions of the PSD of the BRWI and BRTE noise to take into account these effects, as presented in this Appendix.

First, if the engine is flying-over an observer in the far-field at a flight Mach number M_x and in the direction of the $\theta = 0$ axis (see Fig. 2.3), the retarded time equation (Eq. 2.28) is modified as

$$\tau = \frac{t - R_0/c_0}{1 + M_x \cos\theta}. \tag{C.1}$$

Following the same steps as in Chapter 2 and 3 yields the same final results for the PSD of the BRWI and BRTE noise, respectively, except that a Doppler shift is included in the expressions for the chordwise wavenumber k_X. The effects of 'fly-over' can therefore be simply taken into account in the BRWI model by setting

$$K_{X,qmn} = \frac{\omega\,(1 + M_x \cos\theta) + \omega_{qmn}}{U_{X2}}, \tag{C.2}$$

into Eq. 2.58, and in the BRTE model by setting

$$K_{X,l} = \frac{\omega\,(1 + M_x \cos\theta) + l\Omega}{U_c}, \tag{C.3}$$

into Eq. 3.18.

Note that the full derivation of the BRWI noise model with 'fly-over effects' included was presented as a conference paper by the author in Ref. [28]. A factor $1/\pi$ was missing in Eq. 33 of Ref. [28], but this has been corrected in this thesis.

Appendix D

Detailed derivation of turbulence wavenumber cross-spectra

D.1 Wake turbulence

The mathematical details of the derivation of Eq. 2.53 are presented in this section. The cross-spectrum of the turbulent upwash velocity in the wavenumber domain $\mathcal{W}(k_r, k_X, k_Y)$ is first rewritten using the inverse Fourier transform of Eq. 2.13 as

$$\lim_{T\to\infty}\frac{\pi}{T}\left\langle \mathcal{W}^*\left(k_r, K_{X,qmn}, K_{Y,qmn}\right)\mathcal{W}\left(k_r^{'}, K_{X,q'm'n'}, K_{Y,q'm'n'}\right)\right\rangle =$$

$$\lim_{T\to\infty}\frac{\pi}{T}\int_{-R}^{R}\int\int\int_{-R}^{R}\int\left\langle \tilde{w}^*\left(r, X_2, Y_2\right)\tilde{w}\left(r', X_2^{'}, Y_2^{'}\right)\right\rangle$$

$$\times e^{-i\left[k_r r + K_{X,qmn}X_2 + K_{Y,qmn}Y_2\right]}e^{i\left[k_r^{'}r' + K_{X,q'm'n'}X_2^{'} + K_{Y,q'm'n'}Y_2^{'}\right]}drdX_2dY_2dr'dX_2^{'}dY_2^{'}\ , \quad \text{(D.1)}$$

where $R = TU_{X2}$. Making the substitutions $X_2^{'} = X_2 + \delta X_2$, $Y_2^{'} = Y_2 + \delta Y_2$, $r' = r + \delta r$ in Eq. D.1 yields

$$\lim_{T\to\infty}\frac{\pi}{T}\left\langle \mathcal{W}^*\left(k_r, K_{X,qmn}, K_{Y,qmn}\right)\mathcal{W}\left(k_r^{'}, K_{X,q'm'n'}, K_{Y,q'm'n'}\right)\right\rangle =$$

$$\times\lim_{T\to\infty}\frac{\pi}{T}\int_{-R}^{R}e^{i\left(K_{Y,q'm'n'}-K_{Y,qmn}\right)Y_2}\int_{-R}^{R}e^{i\left(K_{X,q'm'n'}-K_{X,qmn}\right)X_2}\int_{-R}^{R}e^{i\left(k_r^{'}-k_r\right)r}$$

$$\times\int_{-R-Y_2}^{R-Y_2}\int_{-R-X_2}^{R-X_2}\int_{-R-r}^{R-r}e^{i\left[k_r^{'}\delta r + K_{X,q'm'n'}\delta X_2 + K_{Y,q'm'n'}\delta Y_2\right]}$$

$$\times\left\langle \tilde{w}^*\left(r, X_2, Y_2\right)\tilde{w}\left(r+\delta r, X_2+\delta X_2, Y_2+\delta Y_2\right)\right\rangle d\delta r d\delta X_2 d\delta Y_2 dr dX_2 dY_2. \quad \text{(D.2)}$$

Assuming the turbulence to be homogeneous, the spatial autocorrelation function R_{ww} of the turbulent upwash velocity $\tilde{w}$ can be defined as

$$R_{ww}\left(\delta r, \delta X_2, \delta Y_2\right) = \left\langle \tilde{w}^*\left(r, X_2, Y_2\right) \tilde{w}\left(r+\delta r, X_2+\delta X_2, Y_2+\delta Y_2\right)\right\rangle, \tag{D.3}$$

which is related to the turbulence velocity wavenumber spectrum as

$$\Phi_{ww}\left(k_r, k_X, k_Y\right) = \int_{-\infty}^{\infty}\int\int R_{ww}\left(\delta r, \delta X_2, \delta Y_2\right) e^{i\left[k_r \delta r + k_X \delta X_2 + k_Y \delta Y_2\right]} d\delta r d\delta X_2 d\delta Y_2. \tag{D.4}$$

Substituting Eqs.D.3 and D.4 into D.2 yields

$$\begin{aligned}\lim_{T\to\infty}\frac{\pi}{T}\left\langle \mathcal{W}^*\left(k_r, K_{X,qmn}, K_{Y,qmn}\right)\mathcal{W}\left(k_r^{'}, K_{X,q'm'n'}, K_{Y,q'm'n'}\right)\right\rangle = \\ \lim_{T\to\infty}\frac{\pi}{T}\int_{-R}^{R} e^{i\left(k_r^{'}-k_r\right)r} dr \int_{-R}^{R} e^{i\left(K_{X,q'm'n'}-K_{X,qmn}\right)X_2} dX_2 \int_{-R}^{R} e^{i\left(K_{Y,q'm'n'}-K_{Y,qmn}\right)Y_2} dY_2 \\ \times \Phi_{ww}\left(k_r^{'}, K_{X,q'm'n'}, K_{Y,q'm'n'}\right).\end{aligned} \tag{D.5}$$

The first integral in Eq. D.5 becomes for $R \to \infty$

$$\int_{-R}^{R} e^{i\left(k_r^{'}-k_r\right)r} dr = 2\pi\delta\left(k_r^{'}-k_r\right), \tag{D.6}$$

where $\delta(.)$ is the Dirac delta function. Substituting Eq. 2.33 into the second integral in Eq. D.5 and recalling that $R = TU_{X2}$ gives

$$\lim_{T\to\infty}\frac{\pi}{T}\int_{-R}^{R} e^{i\left(K_{X,q'm'n'}-K_{X,qmn}\right)X_2} dX_2 = \lim_{T\to\infty}\frac{\pi}{T}\int_{-TU_{X2}}^{TU_{X2}} e^{i\left(\omega_{q'm'n'}-\omega_{qmn}\right)X_2/U_{X2}} dX_2. \tag{D.7}$$

Making the change of variable $\bar{t} = X_2/U_{X2}$ in Eq. D.7 yields

$$\lim_{T\to\infty}\frac{\pi}{T}\int_{-TU_{X2}}^{TU_{X2}} e^{i\left(\omega_{q'm'n'}-\omega_{qmn}\right)X_2/U_{X2}} dX_2 = 2\pi U_{X2}\lim_{T\to\infty}\frac{1}{2T}\int_{-T}^{T} e^{i\left(\omega_{q'm'n'}-\omega_{qmn}\right)\bar{t}} d\bar{t}. \tag{D.8}$$

Then, assuming that $\omega_{q'm'n'} = \omega_{qmn}$ only if $(q', m', n') = (q, m, n)$ and from the properties of the Kronecker delta function, denoted by $\delta[.]$, it yields

$$\lim_{T\to\infty}\frac{\pi}{T}\int_{-R}^{R} e^{i\left(K_{X,q'm'n'}-K_{X,qmn}\right)X_2} dX_2 = 2\pi U_{X2}\delta\left[m'-m\right]\delta\left[n'-n\right]\delta\left[q'-q\right]. \tag{D.9}$$

Following the approach of Hanson [86], the limits of the third integral in Eq. D.5 can be reduced to the total azimuthal distance covered by the blade section during one rotation,

i.e. $2R \rightarrow 2\pi r\cos\alpha_2$. Then, using Eq. D.9 and 2.33 yields

$$\int_{-R}^{R} e^{i\left(K_{Y,q'm'n'}-K_{Y,qmn}\right)Y_2} dY_2 = 2\pi r\cos\alpha_2. \tag{D.10}$$

Finally, substituting Eqs. D.6 to D.10 into Eq. D.5 yields

$$\lim_{T\to\infty}\frac{\pi}{T}\left\langle \mathcal{W}^*(k_r, K_{X,qmn}, K_{Y,qmn})\mathcal{W}(k_r^{'}, K_{X,q'm'n'}, K_{Y,q'm'n'})\right\rangle = (2\pi)^3 U_{X2} r\cos\alpha_2 \\ \times \delta\left[m'-m\right]\delta\left[n'-n\right]\delta\left[q'-q\right]\delta(k_r^{'}-k_r)\Phi_{ww}(k_r^{'}, K_{X,q'm'n'}, K_{Y,q'm'n'}). \tag{D.11}$$

D.2 Surface pressure of turbulent boundary layer

The mathematical details of the derivation of Eq. 3.11 are presented in this section. The surface pressure beneath the boundary layer (on one side of an airfoil) is assumed to be a 'frozen' pressure pattern as it is convected passed the trailing edge. The wavenumber cross-spectrum of the surface pressure, on one side of a rotating blade, can therefore be expressed from Eq. 3.2 as

$$\lim_{T\to\infty}\frac{\pi}{T}\left\langle P^*(k_r, K_{X,l})P(k_r^{'}, K_{X,l'})\right\rangle = \lim_{T\to\infty}\frac{\pi}{T}\int_{-R}^{R}\int_{-R}^{R}\int_{-R}^{R}\int_{-R}^{R}\left\langle P^*(r,X)P(r',X')\right\rangle \\ \times e^{-i\left[k_r r + K_{X,l}X\right]} e^{i\left[k_r^{'}r' + K_{X,l'}X'\right]} dr dX dr' dX', \tag{D.12}$$

where $R = TU_c$ is a large but finite number. Making the substitutions $X^{'} = X + \delta X$, $r' = r + \delta r$ in Eq. D.12 yields

$$\lim_{T\to\infty}\frac{\pi}{T}\left\langle P^*(k_r, K_{X,l})P(k_r^{'}, K_{X,l'})\right\rangle = \lim_{T\to\infty}\frac{\pi}{T}\int_{-R}^{R} e^{i\left(K_{X,l'}-K_{X,l}\right)X}\int_{-R}^{R} e^{i\left(k_r^{'}-k_r\right)r} \\ \times \int_{-R-X}^{R-X}\int_{-R-r}^{R-r} e^{i\left[k_r^{'}\delta r + K_{X,l'}\delta X\right]}\left\langle P^*(r,X)P(r+\delta r, X+\delta X)\right\rangle d\delta r d\delta X dr dX. \tag{D.13}$$

Assuming the surface pressure to be homogeneous, the spatial autocorrelation function R_{PP} of the surface pressure P can be defined as

$$R_{PP}\left(\delta r, \delta X\right) = \left\langle P^*(r,X)P(r+\delta r, X+\delta X)\right\rangle, \tag{D.14}$$

which can be related to the wavenumber spectrum of the surface pressure as

$$S_{qq}\left(k_r, k_X\right) = \int_{-\infty}^{\infty}\int R_{pp}\left(\delta r, \delta X\right) e^{i[k_r\delta r + k_X\delta X]} d\delta r d\delta X. \tag{D.15}$$

Substituting Eqs.D.14 and D.15 into D.13 yields

$$\lim_{T\to\infty}\frac{\pi}{T}\left\langle P^*(k_r,K_{X,l})P(k_r^{'},K_{X,l'})\right\rangle = \lim_{T\to\infty}\frac{\pi}{T}\int_{-R}^{R} e^{i\left(K_{X,l'}-K_{X,l}\right)X}dX \times\int_{-R}^{R} e^{i\left(k_r^{'}-k_r\right)r}drS_{qq}\left(k_r^{'},K_{X,l'}\right). \tag{D.16}$$

The integral over dr in Eq. D.16 is solved similarly to Eq. D.6. In the BRTE noise model, the boundary layer turbulence on each blade is assumed to be identical at every blade rotation and, therefore, the limit of $T\to\infty$ in Eq. D.16 can be reduced to $T\to T_0$, where $2T_0 = 2\pi/\Omega$ is the time taken by a complete blade rotation. Recalling that $R = TU_c$ and making the change of variables $\bar{X} = X\Omega/U_c$, the integral over dX in Eq. D.16 can be expressed as

$$\lim_{T\to T_0}\frac{\pi}{T}\int_{-R}^{R} e^{i\left(K_{X,l'}-K_{X,l}\right)X}dX = U_c\int_{-\pi}^{\pi} e^{i(l'-l)\bar{X}}d\bar{X}. \tag{D.17}$$

From the definition of the Kronecker delta function, Eq. D.17 then yields

$$\lim_{T\to T_0}\frac{\pi}{T}\int_{-R}^{R} e^{i\left(K_{X,l'}-K_{X,l}\right)X}dX = 2\pi U_c\delta\left[l'-l\right]. \tag{D.18}$$

Substituting Eqs. D.6 and D.18 into Eq. D.16 finally gives

$$\lim_{T\to\infty}\frac{\pi}{T}\left\langle P^*(k_r,K_{X,l})P(k_r^{'},K_{X,l'})\right\rangle = (2\pi)^2\,\delta\left[l'-l\right]\delta\left(k_r^{'}-k_r\right)S_{qq}\left(k_r^{'},K_{X,l'}\right). \tag{D.19}$$

Appendix E

A modified 'switch' condition between Amiet's response functions

A justification for the choice of a modified 'switch' condition between the low and high frequency response functions of Amiet [5, 7], used in Chapter (6), is presented in this appendix. First, the value $\mu_a = \pi/4$, suggested by Amiet as the 'switch' condition (see Section 6.2), is considered small enough so that the Bessel functions in Eq. 6.21 can be approximated to unity. Using the approximation $S(\zeta) \approx 1/\sqrt{1+2\pi\zeta}$ (see for instance Ref. [16]), $\mathcal{L}_{low}^{\mathrm{LE}}$ can then be approximated in the neighborhood of $\mu_a \approx \pi/4$ as

$$\mathcal{L}_{low}^{\mathrm{LE}}(\theta, K_X, \kappa) \approx \frac{1}{\beta}\sqrt{\frac{M}{M+2\pi\mu_a}}e^{i\mu_a f(M)/M}. \tag{E.1}$$

The value $\mu_a = \pi/4$ is also considered small enough so that $\mathcal{L}_{high}^{\mathrm{LE}} = \mathcal{L}_1 + \mathcal{L}_2$ is assumed to reach its low frequency asymptotic regime. Using the low argument asymptotic expression of the conjugate Fresnel integral given by

$$E^*(\zeta) = \sqrt{\frac{2}{\pi}}\sqrt{\zeta}e^{-i\zeta}\left(1+\mathcal{O}(\zeta)\right), \tag{E.2}$$

the low frequency asymptotic expressions for $\mathcal{L}_1$ and $\mathcal{L}_2$ are deduced from Eqs. 6.23 and 6.24, respectively, as

$$\lim_{\mu_a\to 0}\mathcal{L}_1(\theta, K_X, \kappa) = \frac{1}{\beta}\sqrt{\frac{M}{1+M}}\sqrt{\frac{8}{\pi^3\mu_a}}e^{i(\Theta_2-2\Theta_1)}, \tag{E.3}$$

and

$$\lim_{\mu_a \to 0} \mathcal{L}_2\left(\theta, K_X, \kappa\right) = \frac{1}{\beta}\sqrt{\frac{M}{1+M}}\frac{e^{i\Theta_2}}{\mu_a\left(1-\frac{\cos\theta}{A(\theta,M)}\right)} \tag{E.4}$$
$$\times\left[\frac{i\left(1-e^{-i2\Theta_1}\right)}{\sqrt{2\pi^3\mu_a}} + \frac{2}{\pi^2}\left(1-i\right)e^{-i4\mu_a}\left(\beta e^{i4\mu_a M^2}-1\right)\right].$$

Note that the amplitude terms in the approximate expressions of $\mathcal{L}^{\mathrm{LE}}_{low}$ and $\mathcal{L}_1$ at $\mu_a \approx \pi/4$ (Eqs. E.1 and E.3) do not depend on the observer angle θ, whereas the expression of $\mathcal{L}_2$ (Eq. E.4) exhibits the factor $1/\left(1-\frac{\cos\theta}{A(\theta,M)}\right)$ as an amplitude term. The presence of this factor implies that the low frequency asymptotic expression of the term $\mathcal{L}_2$ tends to infinity as the observer angle tends to zero. This non-physical behavior may come from the fact that the de-coupling of the leading edge and the trailing edge solutions, as $\mathcal{L}^{\mathrm{LE}}_{high} = \mathcal{L}_1 + \mathcal{L}_2$, is not valid at low frequencies. More terms would be needed to capture the complete behavior of $\mathcal{L}^{\mathrm{LE}}$ at low frequencies, i.e. $\mathcal{L}^{\mathrm{LE}} = \mathcal{L}_1 + \mathcal{L}_2 + \mathcal{L}_3 + ...$ Non-physical discontinuities can therefore appear in the noise predictions as μ_a approaches $\pi/4$ and when the observer angle θ is small, as shown in Fig. E.1.

This issue has been resolved here by splitting the solution for $\mathcal{L}^{\mathrm{LE}}$ into the three frequency regimes, for $\theta \leq 90°$, as

$$\mathcal{L}^{\mathrm{LE}}_{low} \qquad \text{for } \mu_a < \frac{\pi}{4}, \tag{E.5}$$

$$\mathcal{L}^{\mathrm{LE}}_{high} \approx \mathcal{L}_1 \qquad \text{for } \frac{\pi}{4} \leq \mu_a \leq \frac{\pi}{4\left(1-\frac{\cos\theta}{A(\theta,M)}\right)}, \tag{E.6}$$

$$\mathcal{L}^{\mathrm{LE}}_{high} \approx \mathcal{L}_1 + \mathcal{L}_2 \qquad \text{for } \mu_a > \frac{\pi}{4\left(1-\frac{\cos\theta}{A(\theta,M)}\right)}. \tag{E.7}$$

For $\theta > 90°$, the sub-range where $\mathcal{L}^{\mathrm{LE}} \approx \mathcal{L}_1$ is not used and the low frequency range $\mathcal{L}^{\mathrm{LE}} \approx \mathcal{L}^{\mathrm{LE}}_{low}$ is used for $\mu_a \leq \frac{\pi}{4\left(1-\frac{\cos\theta}{A(\theta,M)}\right)}$. This correction for Amiet's 'switch' condition minimises significantly the discontinuity observed at $\mu_a = \pi/4$ for low θ values, as shown in Fig. E.1.

Note that the modified 'switch' condition introduced in this appendix has been applied to the single airfoil model presented in Chapter 6, but not to the BRWI model in Chapter 2. The discontinuity between $\mathcal{L}^{\mathrm{LE}}_{low}$ and $\mathcal{L}^{\mathrm{LE}}_{high}$ at $\mu_a = \pi/4$ has not been observed to be a problem for the BRWI model described in Chapter (2), except at very low frequency, due to the large amount of averaging associated with the summations over indices q, m and n.

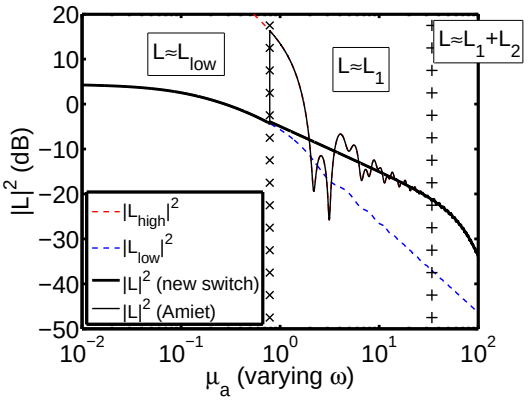

(a) $\theta = 20°$

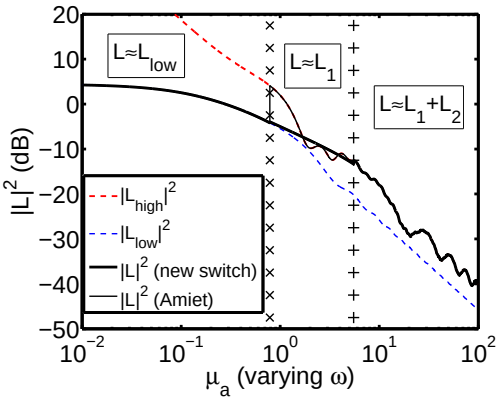

(b) $\theta = 45°$

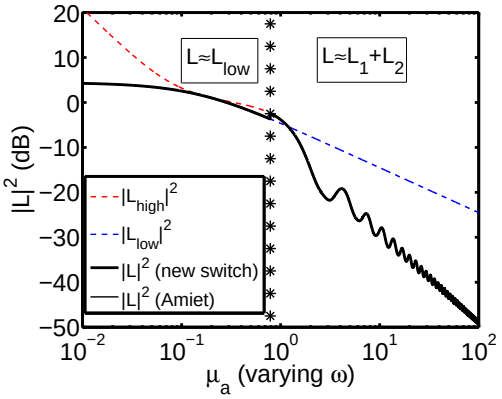

(c) $\theta = 90°$

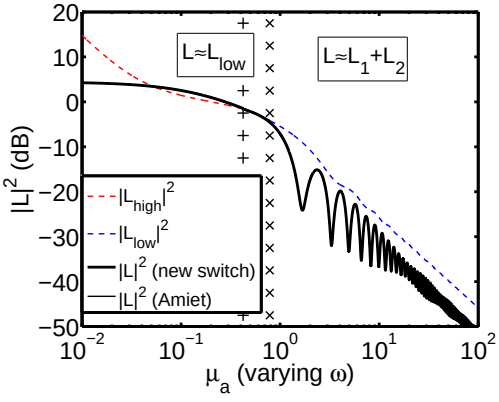

(d) $\theta = 135°$

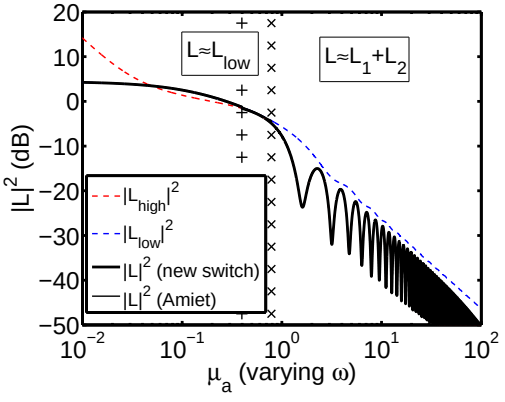

(e) $\theta = 160°$

Figure E.1: Non-dimensional unsteady lift $\left|\mathcal{L}^{\mathrm{LE}}\right|^2$ as a function of μ_a (varying ω) using Amiet's condition ($\times$) and the new condition ($+$) for the 'switch' between low and and high frequency response functions. $M = 0.8$ and (a) $\theta = 20°$, (b) $\theta = 45°$, (c) $\theta = 90°$, (d) $\theta = 135°$ and (e) $\theta = 160°$.

Bibliography

[1] M. Abramowitz and I. A. Stegun. *Handbook of Mathematical Functions with Formulas, Graphs, and Mathematical Table.* Courier Dover Publications, 1965.

[2] ACARE2020. European Aeronautics: A Vision for 2020. 2001 (accessed January 17, 2011). `http://www.acare4europe.org`.

[3] J. J. Adamczyk. Passage of a swept airfoil through an oblique gust. *Journal of Aircraft*, 11(5):281–287, 1974.

[4] Airbus. *Airbus Global Market Forecast 2010-2029*, 2010 (accessed January 17, 2011). `http://www.airbus.com/fileadmin/media_gallery/files/brochures_publications/Global_Market_Forecast/Airbus_Global_Market_Forecast_-_2010-2029.pdf`.

[5] R. K. Amiet. Compressibility effects in unsteady thin-airfoil theory. *AIAA Journal*, 12(2):252–255, 1974.

[6] R. K. Amiet. Acoustic radiation from an airfoil in a turbulent stream. *Journal of Sound and Vibration*, 41(4):407–420, 1975.

[7] R. K. Amiet. High frequency thin-airfoil theory for subsonic flow. *AIAA Journal*, 14(8):1076–1082, 1976.

[8] R. K. Amiet. Noise due to turbulent flow past a trailing edge. *Journal of Sound and Vibration*, 47(3):387–393, 1976.

[9] R. K. Amiet. Noise produced by turbulent flow into a propeller or helicopter rotor. In *3rd AIAA Aeroacoustics Conference*, Paolo Alto, CA, USA, 1976.

[10] R. K. Amiet. Noise produced by turbulent flow into a propeller or helicopter rotor. *AIAA Journal*, 15(3):307–308, 1977.

[11] R. K. Amiet. Effect of the incident surface pressure field on noise due to turbulent flow past a trailing edge. *Journal of Sound and Vibration*, 57(2):305–306, 1978.

[12] R. K. Amiet. Noise due to rotor-turbulence interaction. Technical Report 19780024880, NASA, 1978.

[13] R. K. Amiet. Noise produced by turbulent flow into rotor: Theory manual for noise calculation. Technical Report 181788, NASA, 1989.

[14] R. K. Amiet, J. C. Simonich, and R. H. Schlinker. Rotor noise due to atmospheric turbulence ingestion. part ii. aeroacoustic results. *Journal of Aircraft*, 27(1):15–22, 1990.

[15] H. M. Atassi, A. A. Ali, O. V. Atassi, and I. V. Vinogradov. Scattering of incident disturbances by an annular cascade in a swirling flow. *Journal of Fluid Mechanics*, 499:111–138, 2004.

[16] H. M. Atassi, M. Dusey, and C. M. Davis. Acoustic radiation from a thin airfoil in nonuniform subsonic flows, AIAA Journal. *AIAA Journal*, 31(1):12–19, 1993.

[17] M. Barbarino, A. Pagano, and D. Casalino. Aeroacoustic optimization of a pusher propeller. In *14th CEAS-ASC Workshop on Aeroacoustics of high-speed aircraft propellers and open-rotors*, Warsaw, Poland, 2010.

[18] D. M. Black, R. W. Menthe, and H. S. Wainauski. Aerodynamic Design and Performance Testing of an Advanced 30 Swept, Eight Bladed Propeller at Mach Numbers from 0.2 to 0.85. Technical Report 3047, NASA, 1978.

[19] V. P. Blandeau and P. F. Joseph. A semi-analytical model for the prediction of broadband noise due to wake-rotor interaction in contra-rotating propfans. In *16th International Congress on Sound and Vibration*, Krakow, Poland, 2009.

[20] V. P. Blandeau and P. F. Joseph. Broadband noise due to rotor-wake/rotor interaction in contra-rotating open rotors. *AIAA Journal*, 48(11):2674–2686, 2010.

[21] V. P. Blandeau and P. F. Joseph. Broadband noise predictions from uninstalled contra-rotating open rotors. In *14th CEAS-ASC Workshop on Aeroacoustics of high-speed aircraft propellers and open-rotors*, Warsaw, Poland, 2010.

[22] V. P. Blandeau and P. F. Joseph. On the validity of Amiet's model for propeller trailing-edge noise. In *16th AIAA/CEAS Aeroacoustics Conference*, Stockholm, Sweden, 2010.

[23] V. P. Blandeau and P. F. Joseph. Parameter study of the broadband noise from uninstalled contra-rotating open rotors. In *14th CEAS-ASC Workshop on Aeroacoustics of high-speed aircraft propellers and open-rotors*, Warsaw, Poland, 2010.

[24] V. P. Blandeau and P. F. Joseph. On the validity of Amiet's model for propeller trailing-edge noise. *AIAA Journal*, 49:in press, 2011.

[25] V. P. Blandeau, P. F. Joseph, and G. Gabard. Sound power radiation due to an isolated airfoil in a turbulent stream. In *Proc. of 20th International Congress on Acoustics*, Sydney, Australia, 2010.

[26] V. P. Blandeau, P. F. Joseph, G. Jenkins, and C. J. Powles. Comparison of sound power radiation from isolated airfoils and cascades in a turbulent flow. *Journal of the Acoustical Society of America*, 129:in press, 2011.

[27] V. P. Blandeau, P. F. Joseph, and A. B. Parry. Broadband noise predictions from uninstalled contra-rotating open rotors. *International Journal of Aeroacoustics*, 10:in press, 2011.

[28] V. P. Blandeau, P. F. Joseph, and B. J. Tester. Broadband noise prediction from rotor-wake interaction in contra-rotating propfans. In *15th AIAA/CEAS Aeroacoustics Conference*, Miami, FL, USA, 2009.

[29] P. J. W. Block. Noise radiation patterns of counter-rotation and unsteadily loaded single-rotation propellers. *Journal of Aircraft*, 22(9):776–783, 1985.

[30] P. J. W. Block. Experimental study of the effects of installation on single and counter-rotation propeller noise. Technical Report 2541, NASA, 1986.

[31] P. J. W Block and C. L. Gentry. Directivity and trends of noise generated by a propeller in a wake. Technical Report 2609, NASA, 1986.

[32] P. J. W. Block, R. J. Klatte, and P. M. Druez. Counter-rotating propeller noise directivity and trends. In *10th AIAA/CEAS Aeroacoustics Conference*, Seattle, WA, USA, 1986.

[33] Boeing. *Current Market Outlook 2010-2029*, 2010 (accessed January 17, 2011). `http://www.boeing.com/commercial/cmo/pdf/Boeing_Current_Market_Outlook_2010_to_2029.pdf`.

[34] P. Bradshaw. 'Inactive' motion and pressure fluctuations in turbulent boundary layers. *Journal of Fluid Mechanics*, 30(2):241–258, 1967.

[35] T. F. Brooks and T. H. Hodgson. Trailing edge noise prediction from measured surface pressures. *Journal of Sound and Vibration*, 78(1r):69–117, 1981.

[36] T. F. Brooks, D. S. Pope, and M. A. Marcolini. Airfoil self-noise and prediction. Technical Report 1218, NASA, 1989.

[37] D. Casalino, M. Jacob, and M. Roger. Prediction of rod-airfoil interaction noise using the Ffowcs-Williams-Hawkings analogy. *AIAA Journal*, 41(2):182–191, 2003.

[38] J. Casper and F. Farassat. A new time domain formulation for broadband noise predictions. *international Journal of Aeroacoustics*, 1(3):207–240, 2002.

[39] J. Casper and F. Farassat. Broadband trailing edge noise predictions in the time domain. *Journal of Sound and Vibration*, 271:159–176, 2004.

[40] K. L. Chandiramani. Diffraction of evanescent waves, with applications to aerodynamically scattered sound and radiation from unbaffled plates. *Journal of the Acoustical Society of America*, 55:19, 1974.

[41] C. J. Chapman. Similarity variables for sound radiation in a uniform flow. *Journal of Sound and Vibration*, 233(1):157–164, 2000.

[42] D. M. Chase. Sound Radiated by Turbulent Flow off a Rigid Half-Plane as Obtained from a Wavevector Spectrum of Hydrodynamic Pressure. *Journal of the Acoustical Society of America*, 52:1011, 1972.

[43] D. M. Chase. Noise radiated from an edge in turbulent flow. *AIAA Journal*, 13:1041–1047, 1975.

[44] D. M. Chase. Modeling the wavevector-frequency spectrum of turbulent boundary layer wall pressure. *Journal of Sound and Vibration*, 70(1):29 – 67, 1980.

[45] C. Cheong, P. Joseph, and S. Lee. High frequency formulation for the acoustic power spectrum due to cascade-turbulence interaction. *Journal of the Acoustical Society of America*, 119(1):108–122, 2006.

[46] Y. Colin. CFD predictions to aid rig design and performance analyses. In *DREAM M24 review*, Paris, France, 2010.

[47] G. M. Corcos. The structure of the turbulent pressure field in boundary-layer flows. *Journal of Fluid Mechanics*, 18(3):353–378, 1964.

[48] D. G. Crighton and F. G. Leppington. Scattering of aerodynamic noise by a semi-infinite compliant plate. *Journal of Fluid Mechanics*, 43(04):721–736, 1970.

[49] B. de Gouville, M. Roger, and J. M. Cailleau. Prediction of fan broadband noise. In *4th AIAA/CEAS Aeroacoustic Conference*, Toulouse, France, 1998.

[50] W. J. Devenport, J. K. Staubs, and S. A. L. Glegg. Sound radiation from real airfoils in turbulence. *Journal of Sound and Vibration*, 329:3470–3483, 2010.

[51] M. Dieste and G. Gabard. Random-Vortex-Particle Methods for Broadband Fan Interaction Noise. In *16th AIAA/CEAS Aeroacoustics Conference*, Stockholm, Sweden, 2010.

[52] J. H. Dittmar. Cruise noise of counterrotation propeller at angle of attack in wind tunnel. Technical Report 88869, NASA, 1986.

[53] J. H. Dittmar and D. B. Stang. Noise reduction for model counterrotation propeller at cruise by reducing aft-propeller diameter. Technical report, NASA, 1987.

[54] DREAM. valiDation of Radical Engine Architecture systeMs. *FP7 European project*, 2007 (accessed January 17, 2011). `http://www.dream-project.eu`.

[55] M. Drela. *Low Reynolds numbers aerodynamics, Lecture Notes in Engineering*, volume 54, chapter XFOIL: an analysis and design system for low Reynolds number airfoils, pages 1–12. Springer, 1989.

[56] M. Drela and M. Giles. Viscous-inviscid analysis of transonic and low Reynolds number airfoils. *AIAA Journal*, 25(10):1347–1355, 1987.

[57] E. Envia. NASA Open Rotor Noise Research. In *14th CEAS-ASC Workshop on Aeroacoustics of high-speed aircraft propellers and open-rotors*, Warsaw, Poland, 2010.

[58] I. Evers and N. Peake. On sound generation by the interaction between turbulence and a cascade of airfoils with non-uniform mean flow. *Journal of Fluid Mechanics*, 463:25–52, 2002.

[59] R. Ewert, J. Dierke, A. Neifeld, C. Appel, M. Siefert, and O. Kornow. Caa broadband noise prediction for aeroacoustic design. In *IUTAM Symposium on Computational Aero-Acoustics for Aircraft Noise Prediction*, Southampton, UK, 2010.

[60] F. Farassat, M. H. Dunn, A. F. Tinetti, and D. M. Nark. Open rotor noise prediction methods at nasa langley - a technology review. In *15th AIAA/CEAS Aeroacoustics Conference*, Miami, FL, USA, 2009.

[61] D. Fedala, S. Kouidri, R. Rey, T. Carolus, and M. Schneider. Incident turbulence interaction noise from an axial fan. In *12th AIAA/CEAS Aeroacoustics Conference*, Cambridge, MA, USA, 2006.

[62] J. E. Ffocws Williams and L. H. Hall. Aerodynamic sound generation by turbulent flow in the vicinity of a scattering half plane. *Journal of Fluid Mechanics*, 40(4):657–670, 1970.

[63] J. E. Ffowcs Williams and D. L. Hawkings. Sound generation by turbulence and surfaces in arbitrary motion. *Philosophical Transactions of the Royal Society of London A (Mathematical and Physical Sciences)*, 264(1151):321–342, 1969.

[64] J. E. Ffowcs Williams and D. L. Hawkings. Theory relating to the noise of rotating machinery. *Journal of Sound and Vibration*, 10(1):10–21, 1969.

[65] L. T. Filotas. Response of an Infinite Wing to an Oblique Sinusoidal Gust: A Generalization of Sears' Problem. *NASA Special Publication*, 207:231, 1969.

[66] S. Fujii, H. Nishiwaki, and K. Takeda. Noise performance of a counter-rotation propeller. *Journal of Aircraft*, 23(9):719–724, 1986.

[67] U. W. Ganz, P. D. Joppa, T. J. Patten, and D. F. Scharpf. Boeing 18-inch fan rig broadband noise test. Technical report, Nasa, 1998.

[68] A. Garcia Sagrado. *Boundary Layer and Trailing Edge Noise Sources*. PhD thesis, University of Cambridge, 2007.

[69] A. R. George and S. T. Chou. Broadband rotor noise analyses. Technical Report 3797, NASA, 1984.

[70] J. Gershfeld. Leading edge noise from thick foils in turbulent flows. *Journal of the Acoustical Society of America*, 116:1416, 2004.

[71] S. A. L. Glegg. Airfoil self-noise generated in a cascade. *AIAA Journal*, 36:1575–1582, 1998.

[72] S. A. L. Glegg. The response of a swept blade row to a three-dimensional gust. *Journal of Sound and Vibration*, 227(1):29–64, 1999.

[73] S. A. L. Glegg, S. M. Baxter, and A. G. Glendinning. The prediction of broadband noise from wind turbines. *Journal of Sound and Vibration*, 118(2):217–239, 1987.

[74] S. A. L. Glegg and W. Devenport. Unsteady loading on an airfoil of arbitrary thickness. *Journal of Sound and Vibration*, 319(3-5):1252–1270, 2009.

[75] S. A. L. Glegg and W. J. Devenport. Panel method for airfoils in turbulent flow. *Journal of Sound and Vibration*, 329:3709–3720, 2010.

[76] S. A. L. Glegg and C. Jochault. Broadband self-noise from a ducted fan. *AIAA Journal*, 36(8):1387–1395, 1998.

[77] P. Gliebe, R. Mani, H. Shin, B. Mitchell, and G. Ashford. Aeroacoustic prediction codes. Technical Report 210244, NASA, 2000.

[78] M. Goody. Empirical spectral model of surface pressure fluctuations. *AIAA Journal*, 42(9):1788–1794, 2004.

[79] J. M. R. Graham. Lifting surface theory for the problem of an arbitrarily yawed sinusoidal gust incident on a thin aerofoil in incompressible flow. *Aeronautical Quarterly*, 21:182–198, 1970.

[80] J. M. R. Graham. Similarity rules for thin aerofoils in non-stationary subsonic flows. *Journal of Fluid Mechanics*, 43:753–66, 1970.

[81] W. R. Graham. A Comparison of Models for the Wavenumber-Frequency Spectrum of Turbulent Boundary Layer Pressures. *Journal of Sound and Vibration*, 206(4):541–565, 1997.

[82] L. Gutin. Über das Schallfeld einer rotierenden Luftschraube. *Physikalische Zeitschrift de Sowjetunion*, 9:1, 1936.

[83] L. Gutin. On the Sound Field of a Rotating Propeller. Technical report, NACA Technical Memorandum, 1948.

[84] D. B. Hanson. Helicoidal surface theory for harmonic noise of propellers in the far field. *AIAA Journal*, 18(10):1213–1220, 1980.

[85] D. B. Hanson. Noise of counter-rotation propellers. *Journal of Aircraft*, 22(7):609–617, 1985.

[86] D. B. Hanson. Theory for broadband noise of rotor and stator cascades with inhomogeneous inflow turbulence including effects of lean and sweep. Technical Report 210762, NASA, 2001.

[87] D. B. Hanson and K. P. Horan. Turbulence/cascade interaction: spectra of inflow, cascade response, and noise. In *4th AIAA/CEAS Aeroacoustic Conference*, Toulouse, France, 1998.

[88] G. F. Homicz and A. R. George. Broadband and discrete frequency radiation from subsonic rotors. *Journal of Sound and Vibration*, 36(2):151–177, 1974.

[89] M. S. Howe. A review of the theory of trailing edge noise. *Journal of Sound and Vibration*, 61(3):437–465, 1978.

[90] M. S. Howe. *Acoustics of fluid-structure interactions*. Cambridge University Press, 1998.

[91] M. S. Howe. Edge-source acoustic green's function for an airfoil of arbitrary chord, with application to trailing-edge noise. *The Quarterly Journal of Mechanics and Applied Mathematics*, 54(1):139, 2001.

[92] H. H. Hubbard. Sound from dual-rotating and multiple single-rotating propellers. Technical Report 1654, NACA, 1948.

[93] H. H. Hubbard. *Aeroacoustics of flight vehicles. Theory and practice volume 1. Noise sources*, volume 1. NASA Reference Publication, 1991.

[94] Y. F. Hwang, W. K. Bonness, and S. A. Hambric. Comparison of semi-empirical models for turbulent boundary layer wall pressure spectra. *Journal of Sound and Vibration*, 319(1-2):199–217, 2009.

[95] J. Ricouard, E. Julliard, M. Omaïs, V.Regnier, A. B. Parry and S. Baralon. Installation effects on contra-rotating open rotor noise. In *16th AIAA/CEAS Aeroacoustics Conference*, Stockholm, Sweden, 2010.

[96] L. E. Jones, R. D. Sandberg, and N. D. Sandham. Direct numerical simulations of noise generated by turbulent flow over airfoils. In *14th AIAA/CEAS Aeroacoustics Conference*, Vancouver, Canada, 2008.

[97] V. Jurdic, P. Joseph, and J. Antoni. Investigation of rotor wake turbulence through cyclostationary spectral analysis. *AIAA Journal*, 47(9):2022–2030, 2009.

[98] V. Jurdic, A. Moreau, P. F. Joseph, L. Enghardt, and J. Coupland. A comparison between measured and predicted fan broadband noise due to rotor-stator interaction. In *13th AIAA/CEAS Aeroacoustics Conference*, Rome, Italy, 2007.

[99] W. L. Keith, D. A. Hurdis, and B. M. Abraham. A comparison of turbulent boundary layer wall-pressure spectra. *Journal of Fluids Engineering*, 114(3):338–347, 1992.

[100] Y. N. Kim and A. R. George. Trailing-edge noise from hovering rotors. *AIAA Journal*, 20(9):1167–1174, 1982.

[101] M. J. Kingan and R. H. Self. Counter-Rotation Propeller Tip Vortex Interaction Noise. In *15th AIAA/CEAS Aeroacoustics Conference*, Miami, FL, USA, 2009.

[102] T. J. Kirker. Procurement and testing of a 1/5 scale advanced counter rotating propfan model. In *13th AIAA Aeroacoustics Conference*, Tallahassee, FL, USA, 1990.

[103] M. T. Landahl. *Unsteady Transonic Flow*. Pergamon Press, 1961.

[104] M. J. Lighthill. On sound generated aerodynamically. I. General theory. *Proceedings of the Royal Society of London. Series A, Mathematical and Physical Sciences*, 211(1107):564–587, 1952.

[105] A. E. D. Lloyd and N. Peake. Rotor - stator broadband noise prediction. In *14th AIAA/CEAS Aeroacoustics Conference*, Vancouver, Canada, 2008.

[106] M. V. Lowson. The sound field for singularities in motion. *Proceedings of the Royal Society of London. Series A, Mathematical and Physical Sciences*, 286, No 1407:559–572, 1965.

[107] B. Magliozzi, P. Brown, and D. Parzych. Acoustic test and analysis of a counterrotating prop-fan model. Technical Report 179590, NASA, 1987.

[108] R. K. Majjigi, K. Uenishi, and P. R. Gliebe. An investigation of counterrotating tip vortex interaction. Technical Report 185135, NASA, 1989.

[109] R. Mani. Noise due to interaction of inlet turbulence with isolated stators and rotors. *Journal of Sound and Vibration*, 17(2):251–260, 1971.

[110] F. B. Metzger and P. C. Brown. Results of acoustic tests of a prop-fan model. *Journal of Aircraft*, 25(7):653–658, 1988.

[111] S. Moreau and M. Roger. Competing broadband noise mechanisms in low-speed axial fans. *AIAA Journal*, 45(1):48–57, 2007.

[112] S. Moreau and M. Roger. Back-scattering correction and further extensions of amiet's trailing-edge noise model. part ii: Application. *Journal of Sound and Vibration*, 323(1-2):397–425, 2009.

[113] C. L. Morfey. Acoustic energy in non-uniform flows. *Journal of Sound and Vibration*, 14(2):159–170, 1971.

[114] C. L. Morfey and H. K. Tanna. Sound radiation from a point force in circular motion. *Journal of Sound and Vibration*, 15(3):325–351, 1971.

[115] M. Nallasamy and E. Envia. Computation of rotor wake turbulence noise. *Journal of Sound and Vibration*, 282(3-5):649–678, 2005.

[116] S. Oerlemans, P. Sijtsma, and B. Mendez Lopez. Location and quantification of noise sources on a wind turbine. *Journal of Sound and Vibration*, 299(4-5):869–883, 2007.

[117] Omaïs, M. Experimental and numerical analysis of the pylon-rotor interaction noise radiated by a Contra Rotating Open Rotor. In *14th CEAS-ASC Workshop on Aeroacoustics of high-speed aircraft propellers and open-rotors*, Warsaw, Poland, 2010.

[118] C. Osborne. Unsteady thin-airfoil theory for subsonic flow. *AIAA Journal*, 11(2):205–209, 1973.

[119] A. Pagano, M. Barbarino, D. Casalino, and L. Federico. Tonal and broadband noise calculations for aeroacoustic optimization of pusher propeller. *Journal of Aircraft*, 47(3):835–848, 2010.

[120] A. Pagano, L. Federico, M. Barbarino, F. Guida, and M. Aversano. Multi-objective Aeroacoustic Optimization of an Aircraft Propeller. In *12th AIAA/ISSMO Multidisciplinary Analysis and Optimization Conference*, Victoria, Canada, 2008.

[121] A. B. Parry. *Theoretical Prediction of Counter-rotating Propeller Noise*. PhD thesis, University of Leeds, 1988.

[122] A. B. Parry and D. G. Crighton. Prediction of counter-rotation propeller noise. In *12th AIAA Aeroacoustics Conference*, San Antonio, TX, USA, 1989.

[123] R. W. Paterson and R. K. Amiet. Acoustic radiation and surface pressure characteristics of an airfoil due to incident turbulence. Technical Report 2733, NASA, 1976.

[124] R. W. Paterson and R. K. Amiet. Noise and surface pressure response of an airfoil to incident turbulence. *Journal of Aircraft*, 14(8):729–736, 1977.

[125] R. W. Paterson and R. K. Amiet. Noise of a model helicopter rotor due to ingestion of turbulence. Technical Report 3213, NASA, 1979.

[126] N. Peake. The scattering of vorticity waves by an infinite cascade of flat plates in subsonic flow. *Wave Motion*, 18(3):255–271, 1993.

[127] H. Posson, S. Moreau, and M. Roger. Fan-ogv broadband noise prediction using a cascade response. In *15th AIAA/CEAS Aeroacoustics Conference*, Miami, FL, USA, 2009.

[128] H. Posson, S. Moreau, and M. Roger. On the use of a uniformly valid analytical cascade response function for fan broadband noise predictions. *Journal of Sound and Vibration*, 329:3721–3743, 2010.

[129] H. Posson, M. Roger, and S Moreau. On a uniformly valid analytical rectilinear cascade response function. *Journal of Fluid Mechanics*, 663:in press, 2010.

[130] M. Roger and S. Moreau. Back-scattering correction and further extensions of amiet's trailing-edge noise model. part 1: theory. *Journal of Sound and Vibration*, 286(3):477–506, 2005.

[131] M. Roger and S. Moreau. Extension and limitations of analytical airfoils broadband noise models. *International Journal of Aeroacoustics*, 9(3):273–305, 2010.

[132] M. Roger, S. Moreau, and A. Guedel. Broadband fan noise prediction using single-airfoil theory. *Noise Control Engineering Journal*, 54(1):5–14, 2006.

[133] Y. Rozenberg. *Modélisation analytique du bruit aérodynamique à large bande des machines tournantes : utilisation de calculs moyennés de mécanique des fluides.* PhD thesis, École centrale de Lyon, 2007.

[134] Y. Rozenberg, M. Roger, and S. Moreau. Rotating blade trailing-edge noise: Experimental validation of analytical model. *AIAA Journal*, 48(5):951–962, 2010.

[135] R. D. Sandberg and L. E. Jones. Direct numerical simulations of airfoil self-noise. *Procedia Engineering*, 6:274 – 282, 2010. IUTAM Symposium on Computational Aero-Acoustics for Aircraft Noise Prediction.

[136] R. D. Sandberg and N. D. Sandham. Direct numerical simulation of turbulent flow past a trailing edge and the associated noise generation. *Journal of Fluid Mechanics*, 596:353–385, 2008.

[137] R. D. Sandberg, N. D. Sandham, and P. F. Joseph. Direct numerical simulations of trailing-edge noise generated by boundary-layer instabilities. *Journal of Sound and Vibration*, 304(3-5):677–690, 2007.

[138] R. H. Schlinker and R. K. Amiet. Helicopter rotor trailing edge noise. Technical Report 3470, NASA, 1981.

[139] J. R. Scott and H. M. Atassi. A finite-difference, frequency-domain numerical scheme for the solution of the gust response problem. *Journal of Computational Physics*, 119(1):75–93, 1995.

[140] W. J. Sears. Some aspects of non-stationary airfoil theory and its practical applications. *Journal of Aeronautical Sciences*, 8(3):104–108, 1941.

[141] H. Siller and S. Funke. Acoustic measurements of a counter rotating open rotor in the DREAM project. In *14th CEAS-ASC Workshop on Aeroacoustics of high-speed aircraft propellers and open-rotors*, Warsaw, Poland, 2010.

[142] S. Sinayoko, P. Joseph, and A. McAlpine. Multimode radiation from an unflanged, semi-infinite circular duct with uniform flow. *Journal of the Acoustical Society of America*, 127:2159–2168, 2010.

[143] S. N. Smith. Discrete frequency sound generation in axial flow turbomachines. *Reports and memoranda, Aeronautical Research Control Council, London*, 3709, 1972.

[144] P. Spalart, A. K. Travin, M. L. Shur, and M. K. Strelets. Initial Noise Predictions for Open Rotors Using First Principles. In *16th AIAA/CEAS Aeroacoustics Conference*, Stockholm, Sweden, 2010.

[145] W. C. Strack, G. Knip, A. L. Weisbrich, J. Godston, and E. Bradley. Technology and benefits of aircraft counter rotation propellers. Technical Report 82983, NASA, 1981.

[146] A. Stuermer and J. Yin. Low-Speed Aerodynamics and Aeroacoustics of CROR Propulsion Systems. In *15th AIAA/CEAS Aeroacoustics Conference*, Miami, FL, USA, 2009.

[147] A. Stuermer and J. Yin. Low-Speed Aerodynamics and Aeroacoustics of CROR Propulsion Systems. In *28th AIAA Applied Aerodynamics Conference*, Chicago, IL, USA, 2010.

[148] C. S. Ventres, M. A. Theobald, and W. D. Mark. Turbofan noise generation. volume 1: Analysis. Technical Report 167951, NASA, 1982.

[149] D. S. Whitehead. Classical two-dimensional methods. *In Manual on Aeroelasticity in Axial-Flow Turbomachines: Unsteady Turbomachinery Dynamics*, 1:1–22, 1987.

[150] C. E. Whitfield, P. R. Gliebe, R. Mani, and P. Mungur. High speed turboprop aeroacoustic study (counter-rotation), vol. 1: Model development. Technical Report 185241, NASA, 1990.

[151] C. E. Whitfield, R. Mani, and P. R. Gliebe. High speed turboprop aeroacoustic study (counter-rotation), vol. 2: Computer programs. Technical Report 185242, NASA, 1990.

[152] W. W. Willmarth and F. W. Roos. Resolution and structure of the wall pressure field beneath a turbulent boundary layer. *Journal of Fluid Mechanics*, 22(01):81–94, 1965.

[153] R. P. Woodward, D. G. Hall, G. G. Podboy, and R. J. Jeracki. Takeoff/approach noise for a model counterrotation propeller with a forward-swept upstream rotor. Technical Report 105979, NASA, 1993.

[154] R. P. Woodward, I. J. Loeffler, and J. H. Dittmar. Measured far-field flight noise of a counterrotation turboprop at cruise conditions. Technical Report 101383, NASA, 1989.

[155] I. Wygnanski, F. Champagne, and B. Marasli. On the large-scale structures in two-dimensional, small-deficit, turbulent wakes. *Journal of Fluid Mechanics*, 168:31–71, 1986.

[156] J. C. Yu and M. C. Joshi. On sound radiation from the trailing edge of an isolated airfoil in a uniform flow. Technical Report AIAA-1979-603, AIAA, 1979.

[157] A. Zachariadis. *Open rotor design for low noise.* PhD thesis, Whittle Laboratory, University of Cambridge, 2010.

[158] Q. Zhou. *A model for rotor broadband noise prediction.* PhD thesis, University of Southampton, ISVR, 2004.

[159] Q. Zhou and P. F. Joseph. Frequency-domain method for rotor self-noise prediction. *AIAA Journal*, 44(6):1197–1206, 2006.